

Diss. ETH No. 30039

Testing Lepton Flavour Universality: A Measurement of the
 $R(J/\psi)$ Ratio at CMS

A thesis submitted to attain the degree of
DOCTOR OF SCIENCES
(Dr. sc. ETH Zurich)

presented by
Federica Riti
M.Sc. Physics
University of Rome “La Sapienza”
born on 12 March 1995

accepted on the recommendation of
Prof. Dr. Günther Dissertori, examiner
Prof. Dr. Anna Soter, co-examiner
Prof. Dr. Shahram Rahatlou, co-examiner

2024

Federica Riti: *Testing Lepton Flavour Universality: A Measurement of the $R(J/\psi)$ Ratio at CMS*, © 2024

A mamma

Abstract

This thesis presents a search for lepton flavour universality violation through semileptonic B_c meson decays in the CMS experiment at the Large Hadron Collider.

The Standard Model of particle physics, while successful in unifying the electromagnetic, weak, and strong interactions and in accurately predicting various phenomena that have been measured with extreme precision by multiple experiments, remains incomplete. In fact, it does not incorporate gravity and fails to provide explanations for certain experimental phenomena. Therefore, efforts are underway to test the Standard Model predictions and identify potential deviations. An interesting field to investigate is the lepton flavour universality, an accidental symmetry that implies identical couplings in electroweak interactions for all leptons. Several measurements challenge this symmetry and suggest a potential deviation from its predictions, making this a compelling field for exploring physics beyond the Standard Model.

This thesis focuses on the search for lepton flavour universality violation, with the measurement of $R(J/\psi) = \mathcal{B}(B_c^+ \rightarrow J/\psi \tau^+ \nu_\tau) / \mathcal{B}(B_c^+ \rightarrow J/\psi \mu^+ \nu_\mu)$, using data from proton-proton collisions at 13 TeV centre-of-mass energy collected by the CMS experiment in 2018, corresponding to an integrated luminosity of 59.7 fb^{-1} . Both decays of interest, $B_c^+ \rightarrow J/\psi \tau^+ \nu_\tau$ and $B_c^+ \rightarrow J/\psi \mu^+ \nu_\mu$, have three muons in the final state, considering that only the muonic decays of the τ and J/ψ meson are considered, enabling simultaneous reconstruction. The CMS detector high-efficiency muon recognition plays a crucial role, allowing for the accurate identification and reconstruction of the final state muons.

Since neutrinos, present in both signals final states, escape detection, it is not possible to fully reconstruct the B_c resonance. Therefore there is no invariant mass peak and template fits are employed to analyse the data. Kinematic variables that leverage the difference between the number of final state neutrinos for the two signals are used, together with topological variables, which are employed to distinguish the signals and measure and constrain the background contributions. The dominant background includes hadrons incorrectly reconstructed as muons, and its contribution is extracted from data.

A simultaneous fit of the two signals is performed, resulting in the measurement of the $R(J/\psi)$ value. The final result, $R(J/\psi) = 0.17^{+0.18}_{-0.17}$ (stat) $^{+0.21}_{-0.22}$ (syst) $^{+0.19}_{-0.18}$ (theo), aligns with the SM prediction within 0.3σ and is compatible with previous measurements. This result shows the potential of the CMS experiment in exploring lepton flavour universality violation and contributing significantly to the search for new physics.

Abstract

Questa tesi presenta una ricerca di violazione dell'universalità del sapore dei leptoni attraverso la misura di decadimenti semileptonici dei mesoni B_c , utilizzando dati raccolti dall'esperimento CMS presso il Large Hadron Collider.

Il Modello Standard della fisica delle particelle, sebbene spieghi con successo l'unificazione delle interazioni elettromagnetiche, deboli e forti e predica accuratamente molti fenomeni che sono stati misurati con estrema precisione da vari esperimenti, non è completo. Infatti non include la quarta interazione fondamentale, la gravità, e non fornisce spiegazioni per alcuni fenomeni sperimentali. Di conseguenza, numerosi test e misure sono in corso per verificare le predizioni del Modello Standard e individuare eventuali deviazioni. Un campo interessante da esplorare è quello dell'universalità del sapore dei leptoni, una simmetria accidentale che implica gli stessi accoppiamenti nelle interazioni elettrodeboli per tutti i leptoni. Diversi risultati sperimentali suggeriscono una possibile deviazione dalle previsioni, rendendolo un campo promettente per esplorare la fisica oltre il Modello Standard.

Questa tesi si concentra sulla ricerca di violazioni dell'universalità del sapore dei leptoni, attraverso la misura del rapporto $R(J/\psi) = \mathcal{B}(B_c^+ \rightarrow J/\psi \tau^+ \nu_\tau) / \mathcal{B}(B_c^+ \rightarrow J/\psi \mu^+ \nu_\mu)$, utilizzando dati provenienti da collisioni protone-protone a un'energia nel centro di massa di 13 TeV, raccolti dall'esperimento CMS nel 2018, che corrispondono ad una luminosità integrata di 59.7 fb^{-1} . Entrambi i decadimenti di interesse, $B_c^+ \rightarrow J/\psi \tau^+ \nu_\tau$ e $B_c^+ \rightarrow J/\psi \mu^+ \nu_\mu$, presentano tre muoni nello stato finale, poiché solo i decadimenti muonici del leitone τ e del mesone J/ψ sono selezionati, consentendo una ricostruzione simultanea. L'efficienza del rivelatore CMS nel riconoscere e ricostruire i muoni è cruciale in questa analisi, poiché consente l'identificazione e la ricostruzione accurata dei muoni nello stato finale.

Poiché i neutrini, presenti nello stato finale per entrambi i segnali, non sono rivelati, non è possibile ricostruire la risonanza del mesone B_c . Quindi, in mancanza di un picco di massa invariante, viene utilizzato un template fit. Vengono scelte variabili cinematiche che sfruttano la differenza tra il numero di neutrini nello stato finale dei due segnali, insieme a variabili topologiche, per distinguere i due segnali e misurare i contributi del fondo. Il fondo dominante comprende adroni ricostruiti

come muoni ed è estratto dai dati.

Viene eseguito un fit simultaneo dei due segnali, che restituisce la misura del valore di $R(J/\psi)$. Il risultato finale, $R(J/\psi) = 0.17^{+0.18}_{-0.17}$ (stat) $^{+0.21}_{-0.22}$ (sist) $^{+0.19}_{-0.18}$ (teor), si allinea con la previsione del Modello Standard entro 0.3σ ed è compatibile con misure precedenti. Il risultato dimostra il potenziale dell'esperimento CMS nell'esplorare violazioni dell'universalità del sapore dei leptoni e contribuire in modo significativo alla ricerca di nuova fisica in questo ambito.

Acknowledgements

First of all, I am deeply grateful to Günther for the amazing opportunity to pursue my PhD in his group and for believing in me from the very beginning. Even with his busy schedule and many responsibilities, I have always felt that I could reach out to him.

Special thanks goes to Riccardo for his invaluable contribution to this thesis. It is impossible to enumerate all that he has done for me during the PhD. His guidance and support have been incredibly important in these four years. Our regular discussions and brainstorming in the offices were both enjoyable and enriching, also thanks to his extensive knowledge in physics and incredible intuition. Riccardo has always been open, available, and easy to talk to, which have made me feel comfortable in asking questions and possibly sharing personal matters. Beyond his mentorship for this project, I am deeply grateful for his interest in my professional growth. I consider myself extremely lucky to have had the opportunity to work with him and to have learned so much from his expertise.

My gratitude also goes to the fellow member of the $R(J/\psi)$ team, Luigi, and the members of the $R(J/\psi)$ hadronic channel, particularly Yuta and Camilla, for the exchange of ideas, sharing of material, and constructive discussions. My appreciation also extends to everyone involved in the review of our analysis, with special thanks to Chiara, Rob, Alberto, Marco Pieri, and all the ARC members. Their insights and feedback were very important in improving the quality of this project.

I would also like to express my gratitude to Anna Soter for her keen interest in this project. My thanks also extend to Shahram Rahatlou for his consistent interest in my academic journey and for believing in me since my early days as a university student in his course during the bachelor.

I also want to thank all my colleagues from ETH here at CERN. They have not only been colleagues but have become friends and their presence has incredibly enriched my everyday life here. I am grateful for all the moments we have shared, from train rides to pizza parties, and everything in between. I also extend my thanks to the ETH colleagues based in Zürich. Their warm hospitality has always made me feel welcome in the Zürich offices, and their willingness to spend time

with us made the trips an enjoyable experience.

I want to thank all the friends I've made in Geneva. They have not only made my life here better, but have also given me more reasons to stay. Their friendship has provided me with a sense of family even while being far from home.

Sono profondamente grata alle mie amiche di sempre per la loro costante e positiva presenza nella mia vita. Un ringraziamento speciale va ai miei amici dell'università, che occupano un posto speciale nel mio cuore. La loro amicizia è molto preziosa per me, e anche se siamo ora sparsi per il mondo, so che il nostro legame rimarrà intatto.

Un ringraziamento speciale ad Agostino, per il suo sostegno, la sua pazienza e la sua forza. Questi anni sono stati incredibili, ma anche molto impegnativi, e sono grata di averlo affianco.

Infine, ringrazio la mia famiglia per essere stata sempre al mio fianco durante questo percorso. Un ringraziamento speciale va a mia madre, che mi ha sostenuta in ogni decisione e mi ha dato costantemente l'opportunità di perseguire le mie aspirazioni. Le sono grata per la sua pazienza, la sua fiducia in me e per l'incoraggiamento.

Contents

Introduction	1
I Theoretical and Experimental Context	3
1 The Standard Model of Particle Physics	4
1.1 Particles in the Standard Model	5
1.2 Quantum electrodynamics	6
1.3 Quantum chromodynamics	7
1.4 The electroweak interactions	9
1.4.1 The Higgs mechanism	10
1.4.2 Flavour in the quark sector	12
1.5 Beyond the Standard Model	13
2 Lepton Flavour Universality	15
2.1 Purely leptonic decays	15
2.2 The electroweak sector	17
2.3 LFU in b-quark decays	19
2.3.1 Effective Field Theory	21
2.4 SM prediction for $R(J/\psi)$	22
2.5 Experimental status of LFU tests	25
2.6 Interpretations	26
3 LHC and the CMS experiment	29
3.1 The Large Hadron Collider	29
3.1.1 Bottom quark production at the LHC	33
3.2 The CMS experiment	34
3.2.1 Coordinate system	34
3.2.2 Sub-detectors	35
3.2.3 Trigger system	39
3.2.4 Physics objects	41

II Measurement of $R(J/\psi)$ with CMS Data	46
4 Overview	47
4.1 $R(J/\psi)$ measurement at CMS	48
4.2 Analysis strategy	49
5 Event Selection	51
5.1 Data samples	51
5.2 Monte-Carlo samples	52
5.2.1 $B_c \rightarrow J/\psi + \mu$ MC sample	52
5.2.2 $H_b \rightarrow J/\psi + \mu$ MC sample	53
5.3 Triggers for $R(J/\psi)$	59
5.4 Selection	59
5.5 B_c reconstruction	62
5.6 Definition of observables	63
5.6.1 Kinematic observables	63
5.6.2 Topological observables	64
6 Background Estimation	67
6.1 H_b background	68
6.2 B_c background	69
6.3 Fakes background	70
6.3.1 Control regions definition	70
6.3.2 Measurement of ISO fake-rate fr_{ISO}	75
6.3.3 Prediction for the SR	80
6.3.4 Validation	81
6.3.5 Uncertainties on the fakes background estimation	85
6.4 Combinatorial J/ψ dimuon background	89
7 Correction of MC Simulations	93
7.1 Form factors	93
7.2 Pileup	96
7.3 B_c meson properties	97
7.3.1 B_c kinematics	97
7.3.2 B_c lifetime	101
7.3.3 Not-yet-measured B_c decays	101
7.4 Topological variables	104
7.4.1 IP3D correction	104
7.4.2 L_{xy} correction	105
7.5 J/ψ resonance kinematic properties	107
7.6 Muon efficiencies	107

7.6.1	Identification	109
7.6.2	Isolation	110
7.6.3	Trigger	111
8	Fit Strategy	115
8.1	Definition of categories	115
8.2	Fakes background method implementation	121
8.3	Systematic uncertainties	121
8.3.1	Theoretical uncertainties	121
8.3.2	Fakes background uncertainties	123
8.3.3	Uncertainties on the MC corrections	125
8.3.4	Other uncertainties	128
8.4	Blind strategy	136
8.5	Fit diagnostics	136
8.5.1	Expected sensitivity	136
8.5.2	Blind fit to data	137
8.5.3	Bias test	138
9	Results	141
9.1	Post-Fit plots	141
9.2	Final result	144
9.3	Outlook	145
Conclusions		148
Declaration of originality		150
10	Appendix	151
10.1	Form factors: additional plots	151
10.2	Fakes background checks for MC variations during fit	155
10.3	Signal injection test	156
10.4	Luminosity projection	158
10.5	“Blind” post-fit plots	158
10.6	Impacts	159
Bibliography		164

Introduction

The Standard Model (SM) of particle physics has been very successful in describing the elementary particles and their interactions. It unifies the electromagnetic, weak, and strong interactions into a unique theoretical framework. Most of the processes it describes are verified with very high precision by experiments. However, despite its ability in predicting and explaining many phenomena, the SM is not considered a complete theory. It lacks the inclusion of the gravitational interaction and many experimental phenomena, like dark matter, dark energy, and neutrino flavour oscillations, which remain unaccounted for, suggesting the existence of a broader theory that extends the SM, including physics beyond the Standard Model (BSM).

Lepton Flavour Universality (LFU), an accidental symmetry of the SM, asserts that the couplings of the three generations of leptons, i.e. electrons, muons, and tau leptons, are identical in the electroweak (EW) interactions. Deviations from LFU in experimental results could reveal the presence of physics BSM. Theorists have proposed several models that address some of the open questions of the SM and, in turn, predict such deviations, with new mediators for the electroweak interactions of third family leptons, like charged Higgs bosons, new vector bosons like W' and Z' , and leptoquarks. Not flavour-universal interactions involving leptons already exist, such as the Higgs Yukawa coupling, which couples proportionally to the mass. Therefore, it makes sense to explore the possibility of violations to this universality in other interactions.

Both direct and indirect searches are underway for these particles. Some experimental results hint towards potential deviations from LFU, noting discrepancies up to 3.3σ from the SM predictions. These results do not constitute conclusive evidence of new discoveries, but they make the search of BSM physics in the LFU field especially interesting.

In line with these considerations, this thesis presents a direct search for LFU violations. The goal is the measurement of a branching fraction ratio that includes the third family of leptons, where the deviation from the SM is hypothesised to be more visible, which is defined as $R(J/\psi) = \mathcal{B}(B_c^+ \rightarrow J/\psi \tau^+ \nu_\tau) / \mathcal{B}(B_c^+ \rightarrow J/\psi \mu^+ \nu_\mu)$. This search is performed using data collected by the CMS detector at

the Large Hadron Collider (LHC) in 2018. The LHC, the world’s largest and most powerful particle collider, accelerates protons to achieve a centre of mass energy up to 13.6 TeV. The CMS detector, which is one of the main experiments collecting data at the LHC, made it possible to perform this analysis, also thanks to its high muon detection and reconstruction efficiency.

The main challenge is due to the presence of neutrinos, that escape detection, in the final states of the two decays of interest of the $R(J/\psi)$ ratio, which results in the absence of a distinct mass peak for the B_c meson. This aspect adds complexity to the analysis, and it makes the derivation and estimation of backgrounds very central. A correct background estimation is therefore crucial, and it requires accounting for all potential decays of interest. The background coming from the misidentification of muons is especially a critical point of the analysis, due to its significant impact on the results.

This thesis is divided into two main parts. The first part gives a comprehensive theoretical and experimental context, making the foundation for the second part, where the detailed analysis of the $R(J/\psi)$ measurement is described.

Chapter 1 gives an overview of the SM, and Chapter 2 goes deeper into the LFU topic, covering both theoretical aspects and the current experimental status of LFU tests. Chapter 3 is dedicated to the LHC and the CMS experiment descriptions, with a focus on the CMS specific object reconstruction details.

Chapter 4 is the beginning of the description of the $R(J/\psi)$ measurement. The data and simulation samples used for the analysis are described in Chapter 5, along with the event selection. In Chapter 6, the analysis backgrounds are thoroughly described, with significant emphasis given to the background coming from misidentified muons. In Chapter 7 the corrections applied to the simulations are discussed, while in Chapter 8 the fit model and the systematic uncertainties are detailed. Finally, Chapter 9 presents the results of the study.

Part I

Theoretical and Experimental Context

Chapter 1

The Standard Model of Particle Physics

The Standard Model (SM) is a $SU(3) \times SU(2)_L \times U(1)$ quantum field theory [1] that describes the interactions of elementary particles. It describes three out of the four known interactions in nature in a single model: electromagnetism, weak and strong forces. Gravity, the fourth fundamental interaction, is still left out by the SM.

The development of the SM started back in 1961, when Sheldon Glashow [2] pioneered the unification of the electromagnetic and weak interactions. This effort was continued by Steven Weinberg [3] and Abdus Salam [4], who later integrated the Higgs mechanism [5–7]. The SM underwent further refinement during the 60s, when the quantum theory of the strong force, known as quantum chromodynamics, was developed. Contributors to this field included Murray Gell-Mann and George Zweig [8], who proposed the existence of quarks with different flavours, and Moo-Young Han, Yoichiro Nambu [9], and Oscar W. Greenberg [10], who suggested the existence of the *colour*, a new quantum number introducing the $SU(3)_C$ symmetry. Finally, in 1973, David Politzer [11] and David Gross together with Frank Wilczek [12] suggested the theory of the asymptotic freedom of strong interaction. Throughout the following years, the predictions of the SM have been confirmed by countless measurements, including, notably, the discovery of the Higgs boson at CERN in 2012 by the ATLAS [13] and CMS [14] experiments. Despite its unparalleled achievements, the SM is not without limitations. It describes three out of the four existing forces, but gravity, the fourth fundamental interaction, can not be integrated into the SM because until now it can not be represented in terms of quantum field theories. Furthermore, the model leaves certain other phenomena unexplained, hinting at the existence of more general theories.

This chapter provides a description of the SM, starting from its fundamental principles. In Sec. 1.1, a discussion of the various particles within the SM is pre-

Family	Particle	Spin	Charge	Mass [MeV]
I	u	1/2	$2/3e$	2.32 ± 0.10
	d	1/2	$-1/3e$	4.71 ± 0.09
II	c	1/2	$2/3e$	1280 ± 25
	s	1/2	$-1/3e$	92.9 ± 0.7
III	t	1/2	$2/3e$	$173.34 \pm 0.27 \pm 0.71 \times 10^3$
	b	1/2	$-1/3e$	4180 ± 30

Table 1.1: Main properties of the SM quarks [15].

sented. Sections 1.2 and 1.3 are dedicated to introducing quantum electrodynamics and quantum chromodynamics, respectively. The theory of electroweak interaction, including detailed explanations of the Higgs mechanism and the CKM matrix, is covered in Sec. 1.4. Finally, Sec. 1.5 explores some of the known limitations within the SM.

1.1 Particles in the Standard Model

The SM can be described starting from its fundamental constituents. The components of matter are fermions, the interacting particles, and the gauge bosons, the mediators of the forces governing these interactions. Fermions are characterised by half-integer spin and they obey the Fermi-Dirac statistics, while bosons have integer spin and follow Bose-Einstein statistics.

Fermions are further subdivided into leptons and quarks. Leptons can interact only via electroweak force, while quarks, characterised by an additional quantum number called colour, can also interact through the strong force. Fermions are organised into three distinct families, each with increasing mass. Within each family, quarks are divided into two types: up and down. These types differ in electromagnetic charge, with the up quark having $\frac{2}{3}$ times the charge of an electron, and the down quark having $\frac{1}{3}$ of the electron charge, as illustrated in Table 1.1.

Leptons consist of three massive electrically charged particles and three massless (for the SM) neutral ones. Leptons participate in electromagnetic and weak interactions but not in strong interactions. Table 1.2 provides details on the three generations of leptons and their key properties.

For each fermion, an anti-fermion exists with the same mass and spin as the fermion but with opposite values for all other quantum numbers.

The fundamental interactions of the SM are mediated by the Gauge bosons. The photon is the mediator of the electromagnetic force, the gluons of the strong one and the Z and W bosons of weak interactions. W and Z are the only gauge bosons with a mass: they acquire it through the spontaneous symmetry breaking

Family	Particle	Spin	Charge	Mass [MeV]
I	e	1/2	$-e$	0.511
	ν_e	1/2	0	-
II	μ	1/2	$-e$	105.7
	ν_μ	1/2	0	-
III	τ	1/2	$-e$	1776.86
	ν_τ	1/2	0	-

Table 1.2: Main properties of the SM leptons [15]. The mass of the neutrinos is measured to be approximately zero.

mechanism, described in Sec. 1.4.1. More details in Table 1.3.

Interaction	Mediators	Spin	Charge	Mass [GeV]
Electromagnetic	γ	1	0	0
Weak	W^+, W^-	1	$e, -e$	80.354 ± 0.007
	Z	1	0	91.1876 ± 0.0021
Strong	8 gluons (g)	1	0	0

Table 1.3: Mediators and their properties for each interaction [15].

1.2 Quantum electrodynamics

Quantum Electrodynamics (QED) is the quantum field theory governing the electromagnetic interaction. The Dirac Lagrangian that describes the field of a fermion with mass m , is defined as

$$L = \bar{\psi}(i\gamma^\mu \partial_\mu - m)\psi, \quad (1.1)$$

where the first term corresponds to the kinetic term, while the latter represents the mass term. In particular, m is the fermion mass parameter, γ^μ represents the Dirac matrices, and ψ and $\bar{\psi}$ denote the 4-component spinor and its adjoint, respectively.

The interactions in the SM emerge from the invariance of the Lagrangian under local symmetry transformations, known as gauge symmetries. From these symmetries, the conservation of physical quantities is derived using the Noether theorem. The Lagrangian in Eq. (1.1) is invariant under global $U(1)$ transformation such as:

$$\psi \rightarrow \psi' = e^{i\theta}\psi. \quad (1.2)$$

Considering the local transformation $\theta(x)$, where now the θ parameters depend on space-time coordinates, the following transformation is obtained:

$$\psi \rightarrow \psi' = e^{i\theta(x)}\psi. \quad (1.3)$$

The Eq. (1.1) is no longer invariant under this transformation, therefore the covariant derivative $D_\mu = \partial_\mu + ieA_\mu$ is added, where the gauge field A_μ transforms as

$$A_\mu \rightarrow A'_\mu = A_\mu - \partial_\mu\alpha(x). \quad (1.4)$$

To describe the free propagation of the A_μ field, also a kinematic term must be added:

$$L_{gauge} = -\frac{1}{4}F_{\mu\nu}F^{\mu\nu}, \quad (1.5)$$

where $F_{\mu\nu}$ is a field strength tensor, and can be written in terms of A^μ as $F_{\mu\nu} = \partial_\mu A_\nu - \partial_\nu A_\mu$. The full QED Lagrangian density is:

$$L_{QED} = \bar{\psi}\gamma^\mu(iD_\mu - m_\psi)\psi - \frac{1}{4}F_{\mu\nu}F^{\mu\nu}. \quad (1.6)$$

Mass terms for the gauge fields are forbidden, as they would directly violate the gauge symmetries. As a consequence, the mass of the photon is zero.

1.3 Quantum chromodynamics

The Quantum chromodynamics (QCD) [16] is the non-Abelian quantum gauge field theory which describes the strong interaction between quarks, the only particles possessing the quantum colour charge.

The concept of colour in particle physics was introduced during the 1960s in the attempt to model the Δ^{++} baryon, a baryonic resonance with spin 3/2 represented by the uuu state with spin $\uparrow\uparrow\uparrow$. Being it a fermion, to maintain the anti-symmetry of its wave function, the introduction of a new quantum number, colour, became necessary.

The number of colour degree of freedom was experimentally verified through processes such as $e^+e^- \rightarrow \mu^+\mu^-$ and $e^+e^- \rightarrow q\bar{q}$, where an observable quantity R was defined as:

$$R = \frac{\sigma(e^+e^- \rightarrow \text{hadrons})}{\sigma(e^+e^- \rightarrow \mu^+\mu^-)} = 3 \sum_{\text{quarks}} q^2,$$

with q indicating the quarks charge, and 3 is the number of colours. The final plot is shown in Fig. 1.1.

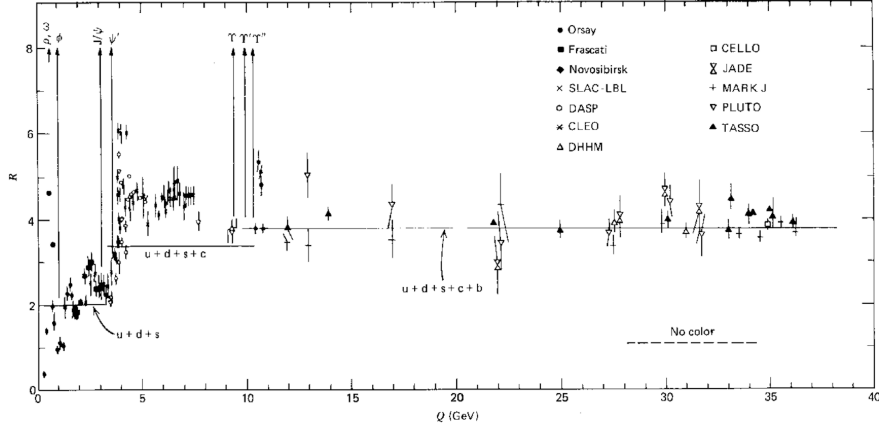


Figure 1.1: Ratio R as a function of the total e^+e^- centre-of-mass energy [17].

QCD is based on the $SU(3)_C$ symmetry, where C denotes the quantum number colour. Under the $SU(3)_C$ transformation the theory is invariant:

$$\psi \rightarrow \psi' = e^{ig_s \vec{\alpha}(x) \cdot \vec{T}} \psi,$$

where $\vec{T} = T^\alpha$ represents the eight generators of the symmetry group, defined as

$$T^a = \frac{1}{2} \lambda_a,$$

with λ_a being the Gell-Mann matrices. If local invariance under the $SU(3)$ group is imposed, the covariant derivative is introduced:

$$D_\mu = \partial_\mu + ig_s \frac{\lambda_a}{2} G_\mu^a.$$

Here, G_μ^a stands for the 8 gluon fields that transform as:

$$G_\mu^a \rightarrow G_\mu'^a = G_\mu^a + ig_s f^{abc} \theta_b(x) G_{c,\mu}.$$

Applying this to the Dirac equation for quarks, and incorporating the contributions of the gluons, the complete Lagrangian density for QCD is:

$$\mathcal{L}_{QCD} = \bar{\psi} \gamma^\mu \partial_\mu \psi - m \bar{\psi} \psi - ig_s \bar{\psi} \gamma^\mu \lambda_a \psi G_\mu^a - \frac{1}{4} G_a^{\mu\nu} G_{\mu\nu}^a,$$

where $G_a^{\mu\nu}$ is the tensor field defined as:

$$G_a^{\mu\nu} = \partial^\mu G_a^\nu - \partial^\nu G_a^\mu - g_s f_{abc} G^{b,\mu} G^{c,\nu},$$

where f_{abc} is the structure constant of $SU(3)$.

The colour charge cannot be directly observed, because it is confined within hadrons. This phenomenon is called the confinement of colour, where the only observable physical states are colour singlets. As the interactions occur among quarks and gluons at higher energies, colour interactions become progressively weaker. This characteristic is known as asymptotic freedom.

1.4 The electroweak interactions

The electroweak (EW) theory aims at creating a unified theory of electromagnetic and weak interactions. It was formulated in the 1960s by Glashow, Weinberg and Salam as an $SU(2) \times U(1)$ local gauge theory. The Lagrangian density is invariant under gauge transformations of the $SU(2)_I \times U(1)_Y$ symmetry group, where $SU(2)_I$ refers to the weak isospin charge I , and $U(1)_Y$ to the weak hypercharge Y , connected with the following relation:

$$Y = 2(Q - I_3), \quad (1.7)$$

where I_3 is the third component of the weak isospin. The generators of this group are four bosons: W^1 , W^2 and W^3 for $SU(2)_L$ and B for $U(1)_Y$.

It is useful to introduce the right and left components of the field:

$$\psi_{R,L} = \frac{1}{2}(1 \pm \gamma^5)\psi. \quad (1.8)$$

Left-handed fermions are isospin doublets, $I^3 = \pm 1/2$, while right-handed fermions are isospin singlets, $I^3 = 0$:

$$\psi_L = \begin{pmatrix} u_L \\ d_L \end{pmatrix}, \quad \psi_R = (u_R), (d_R). \quad (1.9)$$

The local gauge invariance is obtained by defining the covariant derivative D_μ as:

$$D_\mu = \partial_\mu + igI_iW_\mu^i + i\frac{g'}{2}YB_\mu, \quad (1.10)$$

where g and g' are coupling constants and I_i and Y are respectively the components of the weak isospin and of the weak hypercharge. The Lagrangian for the EW interactions is:

$$\mathcal{L}_{EW} = \sum_{j=1}^3 i\bar{\psi}_j \gamma^\mu D_\mu \psi_j - \frac{1}{4}B_{\mu\nu}B^{\mu\nu} - W_{\mu\nu}^a W_a^{\mu\nu}, \quad (1.11)$$

where the last two terms describe the free field propagation and the first is the lepton propagation and interaction term. $W_i^{\mu\nu}$ and $B_i^{\mu\nu}$ are the tensor fields:

$$W_i^{\mu\nu} = \partial^\mu W^\nu - \partial^\nu W^\mu; B_i^{\mu\nu} = \partial^\mu B^\nu - \partial^\nu B^\mu. \quad (1.12)$$

The four gauge fields can be combined to produce the physical mediators of the EW interactions for the W^\pm , Z bosons and the photon:

$$W_\mu^\pm = \sqrt{\frac{1}{2}}(W_\mu^1 \mp iW_\mu^2) \quad (1.13)$$

which represent the two charged W_μ^\pm bosons involved in charged weak interactions,

$$\begin{pmatrix} A_\mu \\ Z_\mu \end{pmatrix} = \begin{pmatrix} \cos \theta_W & \sin \theta_W \\ -\sin \theta_W & \cos \theta_W \end{pmatrix} \cdot \begin{pmatrix} B_\mu \\ W_\mu^3 \end{pmatrix}, \quad (1.14)$$

where θ_W is the weak mixing angle, called Weinberg angle. A_μ and Z_μ are respectively the electromagnetic and neutral weak current interaction bosons.

Substituting these fields in the Lagrangian, it can be shown that the charged currents only act on the left handed components of the fields while the neutral currents act on both.

The Lagrangian, due to gauge invariance, does not naturally allow for mass terms for either the gauge bosons or for the fermions. However, the mass content of the SM and mixing of EW bosons are in contrast with this constraint. In the next section, the mechanism that enables the introduction of mass terms in the gauge-invariant SM is presented.

1.4.1 The Higgs mechanism

A mechanism of spontaneous symmetry breaking allows for the generation of mass without breaking the gauge invariance of the SM Lagrangian. A new term is added in the Lagrangian, Eq. (1.11), given by the Higgs field ϕ , which is an isospin doublet:

$$\phi = \begin{pmatrix} \phi^+ \\ \phi^0 \end{pmatrix}, \quad (1.15)$$

where ϕ^+ and ϕ^0 are respectively the doublet charged and neutral components. The Higgs Lagrangian can be written according to the generic complex field Lagrangian as:

$$L_{Higgs} = (D^\mu \phi)^\dagger (D_\mu \phi) - V(\phi), \quad (1.16)$$

where the covariant derivative D is in Eq. (1.10) and V indicates the potential for the field ϕ , given by:

$$V(\phi) = \lambda(\phi^\dagger \phi)^2 + \mu^2(\phi^\dagger \phi). \quad (1.17)$$

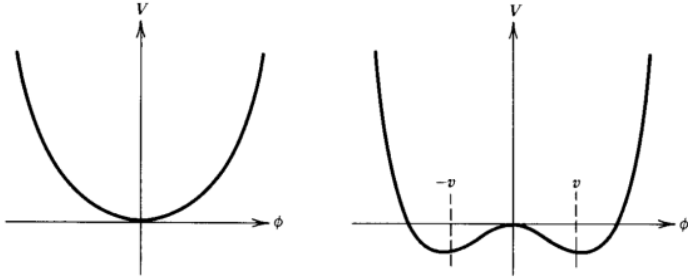


Figure 1.2: Behaviour of the potential $V(\phi)$ according to the sign of μ^2 : $\mu^2 > 0$ (left) and $\mu^2 < 0$ (right).

In order to guarantee a ground state, λ must be positive, and, according to the sign of μ^2 , the ground state can be unique or degenerate, as shown in Fig. 1.2.

The Higgs mechanism that creates the symmetry breaking happens in the second case, with $\mu^2 < 0$. Indeed, the field acquires a vacuum expectation value v which might be different from 0, that follows the following equation:

$$\phi^\dagger \phi = \frac{\mu^2}{\lambda} = \frac{v^2}{2}. \quad (1.18)$$

Substituting the expansion in Eq. (1.16), the gauge bosons acquire their masses as:

$$m_W = \frac{gv}{2} m_Z = \frac{gv}{2 \cos \theta_W} = \frac{m_W}{\cos \theta_W}, \quad (1.19)$$

while the photon, the field A^μ , is mass-less, as in QED.

Similarly, through the incorporation of Yukawa terms, fermions also acquire mass, which is proportional to the coupling constant with the Higgs boson. The fermion mass term $-m\bar{\psi}\psi$ breaks the invariance under the $SU(2)_L \times U(1)_Y$ group due to the different transformations of the right and left-handed chiral components of the fields. To resolve this, a gauge-invariant mass term is incorporated using a Yukawa coupling that links the fermion field with the Higgs field, expressed as:

$$L_Y = Y_f (\bar{\psi}_L \phi \psi_R - \bar{\psi}_R \phi^\dagger \psi_L) \quad (1.20)$$

where ϕ is the Higgs field and Y_f represents the Yukawa coupling. Leptons masses take the form:

$$m_f = \frac{v}{\sqrt{2}} Y_f, \quad (1.21)$$

where this relationship implies that the Higgs boson exhibits stronger couplings to heavier fermions.

The Higgs boson has been discovered in 2012 by the ATLAS [18] and CMS [19] experiments at LHC. The plots of the discoveries for both experiments are shown

in Fig. 1.3. The Higgs boson is a spinless and charge-less particle, with a mass of 125 GeV.

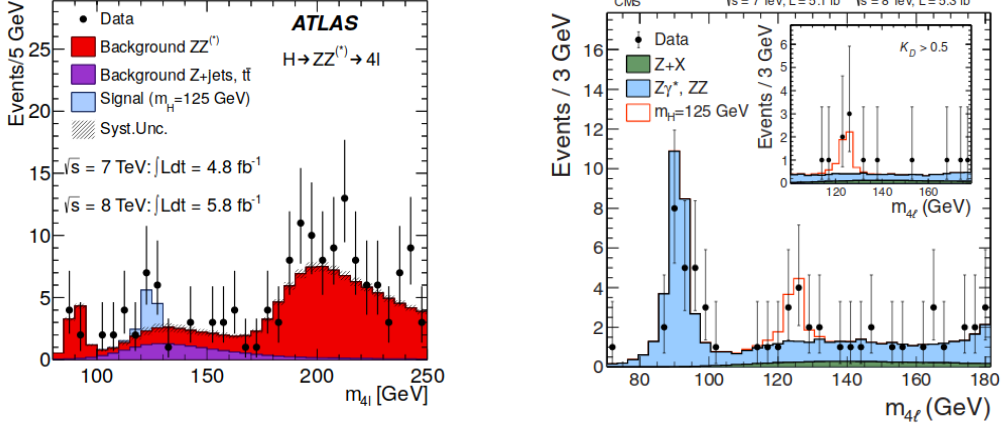


Figure 1.3: $ZZ^* \rightarrow 4l$ channel of the Higgs discovery from the ATLAS experiment (left) and the CMS experiment (right).

1.4.2 Flavour in the quark sector

In the SM, the mass matrix arising from the interaction of quarks with the Higgs field does not align with their flavour states. This discrepancy led to the introduction of the Cabibbo-Kobayashi-Maskawa (CKM) matrix [20], which facilitates the transformation from mass eigenstates to flavour eigenstates of quarks:

$$V_{\text{CKM}} = \begin{pmatrix} V_{ud} & V_{us} & V_{ub} \\ V_{cd} & V_{cs} & V_{cb} \\ V_{td} & V_{ts} & V_{tb} \end{pmatrix}. \quad (1.22)$$

This matrix encapsulates the probabilities of charged current transitions among the up-type quarks (u, c, t) and down-type quarks (d, s, b). Each element of the matrix represents the amplitude of a transition from one quark flavour to another.

It can be parameterised by three mixing angles and a CP-violating phase. Of the many possible conventions, a standard choice has become [21]:

$$V_{\text{CKM}} = \begin{pmatrix} c_{12}c_{13} & s_{12}c_{13} & s_{13}e^{-i\delta} \\ -s_{12}c_{23} - c_{12}s_{23}s_{13}e^{i\delta} & c_{12}c_{23} - s_{12}s_{23}s_{13}e^{i\delta} & s_{23}c_{13} \\ s_{12}s_{23} - c_{12}c_{23}s_{13}e^{i\delta} & -c_{12}s_{23} - s_{12}c_{23}s_{13}e^{i\delta} & c_{23}c_{13} \end{pmatrix} \quad (1.23)$$

where $s_{ij} = \sin \theta_{ij}$ and $c_{ij} = \cos \theta_{ij}$ and δ is the already mentioned phase, responsible for the CP-violating phenomena in flavour changing processes in the SM

matter-antimatter asymmetry. Considering that experimentally it is known that $s_{13} \ll s_{23} \ll s_{12} \ll 1$, it is useful to also introduce another parametrisation, which exhibits this hierarchy, known as Wolfenstein parametrisation [21]:

$$s_{12} = \lambda = \frac{|V_{us}|}{\sqrt{|V_{ud}|^2 + |V_{us}|^2}} \quad (1.24)$$

$$s_{23} = A\lambda^2 = \lambda \left| \frac{V_{cb}}{V_{us}} \right| \quad (1.25)$$

$$s_{13}e^{i\delta}\rho = V_{ub}* = A\lambda^3(\rho + i\eta). \quad (1.26)$$

Using these definitions, the CKM matrix can be rewritten in powers of λ as

$$V_{\text{CKM}} \approx \begin{pmatrix} 1 - \frac{1}{2}\lambda^2 & \lambda & A\lambda^3(\rho - i\eta) \\ -\lambda & 1 - \frac{1}{2}\lambda^2 & A\lambda^2 \\ A\lambda^3(1 - \rho - i\eta) & -A\lambda^2 & 1 \end{pmatrix} + \mathcal{O}(\lambda^4). \quad (1.27)$$

The CKM matrix elements can be most precisely determined using a global fit [22, 23] to all available measurements and imposing the SM constraints:

$$V_{\text{CKM}} = \begin{pmatrix} 0.97435 \pm 0.00016 & 0.22500 \pm 0.00067 & 0.00369 \pm 0.00011 \\ 0.22486 \pm 0.00067 & 0.97349 \pm 0.00016 & 0.04182_{-0.00074}^{+0.00085} \\ 0.00857_{-0.00018}^{+0.00020} & 0.04110_{-0.00072}^{+0.00083} & 0.999118_{-0.000036}^{+0.000031} \end{pmatrix} \quad (1.28)$$

1.5 Beyond the Standard Model

The SM has been successfully validated by many experiments. However, it is not a comprehensive theory, as it fails to account for several phenomena.

A significant unexplained phenomenon is the presence of *dark matter* (DM), which constitutes most of the matter in the universe. Its presence is supported by various cosmological experimental evidences. For example, contrary to expectations that star velocities decrease with distance from a galaxy centre, they remain relatively constant. This and other observations strongly suggest the existence of DM, which is not explained by the SM. Additionally, the SM does not address the dark energy issue, which is responsible of the accelerated expansion of the universe.

The SM also does not explain the amount of *baryonic asymmetry* observed in the universe, the asymmetry between matter and antimatter. Although the SM includes CP-violation mechanism theories that suggest a slight difference between matter and antimatter, these do not fully account for the observed asymmetry.

Another limitation of the SM is its treatment of *neutrino masses*. Contrary to the SM assumption of mass-less neutrinos, experiments have shown that neutrinos possess mass, as evidenced by neutrino oscillations. Neutrinos, created with a

specific flavour (e, μ, τ) , can transform into another flavour, for instance $\nu_\mu \rightarrow \nu_e$. Experiments like SNO, SuperKamiokande, and OPERA have observed these oscillations in solar, atmospheric and beam-produced neutrinos. In the simplified assumption of having only two neutrino flavours, e and μ , the probability of ν_e to oscillate into ν_μ is:

$$P_{e\mu} = \sin^2(2\theta) \sin^2 \left(k \frac{\Delta m^2 L}{E} \right), \quad (1.29)$$

where L is the distance travelled by the neutrino and E its energy. The oscillation probability depends on the quadratic difference of the masses $\Delta m^2 = m_e^2 - m_\mu^2$, which therefore can not be null, though very small (0.01 – 0.1 eV).

Lastly, the SM has not successfully integrated *gravitation interaction*.

The list of phenomena not included in the SM presented here is not exhaustive, but many models have been proposed to include them in a more general model.

Chapter 2

Lepton Flavour Universality

In the SM, the photon, W, and Z bosons, mediators of the EW interactions, exhibit precisely the same couplings to the three lepton generations. This feature, referred to as Lepton Flavour Universality (LFU), is an aspect of the SM that can be challenged to test its validity. Any deviation from the identity, leaving aside any distinction due to different lepton masses, would indicate potential contributions from virtual particles beyond the SM.

LFU can be tested in three classes of decays: Sec. 2.1 provides a discussion of LFU in purely leptonic decays, Sec. 2.2 focuses on LFU in EW decays, and the theoretical framework for LFU in the b-quark decays is explained in Sec. 2.3.

Sec. 2.4 outlines the SM predictions for a specific LFU test in the b-quark sector, the $R(J/\psi)$ ratio, which constitutes the central focus of this thesis. Eventually, in Sec. 2.5 the experimental status of the LFU tests is outlined and in Sec. 2.6 possible interpretations of LFU violations are described.

2.1 Purely leptonic decays

The LFU can be tested through the analysis of pure leptonic decay channels. The muon decay into $\mu^- \rightarrow e^- \bar{\nu}_e \nu_\mu$, detailed in Fig. 2.1, occurs through two weak interaction vertices, $\mu^- \nu_\mu W$ and $W e^- \bar{\nu}_e$ [24]. Considering a potential difference in

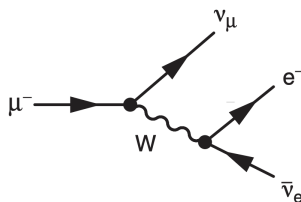


Figure 2.1: Feynman diagram of the muon decay [24].

the coupling at these vertices, the decay rate of the muon can be written as:

$$\Gamma(\mu^- \rightarrow e^- \bar{\nu}_e \nu_\mu) = \frac{G_F^{(e)} G_F^{(\mu)} m_\mu^5}{192\pi^3} \quad (2.1)$$

where $G_F^{(e)}$ and $G_F^{(\mu)}$ indicate the Fermi coupling constant, which is a fairly accurate description at low energies of the weak couplings to the electron and muon, respectively. Similarly, the tau lepton decay to an electron is governed by:

$$\Gamma(\tau^- \rightarrow e^- \bar{\nu}_e \nu_\tau) = \frac{G_F^{(e)} G_F^{(\tau)} m_\tau^5}{192\pi^3}. \quad (2.2)$$

The lifetime of a particle is the inverse of its decay rate. The tau lepton, due to its higher mass, decays through various modes, as shown in Fig. 2.2. Therefore $\tau_\tau = \frac{1}{\Gamma} = \frac{1}{\sum_i \Gamma_i}$, where Γ_i represents the partial decay rates.

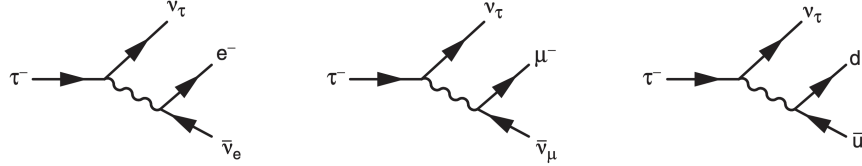


Figure 2.2: Feynman diagram of the tau decays [24].

The branching ratio for the tau decay to an electron, $\mathcal{B}(\tau^- \rightarrow e^- \bar{\nu}_e \nu_\tau)$, can be expressed in terms of its lifetime as $\mathcal{B}(\tau^- \rightarrow e^- \bar{\nu}_e \nu_\tau) = \Gamma(\tau^- \rightarrow e^- \bar{\nu}_e \nu_\tau) \cdot \tau_\tau$. Therefore, using Eq. (2.2), the following relation holds:

$$\tau_\tau = \frac{192\pi^3}{G_F^{(e)} G_F^{(\tau)} m_\tau^5} \mathcal{B}(\tau^- \rightarrow e^- \bar{\nu}_e \nu_\tau). \quad (2.3)$$

By comparing the lifetimes of the tau and muon the ratio of coupling constants can be computed:

$$\frac{G_F^{(\tau)}}{G_F^{(\mu)}} = \frac{m_\mu^5 \tau_\mu}{m_\tau^5 \tau_\tau} \mathcal{B}(\tau^- \rightarrow e^- \bar{\nu}_e \nu_\tau). \quad (2.4)$$

Using measured values for branching ratios, and the masses and lifetimes of the leptons, the ratio of weak charged-current coupling strengths for muon and tau is determined to be [25]:

$$\frac{G_F^{(\tau)}}{G_F^{(\mu)}} = 1.0011 \pm 0.0015. \quad (2.5)$$

With a similar approach, also electron and muon coupling strengths can be compared, with a result of

$$\frac{G_F^{(e)}}{G_F^{(\mu)}} = 1.000 \pm 0.004. \quad (2.6)$$

Given the accuracy of experimental results in leptonic decays, it can be concluded that $G_F^{(e)} = G_F^{(\mu)} = G_F^{(\tau)}$, providing robust experimental evidence for LFU in purely leptonic decays.

2.2 The electroweak sector

In the SM, W and Z bosons interact uniformly with all types of leptons. This characteristic has been tested through numerous experiments where these EW bosons are produced. The most accurate measurements have been obtained from experiments conducted at e^+e^- colliders, such as LEP [26], as well as at $p\bar{p}$ colliders like the Tevatron [27], and at pp colliders like the LHC, which is extensively discussed in Sec. 3.1.

Precise tests of the Z boson universality in its couplings with charged leptons have been performed, focusing on the ratios of leptonic partial-widths. The measurements from LEP can be summarised as [28]:

$$\begin{aligned} \frac{\Gamma_{\mu\mu}}{\Gamma_{ee}} &= \frac{B(Z \rightarrow \mu^+\mu^-)}{B(Z \rightarrow e^+e^-)} = 1.0009 \pm 0.0028; \\ \frac{\Gamma_{\tau\tau}}{\Gamma_{ee}} &= \frac{B(Z \rightarrow \tau^+\tau^-)}{B(Z \rightarrow e^+e^-)} = 1.0019 \pm 0.0032. \end{aligned}$$

LFU of the neutral weak current is established at the per-mille level. Within the framework of the SM, assuming the validity of LFU and considering leptons as mass-less, the SM predicts that all $\Gamma_{l^+l^-}$ partial widths should be identical. At first order, the effects due to the different masses of the leptons do not significantly impact the Z decays measurements. However, for tau leptons, these effects are of approximately 0.2%, and they have been accurately measured. These measurements have also been conducted at the LHC, with compatible results [29].

Precise measurements using W boson decays that can be interpreted as tests of LFU have also been performed. All experimental results involving the first and second generation of leptons are in good agreement with LFU. However the precision of these results is lower than those derived from Z boson decay analyses. A combination of measurements from various experiments, illustrated in Fig. 2.3,

gives the following result:

$$\frac{\Gamma_{\mu\nu}}{\Gamma_{e\nu}} = \frac{B(W \rightarrow \mu^+ \bar{\nu})}{B(W \rightarrow e^+ \bar{\nu})} = 1.004 \pm 0.008. \quad (2.7)$$

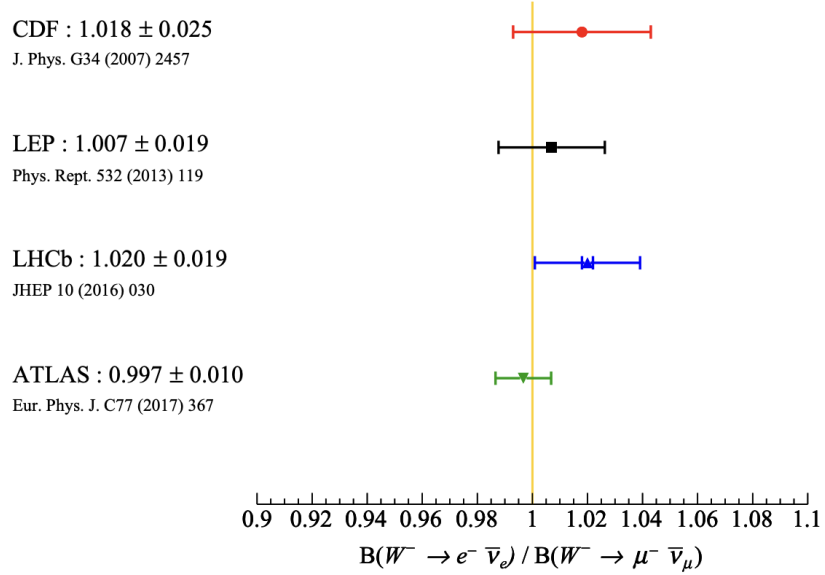


Figure 2.3: Comparison of the ratio of branching fractions for the muon and electron decay of the W boson measured by several experiments. The SM prediction is indicated with a yellow line [30].

The measurements involving the τ lepton from LEP are less precise, and with $\sim 2\sigma$ tension with the SM prediction [31]:

$$\begin{aligned} \frac{\Gamma_{\tau\nu}}{\Gamma_{e\nu}} &= \frac{B(W^+ \rightarrow \tau^+ \bar{\nu})}{B(W^+ \rightarrow e^+ \bar{\nu})} = 1.063 \pm 0.027 \\ \frac{\Gamma_{\tau\nu}}{\Gamma_{\mu\nu}} &= \frac{B(W^+ \rightarrow \tau^+ \bar{\nu})}{B(W^+ \rightarrow \mu^+ \bar{\nu})} = 1.070 \pm 0.026. \end{aligned}$$

Recent measurements from the ATLAS [32] and CMS [33] experiments, shown in Fig. 2.4, solved this tension, and found a result in agreement with the SM prediction:

$$\frac{\Gamma_{\tau\nu}}{\Gamma_{\mu\nu}} = 0.992 \pm 0.013.$$

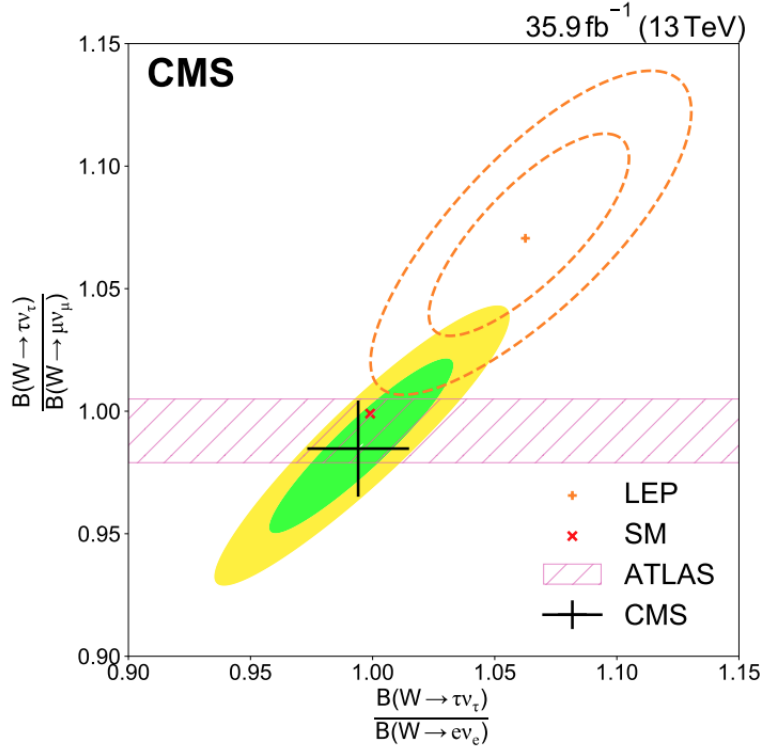


Figure 2.4: Two-dimensional distribution of the ratio $R_{\tau/e}$ versus $R_{\tau/\mu}$ measured by CMS, compared with the corresponding LEP [31] and ATLAS [32] results and with the SM prediction. The green and yellow bands (dashed lines for the LEP results) correspond to the 68% and 95% CL, respectively, for the resulting two-dimensional Gaussian distribution. The corresponding 68% CL one-dimensional projections (black error bars) are also overlaid for a better visual comparison with the ATLAS $R_{\tau/\mu}$ result [33].

2.3 LFU in b-quark decays

The b-sector, including hadron decays involving b quarks, represents an interesting area for testing LFU. Decays can be split into two groups:

- Flavour-Changing Charged-Current (FCCC) transitions, like the “tree-level” $b \rightarrow cl^- \bar{\nu}_l$ decays, where l represents any of the three charged leptons, shown in Fig. 2.5. These transitions are characterised by the involvement of a single element of the CKM matrix, specifically V_{cb} . Excluding the top quark, which decays before hadronisation, the b-quark is the only one with sufficient mass to produce a τ -lepton, providing access to the third generation.
- Flavour-Changing Neutral-Current (FCNC) processes, such as the “loop-

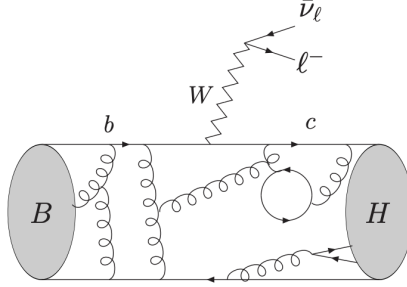


Figure 2.5: Illustration of a $b \rightarrow cl^- \bar{\nu}_l$ transition in the SM, as seen at the hadronic level, in the case of a B meson decaying into an unspecified H meson [30].

level” (penguin/box) $b \rightarrow sl^+l^-$ decays illustrated in Fig. 2.6. The involved CKM matrix elements are determined by the flavour of the intermediate quark. The CKM matrix unitarity and hierarchical structure enable the simplification of these products into a dominant term ($V_{tb}V_{ts}^*$) and a Cabibbo-suppressed term ($V_{ub}V_{us}^*$).

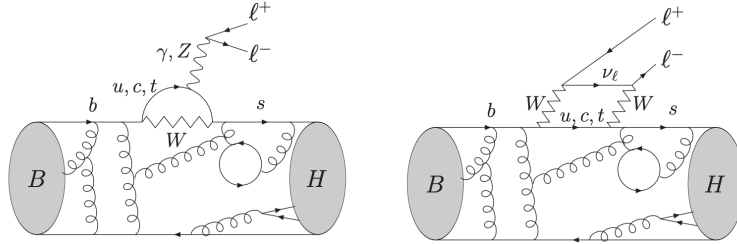


Figure 2.6: Illustration of $b \rightarrow sl^+l^-$ transitions in the SM, as seen at the hadronic level, in the case of a B meson decaying into an unspecified H meson [30]. Penguin diagram (left) and box diagram (right).

To test LFU, identical observables across processes that only differ in the lepton flavours involved can be compared. This could be, for example, specific angular observables describing their kinematics or the ratio of their branching fractions, like:

$$R(X) = \frac{\mathcal{B}(H_b \rightarrow X\tau^-\bar{\nu}_\tau)}{\mathcal{B}(H_b \rightarrow Xl^-\bar{\nu}_l)}, \quad (2.8)$$

where $l = e, \mu$ and H_b is an hadron containing a b quark. Theoretically, ratio-based observables are preferable as they facilitate the cancellation of common hadronic form-factors and CKM matrix elements. Experimentally, employing ratios is also beneficial as it reduces reliance on the absolute knowledge of efficiencies, decreasing the importance of systematic uncertainties.

2.3.1 Effective Field Theory

In order to describe the wide range of scales from the EW regime down to the masses of fermions, an effective field theory (EFT) approach is employed, to separate the effects from different scales [30]. This concept is similar to the development of the Fermi theory for β decays, obtained neglecting the propagation of the W gauge boson, which simplifies the interaction to a point-like interaction between four fermions. The EFT applicable at low energies, or equivalently at large distances, is formulated by neglecting the propagation of heavy and high-energy particles, retaining only those that are light and low-energy and can propagate over extended distances. The influences of the heavier particles are encapsulated within short-distance coefficients, the Wilson coefficients, which then multiply operators composed of the lighter field components. The EFT approach can be applied to both FCCC and FCNC decays.

For FCCC decays, such as $b \rightarrow cl^-\bar{\nu}_l$, the corresponding effective Hamiltonian can be written as:

$$\mathcal{H}_{eff}(b \rightarrow cl^-\bar{\nu}_l) = \frac{4G_F}{\sqrt{2}} V_{cb} \sum_i \mathcal{C}_i \mathcal{O}_i \quad (2.9)$$

where the index i extends over a range of 4-fermion operators, denoted by \mathcal{O}_i , and their associated Wilson coefficients, \mathcal{C}_i . They can be computed perturbatively and involve the masses and the couplings of the heavy degrees of freedom (W, Z, H and t in the SM). Due to the universality of lepton couplings for the three generations, the SM Wilson coefficients have the same value for all three lepton generations. The sum in Eq. (2.9) contains one dominant operator in the SM, called \mathcal{O}_{Vl} . A visualisation of the EFT applied to FCCC decay can be seen in Fig. 2.7.

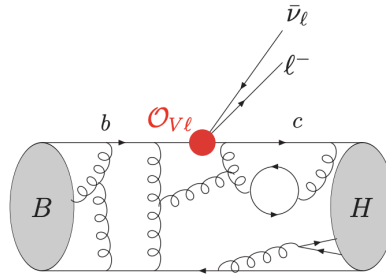


Figure 2.7: Illustration of a $b \rightarrow cl^-\bar{\nu}_l$ transition in the effective Hamiltonian approach. The red dot corresponds to a local two-quark two-lepton operator [30].

For FCNC transitions, such as $b \rightarrow sl^-l^+$, the effective Hamiltonian is formulated as follows:

$$\mathcal{H}_{eff}(b \rightarrow sl^-l^+) = -\frac{4G_F}{\sqrt{2}}V_{tb}V_{ts}^* \sum_i \mathcal{C}_i \mathcal{O}_i \quad (2.10)$$

with additional minor adjustments proportional to $V_{ub}V_{us}^*$. CKM unitarity allows to re-express terms proportional to $V_{cb}V_{cs}^*$ in terms of the other CKM matrix element products, as already mentioned. For the SM, the primary operators relevant to $b \rightarrow sl^-l^+$ are \mathcal{O}_7 , which includes the electromagnetic tensor, and the point-like interaction operators \mathcal{O}_{9l} and \mathcal{O}_{10l} , as depicted in Fig. 2.8. Consistent with the principle of lepton coupling universality in the SM, the Wilson coefficients for these operators are identical across all three lepton generations.

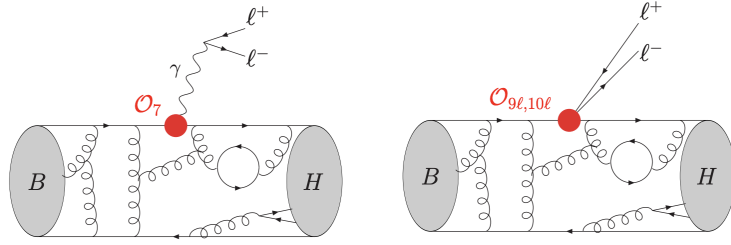


Figure 2.8: Illustration of a $b \rightarrow sl^-l^+$ transition in the effective Hamiltonian approach. The (red) dot corresponds to a local operator [30].

The use of this methodology offers multiple advantages in the analysis of these processes. For example, this framework is easily adaptable to include effects from NP. Such adaptations could lead either to alterations in the existing short-distance Wilson coefficients or to the introduction of new operators, which are either absent or significantly diminished in the SM due to its symmetries.

Since an extension of the SM may provide an explanation to the existence of three families with a similar structure but very different masses, it is possible that NP could contribute in ways that diverge from the SM established symmetries, particularly in terms of flavour. This implies that NP effects might potentially break the standard paradigm of LFU. Consequently, this could result in distinct Wilson coefficients for operators that are structurally identical but vary with respect to lepton flavour.

2.4 SM prediction for $R(J/\psi)$

For semileptonic decays of the first and second lepton generation, such as $B \rightarrow D^{(*)}\mu^-\bar{\nu}_\mu$ and $B \rightarrow D^{(*)}e^-\bar{\nu}_e$, it is commonly assumed that contributions from NP are negligible. These decay processes are used for determining the CKM matrix

element V_{cb} and for analysing the hadronic form factors involved. Furthermore, the branching fraction measurements for $\mathcal{B}(\bar{B}^0 \rightarrow D^+ \mu^- \bar{\nu}_\mu)$, $\mathcal{B}(\bar{B}^0 \rightarrow D^+ e^- \bar{\nu}_e)$, $\mathcal{B}(B^- \rightarrow D^0 \mu^- \bar{\nu}_\mu)$ and $\mathcal{B}(B^- \rightarrow D^0 e^- \bar{\nu}_e)$, are consistent with each other and in agreement with LFU [34, 35].

The large mass of the tau lepton, which is approximately 17 times heavier than the muon and 3500 times heavier than the electron, could make semileptonic B decays involving the third generation more sensitive to NP, if they depend on the mass. To investigate NP effects in these decays, the ratios of branching fractions between decays involving third-generation leptons and first or second-generation leptons can be measured:

$$R(H_c) = \frac{\mathcal{B}(H_b \rightarrow H_c \tau^- \bar{\nu}_\tau)}{\mathcal{B}(H_b \rightarrow H_c l^- \bar{\nu}_l)}, \quad (2.11)$$

where l denotes either an electron or, typically, a muon. As previously mentioned in the introduction of Sec. 2.3, this ratio-based approach effectively cancels a large part of the theoretical uncertainties, such as V_{cb} and common part of the form factors, as well as experimental uncertainties, including branching fraction measurements and reconstruction efficiencies.

This thesis focuses specifically on the $R(J/\psi)$ defined as:

$$R(J/\psi) = \frac{\mathcal{B}(B_c^- \rightarrow J/\psi \tau^- \bar{\nu}_\tau)}{\mathcal{B}(B_c^- \rightarrow J/\psi \mu^- \bar{\nu}_\mu)}. \quad (2.12)$$

In this equation, the generic lepton l of Eq. (2.11) is a muon. The reasons behind this choice, based on experimental considerations, are detailed in the second part of this thesis.

The full differential decay rate [36] for $B_c^- \rightarrow J/\psi l^- \bar{\nu}_l$ is shown in Eq. (2.13), where l is a lepton with mass m_l , with respect to the squared four-momentum transfer, q^2 , and the angles defined in Fig. 2.9.

$$\frac{d^4 \Gamma(B_c^- \rightarrow J/\psi (\rightarrow \mu^+ \mu^-) l^- \bar{\nu}_l)}{d \cos(\theta_{J/\psi}) d \cos(\theta_W) d \chi d q^2} = \mathcal{B}(J/\psi \rightarrow \mu^+ \mu^-) \mathcal{N} \sum_i k_i(\theta_W, \theta_{J/\psi}, \chi) \mathcal{H}_i(q^2), \quad (2.13)$$

where \mathcal{N} is given by:

$$\mathcal{N} = \frac{G_F^2}{(4\pi)^4} |\eta_{EW}|^2 |V_{cb}|^2 \frac{3(q^2 - m_l^2)^2 |\vec{p}|}{8 M_{B_c}^2 q^2}. \quad (2.14)$$

The J/ψ in this calculation only decays through its electromagnetic decay mode, into $\mu^+ \mu^-$ pairs [36].

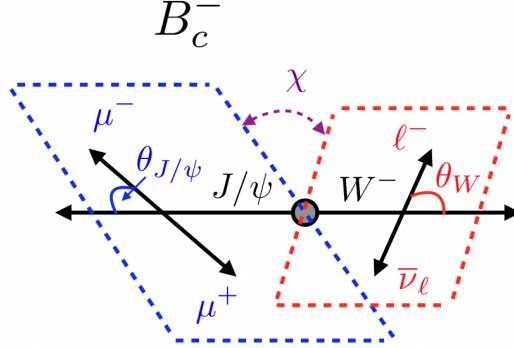


Figure 2.9: Conventions for the angular variables entering the differential decay rate [36].

In this context, $|\vec{p}'|$ indicates the momentum of the J/ψ in the rest frame of the B_c , and η_{EW} represents an EW correction, as defined in Ref. [37]. The specific combinations of helicity amplitudes and coefficients, \mathcal{H}_i and k_i , are listed in Table 1 of Ref. [36].

Integrating over angles, the differential rate in q^2 is then given by:

$$\frac{d\Gamma}{dq^2} = \mathcal{N} \times \frac{64\pi}{9} \left[(H_-^2 + H_0^2 + H_+^2) + \frac{m_l^2}{2q^2} (H_-^2 + H_0^2 + H_+^2 + 3H_t^2) \right], \quad (2.15)$$

with the helicity amplitudes defined in terms of Lorentz-invariant form factors:

$$H_{\pm}(q^2) = (M_{B_c} + M_{J/\psi}) A_1(q^2) \mp \frac{2M_{B_c} |\vec{p}'|}{M_{B_c} + M_{J/\psi}} V(q^2), \quad (2.16)$$

$$H_0(q^2) = \frac{1}{2M_{J/\psi} \sqrt{q^2}} \left(-4 \frac{M_{B_c}^2 |\vec{p}'|^2}{M_{B_c} + M_{J/\psi}} A_2(q^2) \right. \quad (2.17)$$

$$+ (M_{B_c} + M_{J/\psi})(M_{B_c}^2 - M_{J/\psi}^2 - q^2) A_1(q^2) \right),$$

$$H_t(q^2) = \frac{2M_{B_c} |\vec{p}'|}{\sqrt{q^2}} A_0(q^2). \quad (2.18)$$

The form factors A_0 , A_1 , A_2 and V are computed in Ref. [38], and the resulting helicity amplitudes are shown in Fig. 2.10.

Differential and total decay rates are calculated, with the differential rate $d\Gamma/dq^2$ for tau lepton and muon shown in Fig. 2.11. From the computation of the total decay rate, the prediction of the $R(J/\psi)$ ratio can be found [36]:

$$R(J/\psi) = 0.2582(38). \quad (2.19)$$

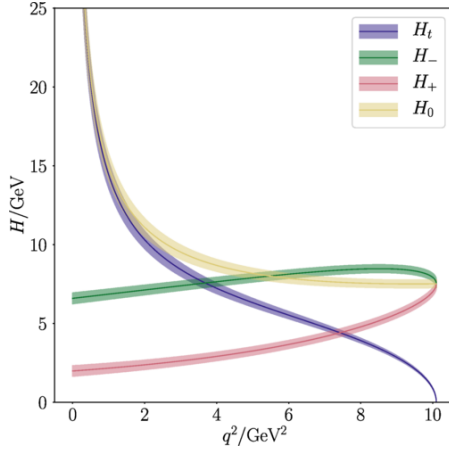


Figure 2.10: Helicity amplitudes as function of q^2 [36].

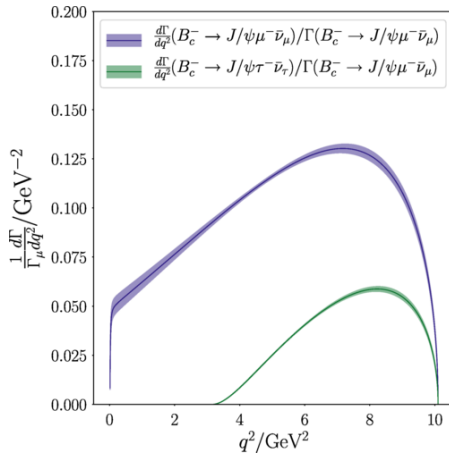


Figure 2.11: $d\Gamma/dq^2$ as function of q^2 in the SM, for the muon and tau case, normalised to the total rate Γ_μ [36].

2.5 Experimental status of LFU tests

Direct searches for LFU violation are mostly performed at the BaBar [39] and Belle [40] experiments, situated at the e^+e^- colliders at SLAC (USA) and at KEK (Japan), respectively, alongside the LHCb [41] experiment at the LHC proton-proton collider.

In the context of the FCNC decay $b \rightarrow sl^+l^-$, the $R_{K^{(*)}}$ ratio is defined as

$$R_{K^{(*)}} = \frac{\mathcal{B}(B \rightarrow K^{(*)}\mu^+\mu^-)}{\mathcal{B}(B \rightarrow K^{(*)}e^+e^-)}, \quad (2.20)$$

which, according to the SM, is predicted to be 1. A recent LHCb analysis of this

ratio over four dilepton invariant mass bins, utilising a dataset of 9 fb^{-1} , has yielded the following results [42, 43]:

$$R_K^{[0.1,1.1]} = 0.994^{+0.094}_{-0.087}, \quad (2.21)$$

$$R_K^{[1.1,6]} = 0.949^{+0.048}_{-0.047}, \quad (2.22)$$

$$R_{K^*}^{[0.1,1.1]} = 0.927^{+0.099}_{-0.093}, \quad (2.23)$$

$$R_{K^*}^{[1.1,6]} = 1.027^{+0.077}_{-0.073}, \quad (2.24)$$

where the square brackets indicate the bins in q^2 . Currently, these measurements exhibit no substantial deviation from the SM predictions. Earlier findings from Belle and BaBar, although with larger uncertainties, similarly align with SM expectations [44, 45]. It is worth noting that up to one year before the writing of this thesis, these ratios were showing an anomaly over 3σ [46].

In the FCCC channel, involving $b \rightarrow cl^-\bar{\nu}_l$ decays, notable deviations from SM predictions are observed in the $R(D)$ and $R(D^*)$ ratios [47], defined as:

$$R(D^{(*)}) = \frac{\mathcal{B}(B \rightarrow D^{(*)}\tau^+\nu)}{\mathcal{B}(B \rightarrow D^{(*)}l^+\nu_l)}. \quad (2.25)$$

The SM predictions for these ratios are:

$$R_{SM}(D) = 0.298 \pm 0.004, \quad (2.26)$$

$$R_{SM}(D^*) = 0.254 \pm 0.005. \quad (2.27)$$

The average of the measurements from BaBar [48], Belle [49] and LHCb [50] shows a tension of 3.2σ with the SM predictions:

$$R(D) = 0.357 \pm 0.029, \quad (2.28)$$

$$R(D^*) = 0.284 \pm 0.013, \quad (2.29)$$

as shown in Fig. 2.12.

2.6 Interpretations

To account for observed deviations from SM predictions, a model-independent analysis can be performed. This involves analysing the pertinent effective Hamiltonian, determining the short-distance Wilson coefficients values from data, and comparing these values against those predicted by the SM. This can be achieved by either only assuming the SM operators basis or including further operators [30]. Specific NP scenarios are defined by adding NP contributions to some Wilson

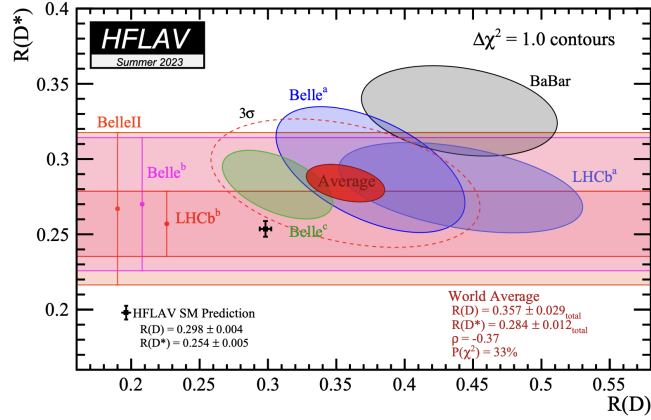


Figure 2.12: Summary of the measurements of $R(D)$ and $R(D^*)$ (including correlations) together with the SM predictions (online HFLAV update 2023) [51].

coefficients, as $\mathcal{C}_i = \mathcal{C}_i^{SM} + \mathcal{C}_i^{NP}$. A global fit of all relevant observables is then conducted to constrain the values of \mathcal{C}_i^{NP} . For simplicity, and due to the limited availability of data, these global fits often assume NP contributions to only a selected few Wilson coefficients, following certain NP models. An example is shown in Fig. 2.13, where global fits to the NP Wilson coefficients are performed using the most updated LFU experimental results [52].

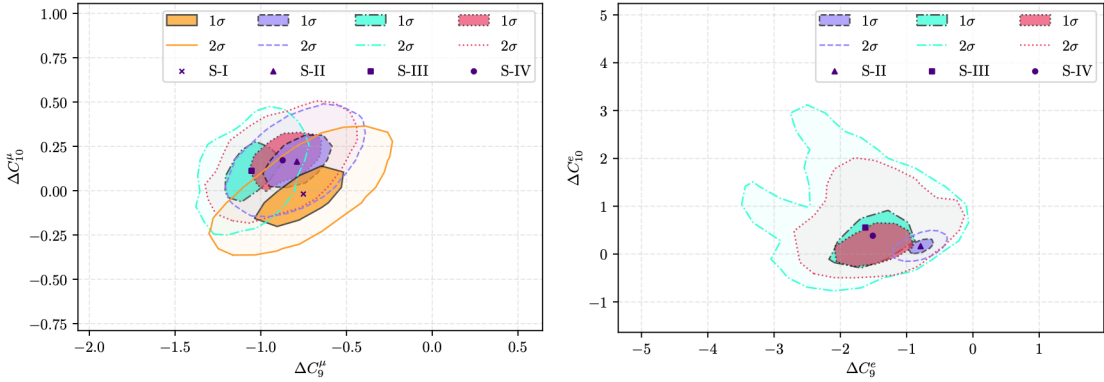


Figure 2.13: Correlations of Wilson coefficients \mathcal{C} involving more than 3σ deviations from SM predictions. The orange(solid), purple(dashed), green(dotdashed) and red(dotted) regions represent the scenarios S-I, S-II, S-III and S-IV, respectively, described in Table 4 of Ref. [52].

To explore various NP possibilities, four combinations of NP operators are studied in this particular measurement and described in Table 4 of Ref. [52]. From these fits it results that ΔC_{10} agrees with the SM within 1σ in all the four scenarios

considered for both muon and electron type, but deviations from the SM in $\Delta\mathcal{C}_9^\mu$ are present for more than 4σ for most scenarios and $\Delta\mathcal{C}_9^e$ for around 3σ in one scenario.

Other than fitting NP Wilson coefficients, also other simpler models are considered, where only one or two heavy intermediate particles are introduced. These models suggest for example the exchange of heavy, colourless vector bosons (W' , Z'), heavy colourless scalars (charged or neutral heavy Higgs bosons), or heavy coloured vector or scalar bosons (leptoquarks) [53].

Chapter 3

LHC and the CMS experiment

One of the primary objectives of the Large Hadron Collider (LHC) was to discover the Higgs boson, responsible for the symmetry breaking mechanism described in Sec. 1.4.1. But the LHC scope extends beyond the SM, for example investigating the phenomena that disagree with the SM predictions, as already mentioned in Sec. 1.5. This includes probing LFU, extensively discussed in Ch. 2, as some tension with the SM predictions have already been found.

An experiment which contributes extensively to all these measurements is the Compact Muon Solenoid (CMS), one of the four main experiments at the LHC, and which collected the data used in this thesis to test LFU.

Sec. 3.1 contains an overview of the LHC, describing its primary characteristics and operational principles. Sec. 3.2 provides an in-depth description of the CMS experiment. Special attention is given to its subdetectors, with a particular focus on the trigger system, Sec. 3.2.3, and the details involved in the reconstruction of physics objects, Sec. 3.2.4.

3.1 The Large Hadron Collider

The LHC [54, 55] is the most powerful particle accelerator ever built. It is designed to collide two up to 7 TeV proton beams, resulting in a centre of mass energy of up to 14 TeV. It can also collide heavy lead ions (Pb) with an energy of 2.8 TeV per ion.

The LHC is located underground, near the Swiss city of Geneva, between 45 m and 170 m below the surface, in the existing 26.7 km tunnel that was firstly built for the Large Electron Positron (LEP) accelerator [56]. The transition from a leptonic collider to an hadronic one allows to reach higher energies, thanks to the lower amount of energy loss through synchrotron radiation emitted by accelerated particles, or the ability of accessing a wider energy spectrum, thanks to the

composite structure of protons. Particles are maintained in a circular orbit with a strong magnetic field of 8.33 T. Dipoles and quadrupoles are used to bend and focalise the beams.

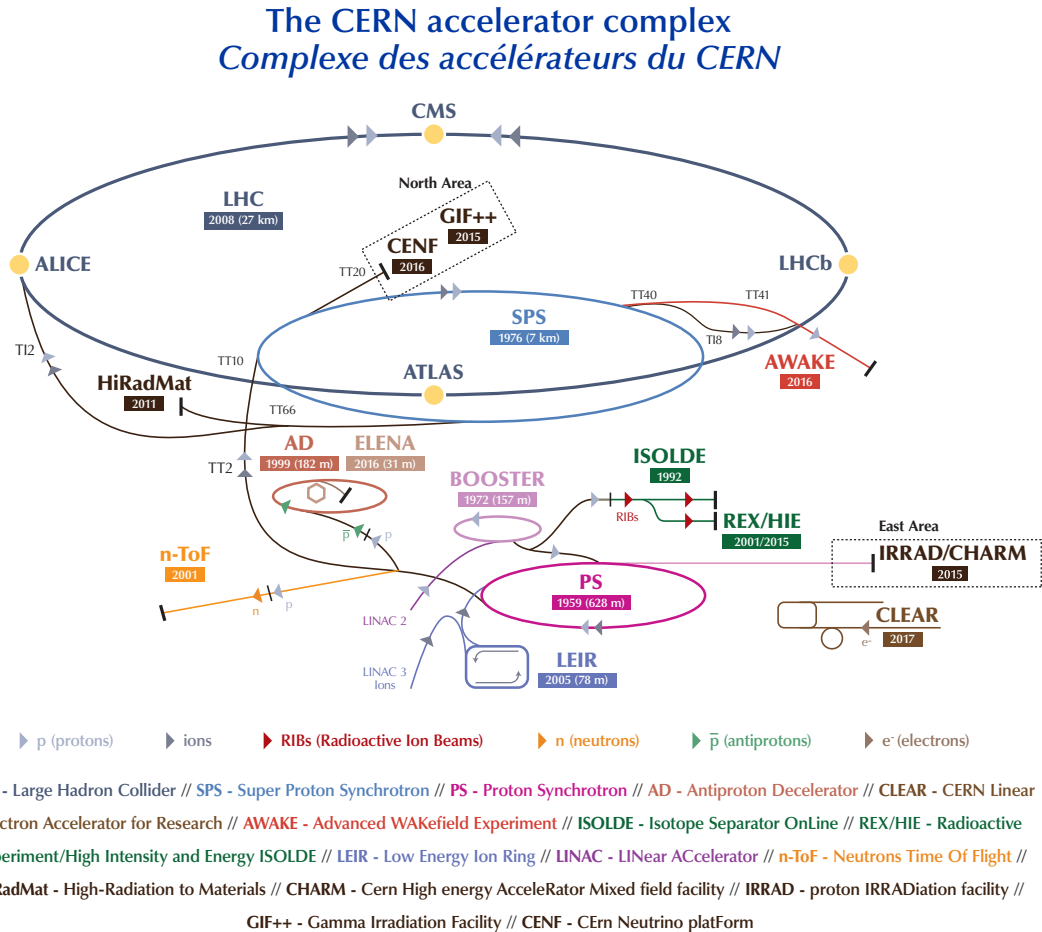


Figure 3.1: Schematic description of the accelerator complex at CERN [57].

The CERN accelerating complex [57] is shown in Fig. 3.1. At first protons are extracted from hydrogen gas and sent to LINAC 2, a linear accelerator, which produces proton beams with an energy of 50 MeV. The beams are subsequently sent to the Proton Synchrotron Booster (PSB), where they reach the energy of 1.4 GeV. The last two steps are the Proton Synchrotron (PS), which arranges the beam in groups called “bunches”, each containing $\sim 10^{11}$ protons, and increases the energy up to 26 GeV, and the Super Proton Synchrotron (SPS), after which the protons, with an energy of 450 GeV, are finally ready to be injected in the LHC, where they reach their maximum energy of up to 7 TeV. The beams are injected

into the LHC main ring in opposite directions and in separate ultrahigh vacuum beam pipes. Here, they are bent to follow the ring by the magnets and accelerated through the radio-frequency cavities. When they reach their maximum energy, the two accelerated beams collide at four interactions points (IP), corresponding to the positions of the four main LHC experiments:

- ALICE (A Large Ion Collider Experiment) [58] is a dedicated detector to study heavy ion collisions, it is optimised for $\sqrt{s} = 2.67$ TeV lead-lead ion collisions aiming at a peak luminosity of $\mathcal{L} = 10^{27} \text{ cm}^{-2} \text{ s}^{-1}$.
- ATLAS (A Toroidal LHC ApparatuS) [59] is a general purpose detector and it is the biggest experiment at the LHC.
- CMS (Compact Muon Solenoid) [60] is extensively described in Sec. 3.2.
- LHCb (LHC-beauty) [41] detector designed and optimised for the study of heavy flavour physics. It operates at lower instantaneous luminosity, but higher acceptance for soft physics.

The number of events per second generated in the LHC collisions is given by:

$$\frac{dN}{dt} = \sigma \mathcal{L}, \quad (3.1)$$

where σ is the cross section for the process under study and \mathcal{L} is the machine luminosity. The instantaneous peak luminosity depends only on the beam parameters and it can be written, for circular proton-proton (pp) accelerators and assuming a Gaussian beam distribution, as:

$$\mathcal{L} = \gamma \frac{n_b N^2 f_{rev} F}{4\pi \epsilon_n \beta^*}, \quad (3.2)$$

where γ is the relativistic gamma factor, N is the number of protons per bunch, n_b is the number of bunches per beam, f_{rev} is the bunches revolution frequency in the ring, β^* is the beam focal length, ϵ_n is the normalised transverse beam emittance and F the geometric luminosity reduction factor due to the crossing angle at the interaction point. These quantities are also useful to define another important quantity, the *pileup*, which is the average number of overlapped pp collisions in a bunch crossing and is defined as a Poisson distribution, with mean value:

$$\mu = \frac{\mathcal{L}\sigma}{f_{rev}n_b}. \quad (3.3)$$

The integrated luminosity $\mathcal{L}_{int} = \int \mathcal{L}(t)dt$ is also an important parameter. In fact, due to continued beam focusing and to the progressive degradation the

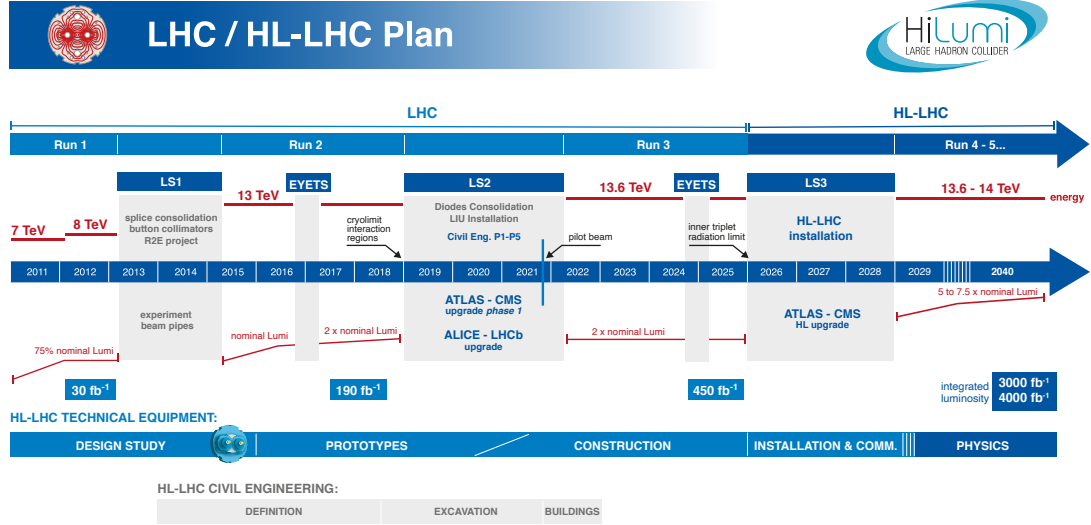


Figure 3.2: LHC baseline plan until 2040, showing the energy of the collisions (upper red line) and luminosity (lower green lines) [61].

beams suffer at each interaction, the peak luminosity varies in time. The integrated luminosity is used to estimate the number of collisions at the LHC

$$N = \sigma_{pp} \mathcal{L}_{int}, \quad (3.4)$$

where N is the number of collisions and σ_{pp} is the cross section for a pp interaction.

An overview of the LHC program is shown in Fig. 3.2. The collider has been fully operational since 2009 and will continue its activity at least until 2040.

The collider operation is articulated in Runs, for collisions and data taking, and Shutdowns, for maintenance and upgrades. The LHC activity started in 2009, with its first collisions useful for analysis starting in 2010, for a period called Run 1 (2010-2012). It started at a centre of mass energy of $\sqrt{s} = 0.98$ TeV, increasing up to 8 TeV in 2012, when the Higgs boson was discovered, with a mass of 125 GeV. After collecting around 30 fb^{-1} of integrated luminosity, the Long Shutdown 1 (LS1) started for the upgrade of the detectors in view of the $\sqrt{s} = 13$ TeV pp collisions. Run 2 started in 2015, delivering $\sqrt{s} = 13$ TeV of centre of mass energy, reaching the design luminosity of the collider. This period ended in December 2018, delivering a peak luminosity of $2.14 \cdot 10^{34} \text{ cm}^{-2} \text{ s}^{-1}$ at $\sqrt{s} = 13$ TeV, doubling the LHC design luminosity. After the LS2, the LHC data taking activities resumed in July 2022, officially starting the Run 3. Summary plots showing the delivered luminosity and the pileup in all the runs are reproduced in Fig. 3.3.

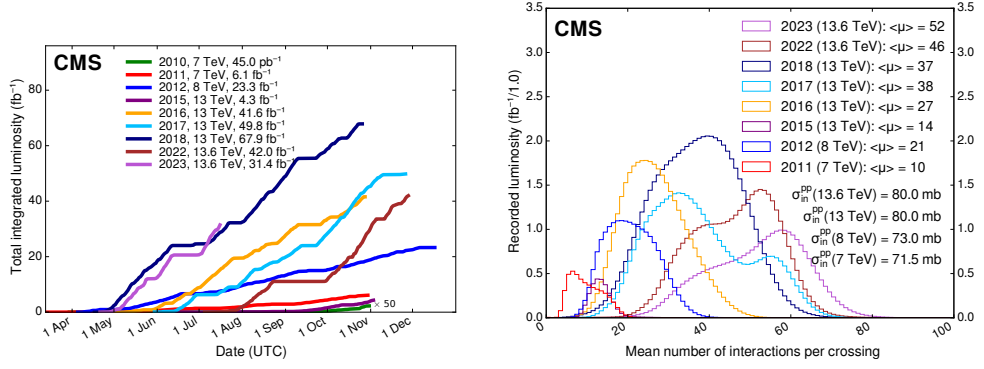


Figure 3.3: Delivered luminosity to CMS versus time (left) and distribution of the average number of interactions per crossing (pileup) for pp collisions (right) for Run 1, Run 2 and Run 3 [62].

3.1.1 Bottom quark production at the LHC

The production of a bottom-quark pair ($b\bar{b}$) is a particularly interesting and important process measured at the LHC. Although being the second heaviest quark, $m_b \sim 4\text{--}5 \text{ GeV}$, bottom quarks do not decay directly into elementary particles. Instead they form b -hadrons, which can be identified via their decays by the experiments as displaced vertices in their detectors, since b -hadrons have a relatively long lifetime as their decay is strongly CKM suppressed [63].

Leading order (LO) Feynman diagrams for this process are shown in Fig. 3.4. Theoretical predictions for $b\bar{b}$ production at next-to-next-to-leading order (NNLO) have been recently computed [64]. The production cross section of $b\bar{b}$ at hadron colliders, at a centre of mass energy of $\sqrt{s} = 13 \text{ TeV}$ is of $\sigma_{NNLO} \sim 500 \mu\text{b}$.

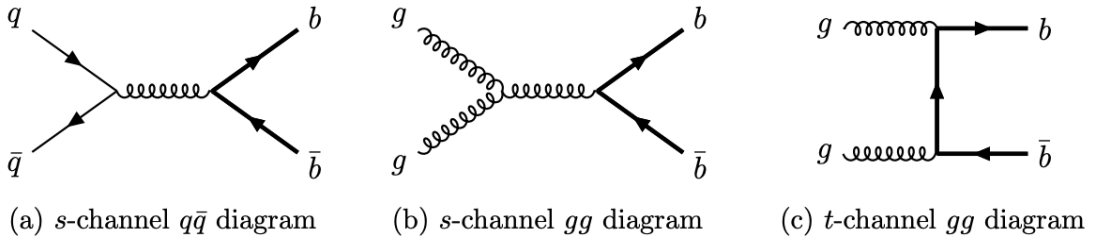


Figure 3.4: Feynman diagrams for the process $pp \rightarrow b\bar{b}$ at LO [63].

3.2 The CMS experiment

The CMS experiment is a general purpose detector, in fact its research program includes a wide range of physics at the LHC, from SM measurements to new physics searches. It is formed by several concentric layers, as shown in Fig. 3.5. Particles produced in the collisions interact in different ways with the several sub-detectors according to their nature. Being the data analysed in this thesis from the Run 2 data taking, in this chapter, the features of the CMS detector during that period are described.

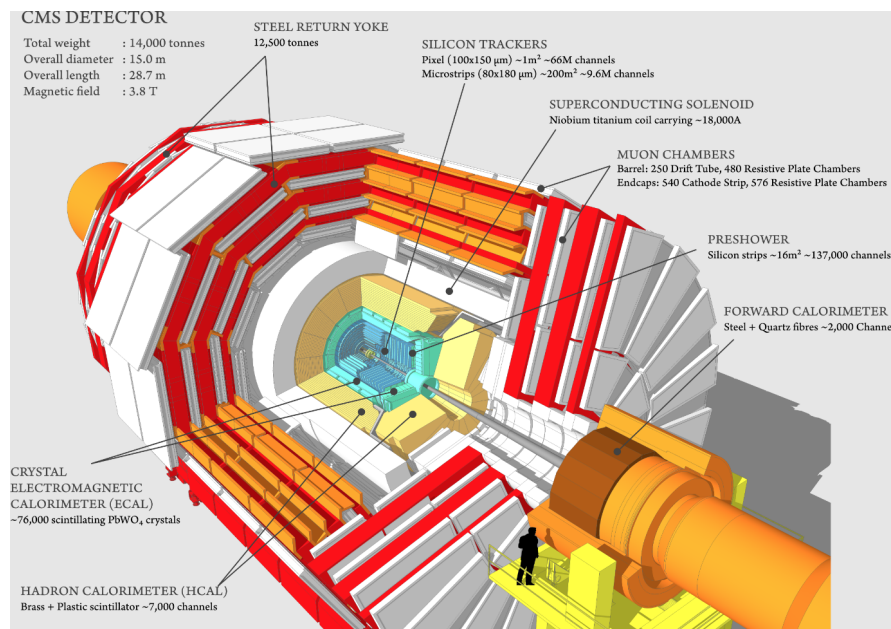


Figure 3.5: Inner structure of the CMS detector [65].

3.2.1 Coordinate system

CMS employs a right-handed coordinate system, shown in Fig. 3.6, with its origin situated at the nominal interaction point at the centre of the CMS detector. In this system, the x-axis points towards the centre of the LHC, the y-axis points vertically upward, perpendicular to its plane and the z-axis aligns with the anticlockwise direction of the beam. The x-y plane is indicated as the transverse plane. In the reconstruction of particle tracks within the CMS detector, a (ϕ, θ) cylindrical coordinate system is commonly employed due to the cylindrical symmetry of the detector. The azimuthal angle ϕ is measured in the xy-plane from the positive side of the x-axis, where $\phi = \pi/2$ corresponds to the positive side of the

y-axis. The polar angle θ is measured from the z-axis towards the x-y plane. The pseudorapidity η is defined as:

$$\eta = -\ln \left(\tan \frac{\theta}{2} \right). \quad (3.5)$$

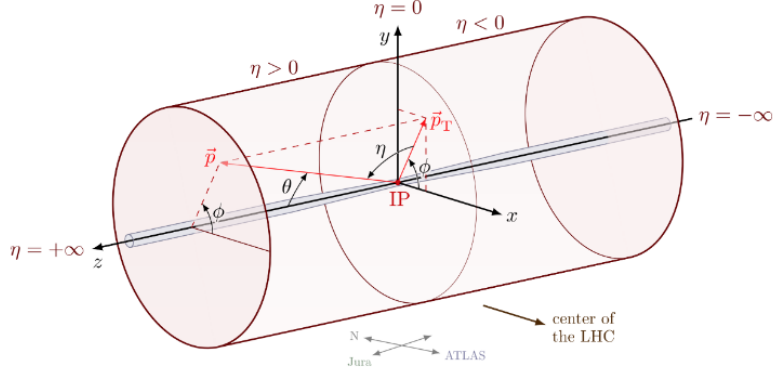


Figure 3.6: CMS coordinate system.

This variable is preferred to θ due to its applicability in the mass-less particle approximation, which is often valid in LHC hard interactions. It can be approximated to rapidity (Y), defined as:

$$Y = \frac{1}{2} \ln \frac{E + p_z}{E - p_z}. \quad (3.6)$$

Differences in rapidity are invariant under Lorenz boosts along the z-axis.

3.2.2 Sub-detectors

Detectors typically have a division into a central *barrel* section, characterised by a cylindrical geometry surrounding the beam line, and two forward regions known as the *endcaps*. This configuration enhances the detector acceptance in regions near the beam line but situated far from the interaction region. In Fig. 3.7 an overview of the CMS sub-detectors is shown.

3.2.2.1 The tracker

The inner tracking system [67] of CMS, measuring 5.8 m in length and 2.5 m in diameter, is designed for precise trajectory measurements of charged particles resulting from LHC collisions and for the reconstruction of secondary vertices. This system surrounds the interaction point, and it has a uniform magnetic field

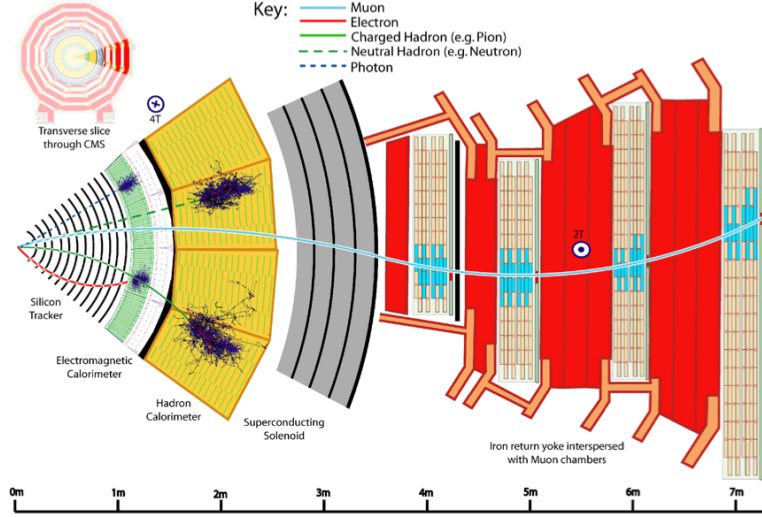


Figure 3.7: The CMS sub-detectors system [66].

of 3.8 T coming from the CMS solenoid. The tracker is formed by silicon detectors and divided into two sections: the Pixel detector, formed by four cylindrical barrel layers of hybrid pixel detectors, and the Silicon Strips detectors, with 10 barrel detection layers. A sketch of the CMS tracking system is shown in Fig. 3.8. Both structures are enclosed by endcaps. This extension widens the tracker acceptance to a pseudorapidity of $|\eta| < 2.5$. The high segmentation and response of silicon provides the position measurement in layers with a $\sim 10\mu\text{m}$ resolution, allowing for precise tracks reconstruction through the different tracker layers. Given its close proximity to the collision centre, this system operates effectively in a high-radiation environment, ensuring a rapid time response.

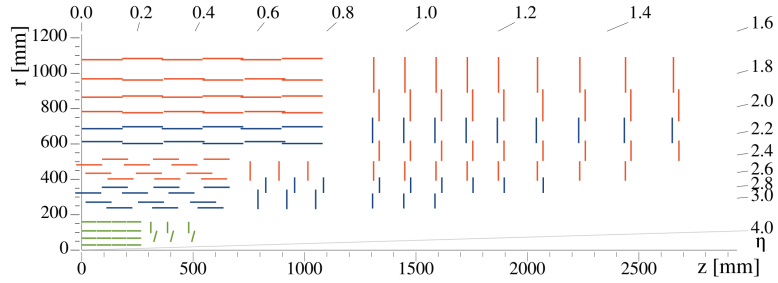


Figure 3.8: Sketch of one quarter of the CMS tracking system in r - z view. The pixel detector is shown in green, while single-sided and double-sided strip modules are depicted as red and blue segments, respectively [67].

3.2.2.2 The electromagnetic calorimeter

The electromagnetic calorimeter [68] of CMS (ECAL) is a hermetic homogeneous calorimeter, with 61200 lead tungstate (PbWO_4) crystals in the barrel section (EB), covering the pseudo-rapidity region $|\eta| < 1.479$, and an additional 7324 crystals in each of the two endcaps (EE), covering the $1.479 < |\eta| < 3.0$ region. A preshower detector (ES), employing lead absorbers with silicon strip sensors, is positioned in front of EE. ES covers the region $1.65 < |\eta| < 2.6$ and helps detecting the signals from high-energy photons resulting from the decay of neutral pions into two closely spaced photons. Additionally, the ES detector improves the measurement precision of the electromagnetic deposit position in EE. In Fig. 3.9, a scheme of ECAL is shown.

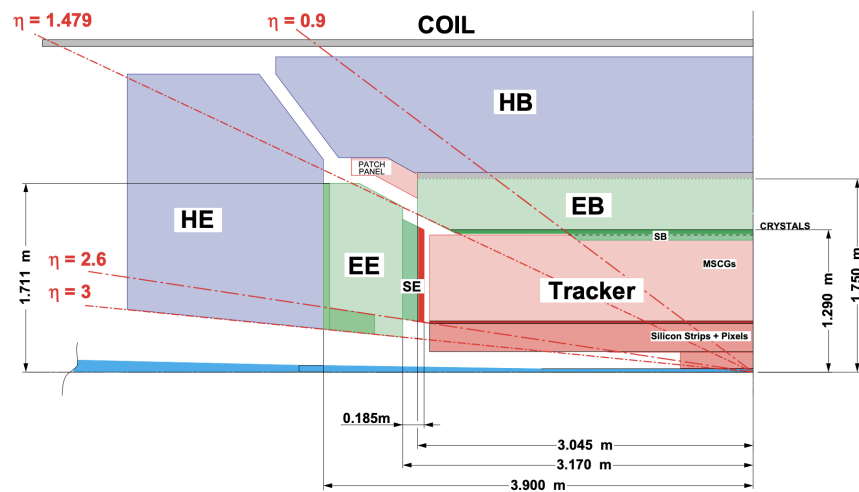


Figure 3.9: Schematic view of one quadrant of the calorimetry and tracking system [68].

PbWO_4 crystals are a suitable choice for LHC operation, given their high density (8.28 g/cm^3), short radiation length (0.89 cm), and small Molière radius (2.2 cm), providing optimal electromagnetic shower containment. The scintillation decay time for these crystals aligns with the LHC bunch crossing time, with approximately 80% of the light emitted within a 25 ns time-frame.

The ECAL energy resolution can be computed as

$$\left(\frac{\sigma}{E}\right)^2 = \left(\frac{S}{\sqrt{E}}\right)^2 + \left(\frac{N}{E}\right)^2 + C^2 \quad (3.7)$$

where $S = 2.8\%$ is the stochastic term, $N = 12\%$ the noise and $C = 0.3\%$ a constant term [68].

3.2.2.3 The hadronic calorimeter

The hadronic calorimeter (HCAL) [69] plays a crucial role in measuring the momentum of hadron jets, and identifying particles that result in apparent missing transverse energy. Positioned behind the tracker and ECAL from the IP, the HCAL space is constrained between the outer boundary of the ECAL and the inner boundary of the magnet coil. Consequently, an outer HCAL, or tail catcher, is situated outside the solenoid to complement the barrel calorimeter. It is a sampling calorimeter made of alternating layers of brass absorber and fluorescent scintillator materials and covering the region up to $|\eta| = 3.0$. The coverage is extended up to $|\eta| = 5$ with forward HCAL modules, using Cerenkov-based, radiation-hard technology. The energy resolution of HCAL is:

$$\left(\frac{\sigma}{E}\right)^2 = \left(\frac{S}{\sqrt{E}}\right) + C^2 \quad (3.8)$$

with $S=125\%$ stochastic term and $C= 5\%$ constant term [70].

3.2.2.4 The superconducting magnet

The superconducting magnet designed for CMS [71] is a 13 m long solenoid, with a diameter of 5.9 m and it is designed to achieve a 3.8 T magnetic field. It includes the tracker and the calorimeters, for which the uniform magnetic field allows the identification of the charge and transverse momentum of the particles thanks to the bending of their trajectory. The magnet flux is returned by a saturated iron yoke located outside the solenoid, which also works as mechanical support structure of the detector. The iron return yoke allows for a constant 1.8 T field also in the region outside the magnet, where the muon chambers are located.

3.2.2.5 The muon system

The detection of muons is a central goal for CMS, since the early stages of the experiment. Apart from neutrinos, muons are the only particles that can escape the calorimeters. They are identified by the external muon chambers [66] embedded in the magnet iron yoke. Due to the shape of the solenoidal magnet, the muon detector also has a cylindrical shape, with a barrel section and two endcap regions. In order to identify and measure muons, three types of gaseous detectors are used, shown in Fig. 3.10, depending on the different radiation environment. In the barrel region, $|\eta| < 1.2$, drift tube chambers are used. In this region, in fact, the background induced by the neutrons is small, and both the muon rate and the magnetic field in the chambers is low. In the endcaps, in regions up to $|\eta| < 2.4$, the muon rate, the magnetic field, and the neutron induced background are high, therefore cathode

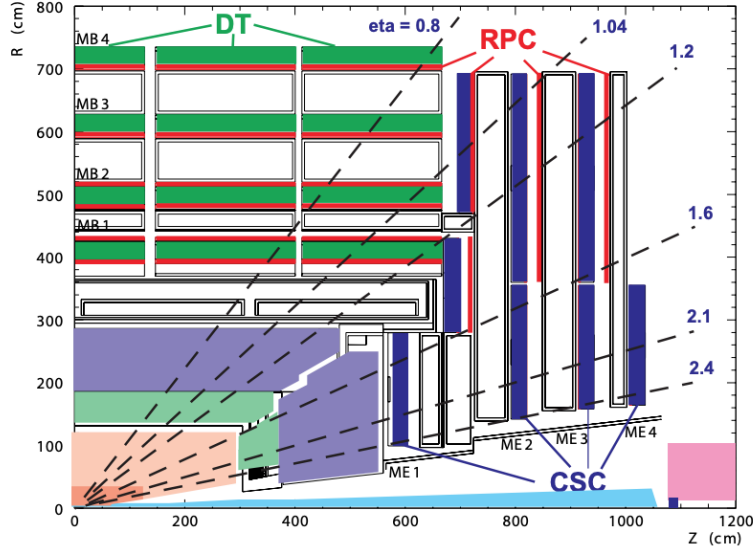


Figure 3.10: Layout of one quarter of the CMS muon system [66].

strip chambers (CSC) are employed. In both barrel and endcaps also resistive plate chambers (RPC) are used. RPCs can provide a fast response with good time resolution but with a coarser position resolution than the DTs or CSCs.

Muon chambers are characterised by high time resolution and a good space resolution. These properties make them the optimal solution for a fast high-efficiency trigger system.

3.2.3 Trigger system

Proton beam crossings at LHC occur at intervals of 25 ns, corresponding to a crossing frequency of not-empty bunches of 30 MHz. Depending on the pileup, multiple collisions occur at each crossing of proton bunches, with a resulting rate of events of 1 GHz. Given that each raw collision event has a size of approximately 1 MB, it is impossible to store all the events, therefore a substantial reduction in the rate has to be performed.

This is achieved with the trigger system. The allowed CMS bandwidth is around 2 GB/s. Considering the typical physics event size, the trigger system must reduce the initial rate down to about 1 kHz, six orders of magnitude lower than the input.

The trigger system is formed by two levels:

- **Level-1 Trigger (L1)** [72]: hardware processors using only information from the calorimeters and the muon chambers;

- **High-Level Trigger (HLT)** [73]: software system, which operates on the L1 output and full detector readout.

The L1 trigger has a design output rate of maximum 100 kHz. It exploits information from only the calorimeters and the muon system to decide whether an event should be saved or not, because the inner track algorithms are too slow for this stage, Fig. 3.11.

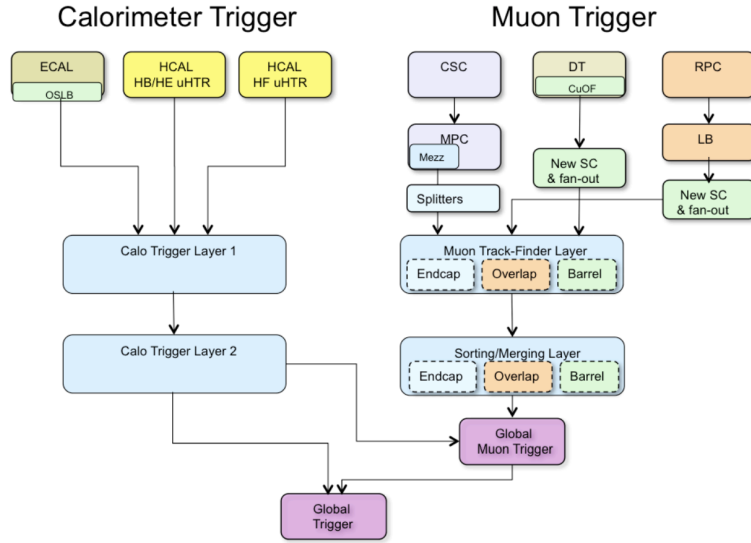


Figure 3.11: Dataflow for the overall L1 trigger [72].

The L1 Trigger hardware uses FPGAs where possible. However, due to needs related to speed, density, and radiation resistance, ASICs and programmable memory lookup tables are also employed. The L1 trigger includes local, regional, and global components.

At the local level, the local triggers are called Trigger Primitive Generators (TPG) and they rely on energy deposits in calorimeter trigger towers and track segments or hit patterns in muon chambers. Regional Triggers use this information and pattern logic to determine ranked and sorted trigger objects.

The Global Calorimeter and Global Muon Triggers identify the highest-ranked calorimeter and muon objects across the entire experiment. These are then transmitted to the Global Trigger, which makes the decision to either reject or accept an event, and send it for further evaluation to the HLT.

The HLT is an array of computers executing high-level physics algorithms, and it works with HLT paths. An HLT path is defined as a series of steps executed in a specific order to both reconstruct physics objects and apply selections to them.

Each HLT path is structured as a sequence of steps with increasing complexity and reconstruction levels.

The HLT provides a rate of 1 kHz to the storage stations, where events are stored in a Primary Dataset (PD) for subsequent offline data analysis. Each PD gathers events with similar topology, typically including more than one HLT path. For instance, in the data analysis detailed in the next chapters, which exploits the presence of J/ψ mesons, the data is stored in the so-called Charmonium PD. This PD includes events selected by the logical OR of various Charmonium HLT paths.

Both L1 and HLT paths could incorporate trigger prescales, where the prescale indicates how many events need to satisfy a trigger path requirement before a single event is recorded. As a general rule, trigger paths dedicated to the detection of rare events might be unprescaled, meaning a prescale of 1. On the other side, for processes with higher cross sections, the prescale factor could be high. This modulation helps to prevent a single physics process from saturating the entire trigger bandwidth.

3.2.4 Physics objects

Particles originating from the interaction point traverse various subsystems that detect their presence, subsequently providing information into their type and characteristics. These subsystems utilise diverse technologies, each optimised for specific tasks and functionalities.

The reconstruction methodology leverages the capabilities of each sub-detector to get a comprehensive and accurate particle reconstruction. For instance, the tracking system is responsible for reconstructing charged particles paths, interaction vertices, and, due to the magnetic field trajectory bending effect, the momentum of these charged particles. The calorimeters focus on measuring the energy carried by the particles. Specifically, the ECAL primarily absorbs electrons and photons, whereas the HCAL jets that result from the hadronisation of quarks, gluons, baryons, and mesons. Moreover, the muon system exclusively concentrates on measuring the paths and momentum of muons, given their ability to traverse the other systems with minimal energy loss. Neutrinos do not interact with any of the subsystems, therefore they cannot be detected.

The CMS particle-flow (PF) event reconstruction algorithm [74] combines information from all CMS subdetectors to identify and reconstruct individual particles like electrons, hadrons or muons. In every collision event, the algorithm detects and reconstructs a complete set of final-state particles, and provides a global event description. Furthermore, the approach discerns particles originating from pileup interactions, facilitating effective pileup mitigation techniques. This is only possible thanks to the fine spatial granularity of CMS detectors, which allow good separation between individual particles.

3.2.4.1 Vertices

In order to determine candidates, selected tracks undergo a vertex fit looking for a common vertex. This is an iterative procedure, as the fitting procedure is performed several times in order to improve the parameters uncertainty in each re-fit step. A successful fit returns the χ^2 of the geometrical fit, the common vertex along with its uncertainty and a post-fit state of the fitted particles. The primary vertex (PV) defined in the following chapters is the element of the PV collection that is the closest in the z -direction to the J/ψ meson selected in the event.

3.2.4.2 Muons

Reconstruction The muon spectrometer, described in Sec. 3.2.2.5, can identify and reconstruct muon tracks with high efficiency, therefore the PF algorithm is not used for muons. This high efficiency is mostly due to the fact that the calorimeters absorb almost all particles except for muons and neutrinos, therefore muons are the only particles that can interact with the muon system. Based on their reconstruction methods, muon candidates can be classified into three distinct categories [66]:

- **standalone muon:** tracks are exclusively reconstructed using the muon spectrometer, both tracking detectors (DT and CSC) and RPCs participate in the reconstruction. All hits from every muon subsystem are assembled using a Kalman Filter (KF) method.
- **tracker muon:** tracks with $p_T > 0.5$ GeV and a total momentum larger than 2.5 GeV are propagated to the muon system. If a match with the hits of the muon system is found, the track qualifies as a tracker muon.
- **global muon:** a standalone muon reconstruction is extended to match the information of the tracker and a global fit to the resulting track is performed.

The global muons turn out to have the highest reconstruction efficiency if their momentum is above 10 GeV, i.e. when they have hits in at least two muon stations [75]. Below this threshold, there is higher probability for muons to suffer from multiple scattering in the iron of the return yoke, so the tracker muon turns out to be the one with higher efficiency. Muons reconstructed only as standalone ones have a contamination from cosmic muons that reach the cavern. Charged hadrons as well may be reconstructed as muons if their shower is not completely blocked in the calorimeters (punch-through).

The PF algorithm applies particular selection criteria to the muon candidates reconstructed with the Global and Tracker Muon algorithms, for example making use of information from other subdetectors like the energy deposition in the calorimeters [76].

Identification Additional quality criteria are applied to reconstructed muon tracks to allow each analysis to tune the desired balance between efficiency and purity. Three main identification (ID) working points (WP) are defined [75]:

- Loose ID;
- Medium ID;
- Tight ID.

Since in the analysis the Medium ID WP will be chosen for the muon selection, in the following more details are given. The criteria for the Medium ID are an extension of the features outlined for the loose ID. Specifically, a muon is characterised as ‘loose’ if it is both chosen by the PF algorithm and categorised as either a tracker or global muon. Hence, a muon is a loose muon if it has hits from over 80% of the inner tracker layers it passes through.

In scenarios where the muon is solely reconstructed as a tracker muon, its muon segment compatibility should exceed 0.451. If the muon is both a tracker and a global muon, the muon segment compatibility should be above 0.303. In this case, the global fit is required to have a goodness-of-fit per degree of freedom (χ^2/dof) below 3. The positional alignment between the tracker muon and the standalone muon should have a χ^2 value less than 12, and the upper limit for χ^2 as determined by the kink-finding algorithm must be less than 20.

The requirements for the Medium ID WP are summarised in Table 3.1.

Plain-text description		Requirement
Group 1	Global muon	yes
	Normalised global-track	$\chi^2 < 3$
	Tracker-Standalone position match	$\chi^2 < 12$
	Kick finder	$\chi^2 < 20$
	Segment compatibility	> 0.303
Group 2	Segment compatibility	> 0.451

Table 3.1: Muon identification requirements for Medium ID WP. Either one of the two groups (1 or 2) must be satisfied [75].

Another identification criteria is used in Sec. 6.3, called the softMVA ID [77]. This selector has been initially developed for a CMS analysis looking for $B_s^0 \rightarrow \mu\mu$, and aims at reducing the fake rate from hadrons for low p_T muons originating from b -hadrons in the barrel. It consists of a Boosted Decision Tree (BDT) trained for global muons, with $p_T > 4 \text{ GeV}$ and $|\eta| < 1.4$, coming from $B_{s/d}$ mesons.

The event samples used for the study of the Multi-Variate Analysis (MVA) muon identification are Monte Carlo (MC) simulations focusing on B and Λ_b meson decays, including muons as well as pions and kaons. This allowed to train the MVA method with true muons as well as misidentified muons. Several selections were imposed on the tracks and are listed in the following:

- track fulfils the *high purity* criterion;
- $p_T > 4 \text{ GeV}$;
- $|\eta| < 1.4$;
- particle is a *global* muon;
- the true muon comes from a decay of a $B_{s/d}$ meson.

The distributions used to train the BDT include variables obtained during the global muon reconstruction, variables describing the hits and general track properties.

The BDT performance is characterised by its discriminating power, i.e. how many events have been classified correctly with respect to the total number of events analysed. To fix these values, however, one needs to define a working point. This working point corresponds to a cut on the BDT response which is a value in the range $[0,1]$ per event analysed. The working point can be chosen arbitrarily. The effect of a chosen cut on the BDT response can be indicated by the Receiver operating characteristic (ROC) curve, which corresponds to the signal efficiency as a function of the background misidentification probability. The BDT provides pion fake rates at the level of 0.05% and kaon fake rates at the level of 0.1%.

Isolation The isolation of a muon is defined by summing up the energy, or p_T , in geometrical cones surrounding the muon, with the distance parameter $\Delta R = \sqrt{(\Delta\phi)^2 + (\Delta\eta)^2}$. This is useful to distinguish between prompt muons from those coming from decays within jets. The isolation variable used in Sec. 6.3 is called *PF isolation*, $\Delta\beta_{corr,iso}$ [75], and it is described here. The particles considered in this computation are subjected to a selection with the impact parameter on the z axis $d_z < 0.2 \text{ cm}$ to be considered as originating from the PV. The transverse momentum (p_T) of charged hadrons within the ΔR cone originating from the PV is summed with the energy sum of all neutral particles (hadrons and photons) in the cone. The contribution from pileup to the neutral particles is corrected by computing the sum of charged hadron deposits originating from pileup vertices, scaling it by a factor $\Delta\beta = 0.5$, and subtracting this from the neutral hadron and photon sums to give the corrected energy sum from neutral particles. The

factor of 0.5 is estimated from simulations to be approximately the ratio of neutral particle to charged hadron production in inelastic proton-proton collisions. The corrected energy sum from neutral particles is limited to be positive or zero. This is summarised as:

$$\Delta\beta_{corr}^{iso} = \frac{I^{ch} + \max(I^n + I^{pho} - \Delta\beta I^{pu}, 0)}{p_T}, \quad (3.9)$$

where I^{ch} is the isolation of the charged hadrons from the PV; I^n of neutral hadrons; I^{pho} of photons; I^{pu} of charged hadrons from the pileup contribution; and $\Delta\beta$ is estimated to be 0.5 from pileup considerations.

The value for the medium working point for PF isolation, which will be used in the following, within $\Delta R < 0.3$ is 0.2, and its efficiency is 95 %. The efficiency of the working points to reject muons in jets was tested in simulated multi-jet QCD events and events containing a W boson plus one or more jets.

Part II

Measurement of $R(J/\psi)$ with CMS Data

Chapter 4

Overview

The LFU is an interesting field for testing the SM using data from the LHC. Notably, several deviations from the SM predictions, particularly in the FCCC sector of b -quark decays, have been measured, as already highlighted in Sec. 2.5. LFU tests can be conducted using experimental measurements of the ratio of branching fractions from analogous semileptonic decays of a B -meson involving two different lepton flavours. Ratios are preferred to absolute branching fractions because common systematic uncertainties, such as efficiencies and theoretical uncertainties, partially or completely cancel out.

The FCCC transition $b \rightarrow c\tau\nu_\tau$ is a tree-level process mediated by the exchange of a virtual W^* boson, as shown in Fig. 4.1 (left). The same process could also occur via contributions of BSM phenomena, as those described in Sec. 2.6. The Fig. 4.1 (centre and right) shows a possible additional contribution to the decay rate, mediated by the exchange of a new, virtual, particle.

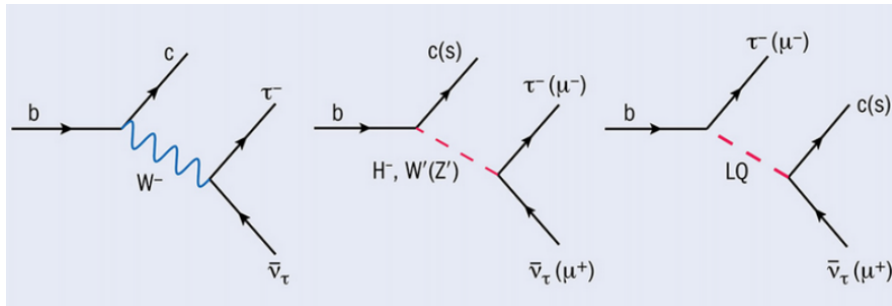


Figure 4.1: Feynman diagram for b -quark semileptonic decay, as predicted by the SM (left) and with possible contributions of new physics (centre and right).

An interesting channel to investigate LFU violations within this transition is

the semileptonic decay $B_c^+ \rightarrow J/\psi \tau^+ \nu_\tau$ ¹. The B_c^+ meson is composed of a \bar{b} quark and a c quark. In the considered process, the \bar{b} quark decays into a \bar{c} quark with the combined production of a lepton and a neutrino. The produced \bar{c} quark then combines with the spectator quark c creating a J/ψ meson.

The $R(J/\psi)$ ratio includes this decay and can be used to test LFU

$$R(J/\psi) = \frac{\mathcal{B}(B_c^+ \rightarrow J/\psi \tau^+ \nu_\tau)}{\mathcal{B}(B_c^+ \rightarrow J/\psi \mu^+ \nu_\mu)}. \quad (4.1)$$

This thesis presents the first measurement of the $R(J/\psi)$ ratio at CMS, using data collected in 2018, corresponding to a total integrated luminosity of $\mathcal{L} = 59.7 \text{ fb}^{-1}$, where only muonic decays of the τ lepton and the $\mu^+ \mu^-$ decay of the J/ψ meson are considered. Hereafter, the $B_c^+ \rightarrow J/\psi \tau^+ \nu_\tau$ channel will be indicated as τ -channel (or τ -signal), and the $B_c^+ \rightarrow J/\psi \mu^+ \nu_\mu$ one as μ -channel (or μ -signal).

4.1 $R(J/\psi)$ measurement at CMS

In the context of LFU tests, B_c decays have not been extensively explored yet. The B_c mesons cannot be produced at the b -factories, which operate at the $\Upsilon(5S)$ peak. The reason is that the Υ has sufficient mass to produce up to a pair of B_s but not a pair of B_c mesons. As a result, the production of B_c mesons is exclusive to the LHC. Only one previous $R(J/\psi)$ measurement has been published by the LHCb collaboration [78], based on data collected in 2016 and total integrated luminosity of 3 fb^{-1} . The result is $R(J/\psi) = 0.71 \pm 0.25$, a value that exceeds by 2σ the SM prediction of $R(J/\psi) = 0.2582(38)$ [36].

In CMS there is the potential to produce a competitive measurement. In fact CMS can benefit from:

- High integrated luminosity: $\mathcal{L} = 3 \text{ fb}^{-1}$ for the full Run 1 for LHCb, and $\mathcal{L} = 59.7 \text{ fb}^{-1}$ for only 2018 data taking in CMS.
- Excellent muon reconstruction and identification performance. Data analysed in this document have been collected in 2018 during Run 2 data-taking using $J/\psi(\mu\mu)$ -based triggers. Furthermore, only the muonic final state is considered for τ leptons, aiming for a visible final state composed of three muons. Hence, as opposed to many other heavy flavour analyses, the lack of particle ID capabilities in CMS is then not critical in this case.

¹This is valid for both channels, $B_c^+ \rightarrow J/\psi \tau^+ \nu_\tau$ and its charge conjugate process. Similarly in the following for $B_c^+ \rightarrow J/\psi \mu^+ \nu_\mu$ and its charge conjugate process.

- Almost 4π solid-angle acceptance compared to the about 0.16π solid-angle acceptance of the LHCb detector [79]. This is relevant for suppression of backgrounds involving additional tracks around the $J/\psi\mu$ vertex. Additionally, it compensates for the CMS detector lower acceptance in muon p_T , starting from 3 GeV, in comparison to LHCb, which can reach as low as 0.8 GeV [80].

The measurement reported in this thesis can contribute to enriching the lepton flavour anomaly scenario with a first measurement of the $R(J/\psi)$ ratio at a general-purpose hadron collider experiment, such as CMS.

4.2 Analysis strategy

An overview of the analysis strategy is presented in this section, with references to the other chapters expanding each step of the analysis.

The analysis uses data collected by the CMS experiment in 2018, corresponding to an integrated luminosity of 59.7 fb^{-1} and leverages the visible final state of 3 muons, common to both B_c decays of interest, $B_c \rightarrow J/\psi\tau(\rightarrow \mu\nu_\mu\nu_\tau)\nu_\tau$ and $B_c \rightarrow J/\psi\mu\nu_\mu$.

Events are selected using HLT triggers requiring 3 muons in the final state, two of which coming from a J/ψ vertex, called μ_1 and μ_2 , and a third muon, referred to as μ_3 . Muons selected in the offline analysis are matched to those that fired the trigger. Their nominal kinematic thresholds used online are reinforced by requiring that all muons be within $|\eta| < 2.5$ and have transverse momenta larger than 6, 4, 4 GeV (a p_T leading, sub-leading and trailing muon is defined in each event) to reduce the impact of possible mismodelings near the threshold.

Vertex fits are performed to determine the $J/\psi \rightarrow \mu\mu$ vertex first, and the $B_c \rightarrow J/\psi\mu\nu$ one afterwards. Both of these fits include a constraint on the J/ψ mass.

Despite sharing the same final state, τ and μ channels present significant differences in the kinematics, due to the presence of 3 or 1 neutrinos, respectively. The 4-vector of the B_c cannot be reconstructed directly because of the undetectable neutrino contribution. The four-momentum is estimated following the *collinear approximation*, where the B_c is assumed to have the same direction of the 4-vector reconstructed from the visible 3-muon candidate, while its magnitude is scaled up by the ratio $m_{B_c}^{PDG}/m_{vis}^{3\mu}$. The approximation used in this study has been compared to an alternative method employed in Ref. [78], which considers the flight direction of the B_c particle to be the same as the one connecting the PV and secondary vertex (SV). The collinear approximation is the one that works best for this analysis, also thanks to the relatively large Lorentz boost of the selected candidates, and it

is described in Sec. 5.5. A number of observables derived from the difference between the 4-vector of the B_c reconstructed with the collinear approximation and the 4-vector of the 3-muon candidate are studied.

The event selection is detailed in Ch. 5 and it is optimised to enhance the presence of the τ and μ channel contributions while minimising the contamination from background processes, which are:

- decays of the B_c meson, including other $J/\psi +$ charmed hadron decays or J/ψ mesons coming from other excited $c\bar{c}$ states (feed-downs);
- misidentified muon backgrounds, where a kaon or a pion from the event is misidentified as μ_3 ;
- combinatorial background where the J/ψ meson and the third muon μ_3 are coupled, but they come either from another b -hadron, or from different mother particles;
- combinatorial J/ψ background where the two muons composing the J/ψ do not come from a J/ψ decay.

Backgrounds are mostly estimated from data. When not possible, the MC-based estimate is complemented with inputs or constraints from data. More details are given in Ch. 6.

MC samples needed to model the B_c decays and the $J/\psi + \mu$ combinatorial background are presented in Ch. 5. The CMS simulation is rather good in reproducing the distributions of interest observed in data. Nevertheless, a number of corrections need to be applied to the MC samples to reach the appropriate data-MC agreement required by this analysis. The list of these corrections includes pileup reweighting, muon reconstruction, and identification, isolation and trigger scale factors. In addition, the lifetime of the B_c in the MC samples is corrected to the PDG value and new hadronic form factors have been made available [38] replacing those [81] provided with the BCVEGPY generator [82]. They are implemented via a generator-level reweighting based on the HAMMER [83] software. All these corrections are described in Ch. 7.

The $R(J/\psi)$ observable is extracted from a binned maximum likelihood fit to the squared energy transfer to the lepton system q^2 and the decay length of the B_c meson distributions. The fit categories are defined by the 3D impact parameter of the third muon and the invariant mass of the three muons. The two B_c decays of interest as well as all background contributions are included in the fit model. Uncertainties are incorporated in the fit as nuisance parameters. Fourteen (7x2) event categories are simultaneously fitted, to constrain and measure the background contributions, and to increase the analysis sensitivity. More details on the fitting strategy are given in Ch. 8 and, finally, results are presented in Ch. 9.

Chapter 5

Event Selection

The dataset selected for this analysis includes only events with a J/ψ meson, which is in the final state of the $R(J/\psi)$ processes of interest. This dataset, further detailed in Sec. 5.1 of this Chapter, is the **Charmonium PD**. For the simulation of signal and background processes, two MC samples are used: the $B_c \rightarrow J/\psi + \mu$ and $H_b \rightarrow J/\psi + \mu$. These samples, specifically generated for this study, are comprehensively described in Sec. 5.2.1 and Sec. 5.2.2, respectively.

The CMS trigger paths chosen for this analysis are outlined in Sec. 5.3. Additionally, the preselection criteria employed to enrich the dataset with signal events are detailed in Sec. 5.4. This chapter also includes a description of the collinear approximation. This, along with the definition of several fundamental variables, is presented in Sec. 5.5 and Sec. 5.6, respectively.

5.1 Data samples

The analysis relies on data recorded by the CMS detector in pp collisions during 2018 at a centre-of-mass energy of $\sqrt{s} = 13$ TeV. This dataset corresponds to approximately 43% of the total integrated luminosity collected by the CMS experiment during Run 2. Only data of high quality, as indicated by the "golden JSON" file [84] provided by CMS to the analysts, is used. This corresponds to an integrated luminosity of 59.7 fb^{-1} . The specific datasets used are detailed in Tab. 5.1.

The CMS Ultra-Legacy (UL) reprocessing of data samples is used, as recommended for all CMS Run 2 analyses. The UL campaigns are the standard campaigns with the corresponding setup schemes to reflect the Run 2 data taking period in CMS, which includes all the most recent and accurate calibrations.

Data Sample	Integrated \mathcal{L} [fb $^{-1}$]
/Charmonium/Run2018A-12Nov2019_UL2018_rsb-v1/MINIAOD	14.0
/Charmonium/Run2018B-12Nov2019_UL2018-v1/MINIAOD	7.1
/Charmonium/Run2018C-12Nov2019_UL2018_rsb_v2-v2/MINIAOD	6.8
/Charmonium/Run2018D-12Nov2019_UL2018-v1/MINIAOD	31.8

Table 5.1: List of the Charmonium PD data samples used to perform the measurement.

5.2 Monte-Carlo samples

Simulated MC samples are used to evaluate signals as well as most of the background processes. Signals include $B_c^+ \rightarrow J/\psi \tau^+ \nu_\tau$ and $B_c^+ \rightarrow J/\psi \mu^+ \nu_\mu$ processes, while backgrounds comprise other B_c meson decays with a J/ψ in the final state and other b -hadron initiated processes where a non-prompt J/ψ meson is accompanied by an additional muon. The backgrounds are further described in Ch. 6.

All processes initiated by a B_c , including both signals and backgrounds, are simulated within a single MC sample. The specifics of this sample are described in Sec. 5.2.1. Non-prompt J/ψ backgrounds from other b -hadron decays are represented in a separate MC sample, characterised by the requirement of a genuine muon coupled with the J/ψ . Further information on this sample is provided in Sec. 5.2.2. Additionally, a similar sample has been generated without the requirement of a real muon as μ_3 . This alternative sample, created to study the impact of fake muon contamination, is also discussed in Sec. 5.2.2. All these samples have been specifically developed and produced for this analysis.

MC simulation in CMS passes through several processing steps before the samples are in a format that is good for analysis, as shown in Fig. 5.1. The initial stage involves simulating the hard scattering of the interesting processes (GEN). Following that, the simulation step (SIM) accounts for impact of detectors and electronics, i.e. the interaction of the particles with matter, and the inclusion of pileup interaction. The output at this stage is analogous to the experimental output. Lastly, the RECO step utilises either simulated or real data for the reconstruction of events resulting from the collisions. The reconstructed data can be then employed in the analyses.

5.2.1 $B_c \rightarrow J/\psi + \mu$ MC sample

This simulated sample comprises all B_c decays of relevance, i.e. B_c decays that can yield a J/ψ and a genuine muon, also including multi-tiered decay chains (i.e. feed-downs decays or decays where the muon comes from a D meson), summarised

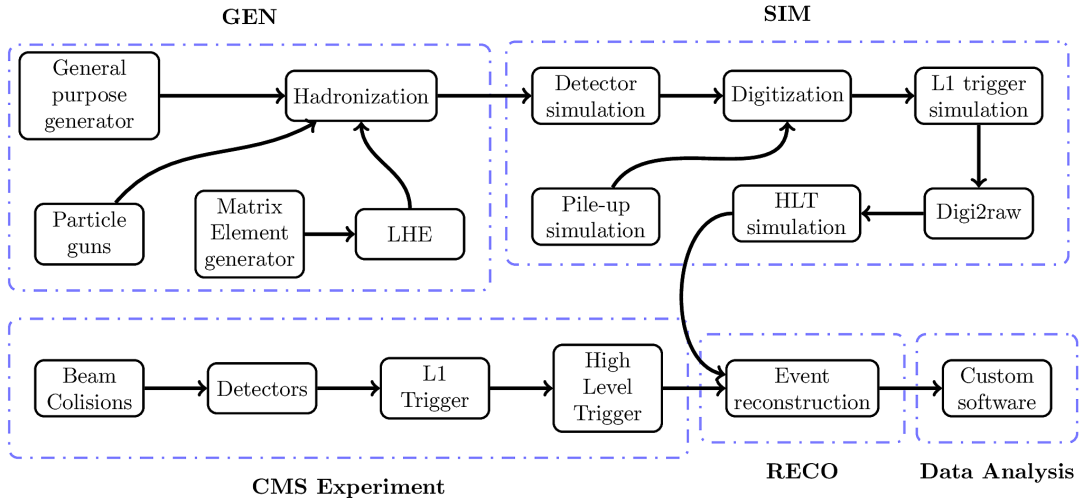


Figure 5.1: Steps of MC production in CMS [85].

in Tab. 5.2.

Processes simulated in this sample include:

- the signals $B_c^+ \rightarrow J/\psi \tau^+ \nu_\tau$ and $B_c^+ \rightarrow J/\psi \mu^+ \nu_\mu$;
- feed-downs decays, i.e. excited $c\bar{c}$ mesons decaying into a J/ψ , coupled with a μ ;
- J/ψ mesons coupled with hadrons, for example charmed hadrons like $B_c \rightarrow D_s^{(*)} J/\psi$, where the μ_3 can derive from semileptonic decays of the D -mesons.

The B_c meson kinematics are produced using the dedicated generator BCVEGPY [82, 93], the decay of the B_c meson is handled by EVTGEN v1.6.0 [94, 95] and the hadronisation and decay of the rest of the event is run by PYTHIA v8.240 [96]. Branching fractions are given relative to that of $B_c^+ \rightarrow J/\psi \mu^+ \nu_\mu$ and their values are based on the most recent literature available. Individual references are given in the last column of the table. To simplify the setup of the fit and extract the value of $R(J/\psi)$ directly, the branching fraction of $B_c^+ \rightarrow J/\psi \tau^+ \nu_\tau$ relative to $B_c^+ \rightarrow J/\psi \mu^+ \nu_\mu$ is set to unity. The implications of this assumption is discussed in Ch. 8.

5.2.2 $H_b \rightarrow J/\psi + \mu$ MC sample

A significant portion of background events consists of 3-muon candidates, involving a J/ψ meson that originates from a b -hadron decay and then decays

Type	idx	Decay	relative \mathcal{B}	Ref.
Signals	1	$J/\psi \mu \nu$	1.	[21]
	2	$J/\psi \tau \nu$	1.	-
Feed-downs	3	$\psi(2S) \mu \nu$	0.05	[86]
	4	$\psi(2S) \tau \nu$	0.0042	[21]
	5	$\chi_{c0}(1P) \mu \nu$	0.1083	[86]
	6	$\chi_{c1}(1P) \mu \nu$	0.1083	[86]
	7	$\chi_{c2}(1P) \mu \nu$	0.1083	[86]
	8	$h_c \mu \nu$	0.154	[86]
	9	$J/\psi \pi$	0.0469	[21]
	10	$J/\psi \pi^\pm \pi^0$	0.11256	[21]
$J/\psi + H$	11	$J/\psi K^\pm$	0.003705	[21]
	12	$J/\psi p \bar{p} \pi$	0.00671	[87]
	13	$J/\psi K^\pm K^\mp \pi^\pm$	0.02486	[88]
	14	$J/\psi D_s$	0.13601	[89, 90]
$J/\psi + H_c$	15	$J/\psi D_s^*$	0.32234	[89, 90]
	16	$J/\psi D_0 K$	0.02026	[91]
	17	$J/\psi D^*(2010) K$	0.10333	[91]
	18	$J/\psi D^* K^*$	0.042546	[91]
	19	$J/\psi D K^*$	0.012764	[91]
	20	$J/\psi D$	0.02084	[92]
	21	$J/\psi D^*$	0.01581	[92]

Table 5.2: List of all B_c decays of relevance included in the $B_c \rightarrow J/\psi + \mu$ MC sample produced for the analysis. Branching fractions are given relative to that of $B_c^+ \rightarrow J/\psi \mu^+ \nu_\mu$ and their values are based on the most recent literature available, whose reference is reported in the last column. Forced decays into J/ψ and muons are not included in the branching fractions.

into two muons, accompanied by a third, combinatorial muon, i.e. $J/\psi + \mu$. This specific background contribution is referred to as H_b background. This third muon may come from the same b -hadron as that of the J/ψ meson (SBH), e.g. $B_s \rightarrow J/\psi (\rightarrow \mu\mu) \phi (\rightarrow \mu\mu)$, or from a different mother (DBH), but must be close to the direction of the J/ψ meson, Fig. 5.2 (left). For the former case, the invariant mass of the three muons is lower than that of the b -hadron, that is lower than about 5 GeV, whereas for the latter case the invariant mass of the three muons can possibly exceed 5 GeV and notably exceed the $m_{B_c} = 6.3$ GeV kinematic limit for signal 3-muon candidates. This signal-depleted high mass ($m_{3\mu} > 6.3$ GeV) region is used as a control sideband to estimate this class of background processes.

In Fig. 5.2 is shown that 98% of H_b background events originate from distinct

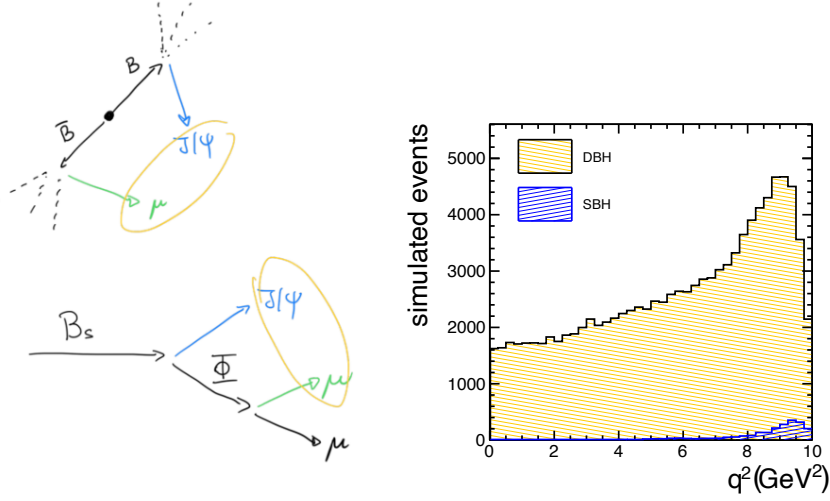


Figure 5.2: The H_b background is composed of two different processes: the J/ψ meson and the muon come from different, DBH (top left), or same, SBH (bottom left), b -hadrons. The two contributions for a fraction of the MC H_b can be seen for the q^2 distribution (right).

mother particles.

The main challenge is to efficiently produce a large number of events reproducing processes with large cross sections from which only events with muons in the kinematic and geometric acceptance of CMS will be later processed. The $b\bar{b}$ cross section is of the order of hundreds of μb [97], while the branching fraction of charmonium decays of b -hadrons ranges from about 2% for non-charmed b -mesons to about 40% for b -baryons [21]. One way to improve the generation efficiency is to force the decay of the b -hadrons: this guarantees that, for each event, a b -hadron eventually decays into a J/ψ meson and, since $\sim 90\%$ of b quarks hadronise into either a B^+ , B^0 or a B_s meson, this translates into a factor $1/\mathcal{B}(b\text{-hadrons} \rightarrow c\bar{c}) \sim 1/2\% \sim 50$ gain compared to a non-forced-decay sample.

Using forced decays is necessary in order to meet the minimum CPU efficiency requirements for the CMS central MC production, but it also introduces additional complications:

- there exist hundreds of possible b -hadron decays that can lead to a J/ψ meson;
- the J/ψ meson can be produced in multi-step or feed-down decays (e.g. $B^+ \rightarrow \psi(2S) \rightarrow J/\psi K^+$), where every step is forced and this can alter the correct branching fraction proportions between different decays, if not corrected;

- since only one of the two (or more) b -hadrons produced in the $b\bar{b}$ event is force-decayed, also the relative abundances of the different b -hadron species need to be adjusted.

In the rest of this section, the solutions developed to address these problems are explained.

Minimum-bias QCD events are generated with PYTHIA v8.240 [96]. Events are filtered before hadronisation based on the presence of a b -quark and, after hadronisation, based on a variety of b -hadron decays that eventually lead to a J/ψ meson (either directly or via charmonium feed-down processes). The decays of b -hadrons into J/ψ mesons and their accompanying muons are forced in the simulation using EVTGEN v1.6.0 [94].

The list of b -hadrons that are subject to forced decays (charge conjugates implied) is B^+ , B^0 , B_s , B_c , Λ_b^0 , Ξ_b^- , Ξ_b^0 , Σ_b^- , Ω_b^- and the full list of forced decays can be found in this reference [98]. The list of forced decays is largely based on the default list of decays known to EVTGEN v1.6.0, as embedded in the CMS software CMSSW [99], where processes that cannot produce a J/ψ meson have been removed and obvious omissions, e.g. $\Lambda_b^0 \rightarrow pJ/\psi K^-$, have been added. As a reference, the PDG [21] and the literature available at the time of writing have been used to produce a list of forced decays as complete as possible. However, it cannot be excluded that some minor or poorly known decays have been left out. In addition, feed-down decays from excited charmonium states are also forced. $\psi(2S)$, $\psi(3770)$, $\chi_{c0}(1P)$, $\chi_{c1}(1P)$, $\chi_{c2}(1P)$ and h_c are forced to decay in ways that give rise to a J/ψ meson. Finally, the J/ψ meson itself, when it is a decay product of a b -hadron, is allowed to decay solely in muon pairs.

An immediate consequence of forcing decays for multiple b -hadron species in the same sample is that the proportions between the different species are skewed. Approximately, the larger the difference of forced branching ratios - in the case at hand from $\sim 2\%$ to $\sim 40\%$, for mesons and baryons respectively - the larger the bias. To accurately assess biases introduced by the enforced decay processes, an empirical methodology was adopted. Therefore another MC sample, where no decays are forced (except for $J/\psi \rightarrow \mu\mu$), has been produced. Being this the only difference in production, this sample is used as a reference for the b -hadron species relative abundances. From the comparison between the forced-decay and non-forced-decay sample, which is shown in Fig. 5.3 (left), some per-event weights are derived. These weights, which are shown in Fig. 5.3 (right), are based on the species of the ancestor b -hadron and are applied to the $J/\psi + \mu$ events at all stages of the analysis.

With such a varied collection of possible decays, it is important to preserve the correct proportions between different processes originating from a given b -hadron species. The complication arises when single-step decays, e.g. $B^+ \rightarrow J/\psi K^+$, and

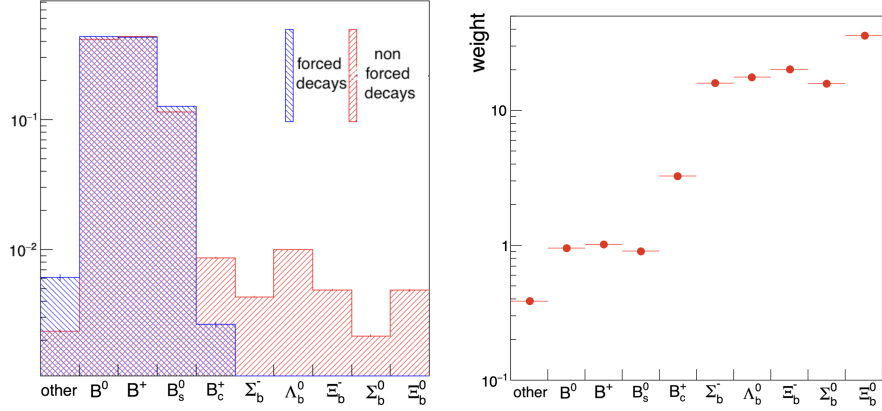


Figure 5.3: Abundances of hadrons (left) and per-event correction weights (right) compared between the pure non-forced-decay PYTHIA (red) and the forced-decay EVTGEN sample (blue).

multi-step decays, e.g. $B^+ \rightarrow \psi(2S)(\rightarrow J/\psi)K^+$, are put together. Each forced decay in the chain gives an enhancement equal to the inverse of the total forced-decay branching ratio, and therefore this factor needs to be accounted for to put different decays on equal basis. This is done in a systematic way via scripts that modify the relevant numbers in the EVTGEN decay file and the correctness of this procedure is checked in a few cases against a manual calculation. Furthermore, the procedure is validated using the non-forced-decay sample described earlier. Figure 5.4 shows the occurrence rate of each decay type in either sample. The closure is mostly good, except for a few cases which were individually investigated finding that the forced-decay sample gives the correct result. For instance, the second and third bin correspond to $B^+ \rightarrow J/\psi K^{*+}(892)$ ($\mathcal{B} = 1.43 \cdot 10^{-3}$) and $B^+ \rightarrow J/\psi \pi^+$ ($\mathcal{B} = 3.92 \cdot 10^{-5}$), respectively. Therefore, the third bin should sit lower than the second, which is what the forced-decay sample correctly predicts. Additionally, B_c decays have been excluded from this sample to avoid duplication, since they are accounted for in the dedicated B_c sample, as described in Sec. 5.2.1. In conclusion, the correct proportions between the different decay processes are preserved in the forced-decay sample.

Analogous to the $H_b \rightarrow J/\psi + \mu$ sample developed for the H_b background, a sample has been generated specifically to perform studies on the fakes background, which is described in Sec. 6.3. Also for this sample the presence of a $J/\psi \rightarrow \mu\mu$ coming from a b -hadron is required, but, differently from the $H_b \rightarrow J/\psi + \mu$ sample, where an additional muon in the vicinity of the J/ψ meson is required, for this other one no further selections are enforced, and it is called $H_b \rightarrow J/\psi + X$ sample. This is more inclusive (in principle it contains the $H_b \rightarrow J/\psi + \mu$ sample) and, as

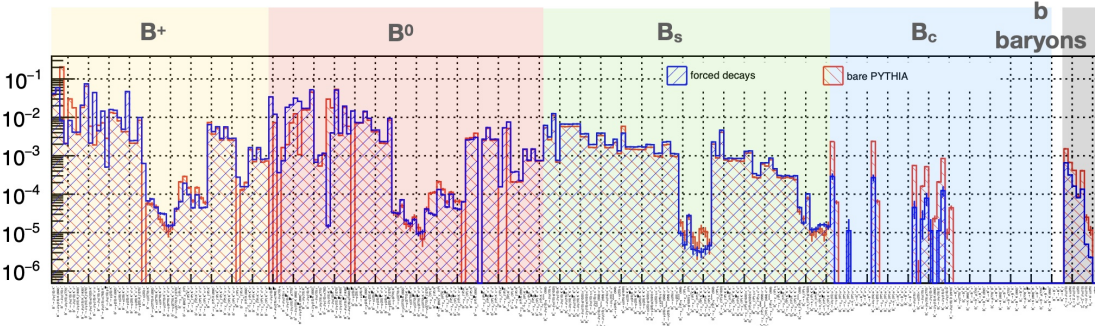


Figure 5.4: Comparison of the abundances of specific decay processes between the non-forced-decay PYTHIA (red) and the forced-decay EVTGEN sample (blue). Differences in the B_c region are of no practical relevance, as B_c initiated processes are estimated using a dedicated MC sample.

already mentioned, it is used for studies and checks on the fakes background, where the third muon found at the reconstruction level is due to a misidentified hadron. The two samples share the same setup as the same generation and decays are concerned[100, 101], but they differ in terms of additional filters used to specialise the samples for different scopes. The $H_b \rightarrow J/\psi + \mu$ sample, thanks to the more stringent requirements at GEN-level, offers comparably better statistics at equal number of events produced.

For the $H_b \rightarrow J/\psi + X$ process, it is required that the J/ψ meson comes from a b -hadron and decays into a pair of μ within $|\eta| < 2.5$ and with $p_T > 3.8$ GeV. No other selections are imposed. For $H_b \rightarrow J/\psi + \mu$, two additional filters are applied at GEN-level: three muons with $p_T > 3.2$ GeV and $|\eta| < 2.5$ must be present in the event and the same-charge muon pair must have an invariant mass below 10 GeV. The same-charge requirement avoids the possibility that the muon pair from the J/ψ meson would always fulfil the condition. The two samples names and the number of events produced is shown in Table 5.3.

Process	Sample name	Number of events
$H_b \rightarrow J/\psi + \mu$	HbToJPsiMuMu_3MuFilter_TuneCP5_13TeV-pythia8-evtgen	92.2 M
$H_b \rightarrow J/\psi + X$	HbToJPsiMuMu_TuneCP5_13TeV-pythia8-evtgen	97.8 M
$H_b \rightarrow J/\psi + X$ extension	HbToJPsiMuMu_TuneCP5_13TeV-pythia8-evtgen	400 M

Table 5.3: Produced $H_b \rightarrow J/\psi + \mu/X$ samples. The extension for the $H_b \rightarrow J/\psi + X$ sample has been recently produced to perform a better validation on the *fakes* background estimation method, see Sec. 6.3.

5.3 Triggers for $R(J/\psi)$

As outlined in Sec. 3.2.3, an event has to pass two independent sets of trigger levels, L1 and HLT, in order to be saved. The following list details the overall selections required at L1 and HLT levels for the analysis trigger:

- The presence of 3 muons in the final state;
- The probability of the $\mu\mu$ vertex fit to be better than 0.5 %;
- The transverse momentum of the muons coming from the J/ψ , $p_T^{\mu_1/2}$, higher than > 3.5 GeV;
- The invariant mass of the two muons coming from the J/ψ in the range $2.95 < m(\mu_1\mu_2) < 3.25$ GeV;
- The transverse momentum of the third muon, $p_T^{\mu_3}$, higher than 2 GeV.

As will be described in detail in Sec. 6.4, for the measurement of one small data-driven background, i.e. the combinatorial J/ψ dimuon background, other datasets (`DoubleMu4_LowMass`) and HLT triggers requiring an additional track are used.

5.4 Selection

Data and MC samples are processed using the same framework, involving identical selections and reconstruction techniques. The initial stage of processing begins with the data-tier called MINIAOD [102] in CMS, where basic kinematic selections are applied, and all necessary vertex fittings are performed. This step results in simplified samples, known as custom NANOAOODs, which may still contain more than one 3μ candidate per event. These intermediate samples are then further processed and skimmed to generate “flat” ROOT trees, each containing only one candidate per event, which are then used for detailed analysis.

At first, J/ψ candidates are reconstructed, looking for opposite-sign muons μ_1 and μ_2 , and afterwards a third muon track from the PF collection, referred to as μ_3 in this document, is coupled with the J/ψ candidates. The final state muons have to satisfy the following requirements to pass the selection:

- they are physics objects reconstructed as described in Sec. 3.2.4;
- $p_{T,lead} > 6$ GeV, $p_{T,sublead} > 4$ GeV and $p_{T,trailing} > 4$ GeV, where lead (sublead) (trailing) refers to the muon with the highest (medium) (lowest) p_T in the triplet;

- $|\eta| \leq 2.4$ and transverse impact parameter $d_{xy} < 0.05$ cm for the three muons;
- both muons from the J/ψ passing the Medium ID criteria, defined in Sec. 3.2.4.2;
- $\Delta d_{z_{12}} = |d_{z_{\mu_1}} - d_{z_{\mu_2}}| < 0.2$, $\Delta z_{13} = |d_{z_{\mu_1}} - d_{z_{\mu_3}}| < 0.2$ and $\Delta z_{23} = |d_{z_{\mu_2}} - d_{z_{\mu_3}}| < 0.2$, with d_{z_μ} being the impact parameter of the muon in the z-direction;
- $\Delta R_{12} > 0.01$, $\Delta R_{13} > 0.01$ and $\Delta R_{23} > 0.01$, with ΔR_{ij} defined as $\Delta R_{ij} = \sqrt{(\Delta\eta)^2 + (\Delta\phi)^2}$. This cut is applied to avoid overlaps between the muons.

The J/ψ meson candidate, produced from μ_1 and μ_2 , is selected with the following requirements:

- $2 \text{ GeV} < m_{\mu\mu} < 4 \text{ GeV}$ where $m_{\mu\mu}$ is the dimuon invariant mass after the vertex fit;
- $p_T(\mu_1\mu_2) > 3 \text{ GeV}$;
- a η -dependent mass cut in order to take into account the different mass resolution when moving from the barrel to the endcap regions of the detector: $|m_{\mu\mu} - m_{J/\psi,PDG}| < 70 \text{ MeV}$ for one muon with $|\eta| < 1$ and one with $|\eta| > 1$, $|m_{\mu\mu} - m_{J/\psi,PDG}| < 50 \text{ MeV}$ for both muons with $|\eta| < 1$ and $|m_{\mu\mu} - m_{J/\psi,PDG}| < 100 \text{ MeV}$ for both muons with $|\eta| > 1$, see Fig. 5.5 and Fig. 5.6 for the $m_{\mu\mu}$ resolution in data;
- the probability of the dimuon vertex $\mu\mu$ being higher than 1%.

Once J/ψ candidates are selected, the B_c meson candidate is produced coupling the J/ψ with μ_3 , with the requirements:

- the B_c candidate with mass $3.5 < m(3\mu) < 10 \text{ GeV}$ and positive cosine of the pointing angle between the 3μ direction and the PV-SV one $\cos(\Delta\alpha_{PV}^{B_c})$;
- the probability of the three-muon vertex $\mu\mu\mu$ being higher than 0.01%.

Once these selections are applied, if more than one B_c candidate is selected for the same event, the one with higher p_T for the 3μ system is chosen. If candidates have the same 3μ p_T , e.g. permutations of the same three muons with different J/ψ hypotheses, the one with higher J/ψ vertex probability is chosen. The efficiency of this choice is 94.8% for the τ signal and 98.1% for the μ signal, with the efficiency defined as the percentage of correct assignments in events with multiple candidates. In total, the events with more than one reconstructed candidate are around 5

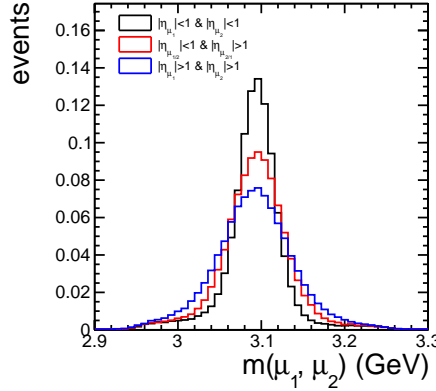


Figure 5.5: Normalised data distributions of the $m_{\mu\mu}$ variable with all selections described in Sec. 5.4 applied, in the three different η bins described in the text.

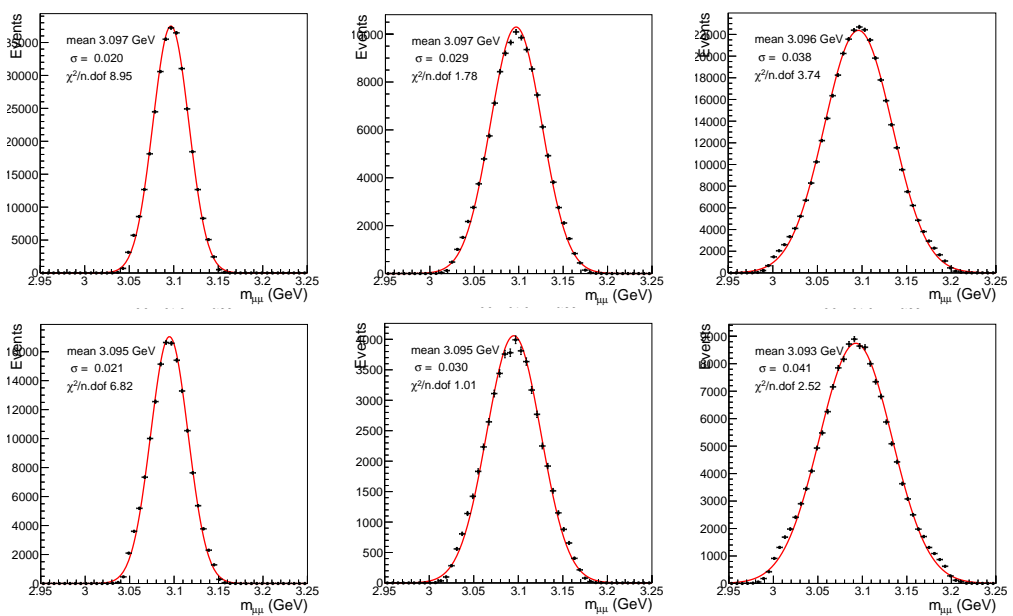


Figure 5.6: The fits to define the mass cuts in the three pseudorapidity bins are shown. The three pseudorapidity bins are: both muons with $|\eta| > 1$ (left column), one muon with $|\eta| > 1$ and one with $|\eta| < 1$ (centre column), and both muons with $|\eta| < 1$ (right column). For MC, the η cuts are defined respectively at 2.5 , 2.4 and 2.6σ of resolution (first row) and at 2.4 , 2.3 and 2.4σ for data (second row).

and 8% for μ and τ signals respectively. All these selections are referred to as "preselection".

The Signal Region (SR) is defined by also applying requirements on the iden-

tification and isolation of μ_3 , to reduce one of the background contribution, Sec. 6.3. The requirements are on the features of μ_3 , defined in Sec. 3.2.4:

- pass the softMVA ID;
- $\Delta\beta_{corr}iso < 0.2$.

All events able to pass the "preselection" requirements are stored in the analysis flat ROOT trees. All the relevant information concerning the analysis candidates is also stored. The corresponding PV for each candidate is redefined as the PV with the closest z distance with respect to the candidate J/ψ . The closest vertex to the B_c direction was also considered as an alternative definition of PV leading to similar results.

The same dataset format is used for the MC candidates, whose generator level information is also stored. This concludes the event preselection processing.

5.5 B_c reconstruction

As mentioned in Ch. 4, the visible final state for both τ and μ channels is composed of three muons, with both channels including neutrinos: 1 ν for the μ channel, and 3 ν for the τ channel. The presence of neutrinos prevents the direct reconstruction of the B_c four-momentum. The approach to reconstruct the four-momentum of the B_c meson in this study is distinct from the method used in the LHCb paper [103]. There are several differences in the LHCb and CMS detectors, which is reflected in the difference in the choices for the B_c reconstruction. LHCb collects forward boosted muons, with an acceptance of $2.5 < |\eta| < 5$. The direction of the B_c meson is taken to be the same as the vector connecting the B_c decay vertex SV and the PV. The component of B_c along the beam axis is approximated as $p_z^B = \frac{m_B}{m_{reco}} \cdot p_z^{reco}$, with $reco$ indicating the variables from the final state reconstructed particle [104]. CMS has a more central acceptance, with $|\eta| < 2.5$, therefore the boost of the collected particles is mostly on the transverse plane. The momentum direction is taken to be the one of the final state muon system, and the four-momentum is defined as $p^B = \frac{m_B}{m_{reco}} \cdot (p_{reco})$. This latter method is named *collinear approximation*, and its comparison with the other options is shown in Fig. 5.7. Among these, the collinear approximation appears to be the closest to the GEN information. The overestimation is a result of the collinearity assumption, which is true only at the limit of infinite boost.

The comparison of the collinear approximation and the LHCb methods of reconstruction has also been performed during a feasibility study for the $R(J/\psi)$ analysis in CMS, which can be found in Sec. 2.3 of Ref. [105]. For this study, only MC samples have been used, and the detection uncertainty of the PV and SV has

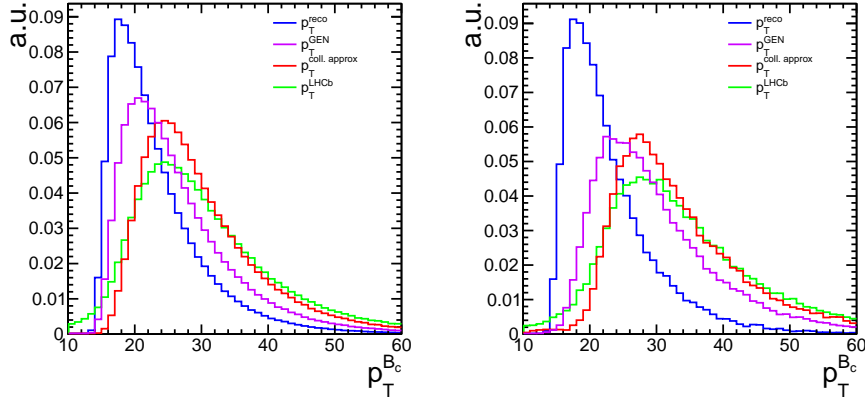


Figure 5.7: Comparison of various $p_T^{B_c}$ for μ (left) and τ (right) signals: p_T^{reco} (blue) indicates the B_c transverse momentum of the final state muons, p_T^{GEN} (violet) corresponds to the GEN information, $p_T^{coll.\,approx}$ (red) illustrates the collinear approximation and p_T^{LHCb} (green) shows the LHCb approximation.

been taken into account with a Gaussian smearing method. Several figures of merit have been compared, like B_c lifetime and the neutrino angle. For each of them, the results that align most closely with expectation are achieved with the collinear approximation, which is the method chosen to reconstruct the four-momentum of the B_c candidate.

5.6 Definition of observables

5.6.1 Kinematic observables

The reconstruction of the B_c four-momentum enables the definition of various discriminating variables that can differentiate between the τ and μ signals. These channels have a different number of neutrinos in the final state, which can be leveraged by defining appropriate features.

The four-momenta of the particles are indicated with p_B , p_{μ_1} , p_{μ_2} , p_{μ_3} , $p_{J/\psi}$ for B_c , μ_1 , μ_2 , μ_3 and J/ψ respectively. The p_B is the one obtained from the collinear approximation. Some interesting observables that can be defined exploiting these four-momenta are:

- E_μ^* , μ_3 energy in the B_c candidate rest frame;
- $m_{miss}^2 = (p_B - p_{\mu_1} - p_{\mu_2} - p_{\mu_3})^2$, missing mass squared;
- $q^2 = (p_B - p_{\mu_1} - p_{\mu_2})^2$, squared four-momentum transfer to the lepton system;

- $p_T^{miss} = (p_T^B - p_T^{\mu_1} - p_T^{\mu_2} - p_T^{\mu_3})$, the scalar missing transverse momentum;
- $E_\mu^\#$, the μ_3 energy in the rest frame of the other two muon system;
- $p_T^{var} = p_T^{J/\psi} - p_T^\mu$, where $p_T^{J/\psi}$ and p_T^μ are scalar transverse momenta of the system of the two muons coming from the J/ψ decay and of μ_3 ;
- $m(3\mu)$, being the invariant mass of the $3-\mu$ system.

Figure 5.8 shows the shapes for the τ and μ signals for these variables.

5.6.2 Topological observables

In this analysis, certain topological variables are employed due to their ability to distinguish between signal and background distributions effectively. The following variables have been used:

- L_{xy} , which represents the decay length of the B_c meson in the xy plane relative to the PV;
- IP3D, the three-dimensional impact parameter of μ_3 , shown in the scheme in Fig. 5.9, which measures the distance of μ_3 to the SV.

In the analysis, the significance of these observables is used, defined as $IP3D_{sig} = IP3D/\sigma_{IP3D}$ and $L_{xy,sig} = L_{xy}/\sigma_{L_{xy}}$, where σ_{IP3D} and $\sigma_{L_{xy}}$ indicate the respective uncertainties for the two observables. Figure 5.10 presents a comparison of the shapes for signals and backgrounds.

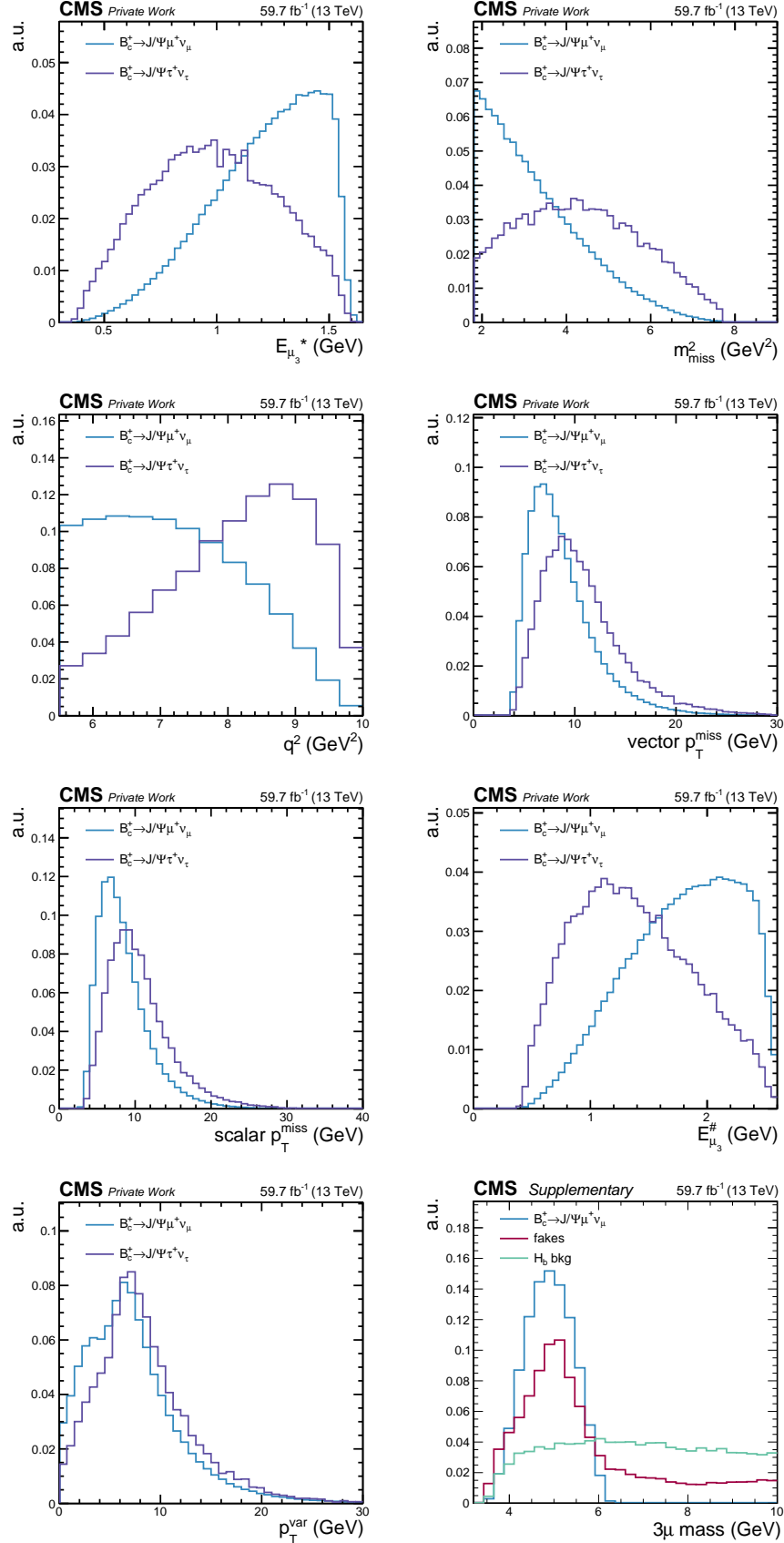


Figure 5.8: Normalised distributions for the τ and μ signals for some kinematic observables. The last plot (bottom right) shows the $m(3\mu)$ distribution for μ signal, fakes background (Sec. 6.3) and H_b background (Sec. 6.1). In these plots the preselection is applied.

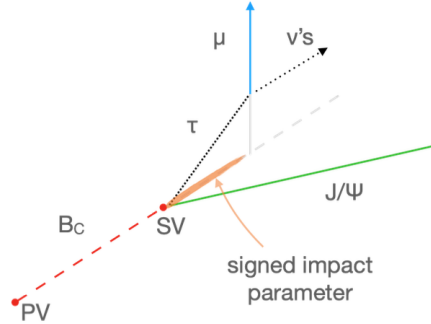
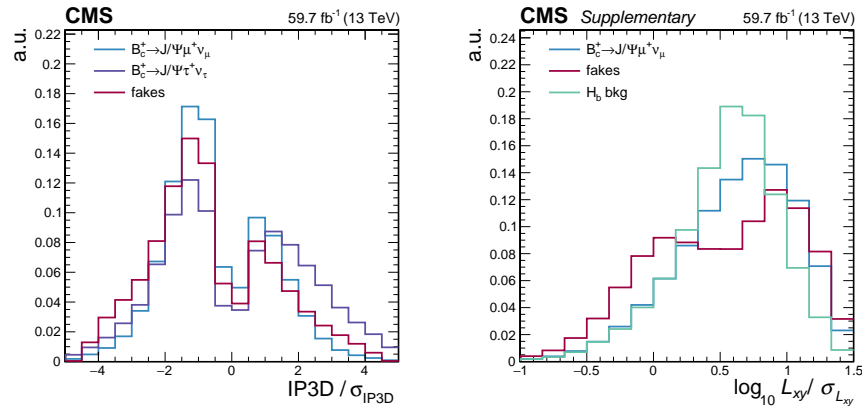


Figure 5.9: Scheme to visualise the IP3D definition.

Figure 5.10: Normalised distributions for the τ and μ signals, fakes background (Sec. 6.3) and H_b background (Sec. 6.1) for the some kinematic observables. In these plots the preselection is applied.

Chapter 6

Background Estimation

In the CMS experiment, the reconstruction efficiency of J/ψ mesons is very high in the selected kinematic range. This implies that the majority of the backgrounds in the analysis are likely to contain a genuine J/ψ meson, making the third muon a critical element of the analysis. Backgrounds that do not include a real J/ψ meson are primarily composed of combinatorial dimuons, which constitute a relatively small portion of the overall backgrounds.

The main background contributions in this analysis are:

- Processes involving a J/ψ meson coming from b -hadron decays, like $B_{u,s,d} \rightarrow J/\psi X$, which is paired with muons from the rest of the event, or when it is paired with muons from the same B . Both of these processes are part of the H_b background. This contribution is estimated from MC simulations with inputs from data and is described in Sec. 6.1.
- The B_c meson decays including a J/ψ and a muon in the final state other than the signals, evaluated from MC simulations, and called B_c background hereafter, in Sec. 6.2.
- Events in which the accompanying kaon or pion of the J/ψ are misidentified as muons. This background is called *fakes* background in this document and it is evaluated directly from data using an orthogonal phase space. It is described in Sec. 6.3.
- The dimuon background, where randomly matched muons, not originating from J/ψ candidates, are paired and reconstructed with an invariant mass $m(\mu\mu)$ close to that of the resonance. This process, described in Sec. 6.4, is estimated from data and will be referred to as *dimuon* background in this document.

In Table 6.1 the percentages of these contributions to the total events at preselection level are shown.

Region	$J/\psi\mu$	$J/\psi\tau$	B_c bkg	H_b bkg	fakes	comb	J/ψ
Inclusive	54%	3%	2%	10%	30%		1%

Table 6.1: In this table, the percentages for the two signals and the different background contributions are shown at the preselection level. The values are all approximated to the second decimal number.

6.1 H_b background

This background relies on MC $H_b \rightarrow J/\psi + \mu$ shape templates, described in Sec. 5.2.2, and a data sideband for normalisation. The H_b background includes both events in which the J/ψ meson and the muon come from different or same b -hadrons, as already shown in Fig. 5.2.

In Fig. 6.1, the distribution of the invariant mass of the three final muons $m(3\mu)$ is shown. In the region with $m(3\mu) > m_{B_c}$, called high-mass (HM) region, there

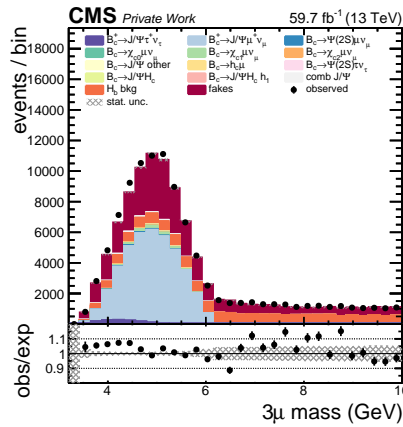


Figure 6.1: Distribution of the $m(3\mu)$ variable with all the preselection cuts applied, Sec 5.4. The HM region is defined as $m(3\mu) > m_{B_c} \sim 6.3$ GeV.

is no contribution from either signals or B_c background. The only H_b background in this region comes from the DBH contribution, as the phase space of SBH is not expected to extend into the HM regime. Since the MC samples are produced with correct relative branching ratios, normalising the entire background using this category is feasible.

The MC sample used for this background is inclusive, containing all decays of the various b -mesons and -baryons. In the analysis, additional degrees of freedom are introduced. These allow for independent variation of the normalisation component for each b -hadron, beyond the overall normalisation derived from the control

region at HM. All the contributions of the H_b background are shown in the q^2 distribution in Fig. 6.2.

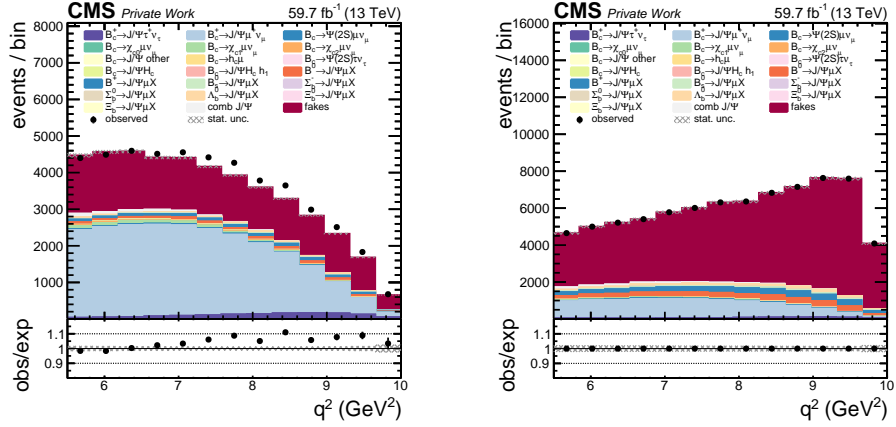


Figure 6.2: Distribution of the q^2 variable in the pass softMVA ID (left) and fail softMVA ID (right) regions of μ_3 . The H_b background is here split into 8 contributions, depending on the H_b mother of the J/ψ meson.

6.2 B_c background

The B_c background is based on the MC B_c signal and background shape templates, whose production is already described in Sec. 5.2.1. This sample includes all the relevant feed-down decays, which are the excited $c\bar{c}$ states that decay into a J/ψ meson, and other J/ψ + charmed hadron decays, like $B_c \rightarrow D_s^* J/\psi$.

The EvtGen tool used to produce this sample is not up-to-date with the latest B_c form factors and with its decay time. Therefore, corrections and systematic uncertainties are applied to this sample. Their description can be found in Sec. 7.1 and Sec. 7.3.2, respectively.

The normalisation of this sample is left floating in the fit, and a specific category is defined to control it. As for the H_b background, a systematic uncertainty is added for each B_c sub-sample shown in Fig. 6.2, to account for possible inaccuracies in the BR predictions.

Hereafter, in the plots presented in this thesis, the contributions from the B_c and H_b processes will be shown in a more compact way. An example of this merged representation can be seen in Fig. 6.3. This format has been chosen to provide a clearer view of the distributions.

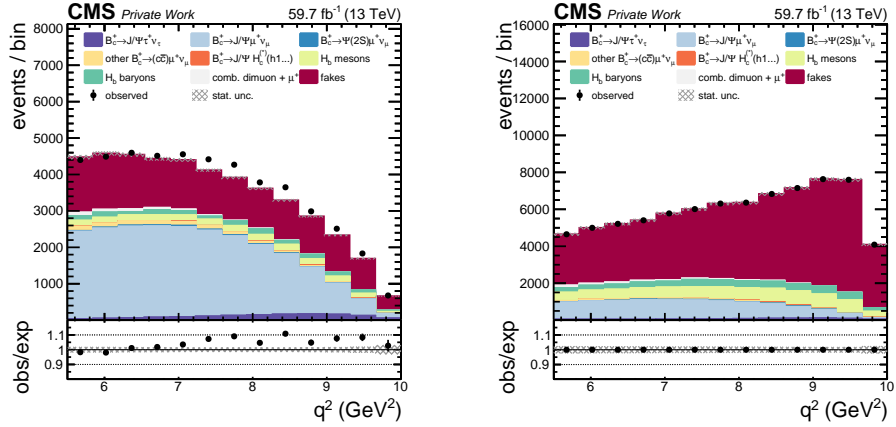


Figure 6.3: Distribution of the q^2 variable with merged contributions from B_c and H_b backgrounds.

6.3 Fakes background

This data-driven background consists of inclusive decays of b -hadrons to J/ψ mesons in which the accompanying pion or kaon is misidentified as a muon. Many studies have been performed and several strategies have been considered to estimate this background. The chosen strategy is described in detail in the following.

Initially, a detailed analysis of how the control regions are defined is presented in Sec. 6.3.1. The estimation of fakes background in the SR then proceeds in two stages. In the first stage the isolation fake-rate in selected regions is measured, as documented in Sec. 6.3.2. This section not only provides an analytical and practical explanation of the measurement process but also includes a comprehensive description of the final neural network (NN) developed for this task. Subsequently, the second stage involves the extrapolation from these measurements of the fakes distribution in the SR, described in Sec. 6.3.3. The robustness and reliability of this method are validated and some uncertainties discussed in Sec. 6.3.4 and 6.3.5.

6.3.1 Control regions definition

The isolation and identification criteria for μ_3 are central in minimising the fakes background events in the SR. These criteria also play a crucial role in defining control regions that are enriched with fakes backgrounds, which are used for measuring and extrapolating the shape of the fakes background in the SR.

6.3.1.1 Identification Studies

The fakes background contribution can be decreased with an optimised ID selection of the third muon in the final state, after applying the preselection described in Sec. 5.4. Different ID selections have been compared to find the best discriminant between the τ signal and fakes background. Given the low relative abundance of τ signal events with respect to fakes background events, this study is performed targeting specifically the τ signal, rather than the μ signal. The simulated sample B_c is used for the τ signal, and the $H_b \rightarrow J/\psi + X$ for the fakes, requiring that $X \neq \mu$, based on generator-level information, to ensure that the particle is not a real muon. To determine the optimal ID selection, the figure of

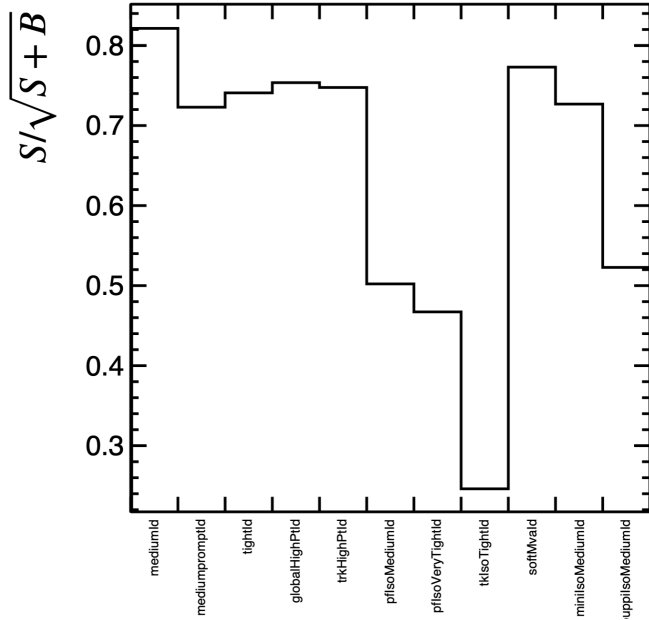


Figure 6.4: $S/\sqrt{(S+B)}$ for several ID WP applied to μ_3 , with S indicating τ signal events, and B the fakes background.

merit $S/\sqrt{(S+B)}$ is computed for each ID WP available in the muon collection [106], where S represents the number of τ signal events and B the number of fake background events. This figure of merit is a simplistic but necessary approach, because of the extensive effort that running precise final fits for each ID WP would require. In Fig. 6.4 the figure of merit $S/\sqrt{(S+B)}$ is shown for some of these ID WP after selecting μ_3 with different ID requirements.

The Medium ID working point is the first one chosen for this selection, because it shows a good $S/\sqrt{(S+B)}$ score. In Fig. 6.5, the distributions of the normalised shapes for the τ signal and fakes MC events are shown for three of the most

impacting variables in Table 3.1, after applying the Medium ID requirement on μ_3 . These plots suggest that, in addition to the Medium ID requirement, a tighter cut should be applied to further reduce the fakes background contribution in the chosen phase space of the analysis, with a small loss of τ signal events.

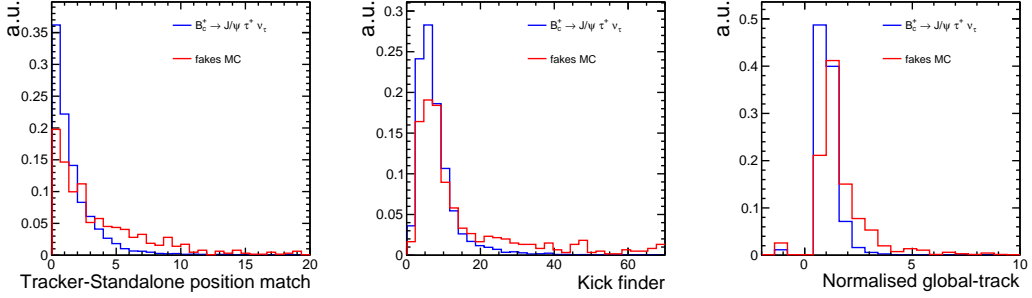


Figure 6.5: Comparison of normalised shapes for τ signal (blue) and fakes MC (red) events for three of the variables of the Medium ID WP definition, after applying the preselection and Medium ID cut on μ_3 . The variables are positional alignment between the tracker muon and the standalone muon (left); χ^2 as determined by the kick-finding algorithm (centre); normalised global-track χ^2 (right).

Since the softMVA ID WP also shows a good figure of merit in Fig. 6.4 and has already been well optimised for similar analyses sensitive to the contamination from fake muons and decays in flight, such as the $B_s \rightarrow \mu\mu$ search, this WP has been preferred. Figure 6.6 shows the distributions of the variables from Fig. 6.5, now with the softMVA ID cut applied. This WP effectively reduces the contribution of fakes, leaving no further room for improvement.

After the application of the softMVA ID WP, the fakes contribution in the SR is diminished by 65% with respect to the Medium ID WP, with just a 15% efficiency reduction for τ signal events.

6.3.1.2 Isolation Studies

ISO constraints on μ_3 can be effectively employed to diminish the contribution from the fakes background. These constraints ensure that the selected muons are isolated, as required for the signals, and also help in reducing the impact of pileup muons.

Similar to the ID requirements, different ISO WP for μ_3 have been compared. Also in this study, the B_c sample is used for the τ signal, and the $H_b \rightarrow J/\psi + X$ MC sample is used for the fakes background. With these samples, a Receiver operating characteristic (ROC) curve, the plot of signal efficiency vs background rejection, is computed for each ISO WP. In Fig. 6.7 all the ROC curves are shown, and it is

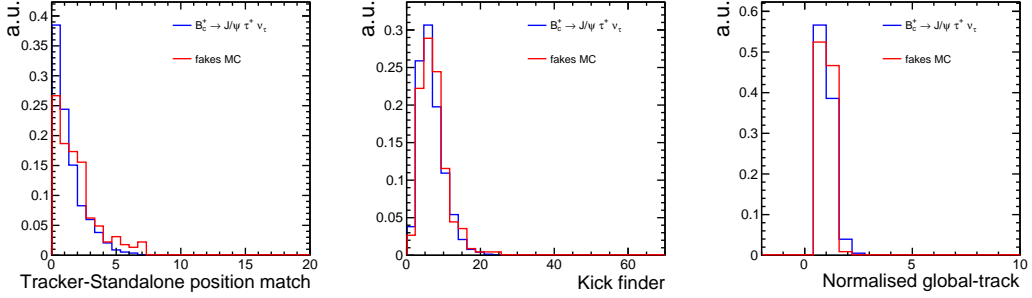


Figure 6.6: Comparison of normalised shapes for τ signal (blue) and fakes MC (red) events for three of the variables of the softMVA ID WP definition, after applying the preselection and softMVA ID cut on μ_3 . The variables are positional alignment between the tracker muon and the standalone muon (left); χ^2 as determined by the kink-finding algorithm (centre); normalised global-track χ^2 (right).

possible to observe that the $\Delta\beta_{corr,iso}$ is one of the best ISO WPs. The chosen cut for this variable is 0.2, indicated in the figure by an arrow, that gives 66% signal efficiency and 73% background rejection.

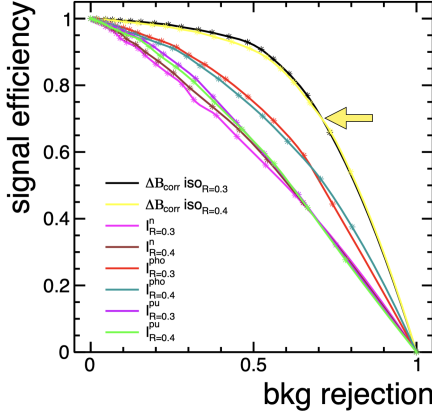


Figure 6.7: ROC curves for the comparison of several ISO WPs applied to μ_3 , aiming for an enhancement of the τ signal from the fakes background contribution. The arrow indicates the position on the ROC curve of the $\Delta\beta_{corr,iso} = 0.2$ selection.

In Fig. 6.8, the $\Delta\beta_{corr,iso}$ distributions for the MC samples used in this analysis are shown.

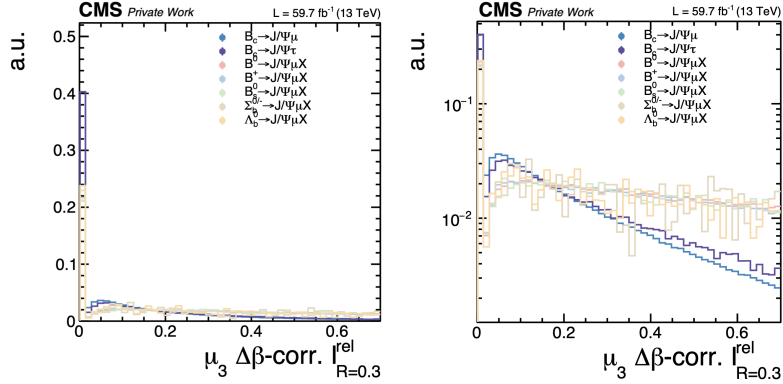


Figure 6.8: $\Delta\beta_{corr,iso}$ distribution for the two signals and the H_b background MC samples, in linear (left) and log scales (right).

6.3.1.3 ABCD Regions

As a result of the studies previously described, four regions are defined using the softMVA ID and $\Delta\beta_{corr,iso}$ on μ_3 , schematically shown in Fig. 6.9.

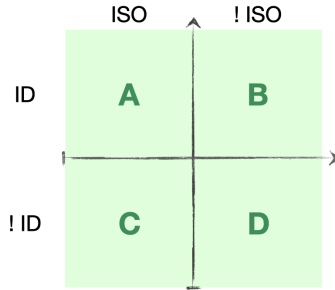


Figure 6.9: Scheme of the ABCD regions used to define the fakes contribution in the SR. “ID” indicates that the identification working point pass softMVA ID is applied to μ_3 , while “!ID” indicates the identification working point fail softMVA ID for μ_3 . “ISO” indicates the requirement $\Delta\beta_{corr,iso} < 0.2$ for μ_3 and “!ISO” the $\Delta\beta_{corr,iso} > 0.2$ for μ_3 . Region A is the analysis SR.

The SR, denoted as region A, is characterised by pass softMVA ID and $\Delta\beta_{corr,iso} < 0.2$. To estimate the fakes contribution in this region, regions B, C, and D are employed following a two-step strategy:

1. The fail softMVA ID regions, hereafter called “fail ID regions” or “!ID regions” are utilised to measure the different behaviours of various contributions between the $\Delta\beta_{corr,iso} < 0.2$ and $\Delta\beta_{corr,iso} > 0.2$ sub-regions, referred to as region C and D in the scheme.

2. The observed behaviours are extrapolated to the pass softMVA ID regions, hereafter called “pass ID regions”, to determine the fakes shape in the SR, region A.

6.3.2 Measurement of ISO fake-rate fr_{ISO}

The method employed to derive the distribution of fakes background in the SR is based on the initial measurement of the ISO fake-rate in the fail ID regions. This measured fake-rate is subsequently applied to region B to predict the fakes contribution in region A. This section details the measurement process, including two main aspects: an analytical derivation followed by a practical implementation in the analysis. The latter begins with a description of a simplified approach and afterwards it transitions to the more sophisticated deep learning method that was ultimately adopted.

6.3.2.1 Analytical Derivation

The first step is to use the fail ID regions, C and D, to learn the behaviour of data and MC when moving from one region to the other. The strategy is based on an analytical derivation, where data are assumed to be composed just of fakes background, signal and background MC events, with the shapes of the latter two indicated as MC in the following formulas. Eqs. (6.1) through (6.4) aim to provide an intuitive explanation of the logical process, whereas Eq. (6.6) explicitly presents the event-by-event dependency of the weights. In region C the following relation holds:

$$data(C) = MC(C) + fakes(C), \quad (6.1)$$

where $data$, MC , $fakes$ indicate their respective distributions. Multiplying and dividing by the respective shapes in D:

$$\frac{data(C)}{data(D)} \cdot data(D) = \frac{MC(C)}{MC(D)} \cdot MC(D) + \frac{fakes(C)}{fakes(D)} \cdot fakes(D). \quad (6.2)$$

The ratios can be redefined as transfer functions (TF), which depend on probability p as $TF = p/(1 - p)$:

$$\frac{data(C)}{data(D)} = TF_{data}; \frac{MC(C)}{MC(D)} = TF_{MC}; \frac{fakes(C)}{fakes(D)} = fr_{ISO}; \frac{MC(D)}{data(D)} = \alpha \quad (6.3)$$

and Eq. (6.2) can then be rewritten using Eq. (6.3):

$$TF_{data} \cdot data(D) = TF_{MC} \cdot MC(D) + fr_{ISO} \cdot fakes(D) \quad (6.4)$$

Since Eq. (6.1) holds also in region D, $fakes(D) = data(D) - MC(D)$, if one divides all the terms of Eq. (6.4) by $data(D)$, the following equation can be obtained:

$$TF_{data} = TF_{MC} \cdot \alpha + fr_{ISO} \cdot (1 - \alpha) \quad (6.5)$$

Solving for fr_{ISO} , and explicitly writing the event by event dependence of the variables, one obtains:

$$fr_{ISO}(x_i) = \frac{TF_{data}(x_i) - TF_{MC}(x_i) \cdot \alpha(x_i)}{1 - \alpha(x_i)}. \quad (6.6)$$

$fr_{ISO}(x_i)$ is defined as in Eq. (6.3), therefore to solve the equation for the shape of the fakes background in the region C, the final equation is:

$$fakes(C) = \left(\frac{TF_{data}(x_i) - TF_{MC}(x_i) \cdot \alpha(x_i)}{1 - \alpha(x_i)} \right) \cdot data(D) - \left(\frac{TF_{data}(x_i) - TF_{MC}(x_i) \cdot \alpha(x_i)}{1 - \alpha(x_i)} \right) \cdot MC(D), \quad (6.7)$$

where $TF_{data}(x_i)$, $TF_{MC}(x_i)$ and $\alpha(x_i)$ are event-per-event weights, to be applied to the events of data and MC in region D, to find the fakes shape in region C.

6.3.2.2 Final measurement: $fr_{ISO}(x_i)$ parametrisation through neural networks

To calculate these sets of weights, classification neural networks (NN) to fit TF_{data} , TF_{MC} and α in many dimensions are used. The application of NN to this problem is justified by the universal approximation theorem, which asserts that every continuous function, $f(x)$, can be approximated by a NN. This enables the extrapolation of function values at a given point x from the NN output. The NN methodology yields a continuous function, also offering the flexibility to parametrise for more than one variable. Consequently, this NN method is employed in this analysis.

Three classification NNs were trained to distinguish between two classes providing the probability for each event to belong to either class. The weights for the fakes background estimation are then determined from the probability output of the NNs using the relation $w = \frac{p}{1-p}$. The NN classes associated with each set of weights are as follows:

- data(C) vs data(D), for the $TF_{data}(x_i)$ weights;
- MC(C) vs MC(D), for the $TF_{MC}(x_i)$ weights;
- MC(D) vs data(D), for the $\alpha(x_i)$ weights.

NNs definition As shown in Eq. (6.6), three classification NNs are needed to compute the final set of weights $fr_{ISO}(x_i)$. Each network is built with the **Keras** package [107] in **PYTHON**, made of a Dense layer with 32 nodes and a final activation layer, a sigmoid function, crucial to be able to interpret the output score as a probability. The chosen optimiser is **ADAM** and the loss function is chosen to be *binary cross-entropy*.

The optimisation of these NNs focuses mostly on the choice of features since the variables chosen for the training have a big impact on the performance and generalisation of the networks. Therefore, a preliminary study is done before the NNs training. ROC curves are computed for each potentially interesting feature, for the three classification problems. The choice of variables is done in three different steps. Firstly, considering that the variables with higher area under the ROC curve (AUC) score are the ones that can better distinguish between two classification terms, these are saved for each NN. Secondly, to simplify the problem, these variable lists are filtered by eliminating variables that are too strongly correlated with each other. Considering that each network has a different problem to solve, different features will pass the firsts two steps for each network. Therefore, the last step consists into harmonising the three lists converging on a common list of features for the three NNs. The final features chosen for the training of the networks are:

- q^2 ;
- m_{miss}^2 ;
- $L_{xy}/\sigma_{L_{xy}}$;
- $IP3D_{sig}$;
- p_T^B ;
- $|\eta^B|$;
- $vtx(\mu_1, \mu_2, \mu_3)$ probability;
- $vtx(\mu_1, \mu_2, \mu_3) \cos(\alpha)$;
- $d_{x,y}^{\mu_3}/\sigma d_{x,y}^{\mu_3}$;
- $d_z^{\mu_3}/\sigma d_z^{\mu_3}$.

In Fig. 6.10 ROC curves for each feature that passed the three-step selection are shown for each NN.

The effectiveness of the three-step strategy is shown in Fig. 6.11, where selected features exhibit negligible linear correlation.

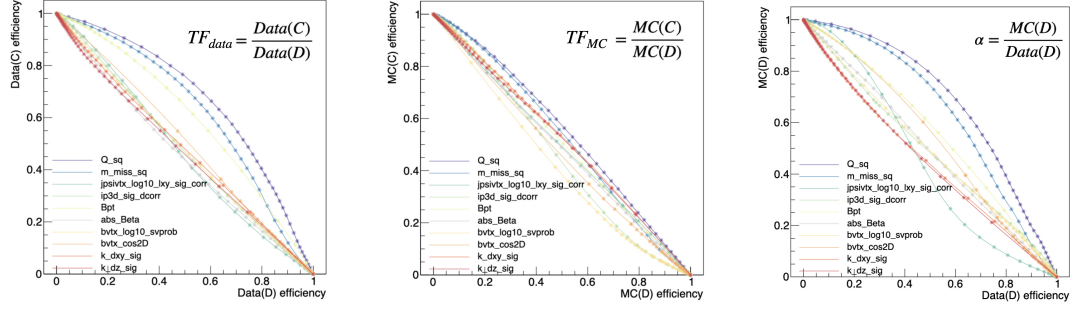


Figure 6.10: Pre-training ROC curves for each single feature chosen for the training of the NN: TF_{data} (left), TF_{MC} (centre) and α (right).

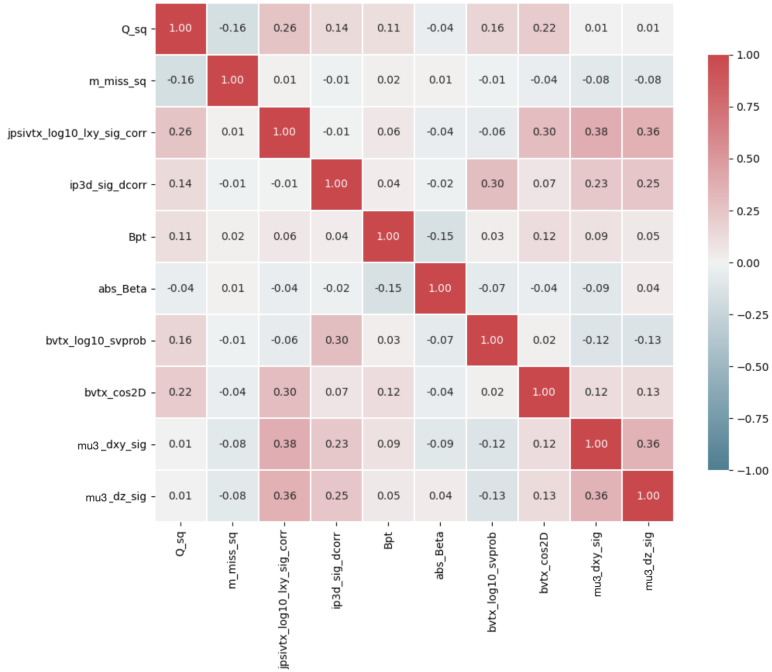


Figure 6.11: Linear correlation for the features chosen for the training, computed using data events to prove the effectiveness of the pre-training strategy.

Once the networks are trained with the features and architecture explained, diagnostic plots are produced to check for possible over-fitting. The strategy to find the fakes shape in the SR deeply relies on generalisation, which could fail if the NNs do not have the desired behaviour. The NN parameterization has to discern the observables and correlations on which the fake-rates depend. This guarantees the applicability of fake-rates to regions with different phase spaces.¹

¹For instance, consider a simple example where the fake-rate linearly depends on p_T . If the

In summary, the success of the strategy to determine the fake shape in the SR heavily relies on the NNs' ability to generalize appropriately. Failure to achieve the desired behavior in the NNs could compromise the effectiveness of this approach. The overfitting can be tested comparing the distributions of the NN predictions of the train and test datasets. If no overfitting is present, the NN is expected to produce a similar prediction distribution for both samples, which is shown in Fig. 6.12 (top row). Train and test shapes are compatible in both pass and fail regions for the three NNs, with a Kolmogorov-test result better than 20% for each shape. In the second row of Fig. 6.12, the training ROC curves for test and training samples are also shown.

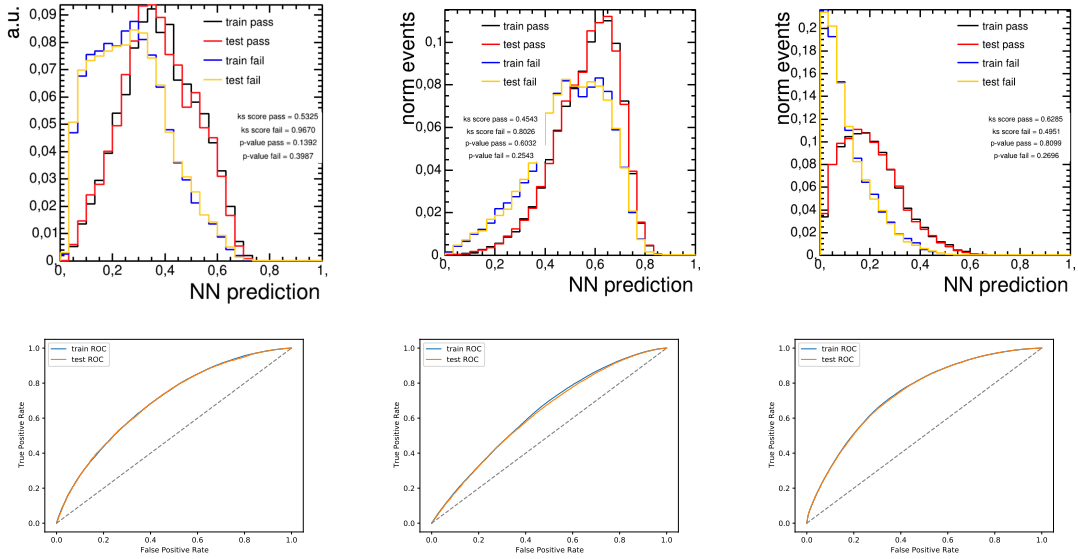


Figure 6.12: Comparison plots between NN output distributions for train and test datasets (top row) and the training ROC curves for test and training samples (bottom row) for both pass and fail regions: NNs results for TF_{data} (left), TF_{MC} (centre) and α (right).

The NN trainings are therefore validated, and for each sample, three weights can be associated to each event allowing the calculation of fr_{ISO} weights for events in region D . The fakes shape in region C can be found starting from data and MC distributions in region D , reweighted with $fr_{ISO}(x_i)$ weights, and subtracted following Eq. (6.7). This is also schematically shown in Fig. 6.13.

fake-rate is measured as a single flat number in a phase space A with an average p_{T_A} , it can not be directly applied to another phase space B with $p_{T_B} = 2 \cdot p_{T_A}$ without introducing errors. However, by measuring the fake-rate as a function of p_T in A, it can be applied to B.

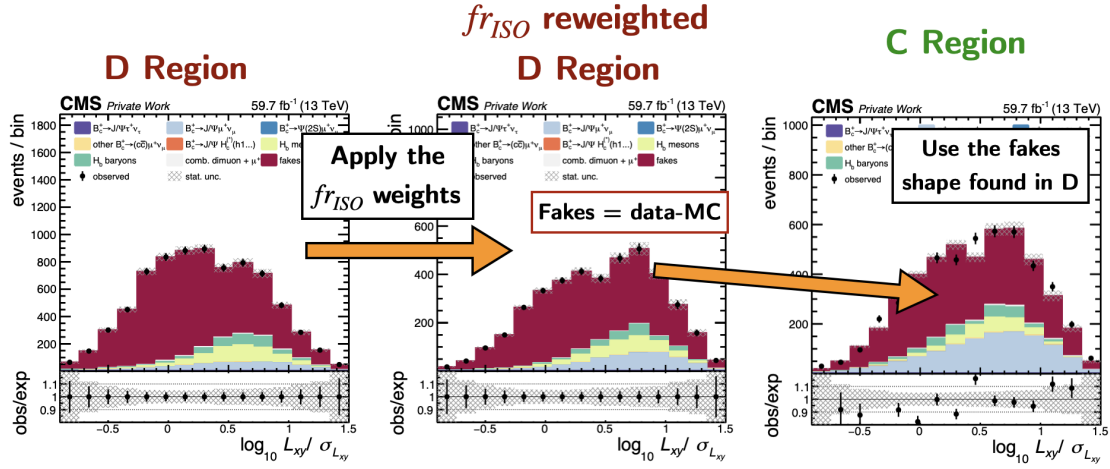


Figure 6.13: Scheme to visually explain the Eq. (6.7). Starting from data and MC (everything but the red contribution in the plots) in region D (left), $fr_{ISO}(x_i)$ weights are applied, resulting in a reweighted region D (centre). The final shape of the fakes to be used in region C (right) is directly the difference between data and MC in the reweighted region D.

Consistency check Since a NN has the ability to approximate any function $f(x)$, this simple check aims to demonstrate that it can approximate the set of weights found considering only their dependency on q^2 .

The weights, which for this check are found using only the q^2 information, are computed using the bin-per-bin ratio of histograms, and they are shown as data points in Fig. 6.14.

Three NNs are trained using only q^2 , and the weights found from their outputs, red points in Fig. 6.14, are compared to the ratios of histograms. The NN model used here is the same as the one described in Section 6.3.2.2, with the only difference being the number of features.

As expected, the distributions are compatible.

6.3.3 Prediction for the SR

After measuring the isolation fake-rate in the fail ID regions, C and D, the NN trained on these regions can be used to predict the weights $fr_{ISO}(x_i)$ for the pass ID regions. This extrapolation allows the derivation of the template of fakes background in the SR. To extrapolate the fakes shape and normalisation in region

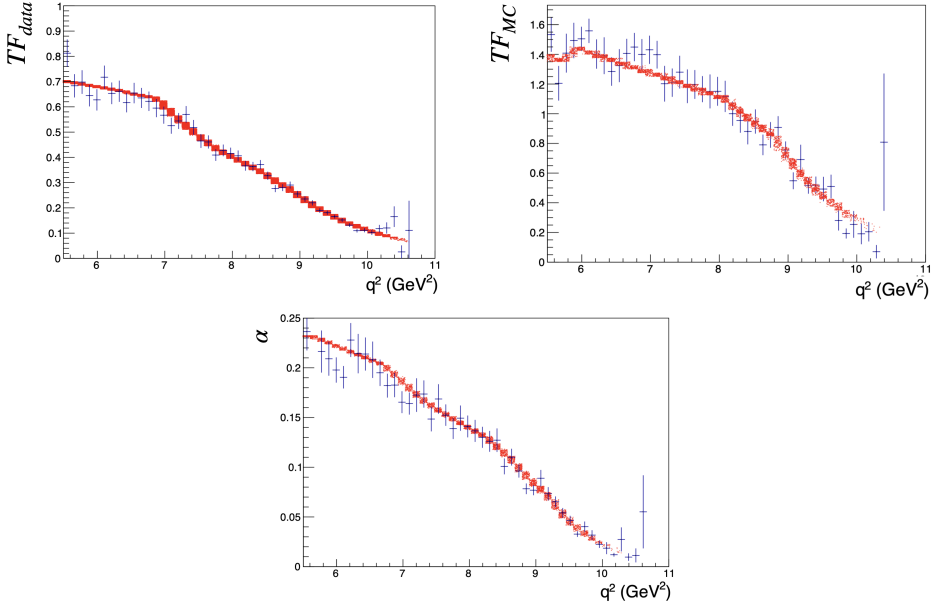


Figure 6.14: Distributions of TF_{data} , TF_{MC} and α computed as ratios of histograms in q^2 (blue), according to their definition in Eq. 6.3, and via the classification NN outputs (red). The distributions are compatible.

A, Eq. (6.7) is used again, after replacing D with B and C with A:

$$fakes(A) = \left(\frac{TF_{data}(x_i) - TF_{MC}(x_i) \cdot \alpha(x_i)}{1 - \alpha(x_i)} \right) \cdot data(B) - \left(\frac{TF_{data}(x_i) - TF_{MC}(x_i) \cdot \alpha(x_i)}{1 - \alpha(x_i)} \right) \cdot MC(B), \quad (6.8)$$

where the operator \cdot indicates the application of the event-by-event weights. The $fr_{ISO}(x_i)$ weights associated to each event in B are found using the already trained (in regions C and D) NNs described in Sec. 6.3.2.2. In Fig. 6.15 a visual representation of the formula can be found.

6.3.4 Validation

The determination of the fakes shape with this method requires validation. Each step of the method is thoroughly validated, both using data and MC samples.

6.3.4.1 Validation of the fakes method on MC

Three validation tests on MC are presented in the following:

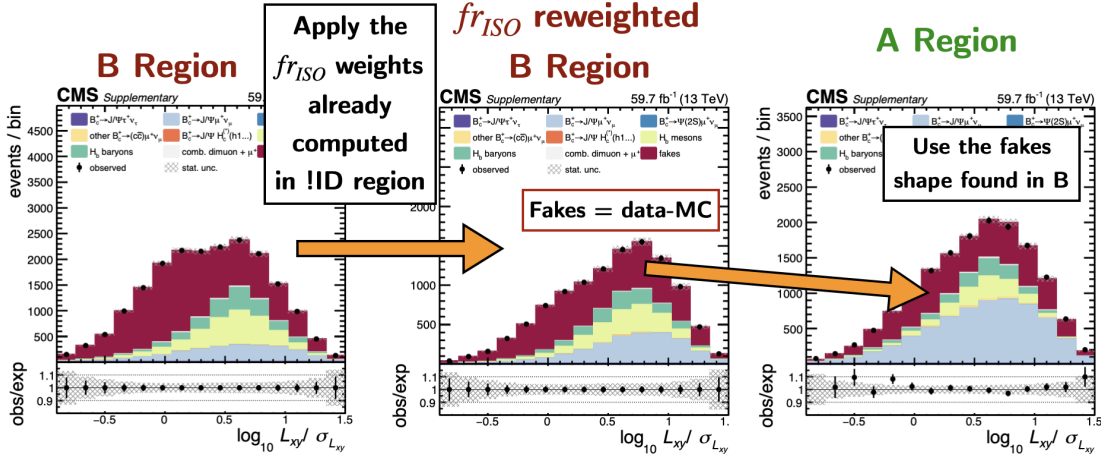


Figure 6.15: Extrapolation of the fakes background method to the A and B regions.

- Closure test in C, which is only a sanity check and is expected to work by construction;
- Extrapolation test, where the generalisation is tested on the pass ID regions;
- Toy model, where the whole method is tested on MC.

Closure in C The first test to be performed on MC is to plot the final distributions for different variables in region C, to check the agreement between data and fakes. This is essentially a sanity check and is expected to be conclusive by design, as its purpose is to predict the fake contributions in the region used for training. Figure 6.16 illustrates some of these plots, which show a good agreement, validating the method in region C.

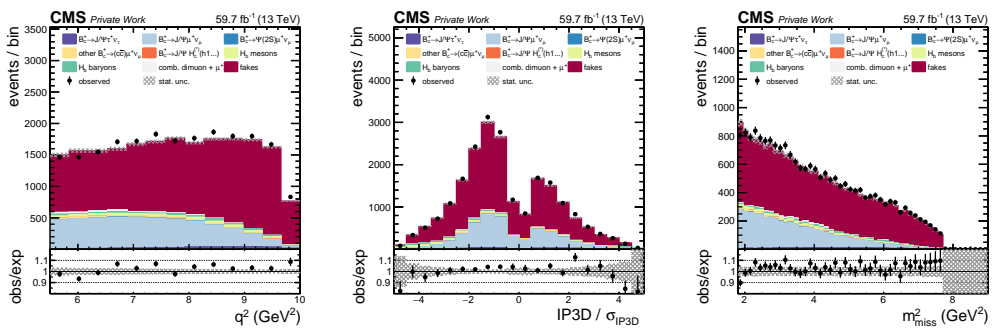


Figure 6.16: Closure test plots in region C for fakes estimation method for some interesting variables.

Extrapolation test The second part of the validation consists in testing the extrapolation of the method to the pass ID regions, B and A, Fig. 6.15. For this, the MC sample $H_b \rightarrow J/\psi + X$ is used requiring $X \neq \mu$. To test the extrapolation in the SR, two validation tests on MC are performed. The first one compares the shape of the fakes MC in region A with the shape predicted applying the $fr_{ISO}(x_i)$ weights found as output of the NNs to the region B. This comparison is done for the four variables that will be used in the fit model. The shapes comparisons are shown in Fig. 6.17, and the Kolmogorov-Smirnov test (KS) for each one of the comparisons shows a good agreement, therefore it is possible to conclude that the shapes are compatible. A non-closure concerning the normalisation, up to 13%, is taken into account in the systematic uncertainties for the fakes in the fit, as it will be explained in Sec. 8.3.

Toy model Another extrapolation test is performed building a toy model using the fakes MC as background and the MC for the μ signal as the only signal. For the latter just a limited number of events is considered, to make it comparable with the limited statistics of the fakes MC sample. The toy data is assumed to be composed only of signal and background events. This approach allows for a comprehensive test of the entire procedure for fakes estimation, based on MC, testing both the generalisation capability and the accuracy of subtraction when there are multiple contributions. The whole method is tested by obtaining the $fr_{ISO}(x_i)$ weights using the toy model, starting from the training of the three NNs (adapted to this simplified case) in regions C and D, and checking the closure test in region C. This closure test is performed also in region A, and results are shown in Fig 6.18 and Fig. 6.19. A good agreement, limited by the finite stats, is obtained, successfully validating the fakes strategy. The KS tests for these comparisons result in 88% for q^2 , 98% for $m(3\mu)$, 99% for $L_{xy}/\sigma_{L_{xy}}$ and 99% for $IP3D_{sig}$. The differences in normalisations are up to 15%, and accounted for in the fit.

6.3.4.2 Validation on data

In this section, a validation of the fakes estimation method on data is presented. Four regions are defined, designed to be sufficiently distant from the SR to ensure minimal real- μ contamination, thus removing almost any reliance on MC inputs for the sake of this test. These regions, denoted as B', B'', D', and D'', are illustrated in Fig. 6.20, with B' and B'' defined with $\Delta\beta_{corr,iso} > 1.5$ to minimise MC contamination.

The method is then tested in these control regions: the NN is trained in the new fail ID regions D' and D'', and applied in the new pass ID region B'' to find the final shape in B'. The ultimate goal is to achieve good agreement between data and predicted fakes background in region B'. The closure test in the D' region

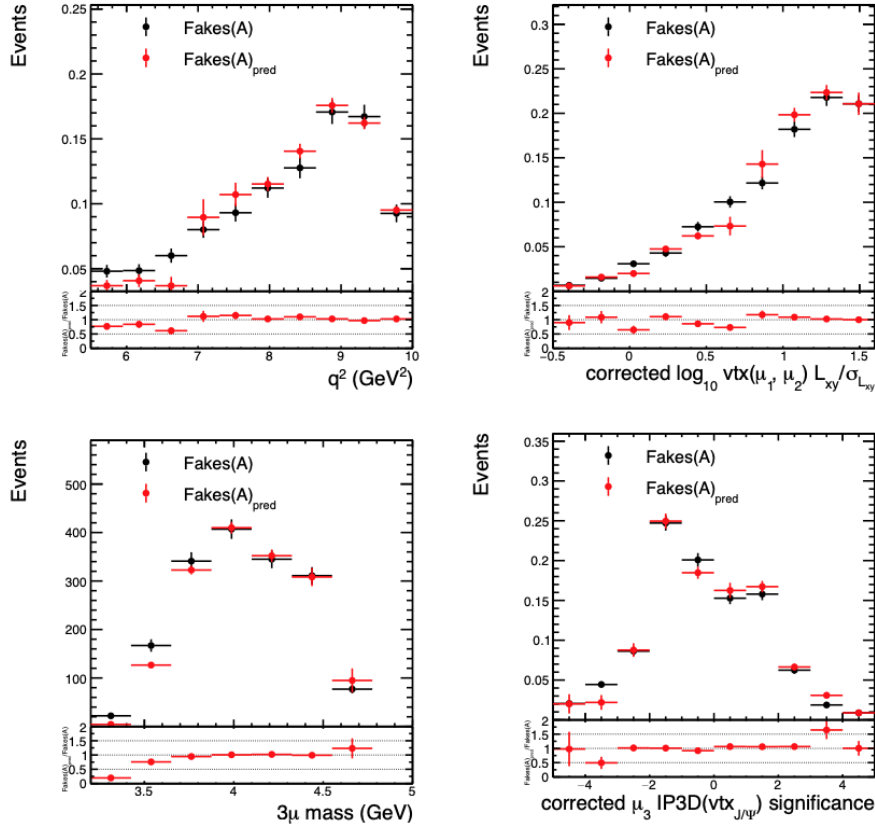


Figure 6.17: Fakes MC distribution in region A (black) compared with the distribution derived from region B (red), which has been reweighted using $fr_{ISO}(x_i)$ weights calculated in the fail softMVA ID regions. Four distributions of interest for this analysis are shown: q^2 (top left) with KS test of 88 %, $m(3\mu)$ (top right), with KS of 66%, $L_{xy}/\sigma_{L_{xy}}$ (bottom left) with KS of 24 % and $IP3D_{sig}$ (bottom right) with KS of 34 %.

is shown for q^2 , $IP3D_{sig}$ and $L_{xy,sig}$ in Fig. 6.21 to verify the correct training of the networks. The final validation in B' is displayed for the same distributions in Fig. 6.22, which shows a good agreement between data and the predicted fakes background.

This test, combined with the tests described in the previous section performed on MC, confirms the robustness of the method implemented to derive the fakes shape in the SR.

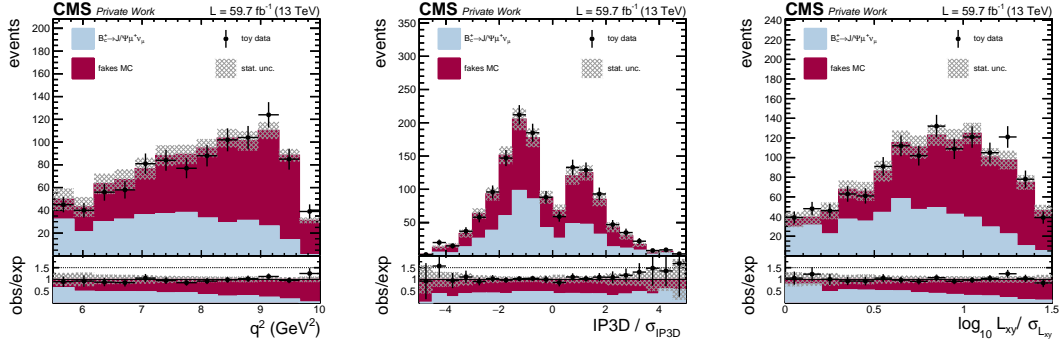


Figure 6.18: Validation of the fakes strategy using the toy model described in the text, in region C, fail softMVA ID and $\Delta\beta_{corr}iso < 0.2$.

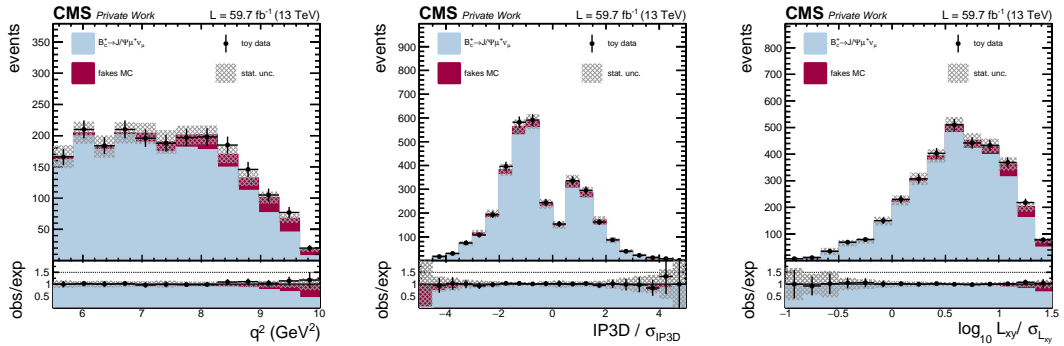


Figure 6.19: Validation of the fakes strategy using the toy model described in the text, in region A, pass softMva ID and $\Delta\beta_{corr}iso < 0.2$.

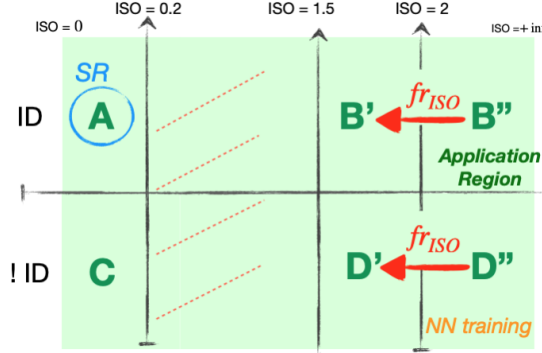


Figure 6.20: New regions far from the SR defined for the validation on data.

6.3.5 Uncertainties on the fakes background estimation

Several systematic uncertainties come from the method employed to derive the fakes background in the SR. Given that this represents the primary background,

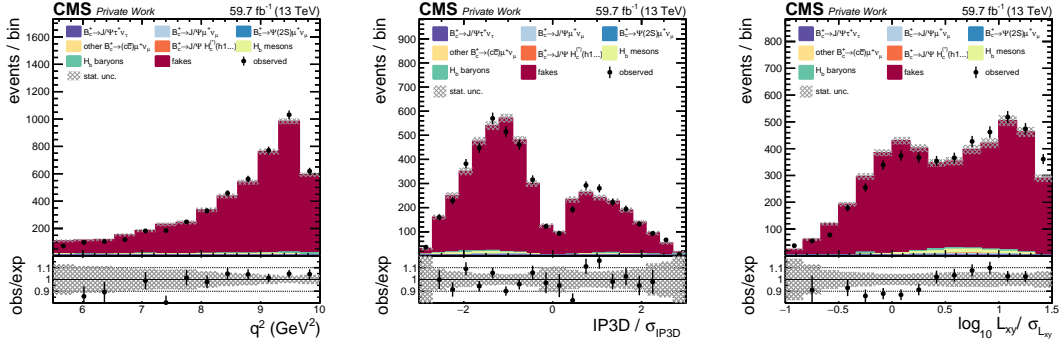


Figure 6.21: q^2 (left), $IP3D_{sig}$ (centre) and $L_{xy,sig}$ (right) distributions in the D' region, which show good agreement between data and fakes background.

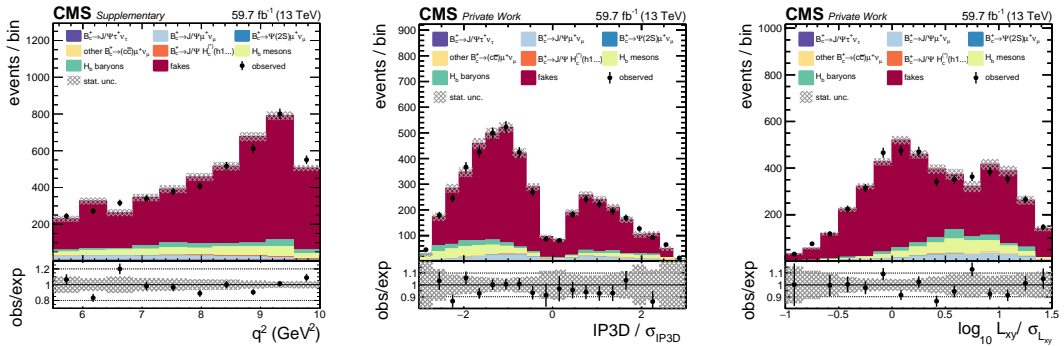


Figure 6.22: q^2 (left), $IP3D_{sig}$ (centre) and $L_{xy,sig}$ (right) distributions in the B' region, which show good agreement between data and fakes background.

the methodology has been meticulously derived, ensuring that uncertainties are thoroughly accounted for. While the most significant of these uncertainties are discussed in this section, a more exhaustive list can be found in Sec. 8.3.

6.3.5.1 Limited statistics in the validation samples

Bin-by-bin uncertainties, which are uncorrelated across each bin, are calculated for the final fakes background shape. These are derived from the validation test on data outlined in the previous section, Fig. 6.22. Each bin uncertainty is computed as $\sqrt{(\text{stat}_{\text{data}}^i)^2 + (\text{stat}_{\text{fakes}}^i)^2}$, where $\text{stat}_{\text{data}}^i$ indicates the statistical uncertainty on data of each bin of the distribution used in this test, and $\text{stat}_{\text{fakes}}^i$ indicates the resulting statistical uncertainty in the corresponding bin of the fakes background template.

This uncertainty, shown in Fig. 6.23, is added in the final fit, uncorrelated for each bin of the fakes and for each category.

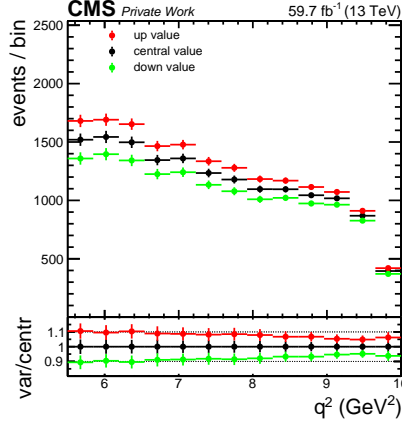


Figure 6.23: q^2 shape uncertainty for the fakes contribution. The upper shape is computed as the nominal fakes value plus $\sqrt{(\text{stat}_{\text{data}}^i)^2 + (\text{stat}_{\text{fakes}}^i)^2}$ from the validation on data test, while for the lower value, the same quantity is subtracted. This uncertainty is added in the fit as a bin-by-bin uncertainty, i.e., each bin can be varied independently of all others in the fit.

6.3.5.2 “Rotated” method

The method described thus far, hereafter referred to as the “nominal” method, follows the scheme in Fig. 6.24 (left). The NNs are trained to compute fr_{ISO} , and this training is conducted in the !ID regions. Region B is where the $fr_{ISO}(x_i)$ weights are applied to determine the fakes shape in A. This reasoning is equally applicable when following the scheme in Fig. 6.24 (right), hereafter called the “rotated” method. In the rotated method, NNs are trained in the !ISO regions, and $fr_{ISO}(x_i)$ is applied in region C to find the fakes shape in region A. The same diagnostic and closure plots have been successfully produced.

By using the two methods, two fakes shapes are found for region A. This introduces a systematic uncertainty to the fakes strategy (see Sec. 8.3). The nominal shape is derived from the final fakes shape using the “nominal” method, while the up shape is obtained from the fakes shape found with the “rotated” method. The down shape is defined as the variation between the up and nominal shapes, mirrored with respect to the nominal one. Fig. 6.25 illustrates the comparison of the three shapes in region A. This is treated as a single nuisance parameter in the fit model.

6.3.5.3 Statistical uncertainty on the NN trainings

A statistical uncertainty must be associated to the training of the three NNs. To compute this, the training sample is divided into 5 sub-samples, referred to as

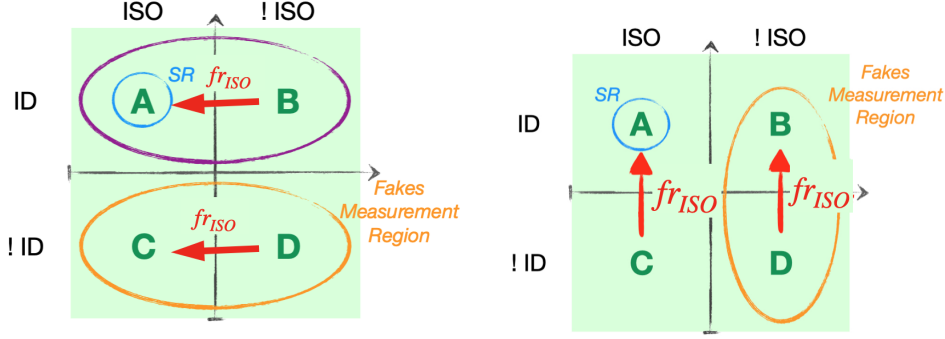


Figure 6.24: ABCD region scheme for the “nominal” method (left), where the training of the NNs to compute fr_{ISO} is done in the !ID regions, while region B is where $fr_{ISO}(x_i)$ weights are applied to find the fakes shape in region A. ABCD region scheme for the “rotated” method (right), where the training of the NNs is performed in the !ISO regions, and $fr_{ISO}(x_i)$ weights are applied in region C to find the fakes shape in region A.

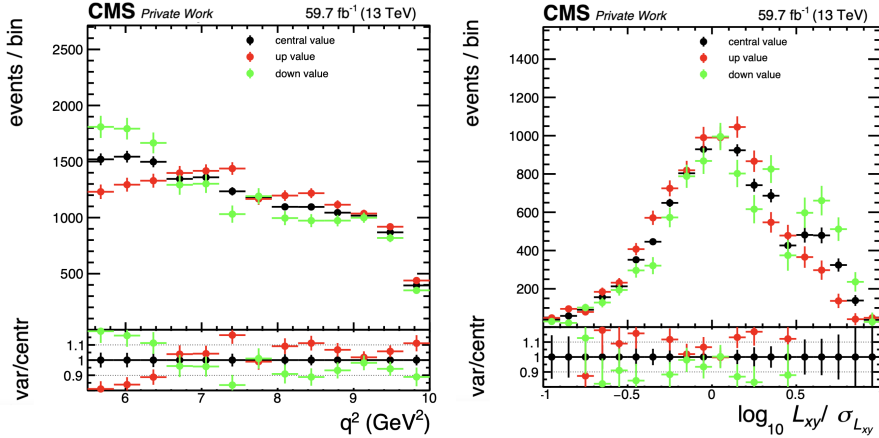


Figure 6.25: The q^2 distribution (left) and $L_{xy,sig} = \frac{L_{xy}}{\sigma_{L_{xy}}}$ (right) for the nominal shape of fakes (black), the up (red) and down (green) uncertainties. The nominal shape comes from the “nominal” method, with up and down being the fakes shapes resulting from the “rotated” method, considered once as a positive variation and once a negative variation from the nominal value.

“chunks,” that are statistically independent. The three NNs are then trained five times, each using a different chunk as the training sample. A fakes shape is derived in region A for each of the training runs. In Fig. 6.26 (left), the fakes shape for the different training runs is shown. The mean of the five histograms is computed bin by bin.

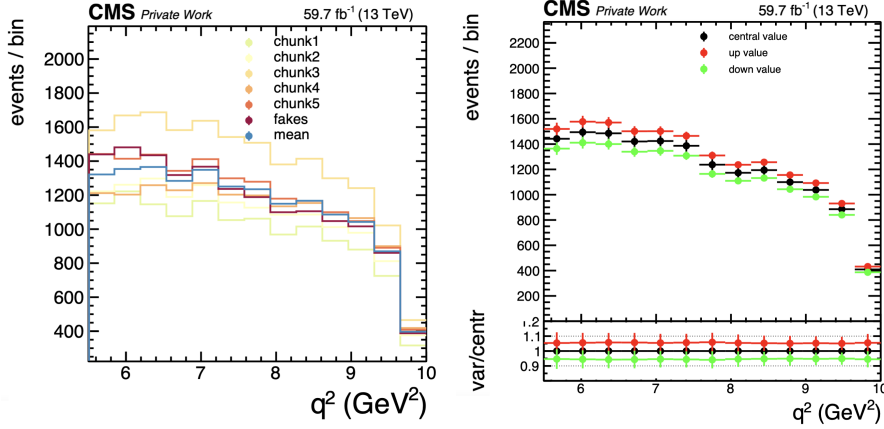


Figure 6.26: The fakes contribution in q^2 computed with different training chunks is shown (left). In the same plot, the mean, computed bin per bin, of the five chunks and the nominal fakes shape (red) is shown. The q^2 distribution for the nominal fakes shape is shown (right), with the up and down shapes computed adding and subtracting to the nominal shape the standard deviation of the mean computed bin per bin from the chunks. This uncertainty is added in the fit as a bin-by-bin uncertainty.

The standard deviation of the mean is also computed, bin per bin, and applied to each bin of the nominal fakes shape, to form an up and down shape, Fig. 6.26 (right). Eventually, this uncertainty is implemented in the fit as a 5% uncertainty, uncorrelated for each bin of the fakes shape. This is added in quadrature to the uncertainty from the validation of the fakes method on data, for a total average of 11% uncertainty for each bin.

6.4 Combinatorial J/ψ dimuon background

In addition to the background sources described above, a J/ψ dimuon combinatorial background contributes to the SR. Two unrelated muons can accidentally return an invariant mass within the J/ψ mass window selected in the analysis.

The number of combinatorial J/ψ dimuon events, $N_{\mu\mu}^{SR}$, is estimated by performing a fit to the dimuon invariant-mass distribution in the SR. A first attempt is performed by applying all the cuts defining the SR in each of the different analysis categories. However, the SR lacks sufficient statistics in most of the analysis categories resulting in a fit of poor quality. Therefore, a Loose Signal Region, “Loose SR”, is defined by applying only the preselection cuts, as described in Sec. 5.4. The final normalisation in the SR of each category is later determined by extrapolating

the number of combinatorial J/ψ dimuon events from the Loose SR to the SR via a data-based Transfer Factor, TF, defined as:

$$N_{\mu\mu}^{SR} = N_{\mu\mu}^{SRloose} \times TF = N_{\mu\mu}^{SRloose} \times \frac{N_{events}^{SR}}{N_{events}^{SRloose}} \quad (6.9)$$

The bulk of the J/ψ peak is modelled by a Crystal Ball function [108] plus a Gaussian function centred on the Crystal Ball function in order to better model the tails of the distribution. The non-resonant combinatorial background is described by an exponential function. The free parameters in the fit are the mass scale and the width $\sigma(m_{\mu\mu})$ of the J/ψ resonance, the Crystal Ball parameters, the Gaussian contribution to the fit function and the number of signal and background events. Due to a trigger cut vetoing the region 5σ -away from the J/ψ peak, the whole invariant mass distribution is fitted in the range $2.96 < m_{\mu\mu} < 3.23$ GeV. This does not allow for a proper modelling of the non-resonant combinatorial background. Therefore, an additional dataset, **DoubleMu4_LowMass**, is examined, and triggers including a track are selected. A region populated only by dimuon combinatorial background is defined with $2.4 < m_{\mu\mu} < 2.8$ GeV. From this region, the slope of the exponential is extrapolated and later fixed in the fit performed in the Loose SR. The result of the fit to extract the combinatorial shape is shown in Fig. 6.27.

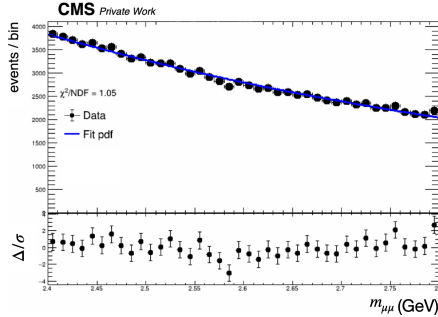


Figure 6.27: Fit to the invariant mass in the region $2.4 < m_{\mu\mu} < 2.8$ GeV to extract the shape of combinatorial J/ψ dimuon events.

The result of the fit in the Loose SR is shown in Fig. 6.28.

In order to estimate the J/ψ dimuon combinatorial shape, a sideband (SB)-based technique is introduced. Due to the analysis trigger cut, in each analysis category a sideband - 3σ away from the J/ψ peak - is defined. The final state observable q^2 used to perform the final fit (see Ch. 8) is kinematically constrained by the invariant mass. Hence, in each analysis category the shape is extrapolated to the SR by scaling the J/ψ four-momentum by the mass ratio $m_{J/\psi,PDG}/\langle m_{SB} \rangle$ where $\langle m_{SB} \rangle$ is the SB centre-of-mass. The method is tested by defining another

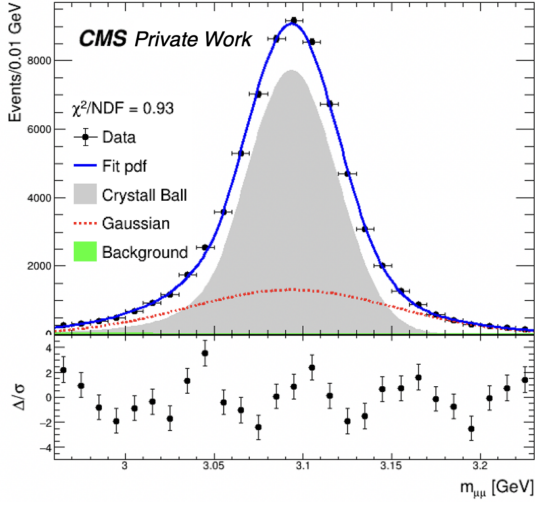


Figure 6.28: Fit to the invariant mass in the Loose SR to extract the contribution of combinatorial J/ψ dimuon events (green).

SB, target SB, and comparing the extrapolated shape with the known shape for this SB. The scale factor used for the target SB is $\langle m_{targetSB} \rangle / \langle m_{SB} \rangle$. The result of this test can be seen in Fig. 6.29.

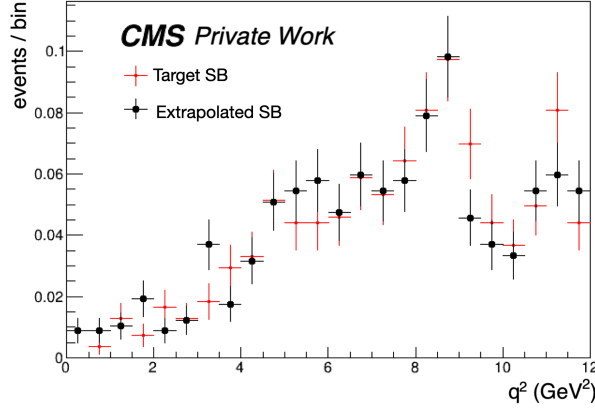


Figure 6.29: q^2 -shape comparison between the extrapolated SB to the target SB and the known shape of the target SB. The extrapolation method is described in the text.

In order to include this data-driven background in the fakes background estimation, it should be added in the NN training, as described in Sec. 6.3.2.2. However, the strategy for obtaining the normalisation of this background in each individual category of the analysis makes it challenging to include it in the training of

the NN without significant approximation. Considering that this background contributes only about $\sim 2\text{-}3\%$ of data events (depending on the different analysis categories), it has been decided not to include it in the training of the networks. Instead, it is simply added to all the categories, influencing the fakes estimate through the subtraction method in the reweighted regions between data and the other contributions.

Chapter 7

Correction of MC Simulations

Correcting simulation is necessary to account for experimental effects that may be poorly modelled. This ensures that the simulation aligns with the actual conditions of real data taking. The corrections implemented can be categorised into five main groups, each detailed in the following sections:

- Corrections to B_c form factors;
- Corrections to pileup;
- Corrections to B_c meson kinematic properties;
- Corrections to topological variables;
- Corrections to J/ψ resonance kinematic properties;
- Corrections to muon efficiencies.

7.1 Form factors

Each MC sample involving hadrons is generated using a hadronic model, represented by a form factors (FF) parametrisation. The B_c MC sample is initially produced using the B_c FF presented in Ref. [81], which are referred to as Kiselev, after the name of the main author of Ref. [81], as the only option available in EvtGen. Recent studies propose alternative values, such as the Boyd, Grinstein, and Lebed (BGL) parametrisation [38]. To update the FF, the MC samples have to be reweighted. To accomplish this, the Hammer tool [83] [109] is employed, as it is specifically designed for updating the FF at GEN level.

A global analysis of lattice-QCD data, employing the model-independent FF parametrisation of BGL, is performed in Ref. [38], where lattice-QCD data refers

to the results obtained from numerical simulations performed on a lattice (four-dimensional grid approximation to describe non-perturbative aspects of QCD). A multi-variable fit to the lattice-QCD data is performed, and the set of BGL FF parameters for B_c decaying into J/ψ is found, with the FF parameters indicated as g , f , F_1 , F_2 in Ref. [38], Fig. 7.1. Every functional form of FF can be expressed

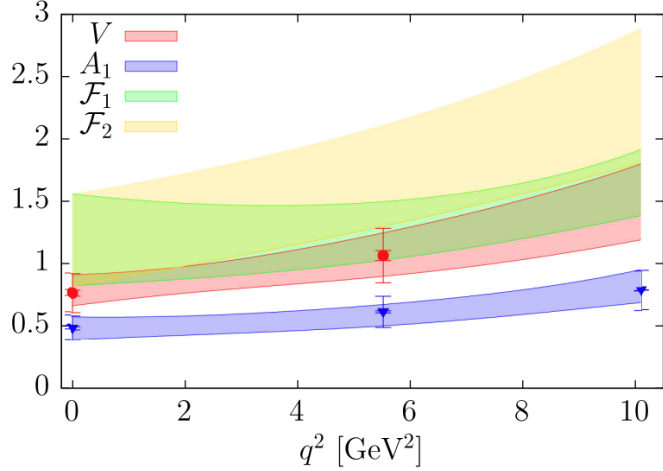


Figure 7.1: $B_c \rightarrow J/\psi$ FF. V and A_1 are proportional respectively to g and f . $V(q^2)$ (red circles) and $A_1(q^2)$ (blue triangles) from the HPQCD Collaboration [110]. The interior bars represent the statistical uncertainty quoted by HPQCD. The exterior bars represent the result of including a flat 20% systematic uncertainty. The coloured bands are the one-standard-deviation, 1σ , best-fit regions obtained from the global analysis [38].

in terms of a set of Taylor coefficients a_n^i , reported in Table 7.1 [38].

FF	$a_0^i [\times 10^2]$	$a_1^i [\times 10^2]$	$a_2^i [\times 10^2]$
g	0.47(9)	-2(3)	20(60)
f	0.34(5)	-2.6(2.0)	40(60)
F_1	0.058(10)	-0.3(3)	9(8)
F_2	4(10)	21(16)	0.8(9)

Table 7.1: The BGL coefficients a_n^i for the $B_c \rightarrow J/\psi$ process [38].

Given the correlation among these parameters, a crucial step involves conducting a principal component analysis (PCA). In this analysis, the eigenvectors and eigenvalues of the covariance matrix for these coefficients are computed. This process aims at identifying the principal components, revealing the primary directions of maximum variance attributed to the BGL FF.

Finally, the Hammer software library is employed to reweight the signals MC samples to the desired BGL FF. It requires the truth-level computation of the ratio of the differential rates:

$$r_I = \frac{d\Gamma_I^{new}/d\mathcal{PS}}{d\Gamma_I^{old}/d\mathcal{PS}} \quad (7.1)$$

applied event-by-event via the mapping $w_I \rightarrow r_I w_I$, where Γ is the partial width and PS the phase space, with the index I that denotes the event and w the associated weight. Additionally, variations to these central weights are computed with the Hammer tool, and these variations are uncorrelated among each other, thanks to the PCA described before.

To validate the entire procedure, a closure test is conducted on both the τ signal and the μ signal. Specifically, two dedicated MC samples are generated for each decay: one with Kiselev weights and the other with the Ebert, Faustov and Galkin (EFG) weights [111]. The Hammer library is employed to transform the latter into the former, and the resulting shapes are compared. In Figure 7.2, the closure test for the μ signal is shown. The KS test yields a result of 0.88 for the comparison between the reweighted EFG and Kiselev, and 10^{-5} for the original EFG and Kiselev.

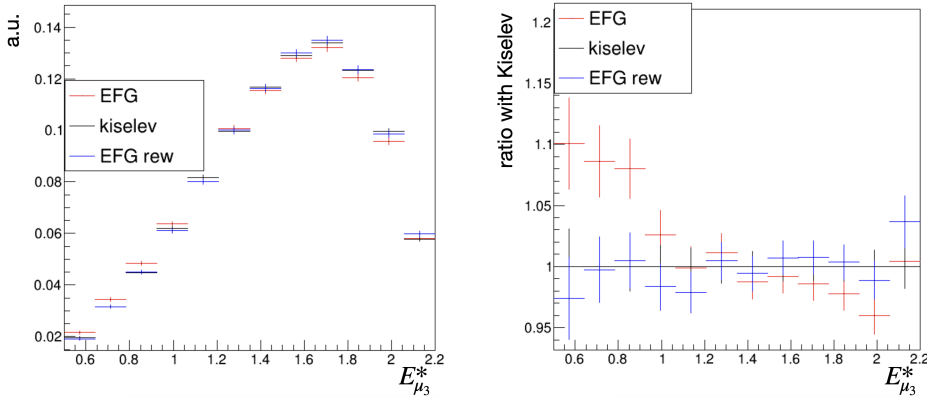


Figure 7.2: Closure test for the form factor reweighting procedure. The test is performed on the μ signal sample, reweighting EFG (red) using Kiselev weights, to find that Kiselev (black) and EFG reweighted (blue) distributions are compatible. The distributions are plotted for the E_μ^* variable, and both the normalised shapes (left) and ratio shapes with respect to Kiselev (right) are shown.

The same closure test has been performed for the τ signal, with similar results.

The validation test was successful, and consequently, weights have been computed for both τ signal and μ signal processes. The uncertainty weights have been

incorporated as shape systematic uncertainties in the fit (refer to Ch. 8 for details), for a total of 10 uncertainties.

As detailed in Sec. 5.2.1, the various B_c decays are simulated with the correct proportions. The FF weights modify not only the shapes but also the normalisations of these decays. Since these normalisations are controlled and accurate only for the FF used in generation, the Kiselev model, any discrepancies in the normalisation introduced by the application of the BGL weights must be corrected. To effectively make these adjustments, a sample that has not been subjected to any filters or selections has to be used. This sample is utilised to compute the average values of FF weights for both τ signal and μ signal. The mean weights were determined to be $\bar{w}_{\text{kis} \rightarrow \text{BGL}}^{\tau} = 0.55$ for the τ signal and $\bar{w}_{\text{kis} \rightarrow \text{BGL}}^{\mu} = 0.60$ for the μ signal. Consequently, the yields are divided by $\bar{w}_{\text{kis} \rightarrow \text{BGL}}^{\tau}$ and $\bar{w}_{\text{kis} \rightarrow \text{BGL}}^{\mu}$ respectively to maintain the relative abundances of processes. The same procedure is applied for the derivation of the systematic uncertainties. In Figure 7.3 the central value is compared to the 1σ variation of the first parameter, for both τ signal (left) and μ signal (right).

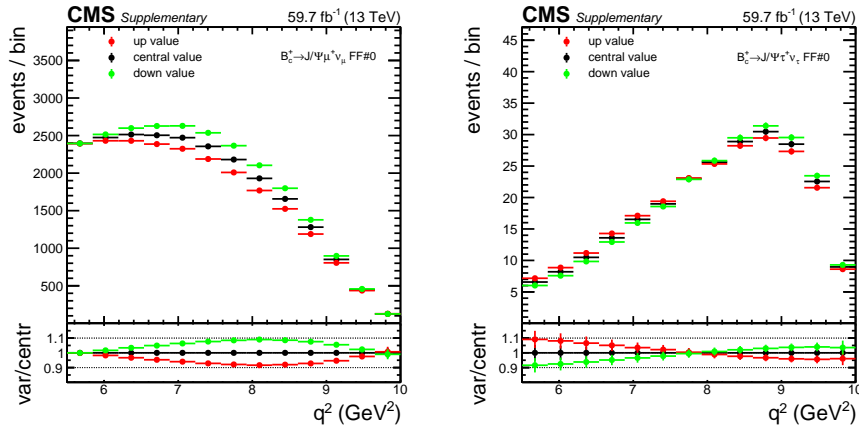


Figure 7.3: q^2 distribution for μ signal (left) and τ signal (right). The nominal value (black) is compared with the up (red) and down (green) distributions obtained applying the Hammer weights for the first parameter of the FF variations.

7.2 Pileup

Pileup is the amount of simultaneous pp interactions per bunch crossing. The MC samples have to be reweighted to have the same number of PV per event as data. The weights and the uncertainties are computed comparing the 2018 centrally produced histogram for UL data with the number of PVs of the MC samples [112].

Pileup weights are applied to each event in the histograms, and uncertainties are added as shape nuisances in the fit, as shown in Fig. 7.4. The impact of this uncertainty on the shapes is very small.

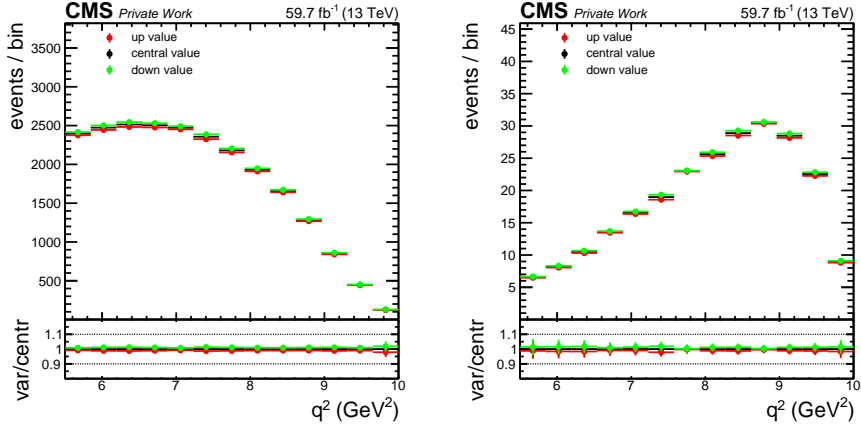


Figure 7.4: q^2 distribution is shown for μ signal (left) and τ signal (right). The nominal value (black) is compared with the up (red) and down (green) distributions obtained applying the pileup weights for 1σ systematic uncertainty.

7.3 B_c meson properties

7.3.1 B_c kinematics

The distributions of the decay products of the signals of interest depend on the kinematic distributions of the B_c meson. The study for possible mismodeling focuses on the $p_T - \eta$ spectrum. MC distributions are compared to the observed ones aiming for a correction map or systematic uncertainty to treat residual mismodelling effects. Experimentally, the presence of the invisible neutrino contributions in the final states of the signal processes prevents any use of them to study B_c kinematic distributions. Hence, the fully-visible control sample $B_c \rightarrow J/\psi \pi$ is used to characterise the B_c kinematics. The selection of $B_c \rightarrow J/\psi \pi$ candidates is as close as possible to the signal selection described in Sec. 5.4. The J/ψ candidates are initially reconstructed. Once J/ψ candidates are produced, π tracks from the PF collection are coupled with the J/ψ candidates. The selections applied to the final state muons and π are:

- $p_{T,lead} > 6$ GeV, $p_{T,sublead} > 4$ GeV, where $lead(sublead)$ refers to the muon with the highest(lowest) p_T in the pair of muons;

- $p_{T,\pi} > 8$ GeV;
- $|\eta| < 2.5$ and transverse impact parameter $d_{xy} < 0.05$ cm for the three tracks;
- both muons passing the Medium ID criteria;
- $\Delta d_{z_{12}} = |d_{z_{\mu_1}} - d_{z_{\mu_2}}| < 0.2$, $\Delta d_{z_{13}} = |d_{z_{\mu_1}} - d_{z_\pi}| < 0.2$ and $\Delta d_{z_{23}} = |d_{z_{\mu_2}} - d_{z_\pi}| < 0.2$
- pion track passing $p_T > 0.5$ GeV, $|\eta| < 2.5$ and the isolation requirements.

The reconstructed J/ψ properties are:

- the probability of the dimuon vertex fit better than 0.001%;
- $p_T(\mu\mu) > 3$ GeV;
- a η -dependent mass cut in order to take into account the different mass resolution when moving from the barrel to the endcap regions of the detector: $|m_{\mu\mu} - m_{J/\psi,PDG}| < 70$ MeV for one muon in the endcap regions and one in the barrel, $|m_{\mu\mu} - m_{J/\psi,PDG}| < 50$ MeV for both muons in the barrel and $|m_{\mu\mu} - m_{J/\psi,PDG}| < 100$ MeV for both muons in the endcap regions.

The final B_c candidate has to follow the requirements:

- the B_c candidate with mass $6 \text{ GeV} < m_{B_c} < 10 \text{ GeV}$ and a vertex-fit pointing cosine $\cos(\Delta\alpha_{PV}^{B_c}) > 0.999$;

The final selection has been designed to maximise the overlap with the analysis phase-space. In Fig. 7.5 the p_T and η distributions of the selected $\mu\mu\pi$ MC candidates are compared with the corresponding $\mu\mu\mu$ MC distributions of this analysis. In contrast to the analysis signature, the control-sample final state does not include any invisible neutrino contributions to the transverse momentum available. This motivates a higher p_T threshold for the pion (8 GeV) compared to that of the third muon in the analysis signature (4 GeV), the trailing muon in the analysis selection reported in Sec. 5.4. While the p_T -distribution overlap is satisfying, some disagreement is observed for the η distribution. To facilitate the extrapolation of the correction maps from the control sample to the analysis samples, a preliminary data-based reweighting of the η -distribution is applied. Before deriving any correction map, the η distribution of the $\mu\mu\pi$ -control sample is reweighted event by event aiming for a better agreement with the η distribution observed in $\mu\mu\mu$ -data. The final result is shown in Fig. 7.6, where a satisfying agreement is achieved.

The strategy to derive the correction map can be summarised as follows:

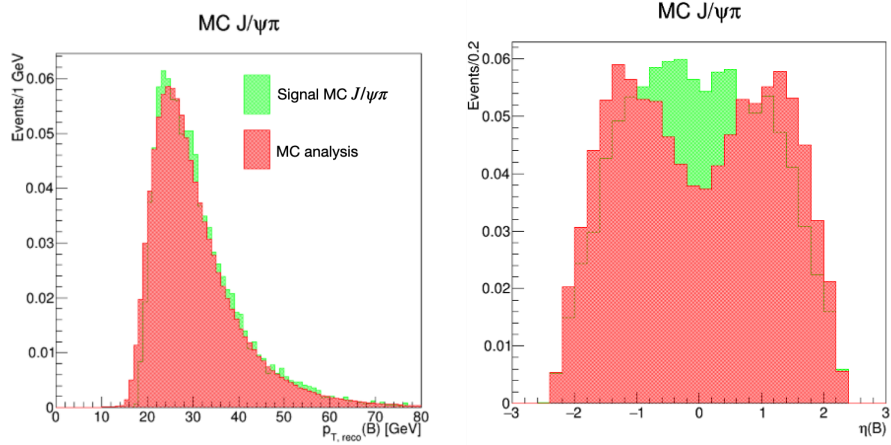


Figure 7.5: Comparison between the B_c p_T (left) and η distributions (right) in the simulated $\mu\mu\mu$ (red) and $\mu\mu\pi$ (green) samples.

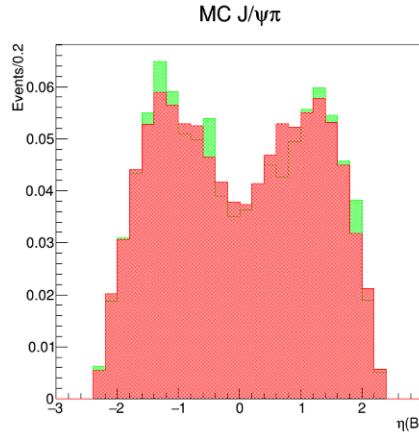


Figure 7.6: The η distribution in the $\mu\mu\pi$ (green) sample is reweighted to better reproduce the $\mu\mu\mu$ (red) phase-space.

1. a fit to the data $\mu\mu\pi$ -invariant mass is performed to separate background and signal contributions. In order to neglect the resolution of the muons, the variable to be fitted is corrected by the J/ψ assumption, meaning that $m_{\mu\mu\pi}$ is redefined as $m_{\mu\mu\pi}^{corr} = m_{\mu\mu\pi} - m_{\mu\mu} + m_{J/\psi, PDG}$.
2. the probability density function extracted from the fit is used as input for the sPlots routine [113] resulting in computed signal sWeights, which allow the production of a signal-only sample.
3. the signal-only sample is compared to the MC $\mu\mu\pi$ sample and p_T -weights are derived.

- the p_T -correction map is fitted to derive a global correction, which will be used as a systematic uncertainty for the $\mu\mu\mu$ simulated sample, as it will be described in Sec. 8.3.

The fit function modelling includes different contributions:

- the searched B_c signal is modelled by a double-Gaussian function sharing the same mean, which corresponds to the average reconstructed B_c mass. The double Gaussian modelling is required to take into account the degrading B_c mass resolution when moving from the barrel to the endcap regions. The fit returns a narrow width of 23 MeV and a wide width of 50 MeV, in agreement with results obtained in the recently published CMS paper on the B_c excited states [114]. In addition, a small contribution from $B_c \rightarrow J/\psi K$ decays must be included. The shape is taken from simulation and the normalisation is fixed taking into account the PDG branching ratio with respect to the $B_c \rightarrow J/\psi\pi$ yield, which is a free parameter in the fit.
- uncorrelated J/ψ -track combinations parameterised by a first-order polynomial. This is referred to as combinatorial background.
- partially reconstructed $B_c \rightarrow J/\psi\pi X$ decays parameterised by a generalised ARGUS function with a Gaussian resolution. This contribution is relevant only in the low-mass spectrum, below 6.2 GeV.

The result of the fit to the data $\mu\mu\pi$ -invariant mass is shown in Fig. 7.7. A fit to the p_T -correction map results in a global factor of 0.008. Considering that the effect is very small and that this measurement has some limitations, this is not used as a correction but as a systematic uncertainty in the analysis.

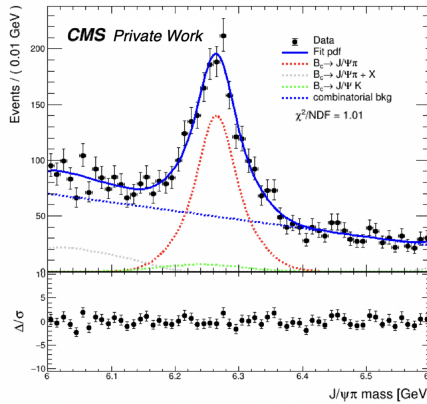


Figure 7.7: Fit to the data $\mu\mu\pi$ -invariant mass.

7.3.2 B_c lifetime

The B_c MC sample is produced with a different lifetime $c\tau$ from the one indicated in the PDG:

- τ pdg = $(0.510 \pm 0.01) \cdot 10^{-12} s$
- τ MC = $0.507 \cdot 10^{-12} s$

The central values have a difference of few %, hence a correction is applied. To evaluate this correction, events are weighted with factors obtained from the ratio of two exponentials with the different mean lifetimes. Also a systematic uncertainty is computed, due to the B_c lifetime uncertainty from the PDG, and it is shown in Fig. 7.8.

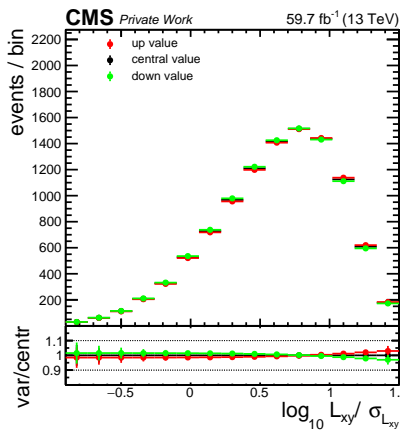


Figure 7.8: q^2 distribution is shown for μ signal. The nominal value (black) is compared with the up (red) and down (green) distributions obtained applying the lifetime uncertainty for 1σ systematic uncertainty.

7.3.3 Not-yet-measured B_c decays

There are possible B_c decays that are not seen or measured yet and that could have an impact on the analysis. A comprehensive study has been conducted to assess the potential impact of these not-yet-measured decays. New MC samples, hereafter referred to as “not-yet-measured samples”, are generated for each potential decay. These samples, distinct from the B_c MC sample described in Sec. 5.2.1 that encompass the decays listed in Table 5.2, are specifically produced only up to the GEN step with EvtGen, to save production time and resources. Their q^2 shape and yield are compared to the one of the τ signal and other decays as shown in Fig. 7.9.

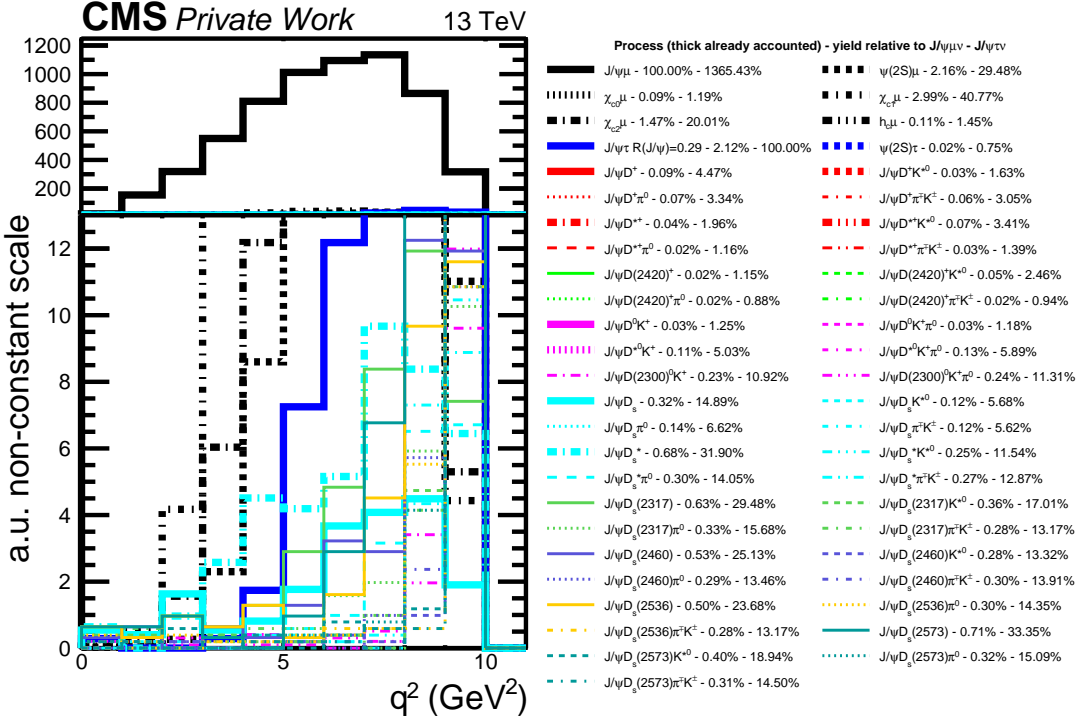


Figure 7.9: q^2 distribution for the produced B_c decays. The contributions with thick lines indicate the decays present in the B_c MC sample, while the others are part of the not-yet-measured samples. On the right, a list of the decays and their yield relative to $B_c^+ \rightarrow J/\psi \mu^+ \nu_\mu$ and $B_c^+ \rightarrow J/\psi \tau^+ \nu_\tau$ is shown. Only the distributions of the decays with a yield $> 10\%$ of that of the τ signal are shown in the plot.

In the simulation of these decays, if no specific model is available in EvtGen, a generic phase space model is used (PHSP), which averages the spins of all particles in the initial and final state. Therefore spin and its possible impact on q^2 is here neglected. Kinematic selections are applied on the three muons in the final state, $p_{T,lead} > 6$ GeV, $p_{T,sublead} > 4$ GeV and $p_{T,trailing} > 4$ GeV, where $lead(sublead)(trailing)$ refers to the muon with the highest(medium)(lowest) p_T in the triplet, to mimic the final selection. Isolation requirements are not applied in this study because the MC samples are simulated only up to GEN level and, at this stage, the isolation variable cannot be computed, because pileup and detector simulation are still missing. Applying a selection based on isolation would decrease contamination from higher multiplicity decays. Therefore, the results presented in this study represent a worst-case scenario.

Eventually, assumptions are made on the branching ratio when estimating the

yields. With these assumptions on the yields, some of these new processes might have non-negligible contributions. Consequently, in the following, a more detailed study is conducted to determine how they might be appropriately handled in the analysis.

- In Fig 7.10 (left), the decay topology $B_c \rightarrow J/\psi D^{(\text{any})} K^{(+/*0)}$ is shown. The shapes of the not-yet-measured samples (thin lines) are compatible with the ones from the B_c MC sample (thick lines).

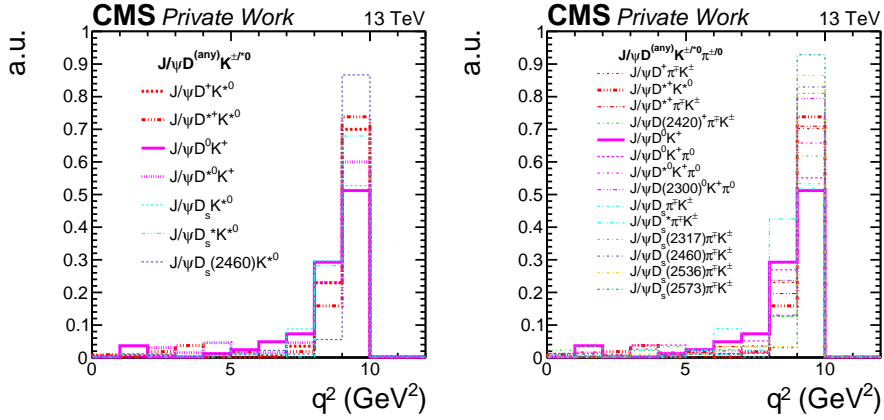


Figure 7.10: q^2 distribution for two types of decays: $B_c \rightarrow J/\psi D^{(\text{any})} K^{(+/*0)}$ (left) and $B_c \rightarrow J/\psi D^{(\text{any})} K^{(+/*0)} \pi^{(\text{any})}$ (right). Thick lines represent contributions from decays in the B_c MC sample, while others belong to not-yet-measured samples. The shapes of these not-yet-measured decays align with those already present in the B_c sample.

- Neglecting phase-space or Cabibbo suppression for excited D states or high-multiplicity decays, the same decays with an additional pion, $J/\psi D^{(\text{any})} K^{(+/*0)} \pi^{(\text{any})}$, can still have sizeable yields. However, their shapes are compatible to the ones already accounted for in the B_c MC sample, as shown in Fig. 7.10 (right).
- Decays into $J/\psi D$ (excited) also could have non-negligible yields. In Fig. 7.11 (left), a comparison of several excited $B_c \rightarrow J/\psi D_s$ states is shown, along with four decays already included in B_c : $B_c \rightarrow J/\psi D_s$, $B_c \rightarrow J/\psi D^+$, $B_c \rightarrow J/\psi D^{*+}$, or $B_c \rightarrow J/\psi D_s^*$. Their shapes are very different. However, the $J/\psi D^{(*)}$ in the B_c MC sample have been produced with decay modes SVS and SVV, while the not-yet-measured samples have been produced via phase space (PHSP). The SVS and SVV modes indicate respectively the decay of a scalar to a vector and a scalar, e.g. B_c (scalar) $\rightarrow J/\psi$ (vector) D_s (scalar), and the decay of a scalar to two vectors, e.g. B_c (scalar) $\rightarrow J/\psi$ (vector)

D^* (vector). To ensure that the decay mode used to produce these decays does not influence their shapes, two samples, $J/\psi D^+$ and $J/\psi D_s(2317)$, have been produced with both modes, as depicted in Fig. 7.11 (centre and right), showing minimal differences between the two.

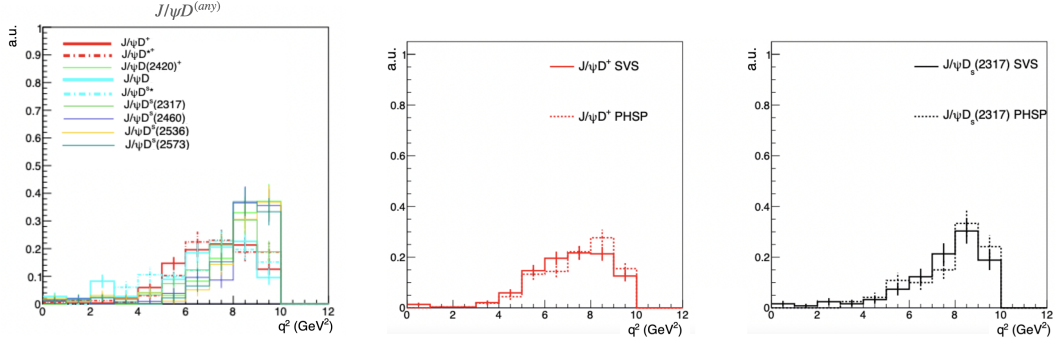


Figure 7.11: q^2 distribution for the produced $B_c \rightarrow J/\psi D$ (excited) decays (left). The decays from the B_c MC samples are $B_c \rightarrow J/\psi D_s$ (thick light blue), $B_c \rightarrow J/\psi D^+$ (thick red), $B_c \rightarrow J/\psi D^{*+}$ (thick dashed red), $B_c \rightarrow J/\psi D_s^*$ (thick dashed light blue). All the contribution with thin lines include all the not-yet-measured decays of the type $B_c \rightarrow J/\psi D$ (excited). Comparison between SVS and PHSP EvtGen models for $B_c \rightarrow J/\psi D^+$ (centre) and $B_c \rightarrow J/\psi D_s$ (right).

The treatment of systematic uncertainties to account for the not-yet-measured decays is discussed in Sec. 8.3.

7.4 Topological variables

In this analysis, special emphasis is placed on two variables, the IP3D and L_{xy} , because their significance is used in the final fit.

7.4.1 IP3D correction

The IP3D distribution, its uncertainty and its significance are shown in Fig. 7.12. The plots in Fig. 7.12 reveal a disagreement between data and MC. To address this MC mismodeling, specifically related to vertex simulation challenges, a simple dilation factor is introduced for the MC. To determine the best correction value for the $IP3D_{sig}$, several fits to this variable are performed, with the same fit model described in Sec. 8, each with a different correction value. The absolute likelihood is saved for each fit and a likelihood scan of the correction value is shown in Fig. 7.13 (left).

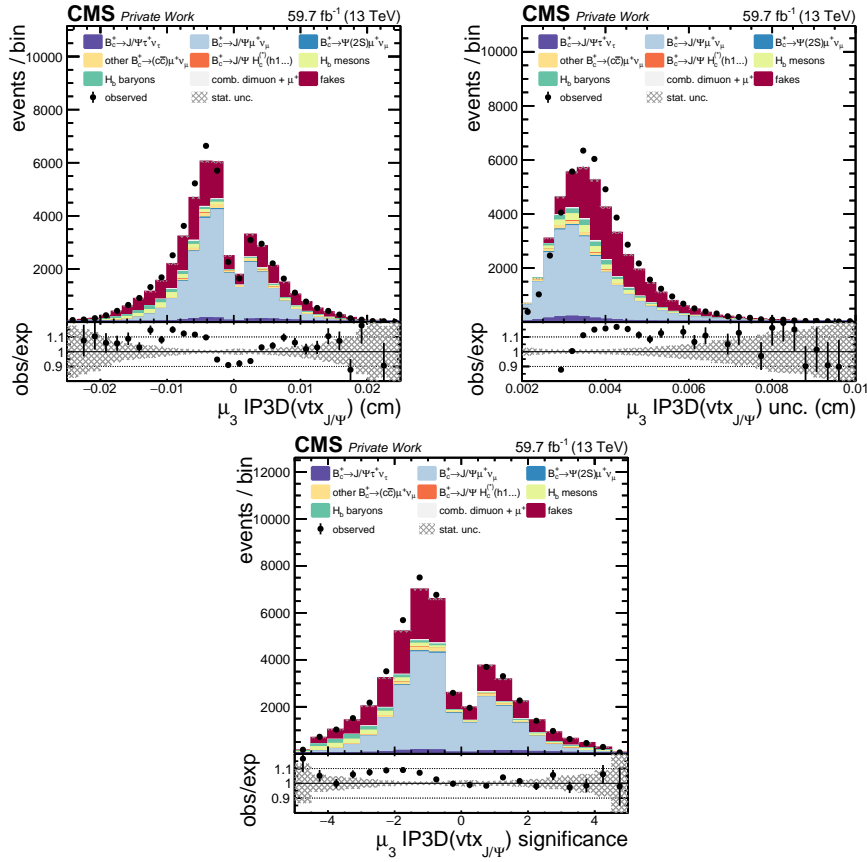


Figure 7.12: IP3D, σ_{IP3D} and IP3D_{sig} distributions in the A region.

From this likelihood scan, the optimal value for the IP3D_{sig} correction is determined to be 1.055. The final corrected IP3D_{sig} distribution is displayed in Fig. 7.13 (right).

An uncertainty is introduced for this correction by considering the distribution with a correction value of 1.0 as the up variation and the distribution with a correction value of 1.1 as the down variation. As this variable is utilised in defining the categories (see Sec. 8.1), this uncertainty results in event migrations between different categories. Further details and plots are available in Sec. 8.3.

7.4.2 L_{xy} correction

In addition to IP3D, the data/MC agreement level for the $L_{xy,sig}$ distribution of the J/ψ meson is also low, as shown in Fig. 7.14 (left). To address this discrepancy, a correction is applied to this variable in the form of a dilation factor on the MC samples. The correction factor used is 9%.

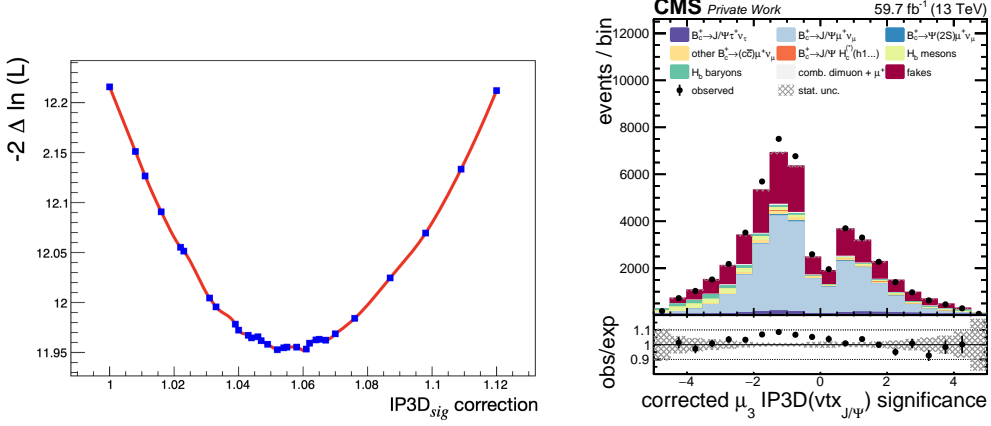


Figure 7.13: For each correction value for $IP3D_{sig}$, a fit is performed and the absolute likelihood is here added. This resulting likelihood scan (left) indicates the best correction value to apply to the $IP3D_{sig}$ variable. Corrected $IP3D_{sig}$ distribution (right) is shown, with a dilation factor of 1.055, as found from the likelihood scan. The application of these corrections results in an improved agreement compared to the case where no correction is applied.

This correction is then applied to the analysis samples, resulting in improved data/MC agreement, as illustrated in Fig. 7.14 (right).

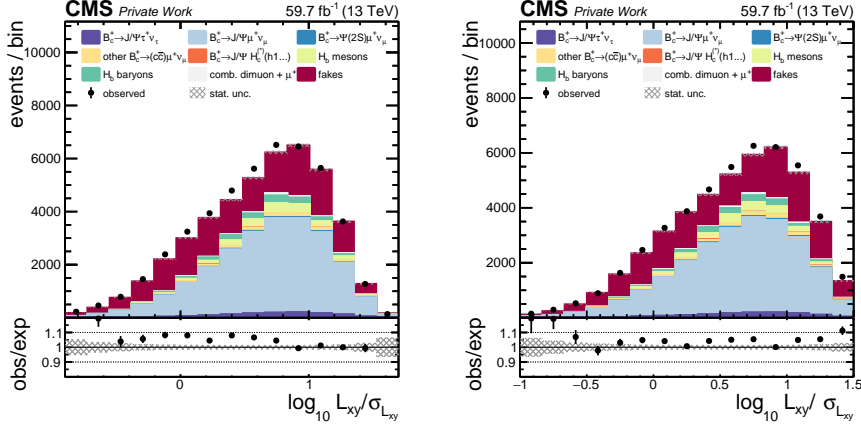


Figure 7.14: $L_{xy,sig}$ distributions in the A region before (left) and after (right) the correction.

Also in this case an uncertainty is added to the correction, taking as up distribution the one with dilation factor of 1.0 and the down distribution the one with factor 1.2. Plots are shown in Sec. 8.3.

7.5 J/ψ resonance kinematic properties

The $m(J/\psi)$ distribution exhibits a data/MC disagreement, as indicated by the slope in the ratio plot in Fig. 7.15 on the left. To address this discrepancy, the shape is corrected for each MC sample using a correction factor of 0.001. Event weights are then computed from the ratio of the corrected to the non-corrected distributions of J/ψ mass histograms and applied to the MC samples. Fig. 7.15 displays the data/MC agreement of the $m(J/\psi)$ distribution before (left) and after (right) the correction. The achieved agreement is satisfactory for the purposes of this analysis.

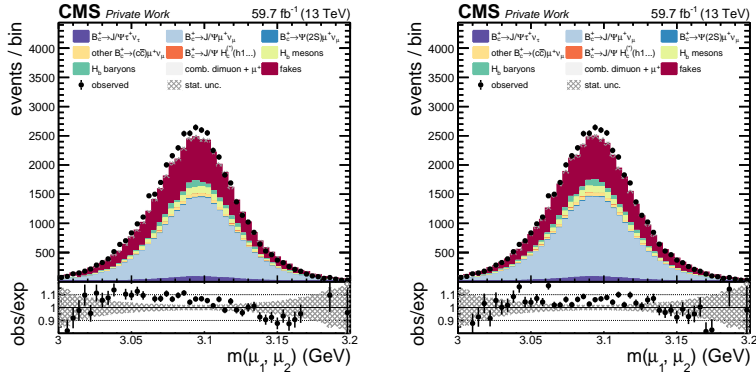


Figure 7.15: Distribution of $m(J/\psi)$ before (left) and after (right) applying the MC correction. There is evident improvement in the slope within the ratio pads in the corrected plot.

7.6 Muon efficiencies

In order to account for discrepancies in muon efficiencies between data and simulation, a series of scale factors (SF) are computed and applied to MC samples. Official muon SFs provided by the CMS collaboration have been used for the reconstruction efficiencies of the three muons and the Medium ID efficiencies of the two muons originating from the J/ψ [115]. These were the only SFs centrally available and the remaining SFs have been computed specifically for this analysis using the tag and probe method [116] on the J/ψ resonance, considering the dependence on the p_T and η of the individual muons. The SF are computed from data and MC efficiencies ϵ as:

$$SF(p_T, \eta) = \frac{\epsilon_{data}}{\epsilon_{MC}}. \quad (7.2)$$

The overall efficiency for muon reconstruction, ID, ISO, and trigger is computed by factorising each contribution:

$$\epsilon_{\text{TOTAL}}^{\mu} = \epsilon_{\text{RECO}}^{\mu} \cdot \epsilon_{\text{ID|RECO}}^{\mu} \cdot \epsilon_{\text{ISO|ID}}^{\mu} \cdot \epsilon_{\text{Trg|ISO}}^{\mu} \quad (7.3)$$

Each “step” of the efficiency computation is measured with the denominator including only the muons passing the previous selection step.

The tag and probe method used to compute the missing SF comprises the following steps:

1. Reconstruct resonance pairs with one muon passing a tight identification (tag) and the other passing a loose identification (probe) criterium. The tag ensures the selected events represent the signal (J/ψ), warranting the application of stringent criteria. The probe muon is utilised to estimate the single muon efficiency. Pair selection criteria (e.g., opposite sign, invariant mass range, beamspot constraints) are applied to ensure the chosen dimuon pair is the signal.
2. Independently fit line shapes for tag + passing probe and tag + failing probe configurations using a signal + background model. An example is shown in Fig. 7.16.

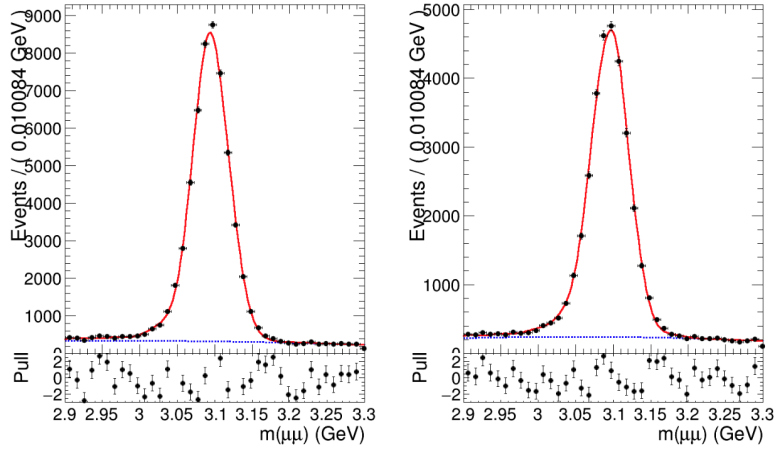


Figure 7.16: Fit to the invariant mass of tag and passing probe muons (left) and tag and failing probe muons (right), both using a fit model including a signal and a background.

3. Compute the efficiency by determining the ratio of signal yields in the two line shapes.

4. Repeat the procedure in bins of probe variables (e.g., $p_T, \eta \dots$) to generate efficiency histograms as functions of those variables.

The method assumes there are no correlations between tag and probe, which is not the case for this analysis. However, the test presented later in Fig 7.20 demonstrates that the approach remains valid.

This method offers a detailed assessment of single muon efficiencies, utilising a well-defined resonance (tag) for signal event identification. Efficiency is estimated through the second muon (probe), and the analysis considers dependencies on key kinematic variables by conducting the procedure across various bins of these variables. In the following, results are shown for:

- softMVA ID SF;
- $\Delta\beta_{corriso}$ SF;
- Trigger SF.

7.6.1 Identification

The μ_3 is required to satisfy the softMVA ID requirement in regions A and B, as shown in Fig. 6.9, and to fail it in regions C and D, where the NN for the fakes estimation method is trained. Consequently two sets of ID SF are computed for μ_3 , that already passed the reconstruction step:

- pass softMVA ID (for regions A and B);
- fail softMVA ID (for regions C and D).

In the following, only the pass softMVA ID SFs are presented, as the second set of SF can be easily derived from the first one by inverting the efficiencies, $\epsilon_{pass} = 1 - \epsilon_{fail}$. Specific datasets and triggers, requiring at least a single muon with $p_T > 20$ GeV, are utilised for this study. The simulation includes J/ψ prompt samples. The selection employed to calculate the efficiencies requires a high-quality tag muon that satisfies a tight ID requirement and $p_T > 20$ GeV. Both tag and probe muons are required to be tracker muons. The efficiencies for both data and MC in four bins of η are shown in Fig. 7.17. The final softMVA ID SF weights along with their statistical uncertainties are eventually computed and applied to the analysis events.

A total uncertainty of 3% is incorporated in the fit model, Sec. 8.3, to also account for potential systematic effects.

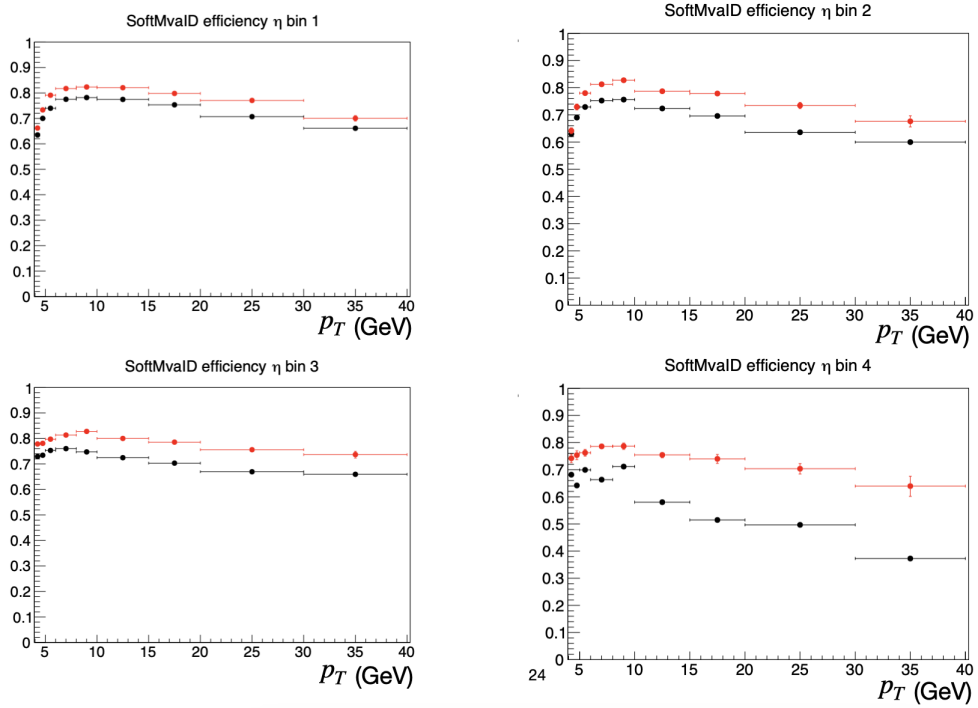


Figure 7.17: μ_3 p_T distributions for MC (red) and data (black) softMVA ID efficiencies. Each plot shows a different bin in η : $|\eta| \leq 0.9$ (top left); $0.9 < |\eta| \leq 1.2$ (top right); $1.2 < |\eta| \leq 2.1$ (bottom left); $2.1 < |\eta| \leq 2.4$ (bottom right).

7.6.2 Isolation

The μ_3 is required to satisfy the $\Delta\beta_{\text{corr,iso}_{\mu_3}} < 0.2$ criterion in regions A and C, and to fail the same criterion in regions B and D. Consequently, taking into account that the ISO efficiencies are computed on top of the ID ones, four sets of ISO SFs need to be derived:

- Pass ISO & Pass ID (region A)
- Pass ISO & Fail ID (region C)
- Fail ISO & Pass ID (region B)
- Fail ISO & Fail ID (region D).

The method employed is the tag and probe method, utilising the J/ψ resonance. For this computation, events requiring the presence of two high-quality muons is utilised. Both tag and probe muons are required to pass the ID selection. For the MC sample, the non-prompt J/ψ sample is used, as the isolation variable is not well

simulated in prompt J/ψ samples. The problem arises from the PYTHIA simulation difference between Charmonium and QCD minimum bias. The selection applied to compute the efficiencies includes high-quality tag and probe muons, with both passing the softMVA ID. Additionally, the two muons are required to originate from a non-prompt J/ψ , thanks to requirements on impact parameters and vertex displacement. The isolation efficiencies for data and MC in region A in two different bins of η are shown in Fig. 7.18.

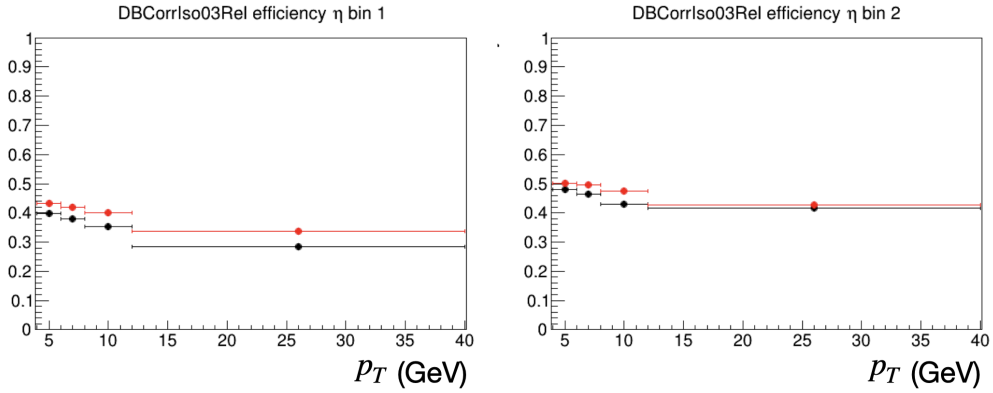


Figure 7.18: p_T of μ_3 distributions for MC (red) and data (black) ISO efficiencies. Each plot shows a different bin in η : $|\eta| \leq 1.4$ (left); $1.4 < |\eta| \leq 2.4$ (right).

The final ISO SFs with their statistical uncertainty are computed and applied to the μ_3 in the corresponding categories.

A total uncertainty of 3% is added in the fit model to take into account possible systematical effects.

7.6.3 Trigger

The three muons have to pass a trigger requiring the presence of three muons in the final state, two of which coming from a J/ψ vertex. Trigger efficiencies (HLT + L1) must be measured for the J/ψ and μ_3 part. To compute these SFs, the tag and probe method is used on the J/ψ resonance, using the same dataset of the analysis and the same non-prompt MC sample used to compute the ISO SFs. The efficiencies are measured separately for the J/ψ and μ_3 part. Alternative methods, like orthogonal datasets, do not have sufficient statistics.

- J/ψ part

The goal is to assess the HLT + L1 efficiency specific to the J/ψ part of the analysis trigger. This involves determining the efficiencies of a secondary trigger

that demands the presence of two muons originating from a J/ψ , with trigger requirements similar to those of the main analysis trigger.

The tag muon is matched with a trigger that requires at least one muon with $p_T^\mu > 8$ GeV. Both the tag and probe muons must satisfy the Medium ID criterion, as mandated in the analysis for muons originating from the J/ψ . The J/ψ mass window is of ± 0.12 GeV around the nominal mass value $m_{J/\psi=3.0969}$ GeV, and no mass fits are conducted for the tag and probe method, because the background is considered negligible.

Due to the trigger requirements of the J/ψ trigger, additional selections are required, namely that the J/ψ has to be displaced, $\cos(\theta) > 0.91$, SV probability > 0.12 and vertex displacement uncertainty > 3 . In addition each muon is required to have $|\eta| < 1.45$.

In Fig. 7.19, the HLT + L1 efficiencies for the J/ψ trigger are illustrated for both data and MC, considering the p_T and η of the single muons, as well as the ΔR of the two muons.

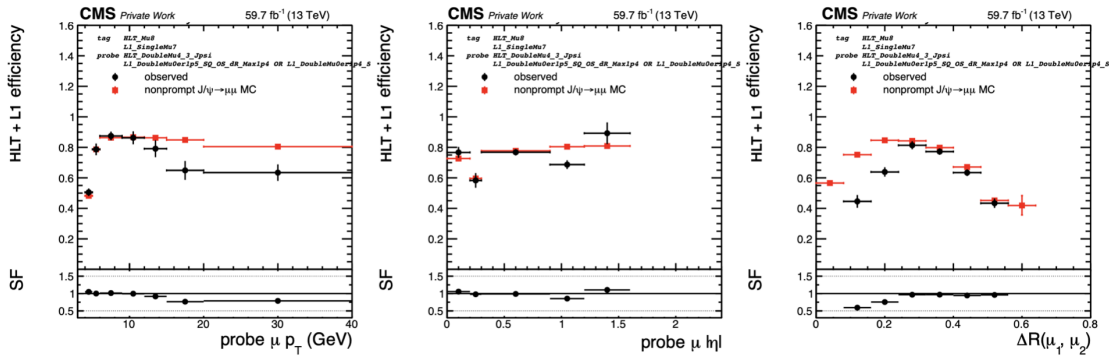


Figure 7.19: HLT + L1 efficiencies for the J/ψ trigger as a function of p_T and η of the single muons and ΔR for the two muons. The data distribution (black) is compared with the non-prompt J/ψ MC distribution (red).

The inefficiencies at high p_T and small ΔR are indicative of the same underlying effect and exhibit a perfect correlation. Hence, correcting p_T also will correct ΔR . As a result, the SF can be computed solely for p_T and η , extending the values at high η from the closest bins. These SFs are applied to each muon coming from the J/ψ , namely μ_1 and μ_2 .

To assess the validity of the assumption that the total efficiency can be represented as the product of J/ψ and μ_3 trigger efficiencies, a test was conducted using the recently computed J/ψ trigger efficiencies. In Fig. 7.20, the ΔR distribution for the MC sample is presented for three scenarios: in black, all events that pass the J/ψ part of the offline selection without any trigger requirement; in red, events

that in addition pass the J/ψ trigger; in blue, events with the efficiencies applied.

The blue and red distributions match in both shape and normalisation within the assigned uncertainty. This outcome serves as evidence supporting the validity of this factorisation assumption.

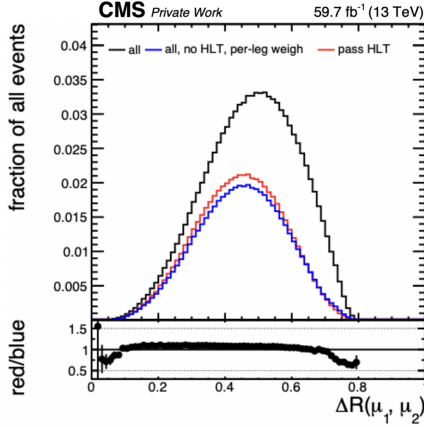


Figure 7.20: The ΔR distribution for the MC sample is examined in three scenarios. In black all events that fulfil the J/ψ part of the offline selection are included, without any trigger requirement. In red, events that in addition pass the J/ψ trigger. In blue events with the SF applied.

- μ_3 part

To finalise the trigger SF, a last step is required, which is to measure the HLT + L1 efficiency for the μ_3 part of the analysis trigger.

Four sets of trigger SF are computed for the third leg, one for each of the four categories used in the analysis for the third muon, Fig. 6.9, with respect to the ISO and ID requirements. A preselection is applied to ensure the reference trigger and offline analysis selections are satisfied. The tag muon is required to pass the J/ψ trigger described earlier, and the probe muon the final analysis trigger. In Fig. 7.21 the HLT efficiencies in the first region are shown.

The final SFs for the μ_3 part are finally computed for each region and applied to the respective μ_3 candidates.

The influence of the trigger SFs on the $R(J/\psi)$ ratio is negligible. This is due to the perfect cancellation of overall normalisation effects in the ratio, which additionally are treated as free parameters in our fit. Consequently, the impact of SFs on normalisations is irrelevant.

Concerning the shape, as shown in Fig. 7.22, the q^2 distribution for the τ signal over the μ signal bin-by-bin ratio (assuming the SM prediction) is presented with

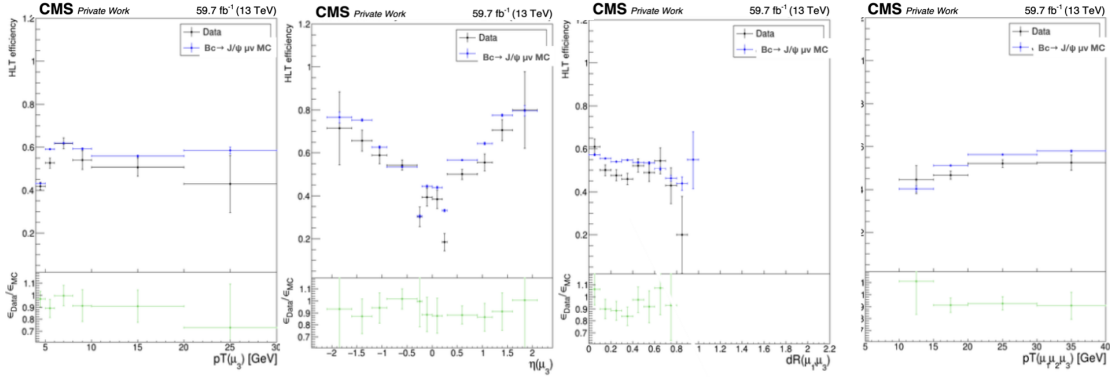


Figure 7.21: HLT efficiency for the μ_3 part of the analysis trigger, for the pass ISO and pass ID requirements (region A).

and without the trigger SFs. The shapes are found to be compatible, reaffirming the negligible effect of the trigger SFs on the final ratio. A final 5% uncertainty is added for each sample, to account for possible systematic effects.

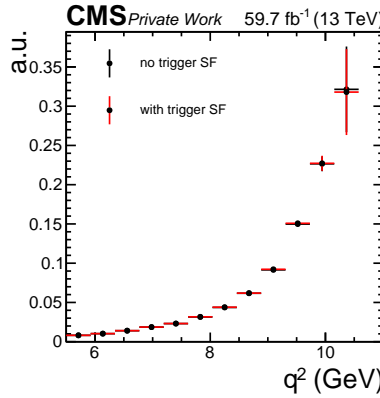


Figure 7.22: q^2 distribution for the τ signal over μ signal bin-by-bin ratio (assuming SM prediction). In blue the shape without applying the trigger SFs, in red the distribution with trigger SFs (both J/ψ and μ_3 part).

Chapter 8

Fit Strategy

To measure the $R(J/\psi)$ ratio, a binned maximum likelihood fit is performed, including all the signal and background processes. The fit employs the observables q^2 , IP3D_{sig} , $L_{xy,\text{sig}}$, and $m(3\mu)$, and uncertainties are integrated into the fit as nuisance parameters.

The overall normalisation for the B_c background contributions is allowed to float via a free parameter in the fit across all the categories. Therefore the correlation between the two signal processes is experimentally established by employing the same normalisation parameter. An independent normalisation parameter is attributed to the τ signal and is treated as the parameter of interest (POI), which corresponds to the $R(J/\psi)$ ratio.

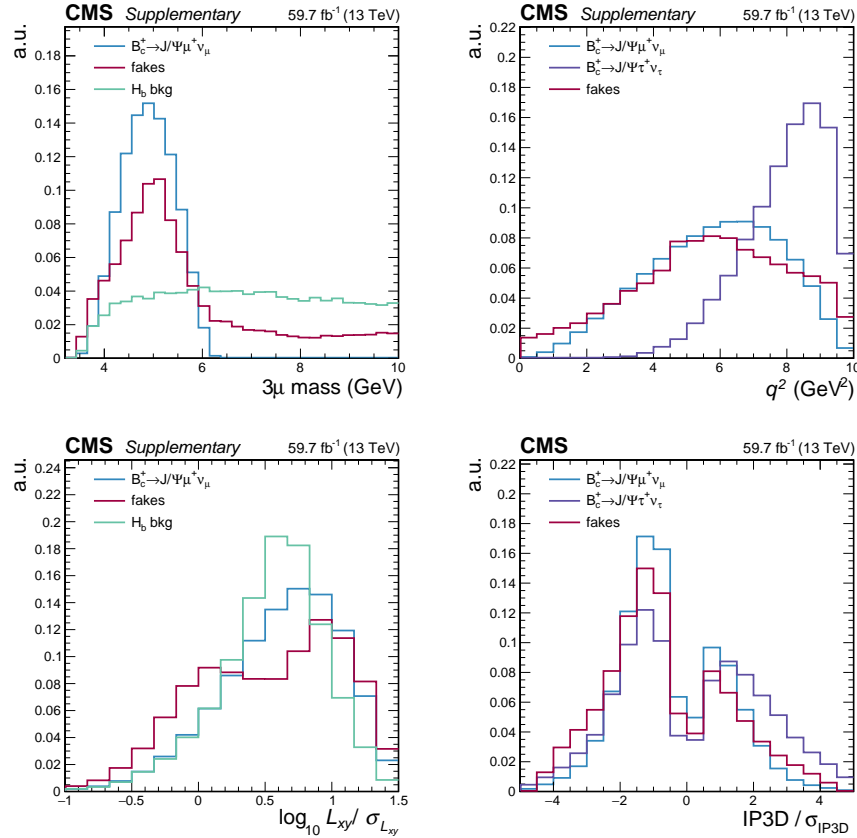
The normalisation for H_b backgrounds constitutes another free parameter in the fit, constrained to maintain correlation among different H_b contributions. In total, the fit includes 16 samples, including the two signals τ and μ . Sec. 8.1 explains the 7x2 categories defined to fit the $R(J/\psi)$ value and to constrain and measure the background contributions. Sec. 8.2 reports the details of the incorporation of the fakes background estimation in the fit model. The systematic uncertainties included in the fit are all described in Sec. 8.3, and the blinding strategy is explained in Sec. 8.4. Eventually, all the tests performed to validate the fit model strength and stability are shown in Sec. 8.5.

8.1 Definition of categories

Events are divided into 7 categories, each chosen to improve the sensitivity or constrain and measure the background contributions. The categorisation is based on the observables $m(3\mu)$, q^2 , and IP3D_{sig} . The fitted variables in these categories are either q^2 or $L_{xy,\text{sig}}$. A summary of the categories is found in Table 8.1 and the distributions of all the observables used in the fit are shown in Fig. 8.1.

Definition	Fit observable	Purpose
$m(3\mu) \leq 6.3 \text{ GeV} \& q^2 > 5.5 \text{ GeV} \& \text{IP3D}_{sig} \leq -2$	q^2	Measure τ -signal
$m(3\mu) \leq 6.3 \text{ GeV} \& q^2 > 5.5 \text{ GeV} \& -1 < \text{IP3D}_{sig} \leq 0$	q^2	Measure τ -signal
$m(3\mu) \leq 6.3 \text{ GeV} \& q^2 > 5.5 \text{ GeV} \& 0 < \text{IP3D}_{sig} \leq 2$	q^2	Measure τ -signal
$m(3\mu) \leq 6.3 \text{ GeV} \& q^2 > 5.5 \text{ GeV} \& \text{IP3D}_{sig} > 2$	q^2	Most sensitive category
$m(3\mu) \leq 6.3 \text{ GeV} \& q^2 < 4.5 \text{ GeV} \& \text{IP3D}_{sig} < 0$	$L_{xy,sig}$	constrain μ/B_c
$m(3\mu) \leq 6.3 \text{ GeV} \& q^2 < 4.5 \text{ GeV} \& \text{IP3D}_{sig} \geq 0$	$L_{xy,sig}$	constrain μ/B_c
$m(3\mu) > 6.3 \text{ GeV}$	$L_{xy,sig}$	constrain H_b bkg

Table 8.1: Table that summarises the 7 categories defined for the fit model.

Figure 8.1: Shape comparison of τ -signal (purple), μ -signal (blue), fakes background (red) and H_b background (teal) for the $m(3\mu)$ (top left), q^2 (top right), $L_{xy,sig}$ (bottom left) and IP3D_{sig} (bottom right) observables.

The observable $m(3\mu)$ is categorised based on the B_c meson mass, $m_{B_c} = 6.3$ GeV, leading to the following selections:

- High Mass (HM): $m(3\mu) \geq 6.3 \text{ GeV}$;

- Low Mass (LM): $m(3\mu) < 6.3$ GeV.

In the HM region, there is no contribution from the B_c MC sample because the invariant mass of the three muons in the final state has to exceed the mass of the B_c meson. This makes the HM region ideal for controlling the normalisation of the H_b background, with the fakes background being the other significant contributor. With only these two residual processes in the HM region, it becomes crucial to fit an observable that provides clear discrimination between them. For this purpose, the variable $L_{xy}/\sigma_{L_{xy}}$ is chosen due to its distinct shapes for the two contributions. The prefit distribution of $L_{xy}/\sigma_{L_{xy}}$ in the HM category is shown in Fig. 8.2 on the left.

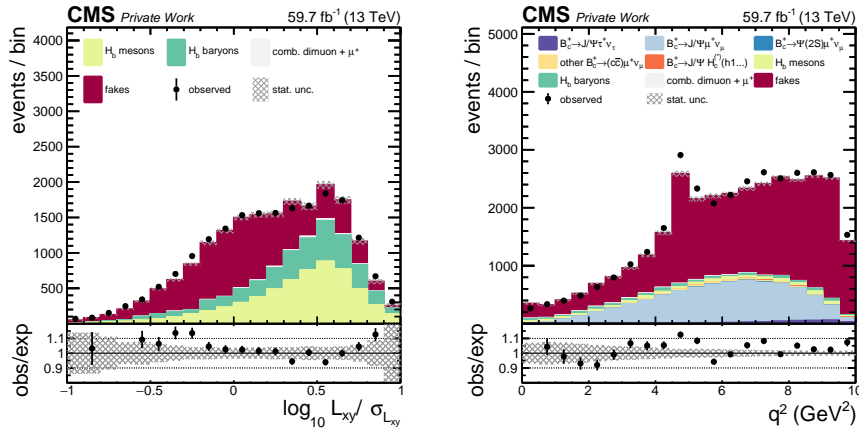


Figure 8.2: Prefit $L_{xy}/\sigma_{L_{xy}}$ distribution in the HM category (left). q^2 distribution for region C in the LM category (right).

A specific selection criterion is also applied to the q^2 variable:

- Low- q^2 (LQ2): $q^2 < 4.5$ GeV;
- High- q^2 (HQ2): $q^2 > 5.5$ GeV,

The range $4.5 \leq q^2 \leq 5.5$ GeV is excluded to eliminate the $B^+ \rightarrow J/\psi K^+$ background. This background is characterised by a distinct peak, making its exclusion straightforward, as illustrated in Fig. 8.2 on the right. This figure shows the q^2 distribution in the region failing the softMVA ID, where the peak is notably prominent.

It is useful to define the LQ2 region because there is no τ -signal, allowing for a more precise constrain of the μ -signal and the overall B_c normalisation. Conversely, the HQ2 region is enriched with τ -signal.

The IP3D_{sig} variable plays a crucial role in this analysis, as it significantly enhances the signal sensitivity. It differentiates between the μ and τ signals, and it is not correlated to the already employed q^2 observable as the other kinematic variables like m_{miss}^2 . For the μ signal, the impact parameter is expected to be more peaked near zero, whereas for the τ signal, it extends to higher values. The IP3D_{sig} variable plays also role in differentiating background contributions. It becomes instrumental in refining the analysis and enhancing the precision of the results.

The HQ2 category is split into four IP3D_{sig} categories, to enhance the signal-over-background ratio, particularly in the last category. The subcategories are defined as follows:

- $\text{IP3D}_{sig} \leq -2$
- $-2 < \text{IP3D}_{sig} \leq 0$
- $0 < \text{IP3D}_{sig} \leq 2$
- $\text{IP3D}_{sig} > 2$.

The q^2 distributions for these four IP3D_{sig} categories are shown in Fig. 8.3.

In the LQ2 region, the IP3D_{sig} variable plays a crucial role in decorrelating the normalisation of the fakes background from that of the B_c sample. In fact, by implementing a further categorisation based on the IP3D_{sig} variable, the analysis gains more insights into the relative abundances of these two contributions. Two distinct IP3D_{sig} regions are defined as:

- $\text{IP3D}_{sig} < 0$
- $\text{IP3D}_{sig} \geq 0$.

The prefit $L_{xy}/\sigma_{L_{xy}}$ distributions for the two IP3D_{sig} categories are shown in Fig. 8.4.

Fig. 8.5 presents a comprehensive summary of all the categories considered in this analysis. The fitting procedure includes a total of 7 categories. This categorisation ensures an accurate measurement of the background contributions, and an increase of the analysis sensitivity.

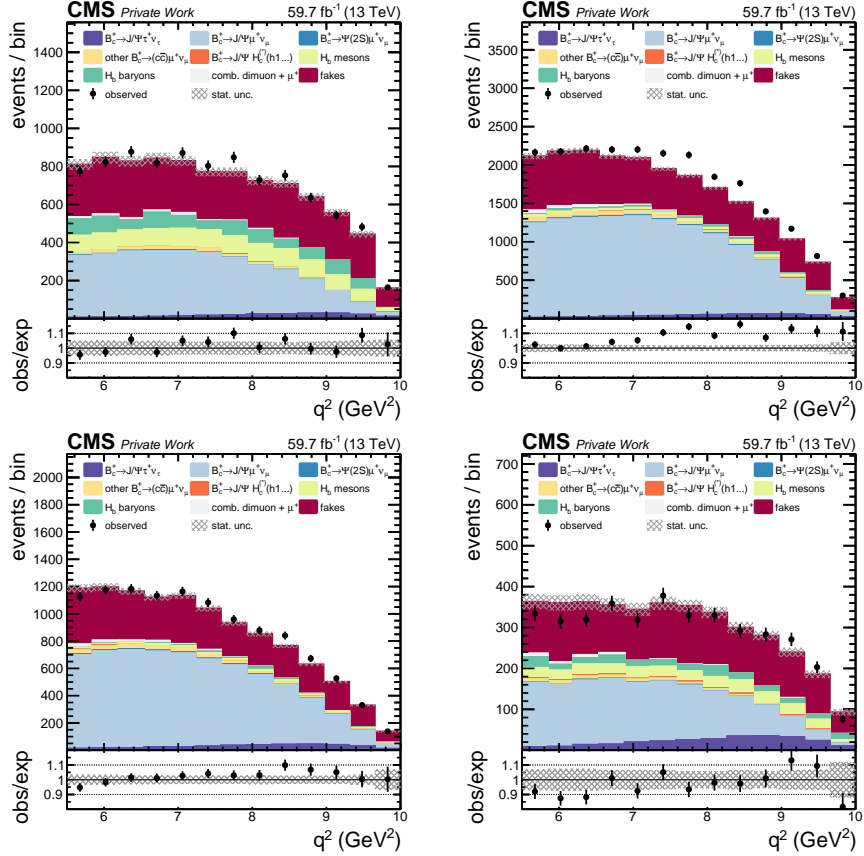


Figure 8.3: Prefit q^2 distributions for the HQ2 category split into four different $IP3D_{sig}$ categories: $IP3D_{sig} < -2$ (top left), $-2 < IP3D_{sig} \leq 0$ (top right), $0 < IP3D_{sig} \leq 2$ (bottom left) and $IP3D_{sig} > 2$ (bottom right). The τ -signal contribution here shown is an unknown value between 0.5 and 8 times the SM prediction, see Sec. 8.4.

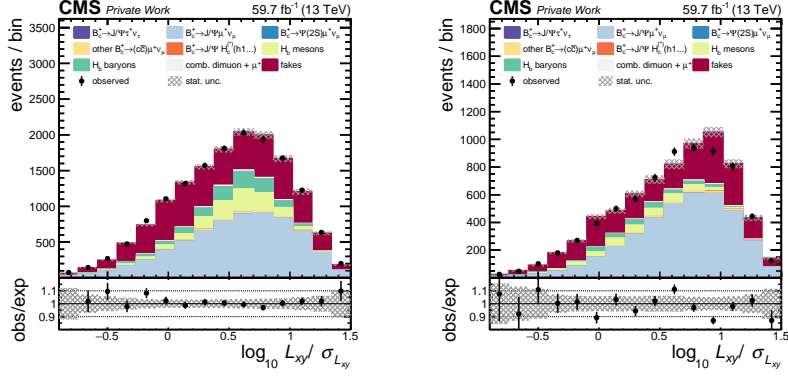


Figure 8.4: Prefit $L_{xy}/\sigma_{L_{xy}}$ distributions in the LQ2 region in the $IP3D_{sig} < 0$ category (top right). Prefit $L_{xy}/\sigma_{L_{xy}}$ distributions in the LQ2 region in the $IP3D_{sig} \geq 0$ category (bottom). The τ -signal contribution here shown is an unknown value between 0.5 and 8 times the SM prediction, see Sec. 8.4.

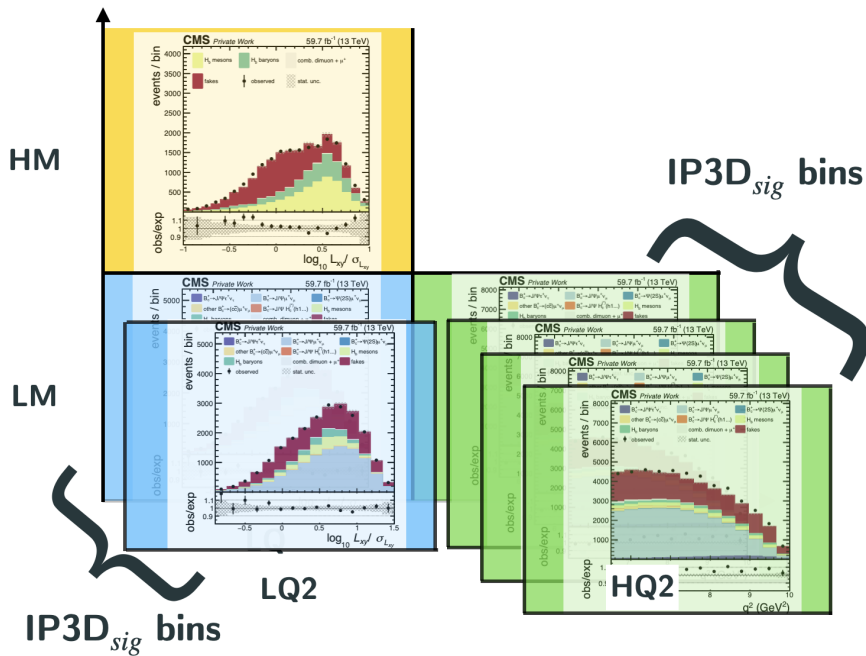


Figure 8.5: Summary of the analysis categories in $m(3\mu)$, q^2 and $IP3D_{sig}$ used for the fitting procedure.

8.2 Fakes background method implementation

Each of the 7 categories just described is splitted into two categories to allow the estimation of the fakes background during the fit. These two categories, defined in Sec. 6.3, are respectively:

- A: Pass ISO & Pass ID ($\Delta\beta_{corr,iso} < 0.2$ and pass softMVA ID);
- reweighted-B: Fail ISO & Pass ID ($\Delta\beta_{corr,iso} > 0.2$ and pass softMVA ID).

To accurately assess the fakes contribution in region A, it is in fact essential to incorporate the reweighted-B region. The latter is defined as the B region events reweighted using the $fr_{ISO}(x_i)$ weights derived from the fakes estimation method.

The normalisations of B_c and H_b samples are treated as floating parameters in the fit, and their shapes are allowed to dynamically evolve during the fitting process in response to associated systematic uncertainties. Consequently, discrepancies between data and MC in the reweighted-B region may undergo modifications during the fit, influencing the fakes shape in region A. Therefore, each bin of the fakes shape identified in the reweighted-B region is defined as a floating parameter in the fit, capable of compensating for the difference between data and MC samples in the reweighted-B region. In Fig. 8.6 a scheme illustrating how the two categories interact during the fit is shown.

Eventually the fit model includes a total of 7x2 categories.

8.3 Systematic uncertainties

This analysis takes into account various sources of systematic uncertainties, which are incorporated as nuisance parameters and profiled in the fitting process.

Detailed information about each systematic uncertainty, including its type (affecting either normalisation or shape), the samples it applies to, the affected regions, and any correlation between regions A and B, is reported in Table 8.2. The following sections outline each systematic uncertainty involved in this analysis, categorised by type. Each uncertainty is assigned a number corresponding to its respective row in the summary table.

8.3.1 Theoretical uncertainties

1. Systematic uncertainties associated with the B_c FF, detailed in Sec. 7.1, include 10 distinct shape contributions. They are exclusively applied to the two signal samples, and they are correlated between regions A and B. All the theoretical systematic uncertainty shapes are shown in Appendix 10.1.

Table 8.2: Table of systematic uncertainties used in the fit. The name of the systematic uncertainties, their type and at which sample they are applied are shown. Pass (fail) column is marked if the systematic is added in the pass (fail) isolation region. Eventually the last column indicates if the nuisance is correlated between pass and fail isolation regions. All systematic uncertainties are applied to all the categories defined in q^2 , $m(\mu_1\mu_2)$ and $IP3D_{sig}$, and are correlated.

Systematic	name in combine	type	$J/\psi\mu$	$J/\psi\tau$	$\chi c\psi\mu$	$\chi c\psi\mu$	$\chi c\psi\mu$	$h\psi\mu$	$J/\psi h\chi$	$\psi(2S)\mu$	$\psi(2S)\tau$	B^0	B^+	B_s^0	Σ_b^{*-0}	Ξ_b^-	A_b^0	fakes	comb J/ψ	A	B	corr
1 form factor	bgvar_z(\#sys)	shape	X	X															X	X	yes	
2 fakes normalisation	fake_rate	lnN																	X			
3 fakes bins (one for each bin)	fakes_bin\#	rateParam																	X			
4 fakes method	fakesmethod	shape																	X			
5 fakes shape	fakesshape	shape																	X			
6 fakes stat (one for each bin)	fakes_stat_bin\#ch\#	shape																	X			
7 pileup weights	puWeight	shape	X	X	X	X	X	X	X	X	X	X	X	X	X	X	X	X	X	X	yes	
8 B_c MC correction	bccorr	shape	X	X	X	X	X	X	X	X	X	X	X	X	X	X	X	X	X	X	yes	
9 B_c decay time	ctau	shape	X	X	X	X	X	X	X	X	X	X	X	X	X	X	X	X	X	X	yes	
10 IP3D _{sig} correction	ip3d_corr_anc	shape	X	X	X	X	X	X	X	X	X	X	X	X	X	X	X	X	X	X	yes	
11 $L_{jet,sys}$ correction	jetvar_corr_unc	shape																	X			
12 SF Reco A	sfReco	lnN	3.1%	3.0%	2.7%	2.9%	3.0%	4.1%	3.2%	2.8%	2.2%	2.9%	2.9%	2.9%	2.9%	2.9%	2.9%	2.9%	X		yes	
13 SF Reco B	sfReco	lnN	2.6%	2.6%	2.6%	2.6%	2.6%	2.6%	2.6%	2.6%	2.6%	2.6%	2.6%	2.6%	2.6%	2.6%	2.6%	2.6%	X		yes	
14 SF MediumID A	sfDijpsi	lnN	2.7%	2.7%	2.6%	2.7%	4.1%	2.9%	2.6%	2.6%	2.4%	2.6%	2.8%	2.8%	2.8%	2.8%	2.8%	2.8%	X		yes	
15 SF MediumID B	sfDijpsi	lnN	2.6%	2.6%	2.6%	2.6%	2.5%	2.5%	2.6%	2.5%	2.8%	2.6%	2.6%	2.6%	2.6%	2.6%	2.6%	2.6%	X		yes	
16 SF SoftMvaID	sfDtk	lnN	3%	3%	3%	3%	3%	3%	3%	3%	3%	3%	3%	3%	3%	3%	3%	3%	X		yes	
17 SF iso	sfIso	lnN	3%	3%	3%	3%	3%	3%	3%	3%	3%	3%	3%	3%	3%	3%	3%	3%	X		no	
18 SF trigger	trigger	lnN	5%	5%	5%	5%	5%	5%	5%	5%	5%	5%	5%	5%	5%	5%	5%	5%	X		yes	
19 BR $\chi_c 0\mu$	br_ch0l0over_mu	lnN																	X		yes	
20 BR $\chi_c 1\mu$	br_ch1l0over_mu	lnN																	X		yes	
21 BR $\chi_c 2\mu$	br_ch2l0over_mu	lnN																	X		yes	
22 BR $h\psi\mu$	br_hpsi0over_mu	lnN																	X		yes	
23 BR $J/\psi h\chi$	br_jpsi0over_mu	lnN																	X		yes	
24 BR $\psi(2S)\mu$	br_psi2s0over_mu	lnN																	X		yes	
25 BR $\psi(2S)\tau$	br_psi2s0tau_over_mu	lnN																	X		yes	
26 B_c not-yet measured decays	missing_mc	shape																	X		yes	
27 norm B^0 (H_b bkg)	psimother_l0zero	lnN																	X		yes	
28 norm B_s^+ (H_b bkg)	psimother_l0plus	lnN																	X		yes	
29 norm B_s^0 (H_b bkg)	psimother_l0zero_s	lnN																	X		yes	
30 norm Σ_b^{*-0} (H_b bkg)	psimother_sigma	lnN																	X		yes	
31 norm Ξ_b^{*-0} (H_b bkg)	psimother_xi	lnN																	X		yes	
32 norm A_b^0 (H_b bkg)	psimother_lambdaZero_b	lnN																	X		yes	
33 Comb J/ψ dimuon norm	dimuon_norm	lnN																	X		yes	
34 MC stat fail (one for each bin)	bbb(\#bin) fail	shape																	X		yes	
35 MC stat pass (one for each bin)	bbb(\#bin) pass	shape																	X		yes	

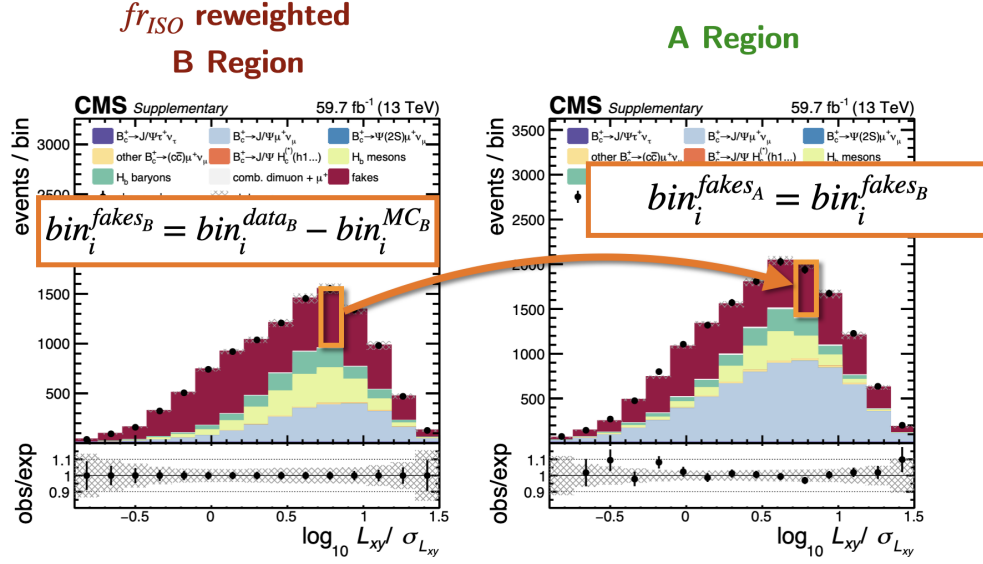


Figure 8.6: This scheme illustrates the fakes estimation process during the fit. It depicts how the fakes background bins, identified in the reweighted-B region through the subtraction of MC from data contributions, are subsequently utilised as nominal fakes bins in the A region.

8.3.2 Fakes background uncertainties

2. A systematic uncertainty of 13% is attributed to the normalisation of the fakes background. This specific uncertainty comes from the observed non-closure of yields in the closure test described in Sec. 6.3.4.1.
3. A free floating parameter is assigned to each bin of the fakes background. This approach is a direct consequence of the methodology used for estimating the fakes background, as described in Sec. 8.2. The inclusion of this parameter accounts for both statistical and systematic effects coming from other contributions that impact the fakes background bins during the fitting process.
4. Systematic uncertainty that comes from the method employed to determine the fakes background. The nominal approach, referred to as the “nominal” method, is complemented by an alternative one, called the “rotated” method. This alternative approach is described in Sec. 6.3.5.2. Due to the differences between these two methodologies, a single systematic uncertainty is applied to account for the variations in the fakes background estimation they produce.

5. A systematic uncertainty on the shape of the fakes background is introduced due to fluctuations in the various MC samples normalisations. As explained in Sec. 6.3, deriving the fakes shapes includes calculating three sets of weights. Notably, the $\alpha(x_i)$ weights depend on the prefit normalisation of the MC samples, as they are defined as $\alpha(x_i) = \frac{MC(D)}{data(D)}$. A second order effect is also present in the $TF_{MC}(x_i)$ weights, because, being defined as $TF_{MC}(x_i) = \frac{MC(C)}{MC(D)}$, they depend on the relative normalisation of the two MC samples. Since MC normalisations in the fit are treated as floating parameters, even if constrained by category definition, the shape of the fakes background in region A is expected to adjust in response to changes in the normalisation of the B_c and H_b samples. Such changes would modify the event-by-event weights applied to region B, which can not be directly incorporated into the fit. Therefore a conservative shape systematic uncertainty is introduced, which accounts for a 10% variation (both upward and downward) in the B_c sample normalisation. This decision is also supported by the observation that the nominal B_c normalisation aligns with the final fitted normalisation. The resulting shape-systematic uncertainty is shown in Fig. 8.7. Other MC changes during the fit have been studied, but their contribution is negligible to the final fakes shape, see Appendix 10.2.

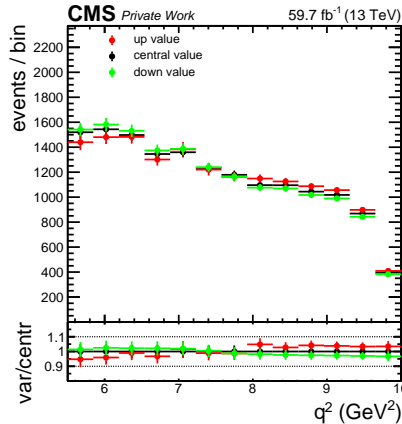


Figure 8.7: Up and down shape uncertainty for the fakes background to take into account a possible 10% change in the normalisation of the B_c MC samples during the fit.

6. Systematic uncertainties are assigned to each bin of the fakes shape in this analysis. These uncertainties are calculated as the square root of the sum in quadrature of two distinct bin-by-bin uncertainties related to the fakes shape. The first component of this uncertainty is 5% (both upward and downward) for each bin. This comes from the limited statistics available for the NN

training, as elaborated in Sec. 6.3.5.3. The second component, around 10% uncertainty, originates from the validation of the fakes method on data, which is detailed in Sec. 6.3.4.2 and shown in Fig. 6.23.

8.3.3 Uncertainties on the MC corrections

7. A systematic uncertainty to account for the pileup correction, detailed in Sec. 7.2, is added. The MC samples are reweighted to have the same number of primary vertices per event as in data. The weights and the uncertainties are computed comparing the distribution of PV number as measured in UL 2018 data and MC. The uncertainties are added as shape nuisances in the fit, as shown in Fig. 8.8.

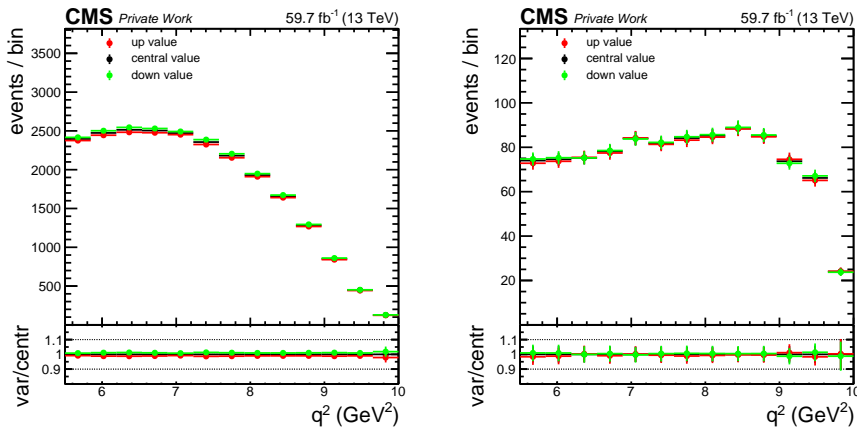


Figure 8.8: Up and down q^2 -shape uncertainties for the pileup systematic uncertainty for the μ signal sample (left) and the $B^+ \rightarrow J/\psi + \mu$ sample from H_b (right).

8. Systematic uncertainties associated with MC corrections are applied to all B_c MC samples, addressing potential kinematic mismodelings. The sPlots method is utilised to derive a slope, which is then used to quantify the uncertainty related to the B_c meson due to kinematic mismodeling. A signal μ MC sample, produced without MC filters, is employed to compute the up (down) weights by shifting the B_c meson p_T up (down) according to the computed slope. The ratio of the nominal p_T to the shifted one is taken as the distribution for the up (down) weights. Subsequently, these weights are assigned to each event in the B_c MC samples, and an up and down shape variations are defined for each B_c sample. An example for the two signals is shown in Fig. 8.9.
9. B_c decay-time systematic uncertainties are applied to all the B_c MC samples,

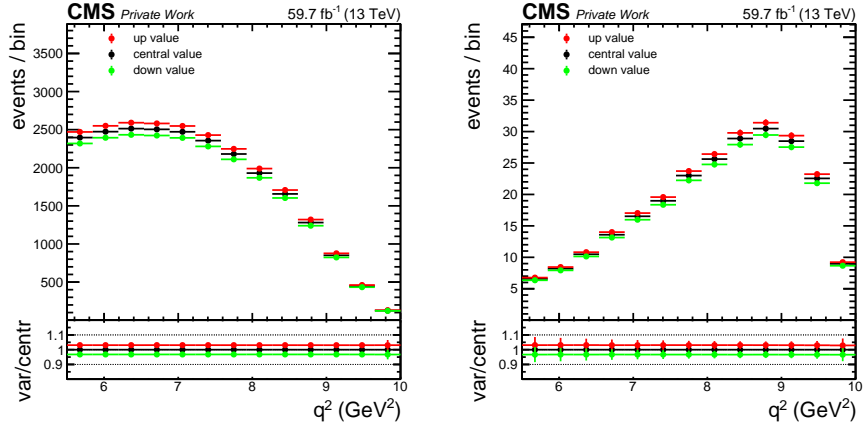


Figure 8.9: μ and τ signals shape uncertainties for the B_c kinematic mismodeling in region A.

to account for the uncertainties coming from the lifetime corrections of B_c explained in Sec. 7.3.2.

10. As described in Sec. 7.4.1, this analysis includes a correction to the $IP3D_{sig}$ variable, to which a specific systematic uncertainty is also applied. The upward shape variations are defined by applying a 1.1 dilation factor to the $IP3D_{sig}$ value, while the downward shape variations correspond to the original MC shapes, hence using a correction factor of 1.0. Given the role of the $IP3D_{sig}$ variable in categorising events within the HQ2 and LQ2 regions, any shape uncertainty associated with this variable leads to potential bin migration across these regions.

This shape uncertainty is applied to all MC samples used in the analysis and is correlated both between different samples and across categories. Fig. 8.10 shows examples of how this uncertainty can lead to bin migration across adjacent bins.

11. A systematic uncertainty for the correction applied to the $L_{xy,sig}$ variable, as detailed in Sec. 7.4.2, is included. This uncertainty is specifically introduced in the fit model for the regions where $L_{xy,sig}$ is a fitting variable, namely the LQ2 and HM regions. The up shape uncertainty for this variable is defined by applying a 1.2 correction factor to the MC samples, whereas the downward shape uncertainty is based on the original MC, with a correction factor of 1.0.

This systematic uncertainty is uniformly applied to all MC samples used in the analysis. Furthermore, it is correlated across all samples and categories

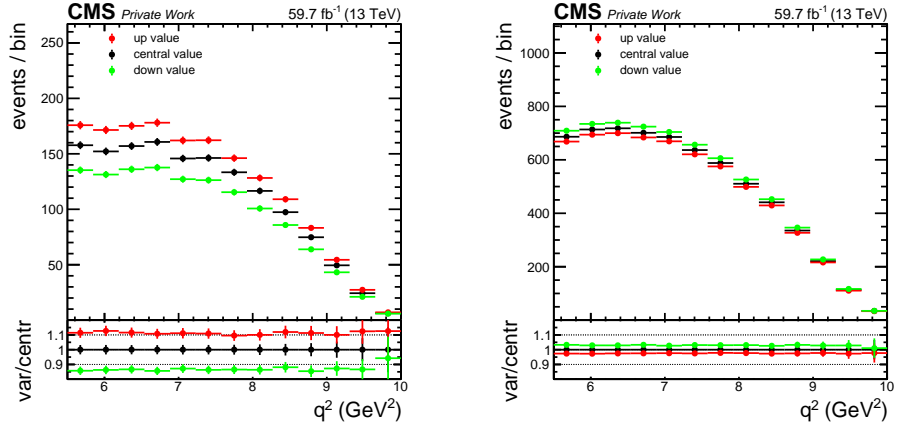


Figure 8.10: $IP3D_{sig}$ correction shape uncertainties applied on the q^2 variable in HQ2 region. The $B_c^+ \rightarrow J/\psi \mu^+ \nu_\mu$ sample distribution, in the HQ2 region, in the $IP3D_{sig} > 2$ bin (left) and $0 < IP3D_{sig} \leq 2$ bin (right). The two bins are adjacent, therefore the event migration due to the $IP3D_{sig}$ correction shape uncertainty is shown: the shape corresponding to the up value of the correction is in different position with respect to the nominal shape in the two plots.

where the $L_{xy,sig}$ variable plays a role in the fitting process. Fig. 8.11 provides several examples.

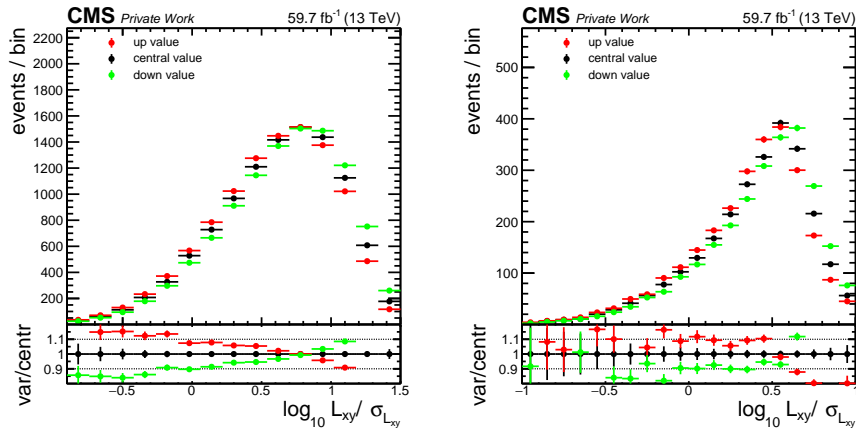


Figure 8.11: $L_{xy,sig}$ correction shape uncertainties. On the left the $B_c^+ \rightarrow J/\psi \mu^+ \nu_\mu$ sample, in the LQ2 region, on the right the $B^0 \rightarrow J/\psi \mu X$ distribution, in the HM region.

12–15. The analysis accounts for systematic uncertainties associated with the reconstruction and identification of the three final state muons. Specifically, the uncertainties to the SF for the reconstruction of all three muons and

the Medium ID for muons originating from the J/ψ are included in these uncertainties, which are estimated to be in the range of 2-4%.

16. A systematic uncertainty is incorporated in the analysis to account for the efficiency of the identification selection of the third muon μ_3 using the soft-MVA ID variable. The SF associated with this variable are detailed in Sec. 7.6.1.
17. The efficiency of the isolation criterium chosen for μ_3 is accounted for in the SF, described in Sec. 7.6.2. The uncertainties associated to this correction are anti-correlated between A and B regions, because of the regions definition.
18. Systematic uncertainties for the trigger SFs, described in Sec. 7.6.3, are also accounted for in the fit. After assessing whether to consider them as shape uncertainties, it is concluded that their effect is only on the normalisation. In fact a final 5% uncertainty on the normalisation is added for each sample, to account for possible systematic effects.

8.3.4 Other uncertainties

- 19–25. Systematic uncertainties due to the B_c BRs are included in the fit model. In order to have the most accurate predictions of these BR, many theoretical models and methods have been studied. Table 8.3 summarises some of these branching fraction predictions and their uncertainties for the semileptonic decays of the B_c^+ . A weighted average for each branching fraction can be extracted from the values listed in the table. Assuming that the predictions of each decay channel are not correlated, the weighted average can be computed through the least-squares procedure as described in Eq. 8.1: x_i and δx_i are the branching fraction value and its relative uncertainty coming from the i -th experiment and N represents the number of models:

$$\bar{x} = \frac{\sum_{i=1}^N w_i x_i}{\sum_{i=1}^N w_i}; \quad \delta \bar{x} = \sqrt{\frac{1}{\sum_{i=1}^N w_i}} \quad w_i = \frac{1}{(\delta x_i)^2}. \quad (8.1)$$

Results of this procedure are listed in Table 8.4. The normalised χ^2 values are not near 1. Even if the branching fraction predictions vary in a wide range, the relative errors of the weighted averages are small (3% - 7%) suggesting that the errors might have been underestimated and that the measurements are correlated.

Ref.	$J/\psi\mu^+\nu_\mu$	$\chi_{c0}\mu^+\nu_\mu$	$\chi_{c1}\mu^+\nu_\mu$	$\chi_{c2}\mu^+\nu_\mu$	$h_c\mu^+\nu_\mu$	$\psi(2S)\tau^+\nu_\tau$	$\psi(2S)\mu^+\nu_\mu$
[117]		0.19 ± 0.06		0.18 ± 0.05	0.34 ± 0.10	0.21 ± 0.06	
[118]	1.4 ± 04						
[119]	1.90 ± 0.06						0.11 ± 0.02
[120]	2.3 ± 0.7	0.17 ± 0.05		0.09 ± 0.03	0.17 ± 0.05	0.27 ± 0.07	
[121]	2.7 ± 0.8						
[122]	1.64 ± 0.27						
[123]	1.69 ± 0.09	0.23 ± 0.02		0.14 ± 0.07	0.29 ± 0.02	0.36 ± 0.04	
[124]	1.7 ± 0.5						
[125]	1.90 ± 0.19					0.011 ± 0.001	0.13 ± 0.01
[126]	2.30 ± 0.05						
[81]	2.2 ± 0.2					0.0080 ± 0.0008	0.094 ± 0.009
[127]	2.6 ± 0.5	0.36 ± 0.07		0.36 ± 0.07	0.36 ± 0.07		0.11 ± 0.02
[128]	2.53 ± 0.25						
[129]	1.5 ± 0.2						0.20 ± 0.02
[130]	1.7 ± 0.1						
[131]	1.44 ± 0.02	0.33 ± 0.03		0.11 ± 0.03	0.17 ± 0.04	0.17 ± 0.02	
[132]	1.90 ± 0.02	0.141 ± 0.007		0.116 ± 0.04	0.13 ± 0.01	0.305 ± 0.009	
[133]	2.24 ± 0.53						0.12 ± 0.01

Table 8.3: Branching fraction predictions (%) from different models

	$J/\psi\mu^+\nu_\mu$	$\chi_{c0}\mu^+\nu_\mu$	$\chi_{c1}\mu^+\nu_\mu$	$\chi_{c2}\mu^+\nu_\mu$	$h_c\mu^+\nu_\mu$	$\psi(2S)\tau^+\nu_\tau$	$\psi(2S)\mu^+\nu_\mu$
Avg(%)	1.73 ± 0.01	0.093 ± 0.004	0.068 ± 0.003	0.097 ± 0.006	0.164 ± 0.005	0.0053 ± 0.0004	0.068 ± 0.003
χ^2_{Norm}	28	12	3	12	11	5	5

Table 8.4: Branching fractions weighted averages (Avg) and normalised χ^2 (χ^2_{Norm}) for the semileptonic decays of the B_c^+ .

Two more conservative procedures can be implemented following the PDG [134]. If it's clear that $\chi_{Norm}^2 > 1$ means that some uncertainties have been underestimated, it is less clear which models underestimated the uncertainty. Assuming that every uncertainty is underestimated by the same factor, a possible solution is to scale each of them by a factor S , given by:

$$S = \sqrt{\frac{\chi^2}{N-1}} \quad (8.2)$$

This results in $\delta x'_i = S \cdot \delta x_i$, meaning that the average $\delta \bar{x}'$ will be scaled by the same factor and the normalised χ^2 will become 1. This procedure includes all the N measurements.

The models listed in Table 8.3 have mean values and uncertainties that vary over a wide range. Alternatively, it is possible to discard measurements with an uncertainty greater than a fixed cutoff. Following the PDG, a reasonable cutoff can be $\delta_0 = 3\sqrt{N}\delta\bar{x}$: measurements with an uncertainty $\delta x_i > \delta_0$ are then discarded. Since measurements with a big uncertainty do not affect much \bar{x} and $\delta\bar{x}$, but they may increase the χ^2 , it is possible to scale the uncertainties below the cutoff by a factor S' :

$$S' = \sqrt{\frac{\chi^2}{N'-1}} \quad (8.3)$$

where N' represents the number of measurements that have an uncertainty below the cutoff.

BR can be finally computed as the ratio between the branching fractions and the $B_c^+ \rightarrow J/\psi \mu^+ \nu_\mu$ branching fraction, used as normalisation factor. Results of the three different procedures to determine their uncertainties are summarised in Table 8.5.

Eventually the uncertainties derived in the first method are chosen to be used in the fit model, i.e. the scaled statistical uncertainties without the cutoff.

In addition to these systematic uncertainties, there is the one associated with the hadronic decays of the B_c^+ . The decay chains, the measurements and the weighted means are shown in Table 8.6. The parameter used in the fit is the branching ratio of the $B_c^+ \rightarrow J/\psi H_c$, where H_c is a charmed hadron. The mean value and its relative error can be extracted from the linear sum of each component described in Table 8.6. The weighted mean is used as the central value for the channels that have been measured from different experiments.

By summing up the components listed above, it is possible to get $\frac{BR(J/\psi H_c)}{BR(J/\psi \mu)} = 0.55 \pm 0.21$, which means a relative uncertainty of about 38%

Systematic	Mean Value (%)	Stat. unc.	Scaled stat. unc.	Scaled stat. unc. with cutoff
$\overline{BR}(\chi_{c0}\mu)$	0.093	4%	16%	24%
$\overline{BR}(J/\psi\mu)$	0.068	4%	10%	6%
$\overline{BR}(\chi_{c1}\mu)$	0.068	6%	22%	24%
$\overline{BR}(J/\psi\mu)$	0.097	3%	15%	16%
$\overline{BR}(\chi_{c2}\mu)$	0.164	7%	15%	17%
$\overline{BR}(J/\psi\mu)$	0.0053	5%	13%	14%
$\overline{BR}(\psi(2S)\tau)$				
$\overline{BR}(J/\psi\mu)$				
$\overline{BR}(\psi(2S)\mu)$				
$\overline{BR}(J/\psi\mu)$				

Table 8.5: Results of the weighted average for the branching fractions of the semileptonic decays of the B_c^+ and the three different treatments of their uncertainties.

Decay Channel	Ref.	Mean Value	Error
$J/\psi D_s^+$	[135]	0.14	0.04
	[136]	0.13	0.02
	Weighted Mean	0.132	0.018
$J/\psi D_s^{*+}$	[135]	0.3	0.2
	[136]	0.25	0.05
	Weighted Mean	0.252	0.049
$J/\psi D^0 K^+$	[91]	0.020	0.009
$J/\psi D^{0*} K^+$	[91]	0.1	0.008
$J/\psi D^{*+} K^{*0}$	[91]	0.04	0.04
$J/\psi D^+ K^{*0}$	[91]	0.01	0.01

Table 8.6: Branching fraction measurements (%) from different experiments

26. Systematic uncertainty on the $B_c \rightarrow J/\psi + H_c$ and $B_c \rightarrow J/\psi + H_c + h1$ (with $h1$ being an hadron different from H_c) samples are incorporated in the fit to address the impact of not-yet-measured B_c decays. The study performed on not-yet-measured decays has been described in Sec. 7.3.3. These decays can be accounted for in the analysis adding shape and normalisation systematic uncertainties on the B_c MC samples.

The B_c decays into a charmed hadron (c-hadron), that are already included in the MC dataset, are categorised into two distinct subgroups:

- The $B_c \rightarrow J/\psi H_c$ sub-sample includes:
 - $B_c \rightarrow J/\psi D_s$;
 - $B_c \rightarrow J/\psi D_s^*$;
 - $B_c \rightarrow J/\psi D^+$;
 - $B_c \rightarrow J/\psi D^{*+}$.

- The $B_c \rightarrow J/\psi H_c$ h1 sub-sample contains:
 - $B_c \rightarrow J/\psi D^+ K^{0*}$;
 - $B_c \rightarrow J/\psi D^0 K^+$;
 - $B_c \rightarrow J/\psi D^{*0} K^+$;
 - $B_c \rightarrow J/\psi D^{*+} K^{0*}$.

The q^2 distributions of these two sub-samples are shown in Fig. 8.12.

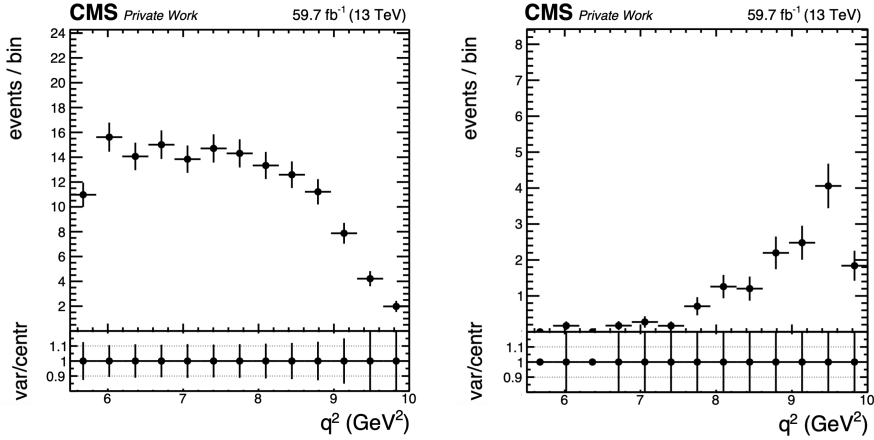


Figure 8.12: q^2 distributions for the $B_c \rightarrow J/\psi H_c$ (left) and $B_c \rightarrow J/\psi H_c$ h1 (right) samples. The normalisation is the same used in the prefit plots.

To approximate the deviation of the existing decay shapes to those of the not-yet-measured B_c decays, a hyperbolic tangent function is employed. The formula for the complete correction applied to the q^2 variable is given by:

$$x \cdot [1 + p_0 \cdot [1 - \tanh(p_1 \cdot x - p_2)]] . \quad (8.4)$$

The chosen parameters for this function are $p_0 = 0.2$, $p_1 = 0.53$, and $p_2 = 4$, as they provide the best approximation to the shape characteristics of the not-yet-measured decays. The impact of this shape shift is shown in Fig. 8.13. This figure compares the adjusted shapes of the existing decays with those of the not-yet-measured decays, highlighting the accuracy of the approximation.

Given the good agreement of the approximation, the chosen function is utilised to estimate the new shapes for the not-yet-measured decays. However, as these decays have not been experimentally measured yet, several approximations are necessary to determine the yield:

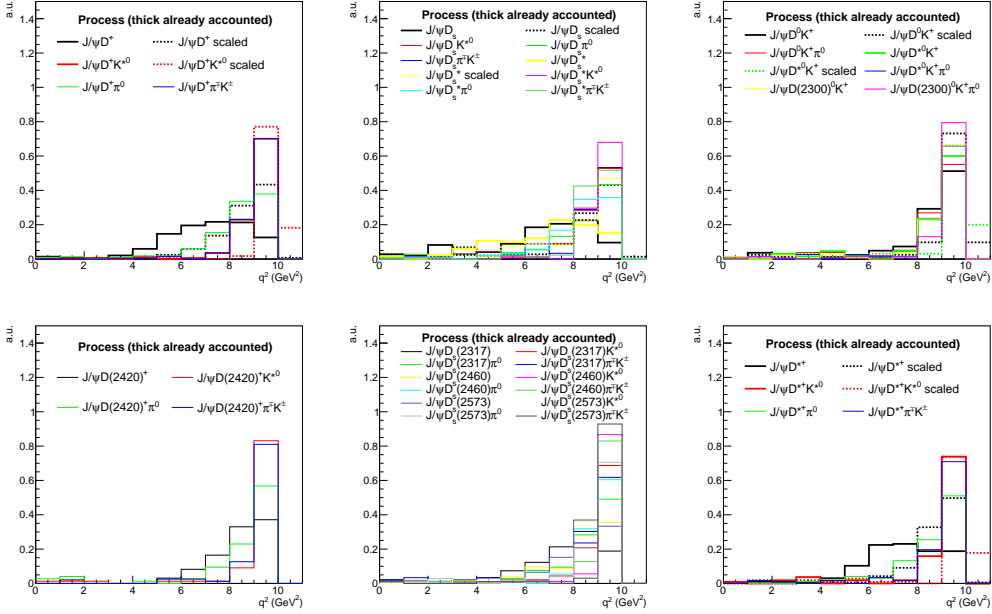


Figure 8.13: q^2 distributions for the decays in the B_c MC sample (thick lines) and the not-yet-measured ones (non-thick lines). The shapes of the already measured decays are scaled (thick dashed) using Eq. (8.4). The dashed shapes well approximate the non-thick lines.

- The ratio of branching fractions $\frac{\mathcal{B}(B_c^+ \rightarrow D_s^0 \pi^0)}{\mathcal{B}(B_c^+ \rightarrow D_s^0 D_s)}$ is assumed to be analogous to $\frac{\mathcal{B}(B_c \rightarrow J/\psi D_s \pi^0)}{\mathcal{B}(B_c \rightarrow J/\psi D_s)}$.
- The ratio $\frac{\mathcal{B}(B_c^+ \rightarrow D_s^0 (\#))}{\mathcal{B}(B_c^+ \rightarrow D_s^0 D_s)}$ is used as abundance ratio also between $D_s(\#)$ and D_s in the B_c decays.
- Cabibbo suppressed processes are estimated to have a BR of 10% compared to the non-Cabibbo suppressed ones.

Regarding the last point, the $b \rightarrow c\bar{c}s$ transitions are not CKM suppressed, while the $b \rightarrow c\bar{c}d$ ones are. Based on these assumptions, an additional normalisation up to 14% is added for the $B_c \rightarrow J/\psi H_c$ sample, and up to 34% for the $B_c \rightarrow J/\psi H_c$ h1 sample, to accommodate the not-yet-measured decays. These normalisation approximations do not account for the phase space, making the estimations here presented conservative.

With these approximations in place, the not-yet-measured decays now have estimated shapes and normalisations, and are added in the analysis. Using the “old” central values as baselines, in Fig. 8.12, the “max” shifts derived

from these studies are computed and presented in Fig. 8.14.

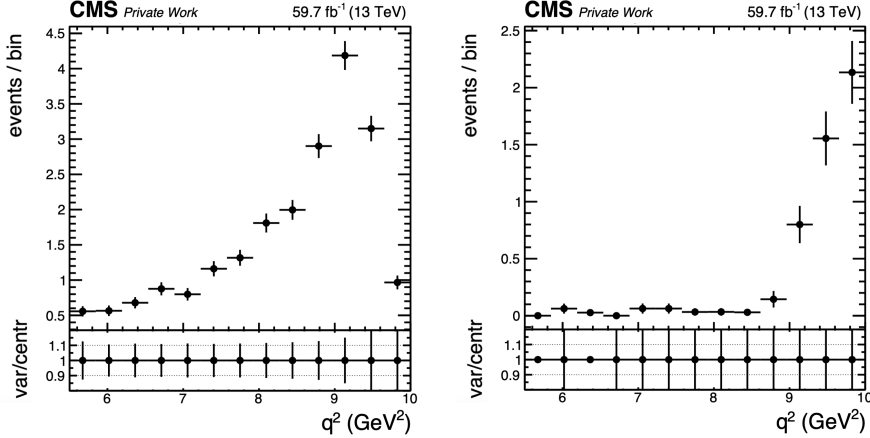


Figure 8.14: q^2 distributions for the $B_c \rightarrow J/\psi H_c$ (left) and $B_c \rightarrow J/\psi H_c h1$ (right) samples shifted with the function in Eq. 8.4, to approximate the shape of the not-yet-measured B_c decays. The normalisation for these distributions is 14 % of the $B_c \rightarrow J/\psi H_c$ (left) and 34% of $B_c \rightarrow J/\psi H_c h1$ (right), as described in the text.

Eventually, the shape systematic uncertainty and the new central values are defined for $B_c \rightarrow J/\psi H_c$ and $B_c \rightarrow J/\psi H_c h1$ sub-samples as:

- **Up Shape:** This is calculated by combining the “old” shape, as shown in Fig. 8.12, with the “max” shift shown in Fig. 8.14.
- **Central Value:** The central value is determined by taking the “old” shape (Fig. 8.12) and adding half of the “max” shift (Fig. 8.14).
- **Down Shape:** The down shape variation corresponds to the “old” shape, as illustrated in Fig. 8.12.

In Fig. 8.15 the final shape uncertainties are shown.

Incorporating these shape uncertainties ensures that the $B_c \rightarrow J/\psi H_c$ and $B_c \rightarrow J/\psi H_c h1$ processes now effectively account for the not-yet-measured B_c decays. Consequently, both the normalisation and the shape of these processes can be adjusted during the fitting process. This shape systematic uncertainty has been computed specifically for the q^2 variable but, in parallel, a consistent normalisation uncertainty has been introduced for the same processes also for $L_{xy}/\sigma_{L_{xy}}$ variable, employed as fitting variable in some control categories (e.g. HM and LQ2).

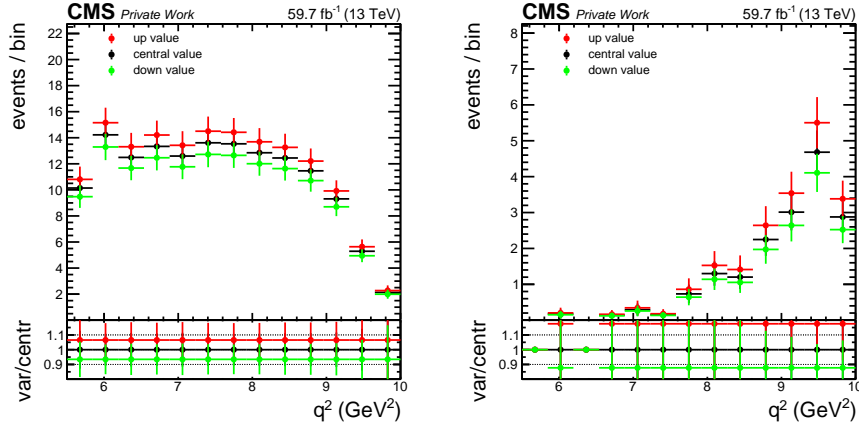


Figure 8.15: q^2 distributions for the $B_c \rightarrow J/\psi H_c$ (left) and $B_c \rightarrow J/\psi H_c h1$ (right) samples shifted with the function in Eq. 8.4, to approximate the shape of the not-yet-measured B_c decays. The normalisation for these distributions is 14 % of the $B_c \rightarrow J/\psi H_c$ (left) and 34% of $B_c \rightarrow J/\psi H_c h1$ (right), as described in the text.

27–32. Systematic uncertainties on the normalisations of the H_b background samples are included in the fit model. The H_b MC sample is composed of several decays from different b -hadrons, as explained in Sec. 5.2.2, therefore conducting a study on the uncertainties similar to that for the B_c MC is not feasible. A systematic uncertainty of 10% is assigned to the normalisation of each H_b decay within the sample.

33. A 20% systematic uncertainty on the normalisation of the combinatorial J/ψ dimuon background, described in Sec. 6.4, is included.

34–35 Bin-by-bin systematic uncertainties are introduced for regions A and B, focusing on the H_b background, which is characterised by relatively lower statistics. The explicit inclusion of these uncertainties in the fitting process is necessary for technical reasons related to the fitting tool. As mentioned in Sec. 6.1, the H_b background is categorised into different decay modes. To simplify the fitting process, the bin-by-bin uncertainties are assessed for each decay mode separately. Notably, the B^+ , B^0 , and B_s^0 decays exhibit minimal impact from statistical uncertainty. Consequently, only the Σ , Ξ , and Λ_0 decays are considered for this systematic uncertainty.

To further decrease the number of bin-by-bin systematic uncertainties, a composite uncertainty for each bin is computed using the formula:

$$err_i = \sqrt{(\Sigma_i^{err})^2 + (\Xi_i^{err})^2 + (\Lambda_i^{err})^2}.$$

The bin-by-bin uncertainty is then assigned only to the sample with the highest statistical uncertainty in each bin.

8.4 Blind strategy

The blinding strategy employed in this analysis involves multiple stages. Initially, both the postfit plots and the postfit comparison plots between data and overall MC have not been examined. Ultimately, given that the final result of the fit is the $R(J/\psi)$ value, this specific value has been masked to ensure unbiased analysis.

The B_c MC sample is generated setting the $R(J/\psi)_{prefit}$ value to $R(J/\psi)_{prefit} = 1$, as detailed in Sec. 5.2.1. The blinding strategy involves multiplying this number by an unknown random factor, R , ranging between 0.125 and 2 (equivalent to 0.5 to 8 times the SM prediction): $R(J/\psi)_{blind} = r_{fit} * R$. This value was chosen blindly at the beginning and has remained unchanged throughout the development of the analysis. This ensures that the outcome of the fit, represented by r_{fit} , diverges from the true $R(J/\psi)$ value.

The unblinding process was performed in stages and the results presented in Ch. 9 is the output derived from this unblinding procedure.

8.5 Fit diagnostics

8.5.1 Expected sensitivity

An Asimov dataset [137] is created by replacing real data with pseudodata that matches the sum of the expected contributions. The key characteristic of an Asimov dataset is that the maximum likelihood best-fit values for all the parameters align with their generated values. The event count in each bin is set to the expected event yield calculated for the chosen model parameters. This construction allows for the simulation of a dataset that mirrors the expected behaviour according to the specified model.

The expected value is set to be the result from the previous LHCb measurement $R(J/\psi) = 0.71$ [78]. Using the fit model described in the previous sections, the Asimov fit has a result of $R(J/\psi) = 0.71_{-0.28}^{+0.30}(Syst)_{-0.16}^{+0.17}(Stat) = 0.71_{-0.33}^{+0.34}$.

Fig. 8.16 displays the likelihood scan for the fitted $R(J/\psi)$ value from the Asimov fit. The uncertainty is divided into three distinct contributions: solely statistical uncertainty (dashed blue), statistical plus theoretical uncertainty (dashed red), and the total uncertainty (black). The result, with this separation, is $R(J/\psi) = 0.71_{-0.16}^{+0.17}(Stat)_{-0.18}^{+0.19}(Theo)_{-0.22}^{+0.22}(Syst)$.

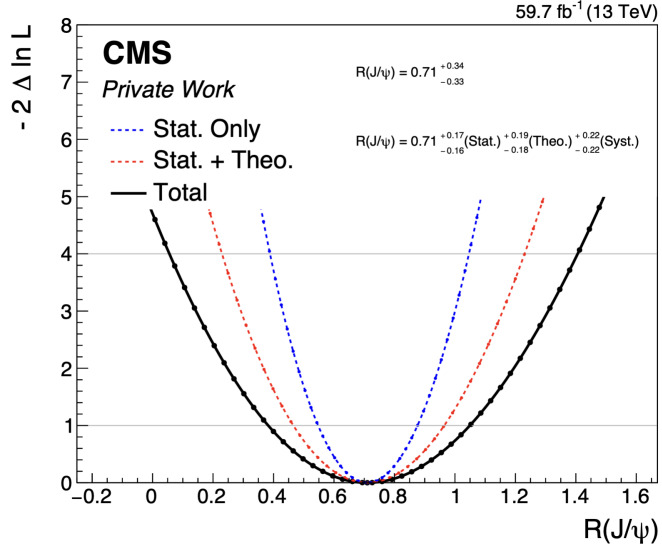


Figure 8.16: Likelihood scan for the $R(J/\psi)$ result of the Asimov fit, assuming the LHCb result as expected value: only statistical uncertainty (dashed blue), statistical plus theoretical uncertainties (dashed red), and total observed sensitivity (black).

The Asimov fit can be computed for different expected values of the result, shown in Fig. 8.17, and in Appendix 10.3.

8.5.2 Blind fit to data

A fit to real data, incorporating the blinding procedure outlined in Sec. 8.4, is performed. Various diagnostic plots are generated to evaluate the fit quality.

Fig. 8.18 illustrates the post-fit values and impacts for the 30 most significant systematic uncertainties implemented in the fit model as nuisance parameters. The post-fit values and corresponding uncertainties are represented as $(\hat{\theta} - \theta_0)/\Delta\theta$, where θ_0 denotes the prefit value of the nuisance parameter θ , $\hat{\theta}$ its best-fit value, and $\Delta\theta$ indicates the 1σ prefit deviation. The coloured bands on the right side of the plot indicate the impact of the nuisance error on the error of the POI, expressed relative to the total error on the POI, i.e., $\Delta\hat{\mu}/\Delta\hat{\mu}_{\text{tot}}$.

Fig. 8.19 presents the goodness-of-fit (GoF) plots, which assess the compatibility of the observed data with the model. The evaluation involves generating hundreds of fake datasets, called toys, from the model, and their compatibility with the data is assessed using two algorithms: the **saturated** and KS tests. The **saturated** test also considers the difference between postfit and prefit values of the systematic uncertainties. Both tests collectively indicate a good quality of the

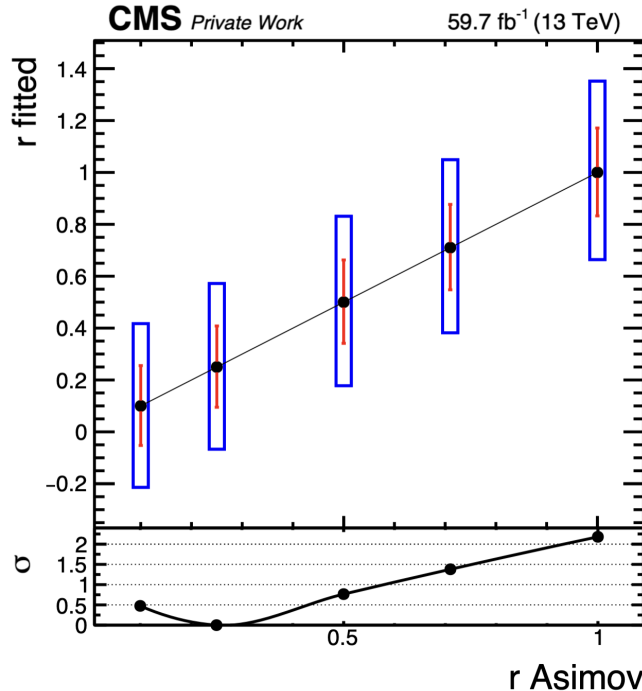


Figure 8.17: Signal injection plot. The Asimov fit is performed for different expected values of $R(J/\psi)$. The red bar indicates the statistical uncertainty of the measurement, while the blue one indicates the total uncertainty. In the ratio plot, the σ from the SM prediction is shown for each measurement.

fit.

8.5.3 Bias test

Two sets of toy models are generated, each with an expected signal value: one with r_{truth} set to the LHCb result of $R(J/\psi) = 0.71$, and the other with the SM prediction of $R(J/\psi) = 0.25$. For each toy model, the fitted value r_{fit} and its uncertainty σ_{fit} are utilised to calculate the pull value P , computed as $P = (r_{\text{truth}} - r_{\text{fit}})/\sigma_{\text{fit}}$. By repeating this process for numerous toys, a pull distribution is derived for each r_{truth} , as shown in Fig. 8.20. If there is no bias, the distribution is expected to resemble a normal distribution centred in 0 with a standard deviation of 1. In this case, the distribution follows the expectations, indicating the absence of bias.

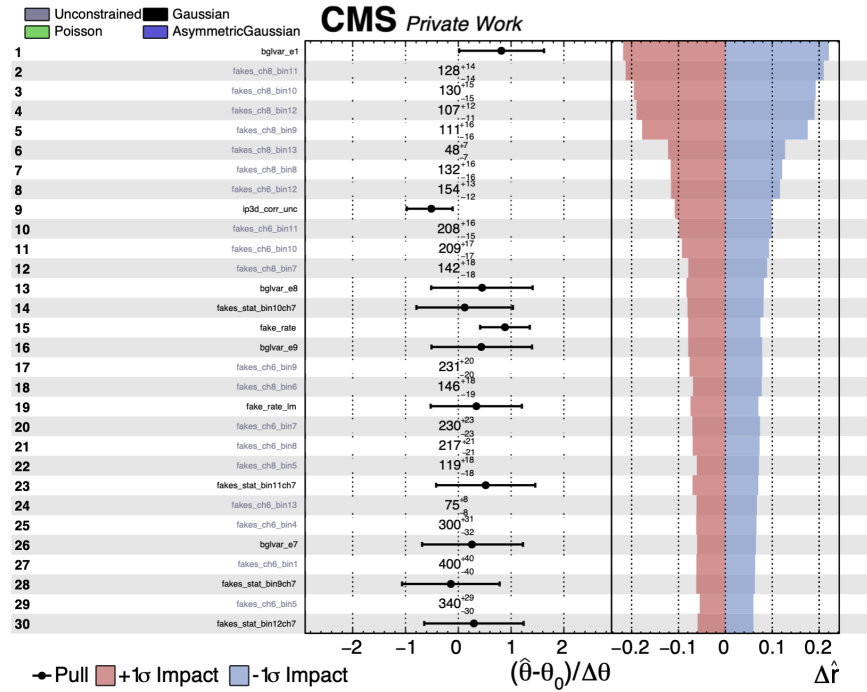


Figure 8.18: Post-fit values and impacts for the 30 most relevant systematic uncertainties in the analysis, listed in order of impact on the result. The total uncertainty on the result does not correspond to the sum in quadrature of the impacts, because correlations are included. More can be found in Appendix 10.6.

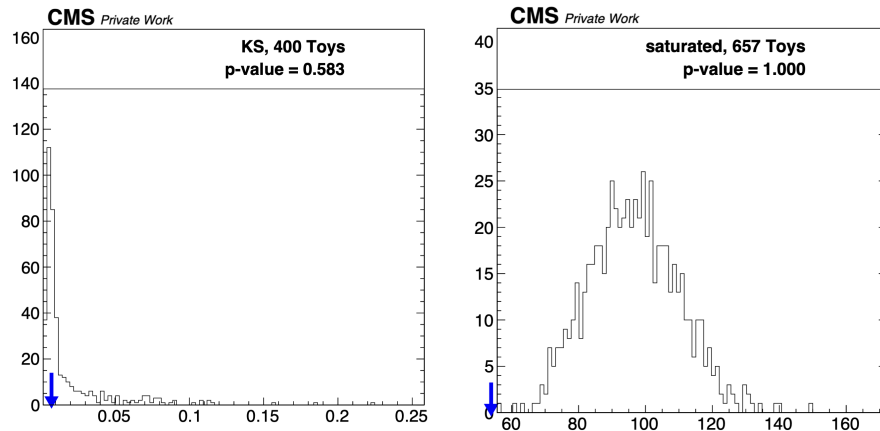


Figure 8.19: Goodness of fit plots for the KS test for the highest sensitive region (left), and with the saturated test (right).

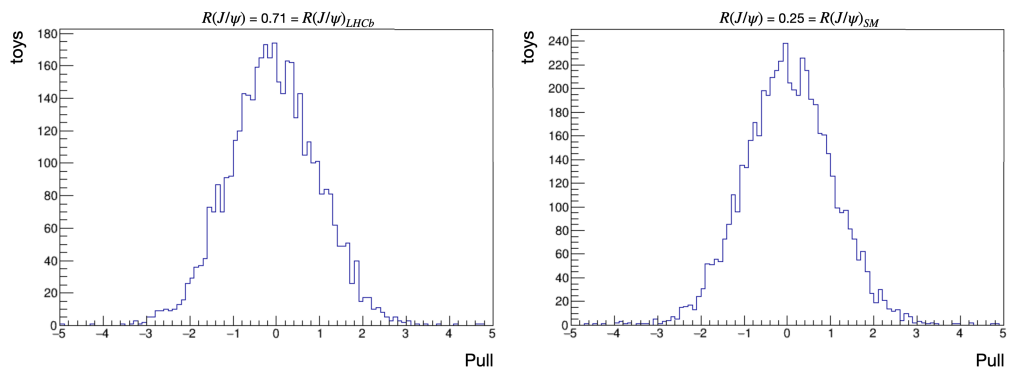


Figure 8.20: Bias tests with toy models produced with the LHCb expected result (left), and SM expected result (right). Both distributions can be fitted with a Gaussian centred in 0 and with a standard deviation of 1.

Chapter 9

Results

The analysis has been conducted applying the blinding strategy outlined in Sec. 8.4. After having established a robust fitting strategy, assessed and incorporated all relevant systematic uncertainties, and verified the stability and reliability of the fit model, the unblinding process can be initiated.

The first step of the unblinding strategy involves looking at the “blind” post-fit plots, where the parameters that can change during the fit are set to their best fit value, and where different contributions from the simulation are masked, Appendix 10.5.

Once it is assessed that the plots meet the desired quality, the fit can be performed without scaling the prefit value of signal τ by the random number described in Sec. 8.4. This approach ensures that the prefit $R(J/\psi)$ value remains equal to 1, so that the outcome of the post-fit represents the final $R(J/\psi)$ with its associated uncertainty.

In this Chapter, post-fit plots in all categories are shown in Sec. 9.1, and the final $R(J/\psi)$ result is presented in Sec. 9.2.

9.1 Post-Fit plots

The initial phase of the unblinding process involves an examination of the post-fit plots and which are presented in Fig. 9.1 and Fig. 9.2. These plots also display the final fit yield of the signal τ .

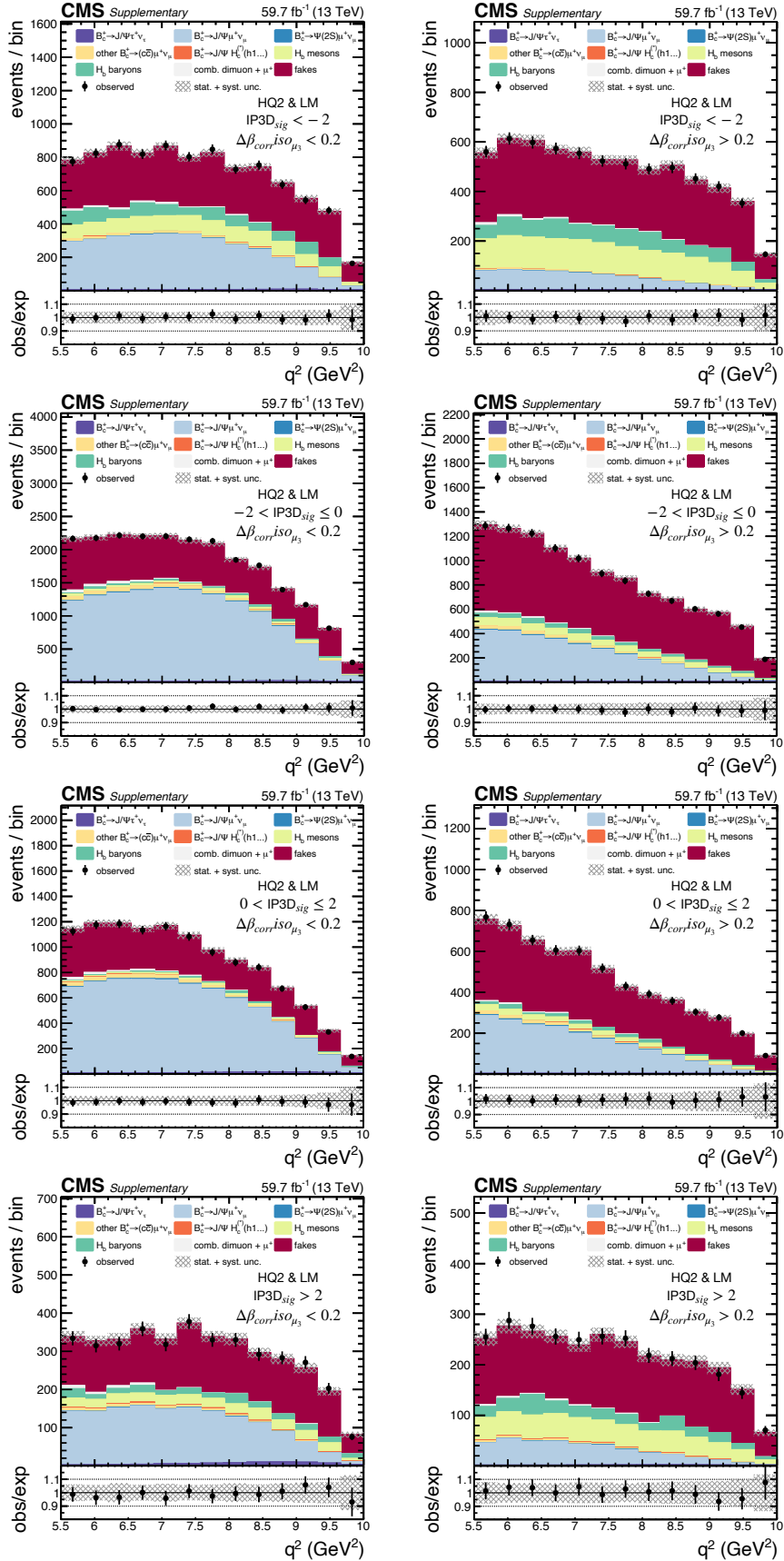


Figure 9.1: Post-fit distributions for the HQ2 LM regions, split into IP3D_{sig} categories. The plots in the rows show the distributions in different IP3D_{sig} categories, from the first to the last row: IP3D_{sig} < -2, -2 < IP3D_{sig} ≤ 0, 0 < IP3D_{sig} ≤ 2 and IP3D_{sig} > 2. First column shows A regions, $\Delta\beta_{corr,iso,\mu_3} < 0.2$, while second column shows reweighted-B regions, $\Delta\beta_{corr,iso,\mu_3} > 0.2$.

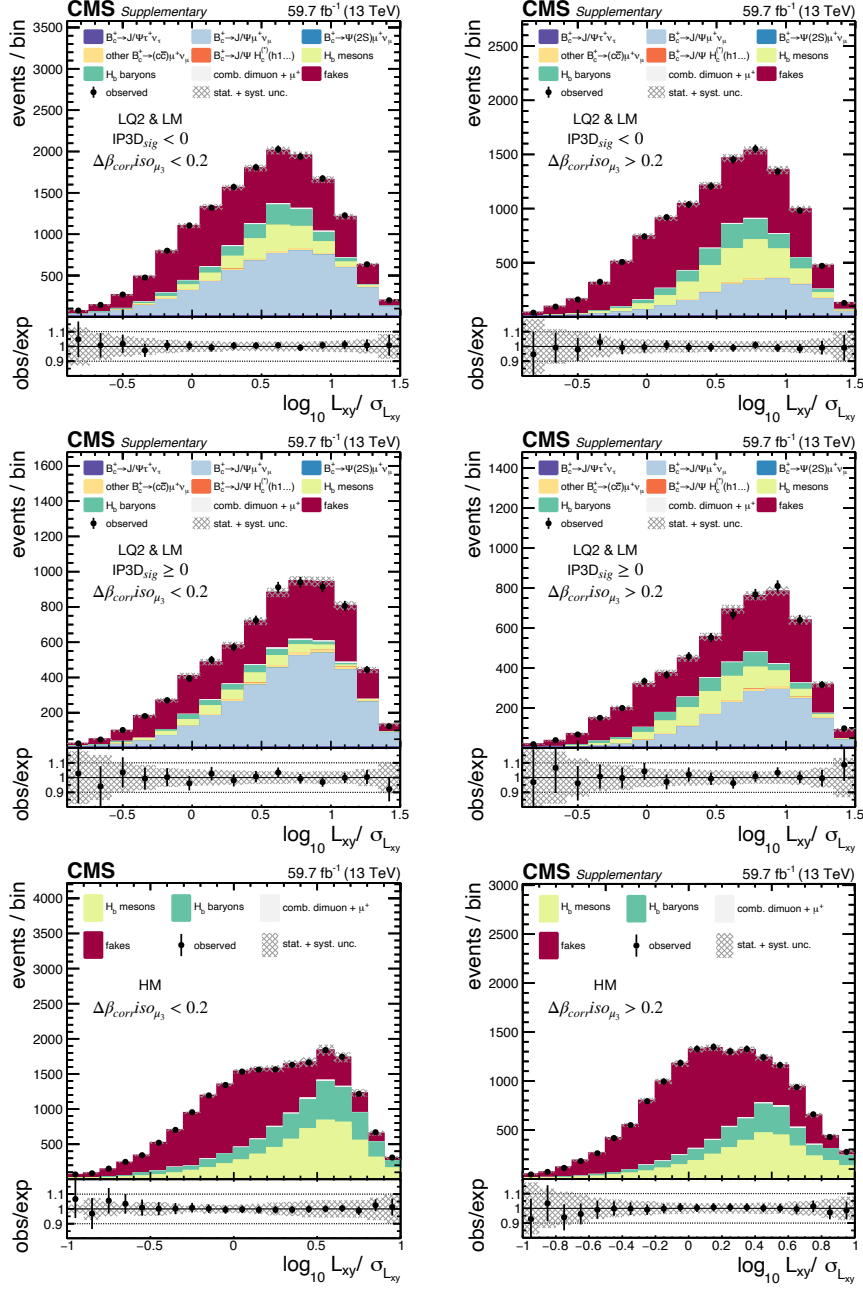


Figure 9.2: Post-fit distributions for the LQ2 LM regions (first two rows), split into IP3D_{sig} categories, and HM regions (last row). The plots in the first two rows show the distributions in different IP3D_{sig} categories, in order: $\text{IP3D}_{\text{sig}} < 0$ and $\text{IP3D}_{\text{sig}} \geq 0$. First column shows A regions, $\Delta\beta_{\text{corr}} \text{iso}_{\mu_3} < 0.2$, while second column shows reweighted-B regions, $\Delta\beta_{\text{corr}} \text{iso}_{\mu_3} > 0.2$.

The most sensitive category is also shown in logarithmic scale in Fig. 9.3.

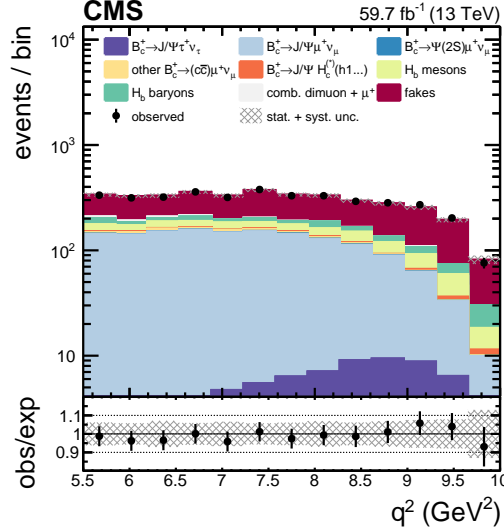


Figure 9.3: Post-fit distribution of the q^2 variable for the most sensitive category, HQ2 and $IP3D_{sig} > 2$ in logarithmic scale on the y-axis.

9.2 Final result

The final fit result is $R(J/\psi) = 0.17 \pm 0.33$, as shown in the likelihood scan in Fig. 9.4. The uncertainty can be split into several components as $R(J/\psi) = 0.17^{+0.18}_{-0.17}$ (stat) $^{+0.21}_{-0.22}$ (syst) $^{+0.19}_{-0.18}$ (theo).

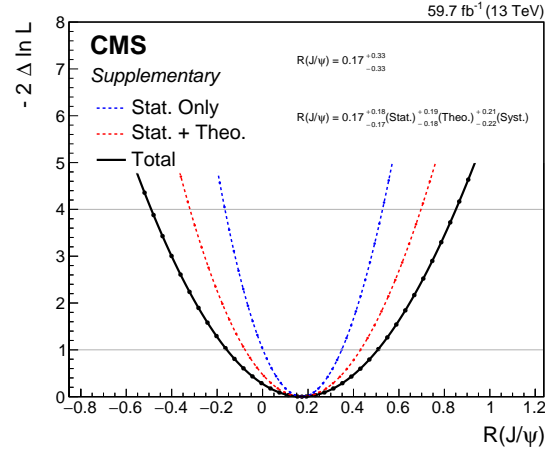


Figure 9.4: Likelihood scan for the $R(J/\psi)$ value.

The impact of the systematic uncertainties on the final result is shown in Table 9.1.

Contribution	Unc. type	$\Delta R(J/\psi) \cdot 10^{-2}$
Theory	S	19
fakes stat.		
nonclosure	S (bin-by-bin)	13
fakes	N	8
fakes	S	7
finite MC size	S (bin-by-bin)	9
$IP3D/\sigma_{IP3D}$, $L_{xy}/\sigma_{L_{xy}}$ corr.	S	9
muon ID, iso, trigger	N	6
H_b sample	N	0.8
B_c^+ bkg. BRs	N	0.6
dimuon comb. norm.	N	0.1
pileup, B_c^+ lifetime and kinematics	N	< 0.1
Total systematic uncertainty		28

Table 9.1: Leading systematic uncertainties for the measurement of $R(J/\psi)$. The second column reports the uncertainty type: shape (S) or normalisation (N). The last column shows the resulting uncertainty on the $R(J/\psi)$ measurement.

This result is compatible with the SM prediction within 0.3σ , and the LHCb measurement within 1.3σ .

9.3 Outlook

The result presented in this thesis is the first search for LFU violation within the $b \rightarrow cl\nu_l$ transitions in CMS. Given that the measurements in this channel show a deviation of 3σ from the SM predictions, it is ever more important to test these anomalies. The CMS collaboration has only presented one other result related to LFU violation studies, focusing on a different channel, the $b \rightarrow sll$ transitions, through the measurement of the R_K ratio [138].

This achievement marks CMS entrance into LFU studies and highlights the experiment potential to make meaningful contributions to this domain. Traditionally, such investigations were dominated by the b-factories like Belle II and BaBar, or LHCb at the LHC. For the specific measurement described in this thesis, the fact that the B_c mesons can only be produced at the LHC made it necessary to have an alternative experiment to validate the LHCb findings.

Given that it is the first analysis of its kind within the entire CMS collaboration, expertise and methodologies needed to be developed, making this the first iteration of what has the potential to evolve into a better refined, sensitive, and competitive analysis. The $R(J/\psi)$ measurement presented here has a larger uncertainty than the corresponding LHCb one, but in a next iteration of the analysis in CMS, various improvements that would enhance its sensitivity could be applied.

One potential improvement could be to incorporate additional data to the analysis. Currently, only the 2018 dataset is utilised, because the primary focus of this initial version was dedicated to building a robust analysis. Therefore, the addition of other datasets has been postponed to subsequent iterations. Moreover, there was an initial expectation that the analysis would be more limited by systematic uncertainties than statistical ones. While this assumption remains true, some of the systematic uncertainties are of statistical nature and therefore they can be reduced with more data.

The luminosity projections likelihood scan, as detailed in Appendix 10.4, demonstrates that if the 2018 luminosity is increased by a factor of 3, the expected outcome is a straightforward decrease in the statistical component of the uncertainty by $1/\sqrt{3}$. This reduction could be achieved by incorporating the remaining data from Run 2, with a total integrated luminosity of 137 fb^{-1} , and the dataset from Run 3, which has collected 67.37 fb^{-1} to date.

With the increase in the number of data events, another direct consequence is the reduction of the uncertainty coming from the correlations between the statistical component of the fakes estimation and the systematic part. In fact the fakes bins, defined as free floating parameters, are determined during the fit as the difference between data and the MC samples. As more data events are included, the part of the uncertainty due to the correlations between the statistical and systematic aspects of the fakes estimation decreases.

Finally, the addition of more data would also reduce the uncertainties associated with the fakes background estimation. Some of the most impactful uncertainties come from the dependence on data in control regions defined to measure the fakes background. For instance, uncertainties arising from limited statistics in the regions used for training the NNs or in the validation regions employed to validate the fakes method would decrease with an increased dataset. This final aspect is not accounted for in the luminosity projection.

Apart from increasing the dataset, another possible improvement includes updating the B_c FFs to a recently measured set that is more accurate [37]. The new central values of the FF corrections could potentially change the shape of the signals, but most importantly, the new FF uncertainties will be smaller. Hence, considering that the theoretical uncertainty of the current $R(J/\psi)$ analysis accounts for 18% of the total uncertainty, updating the B_c FFs with the latest theoretical

calculations becomes crucial for refining the precision of the analysis.

Other improvements involve refining the methods employed, specifically focusing on the fakes background estimation, which significantly impacts the sensitivity of the analysis. For instance, specific variables could be further explored, like the B_c meson decay length significance $L_{xy,sig}$ observable. In fact this variable distinctly shows the composition of the fakes background into prompt and non-prompt J/ψ mesons. Although this observable is already included, a deeper investigation might reveal better ways to employ it to improve the analysis sensitivity. In general, continue exploring the already used observables and possibly introducing new ones could contribute to a more refined and accurate characterisation of the fakes background, improving the overall precision of the analysis.

In conclusion, while this analysis has certain limitations and its result might not make a definitive impact in the LFU field yet, it is an initial step in the right direction for CMS. It can be significantly improved in the next iterations, leveraging the expertise and methodologies already acquired within the collaboration. This analysis has showed CMS potential to make meaningful contributions to shedding light on the flavour anomalies puzzle.

Conclusions

This thesis presented a direct search for Lepton Flavour Universality (LFU) violation in the CMS experiment, with the measurement of the $R(J/\psi)$ value, defined as $R(J/\psi) = \mathcal{B}(B_c^+ \rightarrow J/\psi \tau^+ \nu_\tau) / \mathcal{B}(B_c^+ \rightarrow J/\psi \mu^+ \nu_\mu)$. The analysis was conducted using proton-proton collision data, collected at a centre-of-mass energy of 13 TeV by the CMS experiment at the LHC in 2018. The dataset analysed corresponds to an integrated luminosity of 59.7 fb^{-1} .

The measurement of this ratio is particularly sensitive to potential deviations from the Standard Model (SM) predictions, especially because it includes a third-generation lepton, for which these deviations are hypothesised to be more evident. A deviation from the SM predictions in this context could indicate the existence of physics beyond the SM. Several theories, trying to explain these potential deviations, propose the existence of new particles that mediate electroweak interactions involving third-generation leptons. These particles could include charged Higgs bosons, leptoquarks, or new vector bosons.

For the decays of interest, $B_c^+ \rightarrow J/\psi \tau^+ \nu_\tau$ and $B_c^+ \rightarrow J/\psi \mu^+ \nu_\mu$, only the muonic decays of the J/ψ and tau leptons are examined, because of the high reconstruction efficiency of the CMS detector for these particles. The final state of these decays include exclusively muons and neutrinos. The neutrinos can not be detected, therefore kinematic variables such as q^2 are fundamental for distinguishing between the two decay channels. Additionally, to overcome the impairment brought by the missing momentum associated to the neutrinos, the reconstruction of the B_c meson four-momentum is approximated assuming that the B_c trajectory aligns with the direction of the final state muons.

The dataset utilised for this analysis includes events with J/ψ mesons, and the trigger requirements assure that they decay into two muons, accompanied by an additional displaced muon. Simulations account for potential background contributions from other B_c decays and those arising from J/ψ mesons and muons originating from other b-hadrons. A data-driven approach is employed to measure the background associated with misidentified muons, through the categorisation of events into four categories based on the isolation and identification quality of the muon not coming from the J/ψ decay. To quantify this background, neural

networks are employed to model the probability of misidentifying this muon and subsequently, this is applied to find this contribution in the signal region. This data driven method is partially integrated into the fit model, which is designed to determine the $R(J/\psi)$ value, and constrain and measure the various background contributions. The final maximum likelihood binned fit to extract $R(J/\psi)$ is organised into 7x2 categories, each defined based on specific displacement characteristics and kinematic variables. Systematic uncertainties, including theoretical uncertainties on the B_c form factors, are computed and incorporated in the fit.

The measured result for the ratio is:

$$R(J/\psi) = 0.17^{+0.18}_{-0.17} \text{ (stat)}^{+0.21}_{-0.22} \text{ (syst)}^{+0.19}_{-0.18} \text{ (theo).}$$

This is compatible with the SM prediction within 0.3σ and the LHCb measurement within 1.3σ . The uncertainty on the result includes a theoretical uncertainty associated with the form factor estimation. The statistical component of the uncertainty could be reduced in future iterations of the analysis with the inclusion of additional data.

This result represents one of the first searches for LFU violations in the CMS experiment, and the first one in the $b \rightarrow cl^+ \nu_l$ channel. This study definitely demonstrates the potential for CMS to contribute to this intriguing field and explore new physics in the LFU violation domain.

Declaration of originality

The work presented in this thesis was performed within the CMS Collaboration at CERN. I conducted the $R(J/\psi)$ measurement in CMS, as elaborated in Part II of this thesis. Additionally, I was the contact person for the analysis within the CMS collaboration. This work has been published in a Physics Analysis Summary (PAS) [139] and is currently under review to be published in a peer-reviewed journal. Parts of this article have been included into this thesis.

In collaboration with my advisor, Dr. Riccardo Manzoni, I adapted the existing CMS reconstruction framework to reconstruct the final state muons, and I refined the final selection criteria for the analysis, as detailed in Chapter 5. I developed the data-driven method for estimating the fakes background and applied corrections to the MC simulations, which are discussed in Chapters 6 and 7. This included measuring the efficiency of low p_T muon identification and isolation in 2018. I designed and implemented the fitting strategy for this analysis, incorporating systematic uncertainties, and conducting several tests to ensure its robustness and reliability. The details are outlined in Chapter 8. Eventually, I was responsible for the unblinding process and the measurement of the final result, as elaborated in Chapter 9.

Chapter 10

Appendix

10.1 Form factors: additional plots

In Sec. 7.1 corrections to the FF are described. In Figures 10.1, 10.2 and 10.3 the central value is compared to the variation of 1σ for all the parameters.

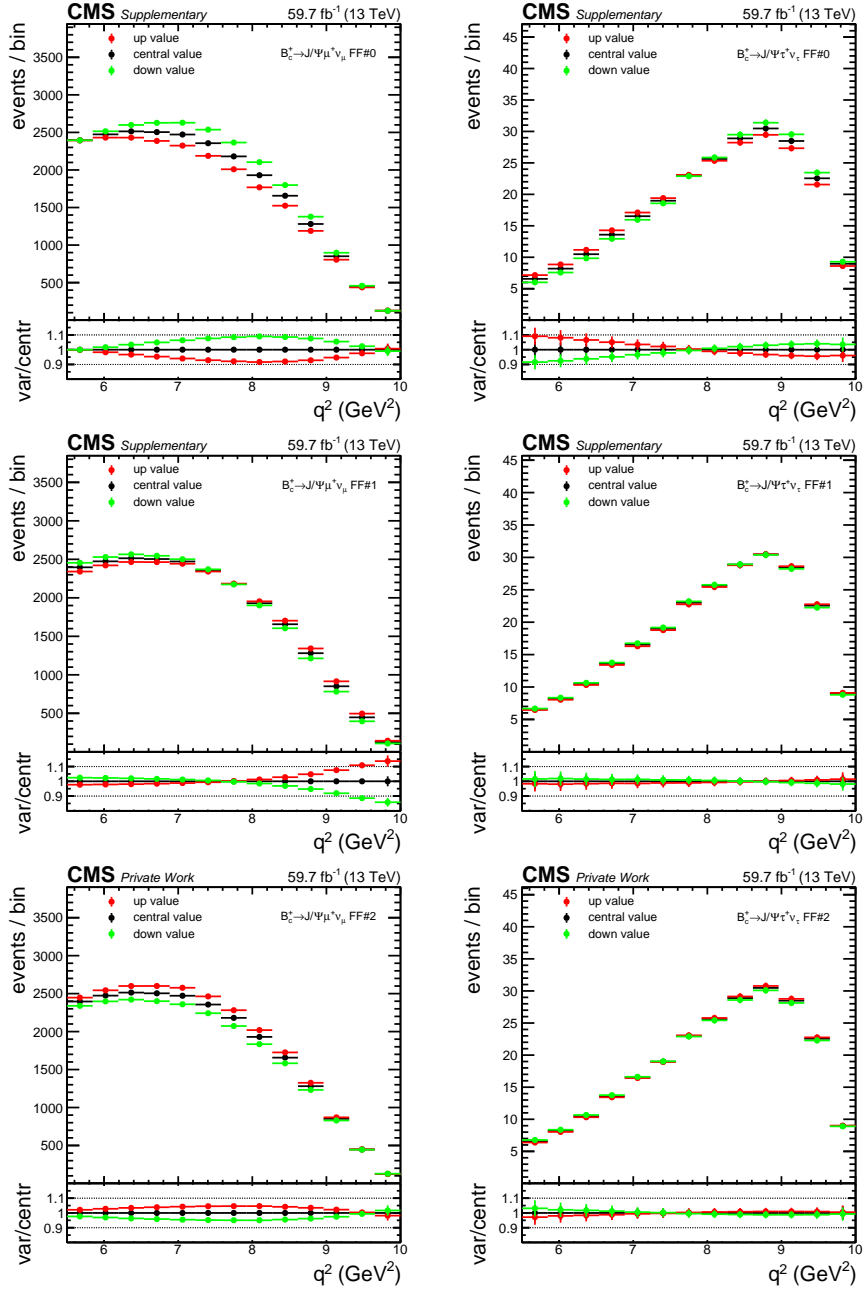


Figure 10.1: q^2 distribution is shown for signal μ (left) and signal τ (right). The nominal value (black) is compared with the up (red) and down (green) distributions obtained applying the Hammer weights for 1σ systematic uncertainty. For each row a different uncertainty on the form factors is shown.

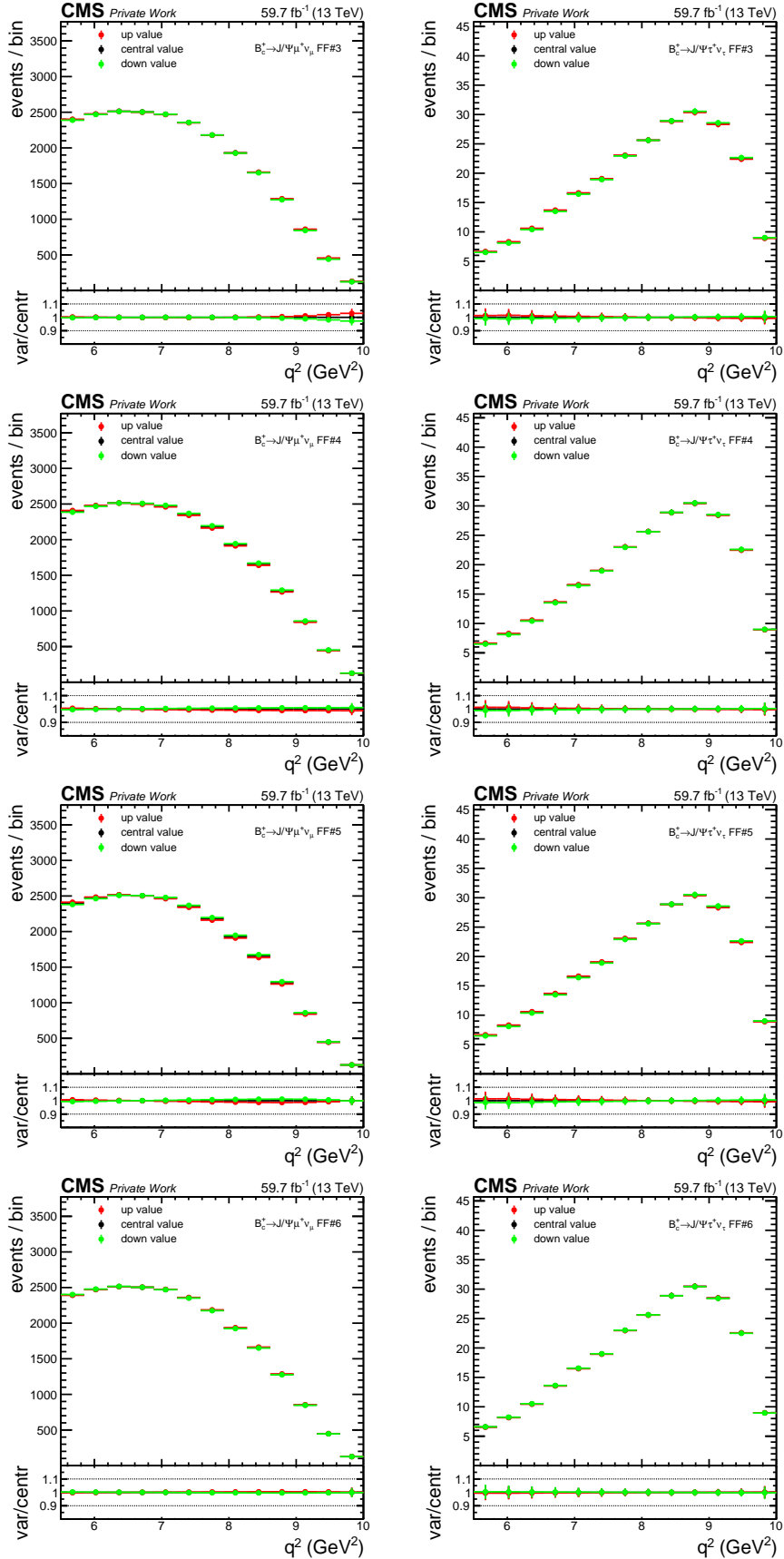


Figure 10.2: q^2 distribution is shown for signal μ (left) and signal τ (right). The nominal value (black) is compared with the up (red) and down (green) distributions obtained applying the Hammer weights for 1σ systematic uncertainty. For each row a different uncertainty on the form factors is shown.

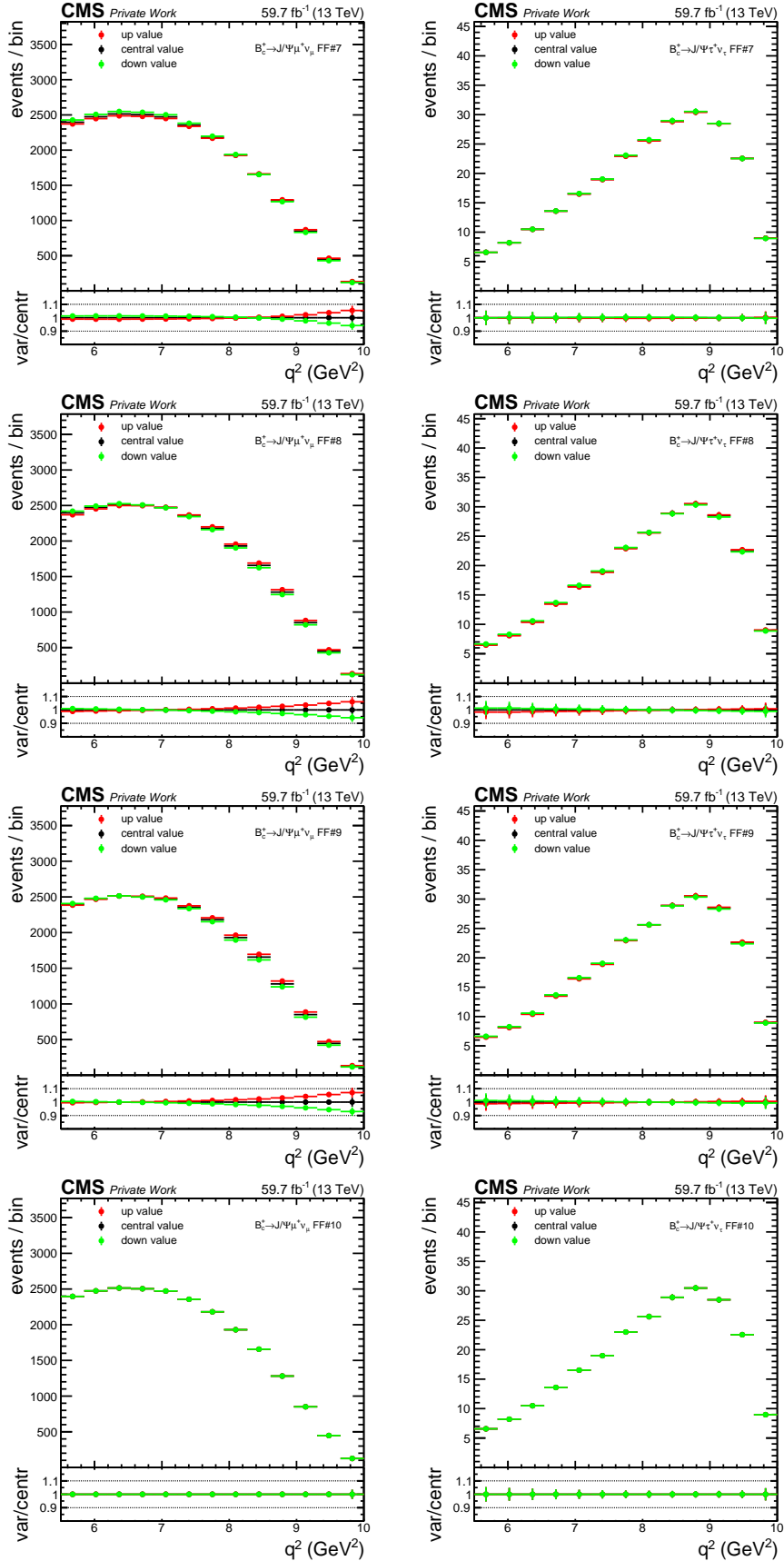


Figure 10.3: q^2 distribution is shown for signal μ (left) and signal τ (right). The nominal value (black) is compared with the up (red) and down (green) distributions obtained applying the Hammer weights for 1σ systematic uncertainty. For each row a different uncertainty on the form factors is shown.

10.2 Fakes background checks for MC variations during fit

In the fit model, the MC samples have degrees of freedom (both shape and normalisation) that they don't have during the training of the NNs used to find the fakes shape and normalisation, Sec. 6.3.2.2.

In fact, in the training of the NNs for the fakes background estimation, the B_c and H_b normalisations are fixed to the ones found after a first fit; the relative abundances of the various subprocesses are the same used at production level (taken from literature and PDG values). Central weights are applied to MC during training (like form factor corrections, pile-up corrections etc.), and the $R(J/\psi)$ value is fixed to be equal to 1 during training.

In the fit model, as shown in Sec. 8.3, there are many systematic uncertainties that affect the shape and normalisation of the MC samples, and rate parameters that allow the $R(J/\psi)$ value, and the B_c and H_b normalisations to float during the fit.

It is impossible to account for all the possible variations of the MC samples in the training of the networks, because it would mean to train the networks and find the weights for each MC variation. Therefore, few important MC variations are studied to check their impact on the final fakes shape estimation:

- FF uncertainty number 1:

It is one of the most impacting nuisances of the fit, Fig. 8.18. If the NNs are trained with the up value of the FF uncertainty to find the up shape of the fakes, and with their down value to find the down shape, the fakes shape uncertainty in Fig. 10.4 is found. This difference in shape is negligible, therefore not accounted for in the fit.

- $R(J/\psi)$ variation:

The NNs for the fakes shape estimation are trained with the $R(J/\psi)$ value equal to 1. To check the impact of the $R(J/\psi)$ value variation on the fit result, the NNs are trained using different values of $R(J/\psi)$, to check how the fakes shape change. In Fig. 10.5, fakes shapes with different $R(J/\psi)$ values in the NN trainings are compared, and the difference results to be negligible.

The result of the fit doesn't seem influenced by the $R(J/\psi)$ value used in the training of the networks, as it can be also seen in the injection test in Fig. 8.17.

- B_c normalisation.

This is the only fakes shape systematic due to MC variation that is added in the fit, as can be seen in Sec. 8.3.

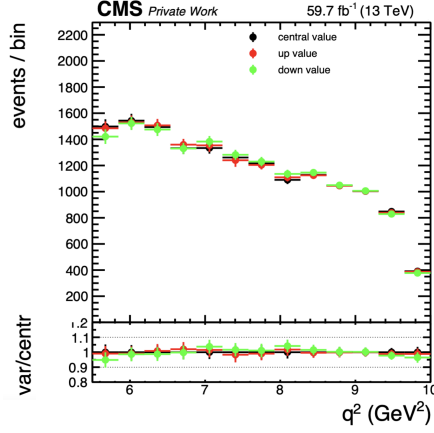


Figure 10.4: Fakes shape comparison between the central value, found with NNs trained on the central values of the FF corrections, and the up and down shapes, found with NNs weights trained on the firsts up and down uncertainty on the FFs.

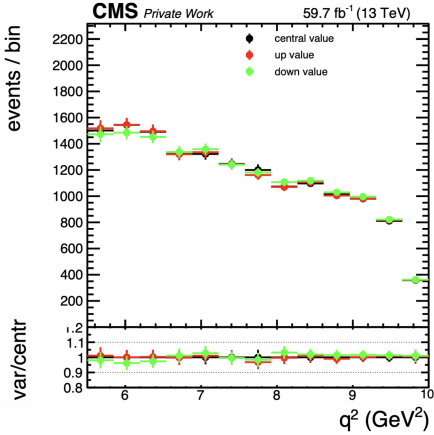


Figure 10.5: Fakes shape comparison between the central value, found with NNs trained with $R(J/\psi) = 1$, and the up and down shapes, found with NNs weights trained with $R(J/\psi) = 1.5$ and $R(J/\psi) = 0.25 = SM$.

10.3 Signal injection test

In Sec. 8.5.1, the expected sensitivity of the fit is shown in comparison to the LHCb result. The Asimov Fit can be performed for different values of $R(J/\psi)$, which are compared in Fig. 8.17. In this section, the likelihood scans of each fit are shown, Fig. 10.6.

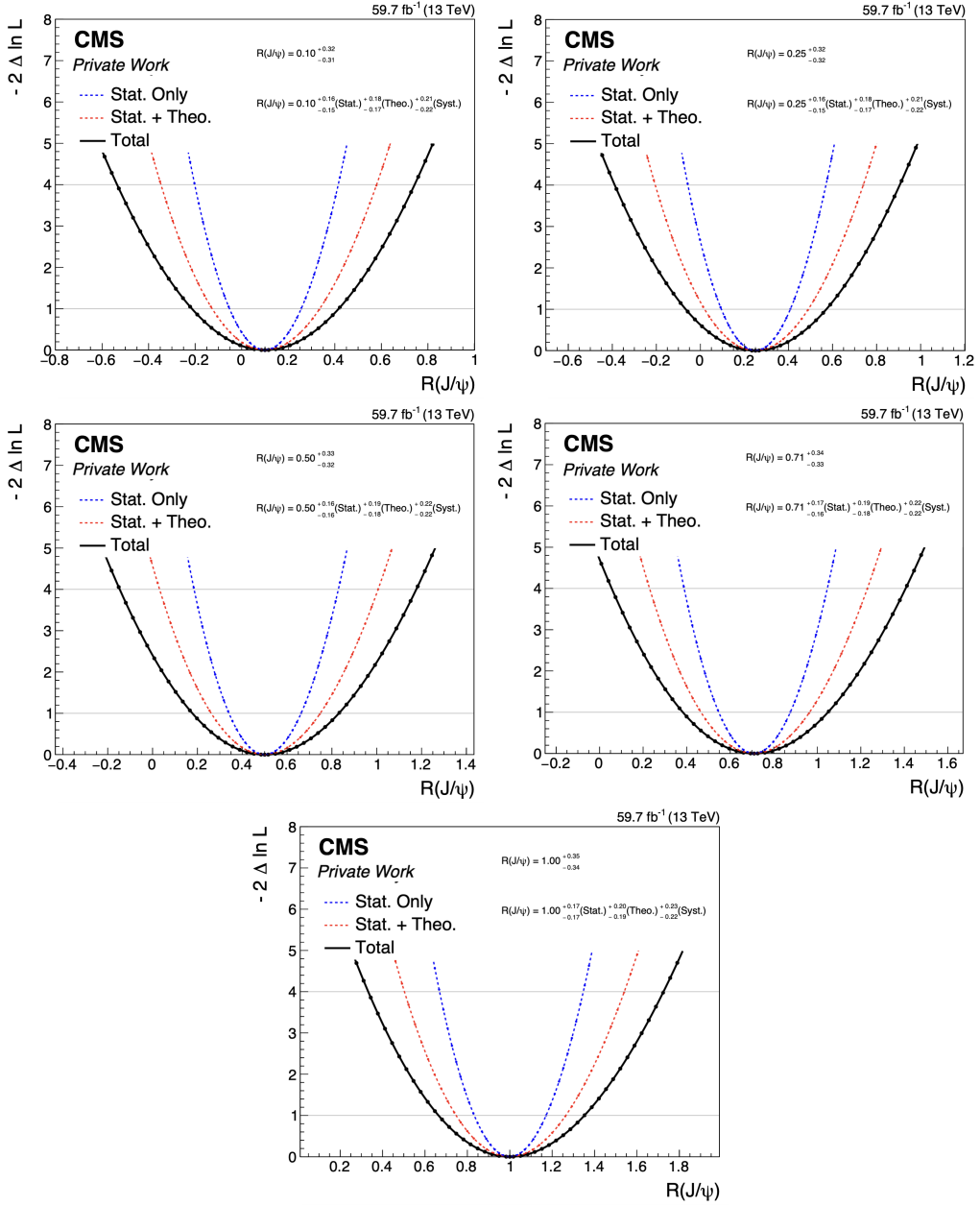


Figure 10.6: Likelihood scans for the results of the Asimov fits with several expected signals. In each plot: fit with frozen systematic uncertainties and bins for the fakes background (dashed red), fit with only frozen systematic uncertainties (dashed blue) and total observed sensitivity of the Asimov fit with statistical+systematic uncertainties (black). The total uncertainty does not vary significantly for different values of $R(J/\psi)$.

10.4 Luminosity projection

A luminosity projection is implemented on the Asimov test to anticipate the potential reduction in uncertainty with increased data events for the analysis. All process yields are tripled compared to the 2018 statistics, and the resulting likelihood scan is shown in Fig. 10.7. The statistical uncertainty decreases as expected,

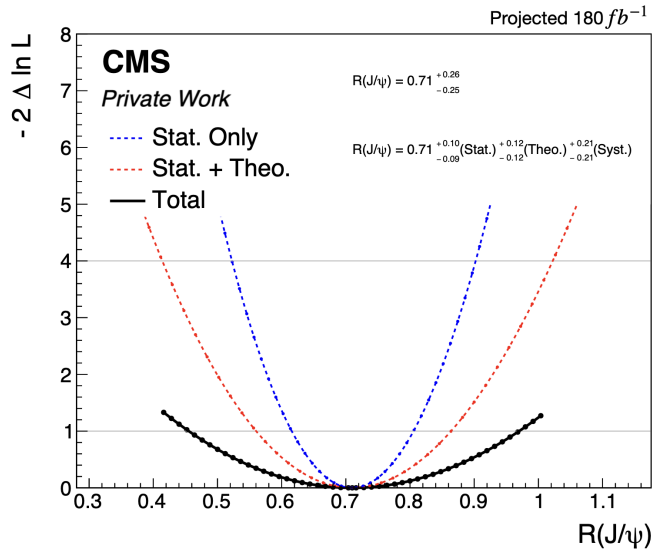


Figure 10.7: Likelihood scan with three times the 2018 luminosity.

following a $1/\sqrt{3}$ reduction. Consequently, the systematic uncertainty also experiences a slight decrease, given its correlations with the statistical components of the fakes bin nuisances.

The presented scenario represents a pessimistic situation. The simplified test conducted here does not consider other effects resulting from the statistical increase. For instance, the derivation of the fakes background is also anticipated to improve, as the increased statistics in the training regions of the NN will likely contribute to enhanced performance and decrease the total uncertainty of the analysis.

10.5 “Blind” post-fit plots

The second-to-last step of the unblinding procedure involves studying the “blind” post-fit plots. These plots show the comparison between data and the overall MC without revealing the individual signal (and background) contributions. This allows for an evaluation of the post-fit plot quality without disclosing the $R(J/\psi)$ result. Figures 10.8 and 10.9 show these blind post-fit plots.

10.6 Impacts

The firsts 120 post-fit values for the systematic uncertainties and their impact on the analysis is shown in Figures 10.10 and Fig. 10.11.

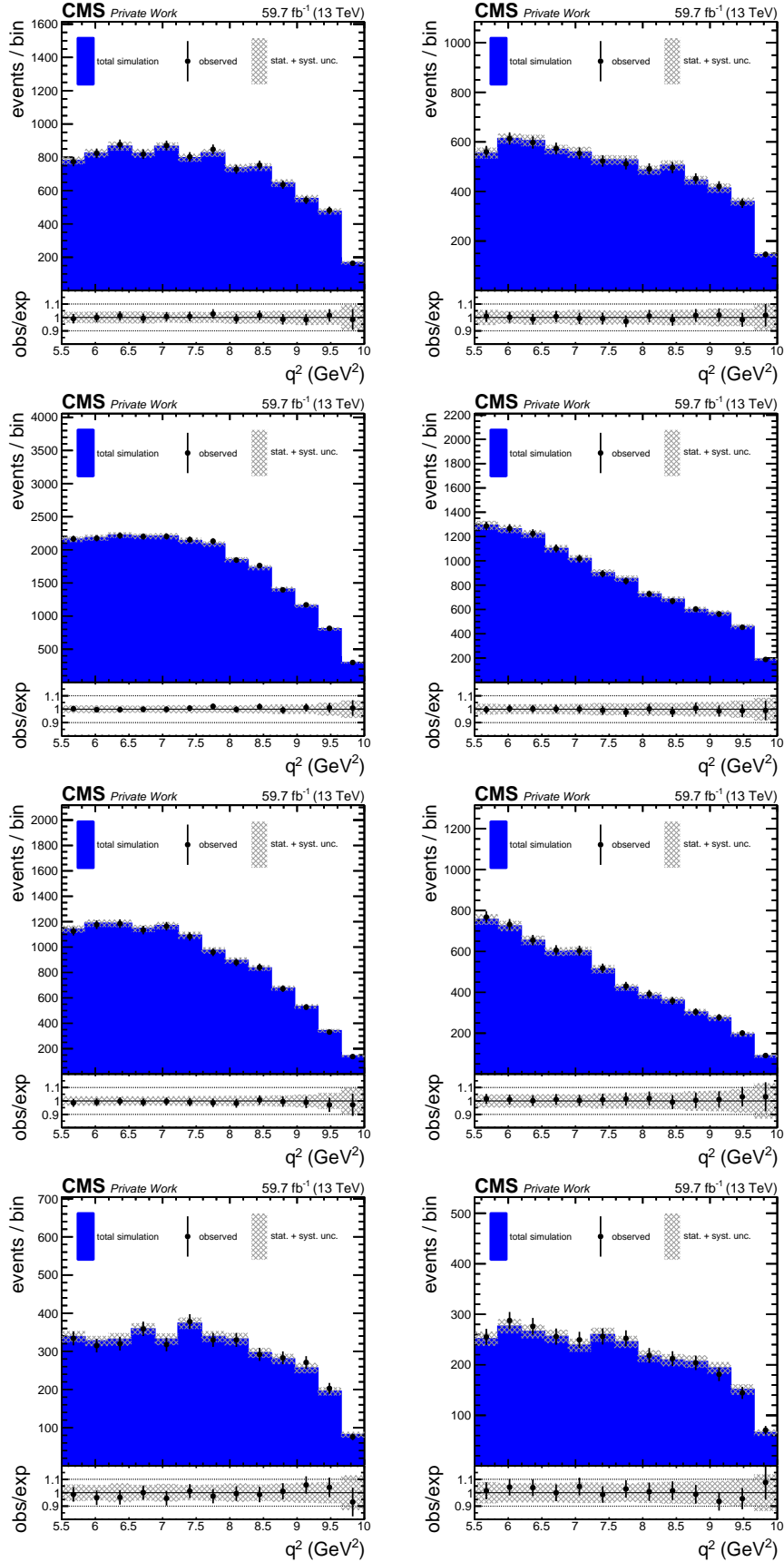


Figure 10.8: Blind Post-fit distributions for the HQ2 LM regions, split into IP3D_{sig} categories. The plots in the rows show the distributions in different IP3D_{sig} categories, from the first to the last row: IP3D_{sig} < -2, -2 < IP3D_{sig} < 0, 0 < IP3D_{sig} < 2 and IP3D_{sig} > 2. First column shows A regions, $\Delta\beta_{corr,iso\mu_3} < 0.2$, while second column shows reweighted-B regions, $\Delta\beta_{corr,iso\mu_3} > 0.2$.

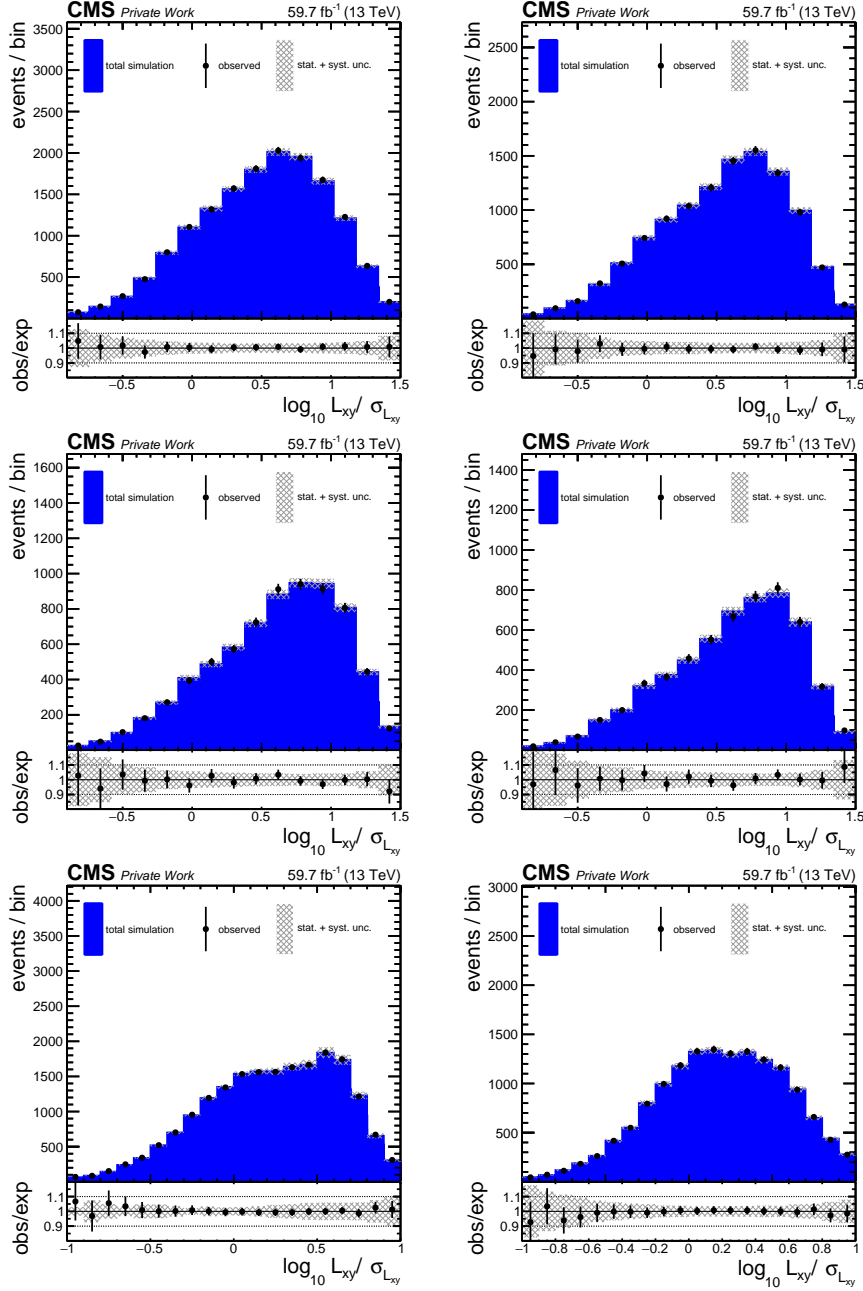


Figure 10.9: Blind Post-fit distributions for the LQ2 LM regions (first two rows), split into $IP3D_{sig}$ categories, and HM regions (last row). The plots in the first two rows show the distributions in different $IP3D_{sig}$ categories, in order: $IP3D_{sig} < 0$ and $IP3D_{sig} \geq 0$. First column shows A regions, $\Delta\beta_{corr iso\mu_3} < 0.2$, while second column shows reweighted-B regions, $\Delta\beta_{corr iso\mu_3} > 0.2$.

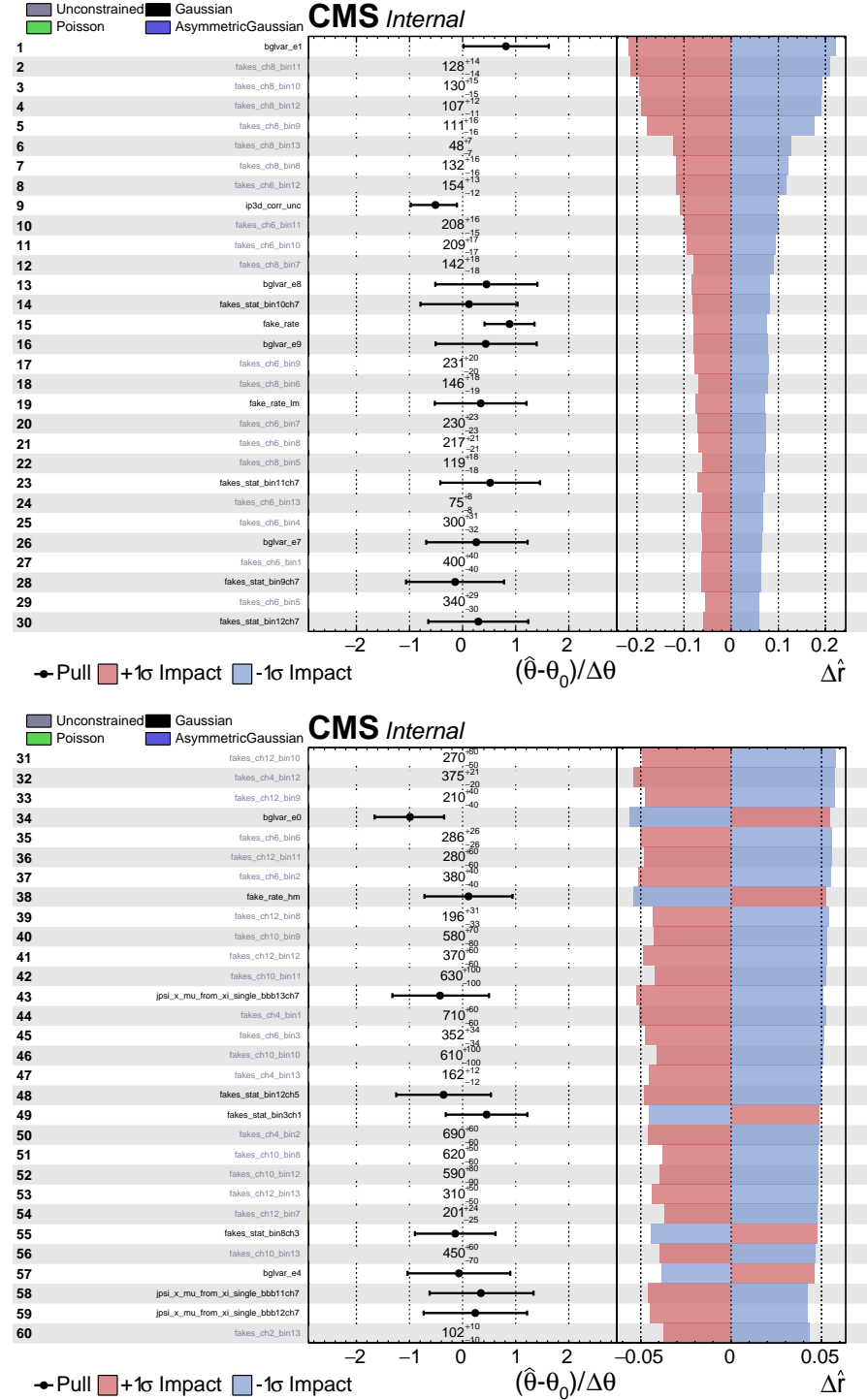


Figure 10.10: Post-fit values and impacts of the first 60 relevant systematic uncertainties in the analysis, listed in order of impact on the result.

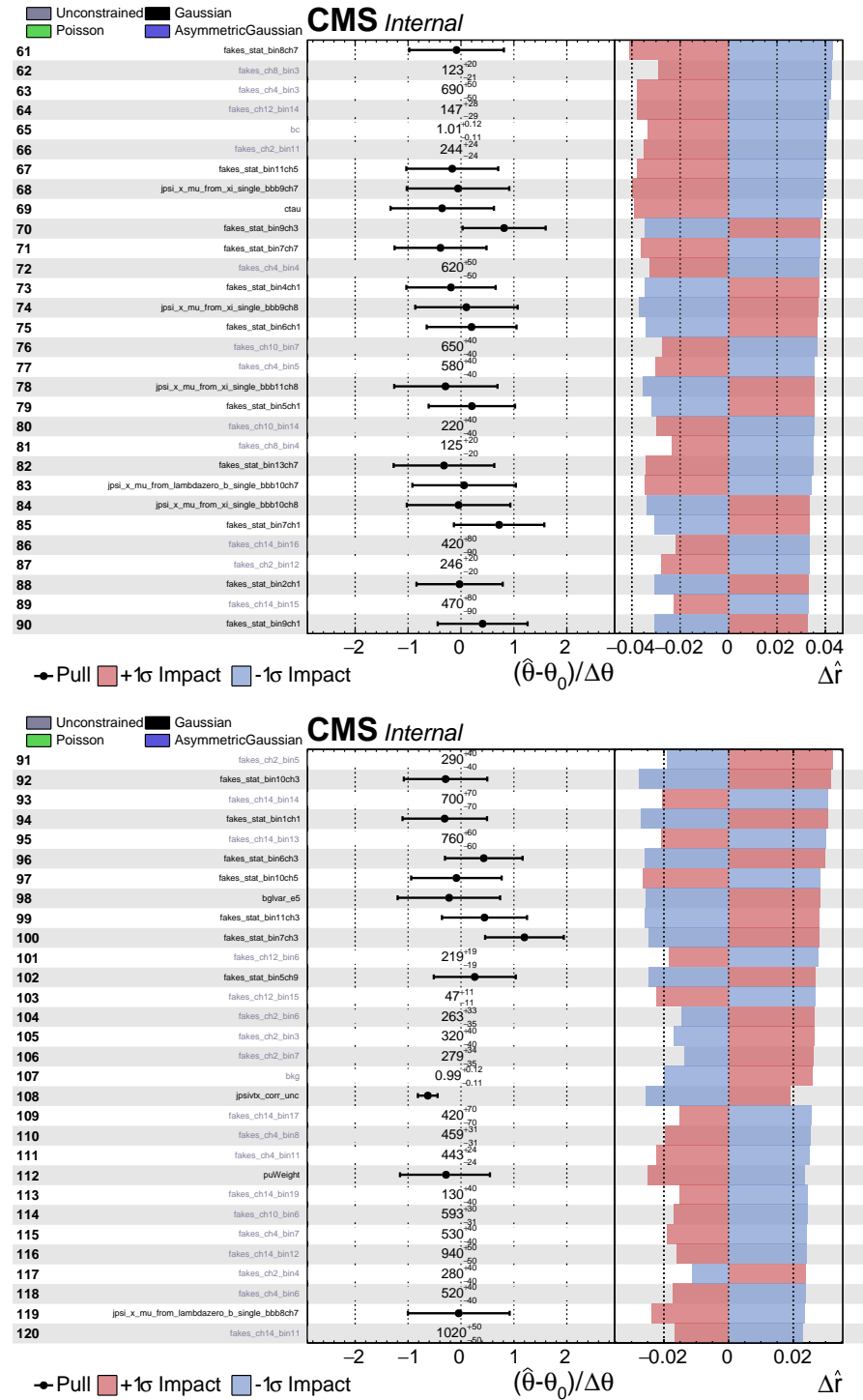


Figure 10.11: Post-fit values and impacts of the second 60 relevant systematic uncertainties in the analysis, listed in order of impact on the result.

Bibliography

- [1] D. Schroeder M.Peskin. “An Introduction To Quantum Field Theor”. In: *Levant Books* (2005).
- [2] S. L. Glashow. “Partial Symmetries of Weak Interactions”. In: *Nucl. Phys.* 22 (1961), pp. 579–588. DOI: [10.1016/0029-5582\(61\)90469-2](https://doi.org/10.1016/0029-5582(61)90469-2).
- [3] Steven Weinberg. “A Model of Leptons”. In: *Phys. Rev. Lett.* 19 (1967), pp. 1264–1266. DOI: [10.1103/PhysRevLett.19.1264](https://doi.org/10.1103/PhysRevLett.19.1264).
- [4] Abdus Salam. “Weak and Electromagnetic Interactions”. In: *Conf. Proc. C* 680519 (1968), pp. 367–377. DOI: [10.1142/9789812795915_0034](https://doi.org/10.1142/9789812795915_0034).
- [5] F. Englert and R. Brout. “Broken Symmetry and the Mass of Gauge Vector Mesons”. In: *Phys. Rev. Lett.* 13 (1964). Ed. by J. C. Taylor, pp. 321–323. DOI: [10.1103/PhysRevLett.13.321](https://doi.org/10.1103/PhysRevLett.13.321).
- [6] Peter W. Higgs. “Broken symmetries, massless particles and gauge fields”. In: *Phys. Lett.* 12 (1964), pp. 132–133. DOI: [10.1016/0031-9163\(64\)91136-9](https://doi.org/10.1016/0031-9163(64)91136-9).
- [7] G. S. Guralnik, C. R. Hagen, and T. W. B. Kibble. “Global Conservation Laws and Massless Particles”. In: *Phys. Rev. Lett.* 13 (1964). Ed. by J. C. Taylor, pp. 585–587. DOI: [10.1103/PhysRevLett.13.585](https://doi.org/10.1103/PhysRevLett.13.585).
- [8] G. Zweig. “An SU(3) model for strong interaction symmetry and its breaking. Version 2”. In: *DEVELOPMENTS IN THE QUARK THEORY OF HADRONS. VOL. 1. 1964 - 1978*. Ed. by D. B. Lichtenberg and Simon Peter Rosen. Feb. 1964, pp. 22–101.
- [9] M. Y. Han and Yoichiro Nambu. “Three Triplet Model with Double SU(3) Symmetry”. In: *Phys. Rev.* 139 (1965). Ed. by T. Eguchi, B1006–B1010. DOI: [10.1103/PhysRev.139.B1006](https://doi.org/10.1103/PhysRev.139.B1006).
- [10] O. W. Greenberg. “Spin and Unitary Spin Independence in a Paraquark Model of Baryons and Mesons”. In: *Phys. Rev. Lett.* 13 (1964), pp. 598–602. DOI: [10.1103/PhysRevLett.13.598](https://doi.org/10.1103/PhysRevLett.13.598).

- [11] H. David Politzer. “Reliable Perturbative Results for Strong Interactions?” In: *Phys. Rev. Lett.* 30 (1973). Ed. by J. C. Taylor, pp. 1346–1349. DOI: 10.1103/PhysRevLett.30.1346.
- [12] David J. Gross and Frank Wilczek. “Ultraviolet Behavior of Nonabelian Gauge Theories”. In: *Phys. Rev. Lett.* 30 (1973). Ed. by J. C. Taylor, pp. 1343–1346. DOI: 10.1103/PhysRevLett.30.1343.
- [13] Georges Aad et al. “Observation of a new particle in the search for the Standard Model Higgs boson with the ATLAS detector at the LHC”. In: *Phys. Lett. B* 716 (2012), pp. 1–29. DOI: 10.1016/j.physletb.2012.08.020. arXiv: 1207.7214 [hep-ex].
- [14] Serguei Chatrchyan et al. “Observation of a New Boson at a Mass of 125 GeV with the CMS Experiment at the LHC”. In: *Phys. Lett. B* 716 (2012), pp. 30–61. DOI: 10.1016/j.physletb.2012.08.021. arXiv: 1207.7235 [hep-ex].
- [15] R. L. Workman et al. “Review of Particle Physics”. In: *PTEP* 2022 (2022), p. 083C01. DOI: 10.1093/ptep/ptac097.
- [16] Alessandro Bettini. *Introduction to elementary particle physics*. 2008. ISBN: 978-0-521-88021-3.
- [17] Michael E. Peskin. *Concepts of Elementary Particle Physics*. Oxford Master Series in Physics, 2019.
- [18] Georges Aad et al. “Observation of a new particle in the search for the Standard Model Higgs boson with the ATLAS detector at the LHC”. In: *Phys. Lett. B* 716 (2012), pp. 1–29. DOI: 10.1016/j.physletb.2012.08.020. arXiv: 1207.7214 [hep-ex].
- [19] Serguei Chatrchyan et al. “Observation of a New Boson at a Mass of 125 GeV with the CMS Experiment at the LHC”. In: *Phys. Lett. B* 716 (2012), pp. 30–61. DOI: 10.1016/j.physletb.2012.08.021. arXiv: 1207.7235 [hep-ex].
- [20] R. L. Workman et al. “Review of Particle Physics”. In: *PTEP* 2022 (2022), p. 083C01. DOI: 10.1093/ptep/ptac097.
- [21] *Particle Data Group website*. URL: http://pdg.web.cern.ch/pdg/2020/listings/contents_listings.html.
- [22] *CKM Fitter*. <http://ckmfitter.in2p3.fr>.
- [23] *UT Fitter*. <http://www.utfit.org/UTfit/>.
- [24] Mark Thomson. *Modern particle physics*. New York: Cambridge University Press, 2013. ISBN: 978-1-107-03426-6. DOI: 10.1017/CBO9781139525367.

- [25] Antonio Pich. “Precision tau physics”. In: *Progress in Particle and Nuclear Physics* 75 (2014), pp. 41–85. ISSN: 0146-6410. DOI: <https://doi.org/10.1016/j.ppnp.2013.11.002>. URL: <https://www.sciencedirect.com/science/article/pii/S0146641013001087>.
- [26] *LEP Design Report: Vol.2. The LEP Main Ring*. June 1984.
- [27] *Design Report Tevatron 1 project*. Sept. 1984.
- [28] “Precision electroweak measurements on the Z resonance”. In: *Physics Reports* 427.5 (2006), pp. 257–454. ISSN: 0370-1573. DOI: <https://doi.org/10.1016/j.physrep.2005.12.006>. URL: <https://www.sciencedirect.com/science/article/pii/S0370157305005119>.
- [29] Morad Aaboud et al. “Precision measurement and interpretation of inclusive W^+ , W^- and Z/γ^* production cross sections with the ATLAS detector”. In: *Eur. Phys. J. C* 77.6 (2017), p. 367. DOI: 10.1140/epjc/s10052-017-4911-9. arXiv: 1612.03016 [hep-ex].
- [30] Simone Bifani et al. “Review of Lepton Universality tests in B decays”. In: *J. Phys. G* 46.2 (2019), p. 023001. DOI: 10.1088/1361-6471/aaf5de. arXiv: 1809.06229 [hep-ex].
- [31] “Electroweak measurements in electron–positron collisions at W-boson-pair energies at LEP”. In: *Physics Reports* 532.4 (2013). Electroweak Measurements in Electron-Positron Collisions at W-Boson-Pair Energies at LEP, pp. 119–244. ISSN: 0370-1573. DOI: <https://doi.org/10.1016/j.physrep.2013.07.004>. URL: <https://www.sciencedirect.com/science/article/pii/S0370157313002706>.
- [32] “Test of the universality of τ and μ lepton couplings in W-boson decays with the ATLAS detector”. In: *Nature Physics* 17 (2021), pp. 813–818. DOI: <https://doi.org/10.1038/s41567-021-01236-w>.
- [33] Armen Tumasyan et al. “Precision measurement of the W boson decay branching fractions in proton-proton collisions at $\sqrt{s} = 13$ TeV”. In: *Phys. Rev. D* 105.7 (2022), p. 072008. DOI: 10.1103/PhysRevD.105.072008. arXiv: 2201.07861 [hep-ex].
- [34] E. Waheed et al. “Measurement of the CKM matrix element $|V_{cb}|$ from $B^0 \rightarrow D^{*-} \ell^+ \nu_\ell$ at Belle”. In: *Phys. Rev. D* 100.5 (2019). [Erratum: *Phys. Rev. D* 103, 079901 (2021)], p. 052007. DOI: 10.1103/PhysRevD.100.052007. arXiv: 1809.03290 [hep-ex].

- [35] R. et al. Glattauer. “Measurement of the decay $B \rightarrow D\ell\nu_\ell$ in fully reconstructed events and determination of the Cabibbo-Kobayashi-Maskawa matrix element $|V_{cb}|$ ”. In: *Phys. Rev. D* 93 (3 Feb. 2016), p. 032006. DOI: 10.1103/PhysRevD.93.032006. URL: <https://link.aps.org/doi/10.1103/PhysRevD.93.032006>.
- [36] Judd Harrison, Christine T. H. Davies, and Andrew Lytle. “ $R(J/\psi)$ and $B_c^- \rightarrow J/\psi\ell^-\bar{\nu}_l$ Lepton Flavor Universality Violating Observables from Lattice QCD”. In: *Phys. Rev. Lett.* 125 (22 Nov. 2020), p. 222003. DOI: 10.1103/PhysRevLett.125.222003. URL: <https://link.aps.org/doi/10.1103/PhysRevLett.125.222003>.
- [37] Judd Harrison, Christine T. H. Davies, and Andrew Lytle. “ $B_c \rightarrow J/\psi$ form factors for the full q^2 range from lattice QCD”. In: *Phys. Rev. D* 102 (9 Nov. 2020), p. 094518. DOI: 10.1103/PhysRevD.102.094518. URL: <https://link.aps.org/doi/10.1103/PhysRevD.102.094518>.
- [38] Thomas D. Cohen, Henry Lamm, and Richard F. Lebed. “Precision model-independent bounds from a global analysis of $b \rightarrow c\ell\nu$ form factors”. In: *Phys. Rev. D* 100 (9 Nov. 2019), p. 094503. DOI: 10.1103/PhysRevD.100.094503. URL: <https://link.aps.org/doi/10.1103/PhysRevD.100.094503>.
- [39] Bernard Aubert et al. “The BaBar detector”. In: *Nucl. Instrum. Meth. A* 479 (2002), pp. 1–116. DOI: 10.1016/S0168-9002(01)02012-5. arXiv: [hep-ex/0105044](https://arxiv.org/abs/hep-ex/0105044).
- [40] T. Abe et al. “Belle II Technical Design Report”. In: (Nov. 2010). arXiv: [1011.0352 \[physics.ins-det\]](https://arxiv.org/abs/1011.0352).
- [41] The LHCb Collaboration. “The LHCb Detector at the LHC”. In: *Journal of Instrumentation* 3.08 (Aug. 2008), S08005. DOI: 10.1088/1748-0221/3/08/S08005. URL: <https://dx.doi.org/10.1088/1748-0221/3/08/S08005>.
- [42] R. Aaij et al. “Test of lepton universality in $b \rightarrow s\ell^+\ell^-$ decays”. In: *Phys. Rev. Lett.* 131.5 (2023), p. 051803. DOI: 10.1103/PhysRevLett.131.051803. arXiv: [2212.09152 \[hep-ex\]](https://arxiv.org/abs/2212.09152).
- [43] R. Aaij et al. “Measurement of lepton universality parameters in $B^+ \rightarrow K^+\ell^+\ell^-$ and $B^0 \rightarrow K^{*0}\ell^+\ell^-$ decays”. In: *Phys. Rev. D* 108.3 (2023), p. 032002. DOI: 10.1103/PhysRevD.108.032002. arXiv: [2212.09153 \[hep-ex\]](https://arxiv.org/abs/2212.09153).

[44] J.-T. et al. Wei. “Measurement of the Differential Branching Fraction and Forward-Backward Asymmetry for $B \rightarrow K^{(*)}l^+l^-$ ”. In: *Phys. Rev. Lett.* 103 (17 Oct. 2009), p. 171801. DOI: 10.1103/PhysRevLett.103.171801. URL: <https://link.aps.org/doi/10.1103/PhysRevLett.103.171801>.

[45] J. P. et al. Lees. “Measurement of branching fractions and rate asymmetries in the rare decays $B \rightarrow K^{(*)}\ell^+\ell^-$ ”. In: *Phys. Rev. D* 86 (3 Aug. 2012), p. 032012. DOI: 10.1103/PhysRevD.86.032012. URL: <https://link.aps.org/doi/10.1103/PhysRevD.86.032012>.

[46] Roel Aaij et al. “Test of lepton universality in beauty-quark decays”. In: *Nature Phys.* 18.3 (2022). [Addendum: *Nature Phys.* 19, (2023)], pp. 277–282. DOI: 10.1038/s41567-023-02095-3. arXiv: 2103.11769 [hep-ex].

[47] Bernat Capdevila, Andreas Crivellin, and Joaquim Matias. “Review of Semileptonic B Anomalies”. In: (Sept. 2023). arXiv: 2309.01311 [hep-ph].

[48] J. P. et al Lees. “Evidence for an Excess of $\bar{B} \rightarrow D^{(*)}\tau^-\bar{\nu}_\tau$ Decays”. In: *Phys. Rev. Lett.* 109 (10 Sept. 2012), p. 101802. DOI: 10.1103/PhysRevLett.109.101802. URL: <https://link.aps.org/doi/10.1103/PhysRevLett.109.101802>.

[49] S. et al. Hirose. “Measurement of the τ lepton polarization and $R(D^*)$ in the decay $\bar{B} \rightarrow D^*\tau^-\bar{\nu}_\tau$ with one-prong hadronic τ decays at Belle”. In: *Phys. Rev. D* 97 (1 Jan. 2018), p. 012004. DOI: 10.1103/PhysRevD.97.012004. URL: <https://link.aps.org/doi/10.1103/PhysRevD.97.012004>.

[50] R. et al. Aaij. “Measurement of the Ratios of Branching Fractions $\mathcal{R}(D^*)$ and $\mathcal{R}(D^0)$ ”. In: *Phys. Rev. Lett.* 131 (11 Sept. 2023), p. 111802. DOI: 10.1103/PhysRevLett.131.111802. URL: <https://link.aps.org/doi/10.1103/PhysRevLett.131.111802>.

[51] *Averages of b-hadron, c-hadron, and τ -lepton properties as of 2021*. DOI: <https://hflav.web.cern.ch>. URL: <https://hflav.web.cern.ch>.

[52] Qiaoyi Wen and Fanrong Xu. “Global fits of new physics in $b \rightarrow s$ after the $RK^{(*)}$ 2022 release”. In: *Phys. Rev. D* 108.9 (2023), p. 095038. DOI: 10.1103/PhysRevD.108.095038. arXiv: 2305.19038 [hep-ph].

[53] Dario Buttazzo et al. “B-physics anomalies: a guide to combined explanations”. In: *JHEP* 11 (2017), p. 044. DOI: 10.1007/JHEP11(2017)044. arXiv: 1706.07808 [hep-ph].

[54] Oliver S. Bruning et al., eds. *LHC Design Report Vol.1: The LHC Main Ring*. June 2004. DOI: 10.5170/CERN-2004-003-V-1.

[55] “LHC Machine”. In: *JINST* 3 (2008). Ed. by Lyndon Evans and Philip Bryant, S08001. DOI: 10.1088/1748-0221/3/08/S08001.

- [56] *Design Study of the Large Hadron Collider (LHC): A Multiparticle Collider in the LEP Tunnel*. May 1991. DOI: 10.5170/CERN-1991-003.
- [57] *The CERN acceleration complex*. <https://cds.cern.ch/record/2636343>.
- [58] The ALICE Collaboration. “The ALICE experiment at the CERN LHC”. In: *Journal of Instrumentation* 3.08 (Aug. 2008), S08002. DOI: 10.1088/1748-0221/3/08/S08002. URL: <https://dx.doi.org/10.1088/1748-0221/3/08/S08002>.
- [59] The ATLAS Collaboration. “The ATLAS Experiment at the CERN Large Hadron Collider”. In: *Journal of Instrumentation* 3.08 (Aug. 2008), S08003. DOI: 10.1088/1748-0221/3/08/S08003. URL: <https://dx.doi.org/10.1088/1748-0221/3/08/S08003>.
- [60] The CMS Collaboration. “The CMS experiment at the CERN LHC”. In: *Journal of Instrumentation* 3.08 (Aug. 2008), S08004. DOI: 10.1088/1748-0221/3/08/S08004. URL: <https://dx.doi.org/10.1088/1748-0221/3/08/S08004>.
- [61] *High Luminosity LHC Project*. <https://hilumilhc.web.cern.ch/content/hl-lhc-project>.
- [62] *Public CMS Luminosity Information*. <https://twiki.cern.ch/twiki/bin/view/CMSPublic/LumiPublicResults>.
- [63] Javier Mazzitelli et al. “B-hadron production at the LHC from bottom-quark pair production at NNLO+PS”. In: *Physics Letters B* 843 (2023), p. 137991. ISSN: 0370-2693. DOI: <https://doi.org/10.1016/j.physletb.2023.137991>. URL: <https://www.sciencedirect.com/science/article/pii/S0370269323003258>.
- [64] Grazzini M. et al Catani S. Devoto S. “Bottom-quark production at hadron colliders: fully differential predictions in NNLO QCD”. In: *Journal of High Energy Physics* 29 (2021). DOI: [https://doi.org/10.1007/JHEP03\(2021\)029](https://doi.org/10.1007/JHEP03(2021)029). URL: [https://link.springer.com/article/10.1007/JHEP03\(2021\)029#citeas](https://link.springer.com/article/10.1007/JHEP03(2021)029#citeas).
- [65] *CMS detector*. <https://cms.cern/detector>.
- [66] G. L. Bayatian et al. *CMS Physics: Technical Design Report Volume 1: Detector Performance and Software*. 2006.
- [67] Armen Tumasyan et al. “The Phase-2 Upgrade of the CMS Tracker”. In: (June 2017). Ed. by K. Klein. DOI: 10.17181/CERN.QZ28.FLHW.
- [68] *The CMS electromagnetic calorimeter project: Technical Design Report*. 1997.

- [69] *The CMS hadron calorimeter project: Technical Design Report*. 1997.
- [70] The CMS collaboration. “Determination of jet energy calibration and transverse momentum resolution in CMS”. In: *Journal of Instrumentation* 6.11 (Nov. 2011), P11002. DOI: 10.1088/1748-0221/6/11/P11002. URL: <https://dx.doi.org/10.1088/1748-0221/6/11/P11002>.
- [71] G. Acquistapace et al. *CMS, the magnet project: Technical design report*. May 1997.
- [72] A. Tapper and Darin Acosta, eds. *CMS Technical Design Report for the Level-1 Trigger Upgrade*. June 2013.
- [73] P. Sphicas, ed. *CMS: The TriDAS project. Technical design report, Vol. 2: Data acquisition and high-level trigger*. Dec. 2002.
- [74] A.M. Sirunyan et al. “Particle-flow reconstruction and global event description with the CMS detector”. In: *Journal of Instrumentation* 12.10 (2017), P10003. DOI: 10.1088/1748-0221/12/10/P10003. arXiv: 1706.04965 [physics.ins-det].
- [75] A.M. Sirunyan et al. “Performance of the CMS muon detector and muon reconstruction with proton-proton collisions at $\sqrt{s}=13$ TeV”. In: *Journal of Instrumentation* 13.06 (June 2018), P06015. DOI: 10.1088/1748-0221/13/06/P06015. URL: <https://dx.doi.org/10.1088/1748-0221/13/06/P06015>.
- [76] *Particle-flow commissioning with muons and electrons from J/Ψ and W events at 7 TeV*. 2010.
- [77] Albert M Sirunyan et al. “Measurement of properties of $B_s^0 \rightarrow \mu^+ \mu^-$ decays and search for $B^0 \rightarrow \mu^+ \mu^-$ with the CMS experiment”. In: *JHEP* 04 (2020), p. 188. DOI: 10.1007/JHEP04(2020)188. arXiv: 1910.12127 [hep-ex].
- [78] Aaij et al. “Measurement of the ratio of branching fractions $\mathcal{B}(B_c^+ \rightarrow J/\psi \tau^+ \nu_\tau)/\mathcal{B}(B_c^+ \rightarrow J/\psi \mu^+ \nu_\mu)$ ”. In: *Phys. Rev. Lett.* 120 (12 Mar. 2018), p. 121801. DOI: 10.1103/PhysRevLett.120.121801. URL: <https://link.aps.org/doi/10.1103/PhysRevLett.120.121801>.
- [79] *LHCb technical design report: Reoptimized detector design and performance*. Sept. 2003.
- [80] F. Archilli et al. “Performance of the Muon Identification at LHCb”. In: *JINST* 8 (2013), P10020. DOI: 10.1088/1748-0221/8/10/P10020. arXiv: 1306.0249 [physics.ins-det].
- [81] V. V. Kiselev. *Exclusive decays and lifetime of B_c meson in QCD sum rules*. Nov. 2002. arXiv: hep-ph/0211021.

[82] J Chang C Wang and X Wu. “BCVEGPY2.0: An upgraded version of the generator BCVEGPY with the addition of hadroproduction of the P-wave B_c states”. In: *Comput.Phys.Communication* 174 (2006), p. 11. DOI: 10.1016/j.cpc.2005.09.008.

[83] Florian U. Bernlochner et al. *Das ist der HAMMER: Consistent new physics interpretations of semileptonic decays*. URL: <https://arxiv.org/abs/2002.00020>.

[84] *Golden JSON CMS public*. <https://twiki.cern.ch/twiki/bin/view/CMSPublic/SWGuideGoodLumiSectionsJSONFile>.

[85] *CMS Open Data*. <https://opendata.cern.ch/docs/cms-mc-production-overview>.

[86] Aaij et al. “Measurement of the B_c^- meson production fraction and asymmetry in 7 and 13 TeV pp collisions”. In: *Physical Review D* 100.112006 (2019). ISSN: 112006. DOI: 10.1103/PhysRevD.100.112006. URL: <https://journals.aps.org/prd/abstract/10.1103/PhysRevD.100.112006>.

[87] R. et al. Aaij. “Observation of a baryonic B_c^+ decay”. In: *Phys. Rev. Lett.* 113 (5 2014), p. 152003. DOI: 10.1103/PhysRevLett.113.152003. URL: <https://link.aps.org/doi/10.1103/PhysRevLett.113.152003>.

[88] R. et al. Aaij. “Observation of the decay $B_c^+ \rightarrow J/\psi K^+ K^- \pi^+$ ”. In: *JHEP* 11 (2013), p. 094. DOI: 10.1007/JHEP11(2013)094.

[89] Aaij et al. “Observation of $B_c^+ \rightarrow J/\psi D_s^+$ and $B_c^+ \rightarrow J/\psi D_s^* +$ decays”. In: *Physical Review D* 87 (2014). ISSN: 112012. DOI: 10.1103/PhysRevD.87.112012. URL: <https://journals.aps.org/prd/abstract/10.1103/PhysRevD.87.112012>.

[90] G. Aad et al. “Study of the $B_c^+ \rightarrow J/\psi D_s^+$ and $B_c^+ \rightarrow J/\psi D_s^* +$ decays with the ATLAS detector”. In: *The European Physical Journal C* 76 (1 2016), pp. 1, 4. ISSN: 1,4. DOI: 10.1140/epjc/s10052-015-3743-8. URL: <https://inspirehep.net/literature/1385102>.

[91] R. et al. Aaij. “Observation of $B_c^+ \rightarrow J/\psi D^{(*)} K^{(*)}$ decays”. In: *Phys. Rev. D* 95 (3 Feb. 2017), p. 032005. DOI: 10.1103/PhysRevD.95.032005. URL: <https://link.aps.org/doi/10.1103/PhysRevD.95.032005>.

[92] *B_c GEN Decay files for EvtGen*. URL: https://gitlab.cern.ch/lhcb-datapkg/Gen/DecFiles/-/blob/master/dkfiles/Bc_JpsiCharm2Body_mm, muX=JpsiLeptonInAcceptance.dec.

[93] C Chang et al. “BCVEGPY: an event generator for hadronic production of the B_c meson”. In: *Comput.Phys.Communication* 159 (2004), p. 33. DOI: 10.1016/j.cpc.2004.02.005.

[94] Anders Ryd et al. *EvtGen: A Monte Carlo Generator for B-Physics*. May 2005.

[95] *Fragment for $B_c \rightarrow J/\psi + \mu$* . <https://github.com/friti/RJpsiTools/blob/master/evtgen/RJpsi-BcToXToJpsiMuMu-RunIISummer19UL18GEN-fragment.py>.

[96] Torbjörn Sjöstrand et al. “An introduction to PYTHIA 8.2”. In: *Comput. Phys. Commun.* 191 (2015), pp. 159–177. DOI: 10.1016/j.cpc.2015.01.024. arXiv: 1410.3012 [hep-ph].

[97] Vardan Khachatryan et al. “Measurement of the total and differential inclusive B^+ hadron cross sections in pp collisions at $\sqrt{s} = 13$ TeV”. In: *Phys. Lett. B* 771 (2017), pp. 435–456. DOI: 10.1016/j.physletb.2017.05.074. arXiv: 1609.00873 [hep-ex].

[98] *Forced decays used for the production of $H_b \rightarrow J/\psi \mu/X$ background*. URL: <https://github.com/friti/RJpsiTools/blob/master/evtgen/HbToJpsiMuMuInclusive.dec>.

[99] *Forced decays in CMSSW*. URL: https://github.com/cms-data/GeneratorInterface-EvtGenInterface/blob/master/DECAY_2014_NOLONGLIFE.DEC.

[100] *Fragment for $H_b \rightarrow J/\psi + X$* . <https://github.com/friti/RJpsiTools/blob/master/evtgen/RJpsi-HbToJpsiMuMu-RunIISummer19UL18-fragment.py>.

[101] *Fragment for $H_b \rightarrow J/\psi + \mu$* . <https://github.com/friti/RJpsiTools/blob/master/evtgen/RJpsi-HbToJpsiMuMu-3MuFilter-RunIISummer19UL18-fragment.py>.

[102] Giovanni Petrucciani, Andrea Rizzi, and Carl Vuosalo. “Mini-AOD: A New Analysis Data Format for CMS”. In: *J. Phys. Conf. Ser.* 664.7 (2015), p. 7. DOI: 10.1088/1742-6596/664/7/072052. arXiv: 1702.04685 [physics.ins-det].

[103] R. et al. Aaij. “Measurement of the Ratio of Branching Fractions $\mathcal{B}(B_c^+ \rightarrow J/\psi \tau^+ \nu_\tau) / \mathcal{B}(B_c^+ \rightarrow J/\psi \mu^+ \nu_\mu)$ ”. In: *Phys. Rev. Lett.* 120 (12 Mar. 2018), p. 121801. DOI: 10.1103/PhysRevLett.120.121801. URL: <https://link.aps.org/doi/10.1103/PhysRevLett.120.121801>.

[104] R. Et al. Aaij. “Measurement of the Ratio of Branching Fractions $\mathcal{B}(\bar{B}^0 \rightarrow D^{*+} \tau^- \bar{\nu}_\tau) / \mathcal{B}(\bar{B}^0 \rightarrow D^{*+} \mu^- \bar{\nu}_\mu)$ ”. In: *Phys. Rev. Lett.* 115 (11 Sept. 2015), p. 111803. DOI: 10.1103/PhysRevLett.115.111803. URL: <https://link.aps.org/doi/10.1103/PhysRevLett.115.111803>.

- [105] Jona Motta. *Testing Lepton Flavour Universality in semi-leptonic decays of the B_c meson: a feasibility study in CMS*. 2018. URL: https://indico.cern.ch/event/1220720/contributions/5136871/attachments/2548653/4424563/LFNU_Jona_Motta.pdf.
- [106] *CMS Muon POG*. DOI: <https://twiki.cern.ch/twiki/bin/view/CMSPublic/WorkBookMiniAOD2015#Muons>. URL: <https://twiki.cern.ch/twiki/bin/view/CMSPublic/WorkBookMiniAOD2015#Muons>.
- [107] Python Keras Library. URL: <https://keras.io>.
- [108] M. Oreglia. “A study of the Reactions $\psi' \rightarrow \gamma\gamma\psi$ ”. In: *SLAC-R-0236* (1980).
- [109] *Hammer Website*. <https://hammer.physics.lbl.gov/>.
- [110] Brian Colquhoun et al. *B_c decays from highly improved staggered quarks and NRQCD*. 2016. arXiv: 1611.01987 [hep-lat].
- [111] D. Ebert, R. N. Faustov, and V. O. Galkin. “Weak decays of the B_c meson to charmonium and D mesons in the relativistic quark model”. In: *Phys. Rev. D* 68 (9 Nov. 2003), p. 094020. DOI: 10.1103/PhysRevD.68.094020. URL: <https://link.aps.org/doi/10.1103/PhysRevD.68.094020>.
- [112] *Twiki Pileup*. <https://twiki.cern.ch/twiki/bin/view/CMSPublic/SWGuideFastSimPileUp>.
- [113] *Test of sPlots method*. DOI: https://root.cern/doc/master/TestSPlot_8C.html. URL: https://root.cern/doc/master/TestSPlot_8C.html.
- [114] “Measurement of $B_c(2S)^+$ and $B_c^*(2S)^+$ cross section ratios in proton-proton collisions at $\sqrt{s} = 13$ TeV”. In: *Phys. Rev. D* 102 (Nov. 2020), p. 092007. DOI: 10.1103/PhysRevD.102.092007. URL: <https://doi.org/10.1103/PhysRevD.102.092007>.
- [115] *Twiki Muon Scale Factors CMS*. <https://twiki.cern.ch/twiki/bin/viewauth/CMS/MuonUL2018>.
- [116] *Twiki Tag and Probe CMS*. <https://twiki.cern.ch/twiki/bin/view/CMSPublic/TagAndProbe>.
- [117] D. Ebert, R. N. Faustov, and V. O. Galkin. “Semileptonic and nonleptonic decays of B_c mesons to orbitally excited heavy mesons in the relativistic quark model”. In: *Physical Review D* 82.3 (Aug. 2010). ISSN: 1550-2368. DOI: 10.1103/physrevd.82.034019. URL: <http://dx.doi.org/10.1103/PhysRevD.82.034019>.

[118] D. Ebert, R. N. Faustov, and V. O. Galkin. “Weak decays of the B_c meson to charmonium and D mesons in the relativistic quark model”. In: *Physical Review D* 68.9 (Nov. 2003). ISSN: 1089-4918. DOI: 10.1103/physrevd.68.094020. URL: <http://dx.doi.org/10.1103/PhysRevD.68.094020>.

[119] ChaoHsi Chang et al. “Some of semileptonic and nonleptonic decays of B_c meson in a Bethe-Salpeter relativistic quark model”. In: *Science China Physics, Mechanics & Astronomy* 58.7 (July 2015), pp. 1–13. ISSN: 1869-1927. DOI: 10.1007/s11433-015-5671-x. URL: <https://doi.org/10.1007/s11433-015-5671-x>.

[120] Mikhail A. Ivanov, Jürgen G. Körner, and Pietro Santorelli. “Exclusive semileptonic and nonleptonic decays of the B_c meson”. In: *Phys. Rev. D* 73 (5 Mar. 2006), p. 054024. DOI: 10.1103/PhysRevD.73.054024. URL: <https://link.aps.org/doi/10.1103/PhysRevD.73.054024>.

[121] Tao Huang and Fen Zuo. “Semileptonic B_c decays and charmonium distribution amplitude”. In: *The European Physical Journal C* 51.4 (Aug. 2007), pp. 833–839. ISSN: 1434-6052. DOI: 10.1140/epjc/s10052-007-0333-4. URL: <http://dx.doi.org/10.1140/epjc/s10052-007-0333-4>.

[122] Wei Wang, Yue-Long Shen, and Cai-Dian Lü. “Covariant light-front approach for B_c transition form factors”. In: *Physical Review D* 79.5 (Mar. 2009). ISSN: 1550-2368. DOI: 10.1103/physrevd.79.054012. URL: <http://dx.doi.org/10.1103/PhysRevD.79.054012>.

[123] E. Hernández, J. Nieves, and J. M. Verde-Velasco. “Study of exclusive semileptonic and nonleptonic decays of B_c^- in a non relativistic quark model”. In: *Physical Review D* 74.7 (Oct. 2006). ISSN: 1550-2368. DOI: 10.1103/physrevd.74.074008. URL: <http://dx.doi.org/10.1103/PhysRevD.74.074008>.

[124] Pietro Colangelo and Fulvia De Fazio. “Using heavy quark spin symmetry in semileptonic B_c decays”. In: *Physical Review D* 61.3 (Jan. 2000). ISSN: 1089-4918. DOI: 10.1103/physrevd.61.034012. URL: <http://dx.doi.org/10.1103/PhysRevD.61.034012>.

[125] I. P. Gouz et al. “Prospects for the B_c studies at LHCb”. In: *Physics of Atomic Nuclei* 67.8 (Aug. 2004), pp. 1559–1570. ISSN: 1562-692X. DOI: 10.1134/1.1788046. URL: <http://dx.doi.org/10.1134/1.1788046>.

[126] A. Abd El-Hady, J. H. Muñoz, and J. P. Vary. “Semileptonic and nonleptonic B_c decays”. In: *Physical Review D* 62.1 (June 2000). ISSN: 1089-4918. DOI: 10.1103/physrevd.62.014019. URL: <http://dx.doi.org/10.1103/PhysRevD.62.014019>.

- [127] Chao-Hsi Chang and Yu-Qi Chen. “Decays of the B_c meson”. In: *Phys. Rev. D* 49 (7 Apr. 1994), pp. 3399–3411. DOI: 10.1103/PhysRevD.49.3399. URL: <https://link.aps.org/doi/10.1103/PhysRevD.49.3399>.
- [128] M. A. Ivanov, J. G. Körner, and P. Santorelli. “Semileptonic decays of the B_c meson”. In: *Physical Review D* 63.7 (Mar. 2001). ISSN: 1089-4918. DOI: 10.1103/physrevd.63.074010. URL: <http://dx.doi.org/10.1103/PhysRevD.63.074010>.
- [129] Daryl Scora and Nathan Isgur. “Semileptonic meson decays in the quark model: An update”. In: *Physical Review D* 52.5 (Sept. 1995), pp. 2783–2812. ISSN: 0556-2821. DOI: 10.1103/physrevd.52.2783. URL: <http://dx.doi.org/10.1103/PhysRevD.52.2783>.
- [130] A. Yu. Anisimov et al. “Exclusive and inclusive decays of the B_c meson in the light front ISGW model”. In: *Phys. Atom. Nucl.* 62 (1999), pp. 1739–1753. arXiv: [hep-ph/9809249](https://arxiv.org/abs/hep-ph/9809249).
- [131] Wei Wang and Ruilin Zhu. “Model-independent investigation of the $R(J/\psi, \eta_c)$ and ratios of decay widths of semileptonic B_c decays into a P-wave charmonium”. In: *International Journal of Modern Physics A* 34.31 (Nov. 2019), p. 1950195. ISSN: 1793-656X. DOI: 10.1142/s0217751x19501951. URL: <http://dx.doi.org/10.1142/S0217751X19501951>.
- [132] Zi-Kan Geng et al. “Relativistic effects in the semileptonic B_c decays to charmonium with the Bethe-Salpeter method”. In: *Physical Review D* 99.1 (Jan. 2019). ISSN: 2470-0029. DOI: 10.1103/physrevd.99.013006. URL: <http://dx.doi.org/10.1103/PhysRevD.99.013006>.
- [133] Domagoj Leljak, Blazenka Melic, and Monalisa Patra. “On lepton flavour universality in semileptonic $B_c \rightarrow \eta_c, J/\psi$ decays”. In: *JHEP* 05 (2019), p. 094. DOI: 10.1007/JHEP05(2019)094. arXiv: [1901.08368 \[hep-ph\]](https://arxiv.org/abs/1901.08368).
- [134] P.A. Zyla et al. “Review of Particle Physics”. In: *PTEP* 2020.8 (2020), p. 083C01. DOI: 10.1093/ptep/ptaa104.
- [135] R. et al. Aaij. “Observation of $B_c^+ \rightarrow J/\psi D_s^+$ and $B_c^+ \rightarrow J/\psi D_s^{*+}$ decays”. In: *Phys. Rev. D* 87 (11 June 2013), p. 112012. DOI: 10.1103/PhysRevD.87.112012. URL: <https://link.aps.org/doi/10.1103/PhysRevD.87.112012>.
- [136] *Study of the $B_c^+ \rightarrow J/\psi D_s^+$ and $B_c^+ \rightarrow J/\psi D_s^{*+}$ decays in pp collisions at $\sqrt{s} = 13$ TeV with the ATLAS detector*. Tech. rep. Geneva: CERN, Aug. 2021. URL: <http://cds.cern.ch/record/2779181>.

- [137] Glen Cowan et al. “Asymptotic formulae for likelihood-based tests of new physics”. In: *Eur. Phys. J. C* 71 (2011). [Erratum: Eur.Phys.J.C 73, 2501 (2013)], p. 1554. DOI: 10.1140/epjc/s10052-011-1554-0. arXiv: 1007.1727 [physics.data-an].
- [138] Aram Hayrapetyan et al. “Test of lepton flavor universality in $B^\pm \rightarrow K^\pm \mu^+ \mu^-$ and $B^\pm \rightarrow K^\pm e^+ e^-$ decays in proton-proton collisions at $\sqrt{s} = 13$ TeV”. In: (Jan. 2024). arXiv: 2401.07090 [hep-ex].
- [139] *Test of lepton flavor universality violation in semileptonic B_c^+ meson decays at CMS*. 2023. URL: <https://inspirehep.net/literature/2693338>.